Morphology and dynamics of headland connected sandbanks from high resolution bathymetric surveys:

Helwick and Nash Sands, Bristol Channel, U.K.

Thierry Gilles Schmitt

Thesis submitted for the degree of Doctor of Philosophy
School of Earth, Ocean and Planetary Sciences, Cardiff University

January 2006

ProQuest LLC
789 East Eisenhower Parkway
P.O. Box 1346
Ann Arbor, MI 48106-1346

Acknowledgement

My deepest thanks are due to Dr. Neil Mitchell and Dr. Tony Ramsay who supervised this PhD work. I have especially appreciated Dr. Mitchell comments, help, corrections, criticism and support. I am grateful to the School of Earth, Ocean and Planetary Sciences of Cardiff University for their financial support.

During this work, I met some specialists of the coastal and marine research community who provided me with valuable advice on the interpretation of seabed morphology, on the analysis of tidal and wave current records and on sediment transport processes around sandbanks. Prof. Alex Bastos (Universidade Salvador, Brasil), Dr. Alain Trentesaux (Université de Lille I, France) and Dr. Serge Berné (IFREMER, France) provided valuable comments to a contribution to a Geological Society Special Publication (to be published). I also wish to acknowledge Dr. Richard Soulsby (HR Wallingford, UK), Prof. Mike Collins (SOC, UK) and Dr. Neil Kenyon (SOC, UK) for their words of encouragement and advice on sediment transport. Dr Goff (University of Texas, USA) and Dr. Urgeles (University of Barcelona) provided valuable comments on bathymetric data processing and the estimation of uncertainties. Data acquisition at sea would not have been possible without the financial support of the Royal Society, the NERC, United Utilities Green Energy Ltd., Countryside Council for Wales, Hanson Aggregates, RMC Aggregates and UMD. The crews of the New Ross I and the Strathdoon are warmly thanked for coping with our modification of their boats and our perpetual changes of plans at sea. Some data used here were provided by ABP MER (Mr. Bill Cooper), Longdin and Browning Ltd., the British Oceanographic Data Centre and Llannelli Sand Dredging Ltd. (Dr. Chris Davies).

Finally, I must give my warmest greetings to my Cardiff friends: Carys, Jake, Awen, Cristina, Rubén, Neils, Pedro, Anabela, José, Valente and his family, Màtè and his family and all the others I have unintentionally forgotten. I also have a thought for my my familly: Oncle O, Anne-Françoise, Cédric, Simone, Gilbert, Mireille, Guy, Joris, Victor, Maria; and my best friends Edouard and his family, Vincent, Diego and Geneviève, Thierry, Nicolas, Hakim and Angèle.

Merci, enfin aux plus belles : Marie et Amélie, qui m'ont aidé à dissiper mes angoisses doctorales.

A Pierre et Marion.

Abstract

Morphology and movements of sand dunes are studied using repeated high-resolution bathymetric data in areas where banner banks approach the shore. Two sites in the Bristol Channel were selected for their contrasting environments. The Helwick Sands is characterised by deeper water-depths, stronger wave climates and weaker tidal currents than the Nash Sands.

At the Helwick, migrations of the dunes were measured ranging between 21 and 109 $m.y^{-1}$. Dunes crossing its crest and connecting despite opposite direction of migration on either flank were observed. This geometry is interpreted to be the result of the strong wave climate coupled with a nearly rectilinear tidal flow, which are leading to dune crests extension. A morphometric study of the sand dunes has revealed the tendency for the dunes to flatten in shallow water, which can also be attributed to the effect of the waves.

At the Nash, strong currents and breaking waves have created a strong crestal escarpment. Dune migration rates along the flanks were measured to range from 34 to 180 $m.y^{-1}$, based on a comparison of surveys 263 days apart. However, in the Nash Passage (between East Nash and the coast) short term (19 days) sand dunes migration measurements revealed very fast moving (up to 715 $m.y^{-1}$) small short-living sand dunes.

Celerity and morphology of the dunes were used to compute sand transport specific fluxes. Such fluxes are broadly compatible with fluxes computed from tidal current data using bedload transport formulae. For both banks, the geometry of the flux vector field suggests a clockwise sand transport pattern around the banks. Although different intensities of the fluxes were expected at the two sites, the fluxes of corresponding morphological areas are similar. Differences in the tidal current asymmetry and reduced effective threshold of sand transport due to the wave energy are invoked to explain theses similarities.

Pattern of erosion and deposition were evaluated from the divergence of sand fluxes. This pattern has revealed the occurrence of transients in the sand transport, which are the result of complex interactions between the flow, the headland and the bed morphology.

Extended abstract

Headland-associated banks, also known as banner sandbanks are complex large bedforms present within coastal and estuarine environments that occur near sharp coastal promontories. They are important because they constitute a source of aggregates, provide a natural habitat for biological species and act as wave barriers limiting the erosion of the nearby coasts. Various hydro-sedimentological concepts have been proposed to explain their origin and maintenance. These involve the presence of eddies originating at the headland, associated secondary flows (in the vertical) and the convergence of sand transport towards the crest of the bank. The main motivation of the present thesis is to present quantitative morphological and kinematic evidence describing the dominant tidal and wave-related mechanisms involved in the present day sand transport around banner sandbanks.

Two banner sandbanks, Helwick and Nash Sands, were investigated. The banks were chosen because of their contrasting environments. The Helwick Sands is characterised by deeper water-depths, stronger wave climates and weaker tidal currents than the Nash Sands. The comparison of both sites is based on the interpretation of bathymetric data acquired repeatedly around the connection of these banks with the shore. Multibeam swathe (Reson Seabat 8101) and single-beam sonar surveys were undertaken, providing the first multibeam survey of this type of environment. A method for estimating the relative vertical uncertainties between co-located bathymetric data was developed and provides constraints on the morphological comparison and kinematical analysis of bank-associated sand dunes. The sense of the asymmetry of sand dunes is indicative of the residual tidal currents around the banks. At the crest, dunes are more symmetrical, indicating a zone of convergence. Migration rates were derived by dune tracking between surveys, giving rates between 21 $m.y^{-1}$ and 109 $m.y^{-1}$ at the Helwick site and between 34 and 180 $m.y^{-1}$ at the Nash sites (on the basis quasi-annual surveys comparison). In the Nash Passage (the area between East Nash and the coast) a short-term (19 days) repeated survey revealed very fast moving (up to 715 $m.y^{-1}$) small short-lived sand dunes. The celerity, heights and spacing of the dunes were used to compute sand transport specific flux (typically of the order of 0.02 $kg.m^{-1}.s^{-1}$). The fluxes compare well (within an order of

magnitude) with bedload fluxes computed from current meter and sediment texture data using the widely used Gadd transport formula. Comparison of sand dune associated sand transport with numerical predictions support the idea that sand transport occurs in large part by sand dune migration associated with bedload movements.

For both banks, the geometry of dune migration indicates a clockwise sand transport pattern around the banks, which is compatible with previous observations found in the litterature. Moreover, the sand budget parallel to both banks flanks is in rough equilibrium, within the limits of the estimation method. Across-bank sand transport is more difficult to estimate but is predominantly induced by wave-induced currents. On the Helwick Sands this is particularly evident. There sand dune crests extend across the crest of the bank, despite the opposite direction of migration observed along each of the flanks. This atypical morphology is explained to be the result of the strong wave energy coupled with a quasi-rectilinear tidal flow, resulting in dune crests extension.

The pattern of erosion and deposition was derived from divergence and convergence of the specific sand flux data. For the Nash area and with less confidence for the Helwick area, the magnitudes of the calculated erosion and deposition generally agree with bathymetric changes measured by the direct differencing of co-located bathymetric data. The result revealed transient patterns of erosion and deposition along the banks near their respective headlands. Although no data of the structure of the flow was collected during the period of the study, it is hypothesised that these transients patterns of sand deposition and erosion could be related to transient pattern in the flow as observed near other banner sandbanks.

Keywords: banner sandbank, headland, dune, Bristol Channel, bathymetry, sand transport, tidal, wave, transients.

Table of content

List of figures

List of tables

List of variables

ACF	Magnitude of the autocorrelation function	-
α	Angle between wave induced current and crest of the bank	°
f	Dune shape factor	-
$\exists$	Gadd's calibrating coefficient	$kg.cm^4.s^{-2}$
θ	Angle between the current only and wave induced shear stress vectors	radians
τ	Bed shear stress	$N.m^{-2}$
θ	Angle between the current and wave propagation	rad
Φ, Φ_h, Φ_{total}, Φ_0, Φ_{th}	Standard deviation, standard deviation due to heave only measured on the nadir beam, standard deviation of an off-nadir multibeam beams, unfiltered uncorrelated noise standard deviation, theoretical filtered uncorrelated noise standard deviation of depth	data unit
υ	kinematic fluid viscosity	$m^2.s^{-1}$
ω	wave angular frequency	$rad.s^{-1}$
ρ, ρ_s	Density of the water, density of the sediment	$kg.m^{-3}$
V_{bf}	Volume of individual sand dune	m^3
γ, $\hat{\gamma}$	total semi-variance, Estimate of the variance	m^2
γ_1	Stochastic semi-variance (component of the semi-variogram of sand dunes)	m^2
γ_2	Deterministic semi-variance (component of the semi-variogram of sand dunes)	m^2
ϑ_c	Near bed shear stress vector (tidal current only)	$N.m^{-2}$
τ_{cr}	Critical shear stress for initiation of sediment motion	$N.m^{-2}$
δ_{cw}	thickness of the boundary layer in presence of current and waves	m
θ_{shield}, $\theta_{shield,cr}$	Shield's parameter, Critical Shield's parameter	-
ϑ_{wc}	Combined wave and current induced shear stress vector	$N.m^{-2}$
a	Amplitude of the deterministic (sinusoidal) component of the semi-variogram	m
A_0	Tide amplitude multiplier	-
A_b	Maximum wave orbital amplitude	m
c	Dune celerity	$m.s^{-1}$ (otherwise stated)
s	Semi-variance sill of the semi-variogram model	m^2
C_r	Coefficient of proportionality between the wave-only shear velocity and the wave and current shear velocity	-
d, d_{50}	Grain size diameter, median grain size diameter	m
f_{cw}	Wave factor	-
g	Acceleration due to gravity	$m.s^{-2}$
H_1, H_2	Recorded tidal height, corrected tidal height	m
H	Height of dune	m
h_b	Minimal depth for wave breaking	m

h, h	Lag distance vector, lag distance	m
H_{max}	Highest point along the dune crest	m
H_w	Significant wave height	m
K	Von Karman-Prandtl constant	-
k	Wave number	m^{-1}
L	Dune spacing	m
l	Wavelength of the sinusoidal component of the semi-variogram	m
q **q**	Sediment transport mass flux calculated from informations of the tidal records and wave regime (vector notation)	$kg.m^{-1}.s^{-1}$
Q_{bf}	Sand transport mass (or volume) flux estimated from dune migration	$m^3.s^{-1}.m^{-1}$ (converted to $kg.m^{-1}.s^{-1}$)
r	Semi-variogram range	m
T	Tidal height (above chart datum)	m
t	Time	s
t_0	Tidal time offset	S
T_w	Wave period	s
u_*, u_{*c}	Shear velocity at the seabed, Shear velocity of the current only (in presence of waves)	$m.s^{-1}$
$u_{*,cr}$	Critical shear velocity at seabed for initiation of sediment motion	$m.s^{-1}$
u_{*cw}	Shear velocity under the combined effect of waves and current	$m.s^{-1}$
u_{*w}	Shear velocity under the wave stress only	$m.s^{-1}$
U_0	Wave orbital speed at the seabed	$m.s^{-1}$
U_{100} **U_{100}**	Flow velocity one meter above seabed (vector notation)	$m.s^{-1}$
$u_{cr,100}$	Critical shear velocity at one meter above seabed for initiation of sediment transport	$m.s^{-1}$
U_d	Depth average current	$m.s^{-1}$
Up	Periodic tidal current velocity component	$m.s^{-1}$
Us	Steady tidal current velocity component	$m.s^{-1}$
U_w	Maximum wave orbital velocity	$m.s^{-1}$
U	Vertically averaged shear velocity (in the water column)	$m.s^{-1}$
u_z, u_{100}	Flow velocity at the height z above the seabed, flow speed at one meter above the seabed	$m.s^{-1}$
V	Sound speed velocity (unless othervise stated)	$m.s^{-1}$
y_h, z_h	horizontal and vertical distance with respect to the multibeam sonar head	m
x,y	Orthogonal horizontal coordinates	m
X_S, X_L	Dune stoss slope length, dune lee slope length	m
Y	Yalin parameter	-
z	Water depth below chart datum (unless otherwise stated)	m
z_0, z_{0c}	Friction roughness, apparent bed roughness experienced by the current only (in presence of waves)	m
z_a	Seabed roughness length	m
ξ	linear coefficient encompassing water-depth-dependant bathymetric errors	m^{-1}
Z(x,y), $\overline{Z}$	Bathymetric height at the position x,y; Spatial average of Z(x,y)	m
θ_R, θ_T, θ_L	across-track multibeam sonar angle, across-track multibeam sonar beamwidth, along-track beamwidth	rad

Rp	Regularity parameter	-
Fr	Froude number	-
$Q_{b,w}$	Specific sand transport along dune crest due to wave induced currents	$m^3.m^{-1}.s^{-1}$ (converted to $kg.m^{-1}.d^{-1}$)
Q_L	Specific sand transport induced by shoaling waves	$kg.m^{-1}.d^{-1}$
W_c	maximum width of a dune	m
V_c	Volume of a sand dune	m^3
w	filter size	m (or m^2)
N	number of data encompassed within a filter scale	-
z_w	Wave boundary layer height (above the seafloor)	m

Chapter 1.

Context of the study: banner sandbanks, associated sand dunes and sediment transport in the Bristol Channel

1.1. Introduction

A variety of offshore sand deposits (Figure 1.1) (Belderson et al., 1982; Stride et al., 1982; Dyer and Huntley, 1999) provide modern geological evidence of the across-shelf transport of sedimentary particles (Nittrouer and Wright, 1994). Evidence for these shallow marine deposits and across-shelf sediment transport can also be found in the stratigraphic record (Molgat and Arnott, 2001). The continental shelf, and more especially its shallower part is characterised by a variety of physical forcings (tide, swell, wind and storm waves, fluvial inflow). These forcings are responsible for the organisation, distribution and sedimentary dynamics of these deposits and occur at various spatial and temporal scales (Figure 1.2). Sand banks (also called banks or sand ridges) are one type of these offshore sand deposits. One particular class of sand bank (Dyer and Huntley, 1999) studied in detail in this thesis occurs in the immediate vicinity of coastal promontories and are called banner banks or headland-associated sandbanks.

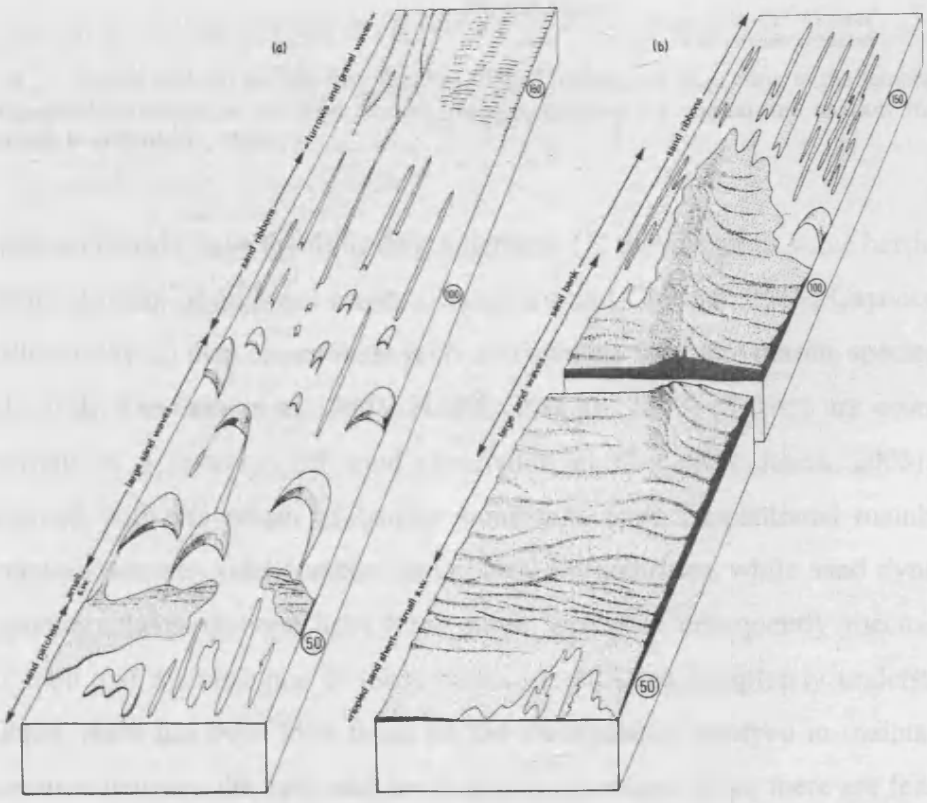

Figure 1.1 Diagram of the distribution of bedforms originating by tidal action (mean spring velocity is given in circles) on the continental shelf in (a) sediment starved and (b) abundant sediment supply environments (from Belderson et al., 1982).

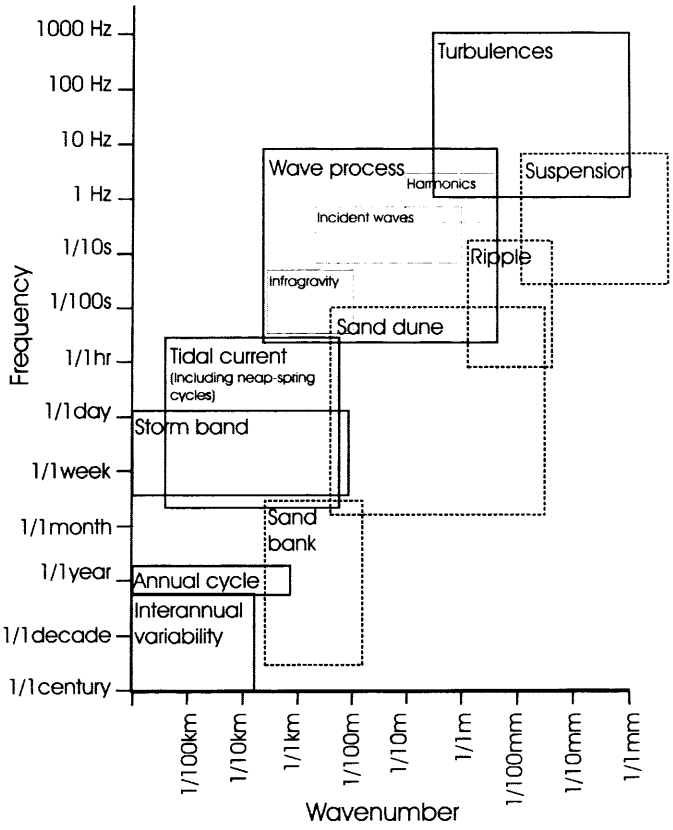

Figure 1.2 Spatial scale of sedimentary features (dotted rectangles) in relation to the temporal scale of the dominant processes in the fluid motion (plain rectangles) for coastal and shallow marine areas (modified from Holman, 1999).

Banner sandbanks have the following functions: (1) they serve as wave barriers which limit the erosion of adjacent coasts (Damgaard and Chesher, 1997; Cayocca and Du Gardin, 2003) (2) they can provide preferred habitats for some marine species (Brown et al., 2001; Dewicke et al., 2003; Harrisson et al., 2003) (3) they are economically important as a resource for sand (Brampton et al., 2002; Jones, 2003). Studies concerned with the origin of banner sandbanks have concentrated mainly on the interaction between tidal currents and coastal irregularities, while sand dynamic and morphology investigations have been more limited. Consequently mechanisms of formation and maintenance of these banks are still not completely understood. For example, there has been little focus on the mechanisms involved in maintaining the connection between the bank and the coastal promontory. Also, there are few detailed high-resolution investigations of the morphology and dynamics of these banks and associated dunes (Table 1.1 on page 1-20). This lack of information has resulted from the difficulty in collecting data at sea in this environment (Squibb, 2004) and the past limitations in surveying techniques (positioning uncertainty and resolution) and in

processing and visualising data. This thesis is intended to present new high resolution co-located bathymetric datasets from banner banks and present quantitative information on sand dune morphology and migration around the nearshore ends of these banks.

1.2. Tidal- and wave-induced sediment transport in the vicinity of sandbanks and coastal promontories

1.2.1. Tidal current interaction with bathymetric irregularities and headlands

Currents on the shelf are mainly generated by tides, which occur in response to the gravitational influence of the moon and the sun. Following Zimmerman (1981), Robinson (1983), Pattiaratchi and Collins (1987) and Huthnance (1982a,b), when the flow passes over a seabed irregularity (a sand ridge), the water is compressed, so that the flow is accelerated up the front slope. The water column is stretched on the downward slope and the flow is decelerated. Therefore the water column experiences a larger Coriolis acceleration (which depends on velocity) on its shallower areas than on its deeper areas. As potential vorticity (sum of the planetary and local vorticity, all divided by the water depth) must be conserved along the fluid trajectory, clockwise (negative) vorticity (in the northern hemisphere) is generated in the shallower part of the bank. Also, bottom friction stress will be larger in the shallower water column (since the current speed is fastest) than in the deeper water column. The tidal flow will therefore experience a friction-induced torque if its orientation is oblique to the crest of the seabed irregularity. This torque produces vorticity which is oriented clockwise (anticlockwise, resp.) as the flow moves upslope and anticlockwise (clockwise, resp.) when the water moves downslope, if the crest of the irregularity is oriented anticlockwise (clockwise, resp.) with respect to the flow. Combining both effects (Figure 1.3) results in an eddy circulation in the residual current around the bank.

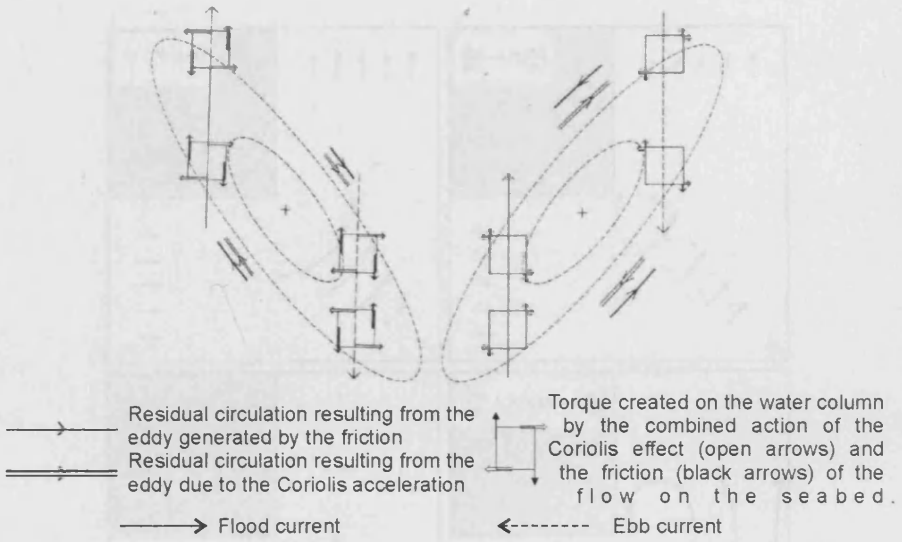

Figure 1.3 Production of eddy residual circulation (over a complete tidal cycle) over a ridge (+) in the Northern Hemisphere (from Zimmerman, 1981). In the case of a seabed feature oriented anticlockwise to the tidal axis (left), Coriolis (open arrows) and friction (filled arrows) mechanisms are additive (left). In the other case (right), the mechanisms counteract each other (right).

Interaction of rectilinear tidal currents with coastal irregularities such as headlands is another source of eddy circulation. Pingree and Maddock (1979) showed that near a headland, bottom frictional torque is induced by the increasing seabed gradient slope towards the promontory (Figure 1.4b). The vorticity is then advected away from the headland by the flow (Figure 1.4d). Because of the tidal nature of the flow tidal eddy systems are then occurring in the lee side of the headland during both the ebb and flood phases.

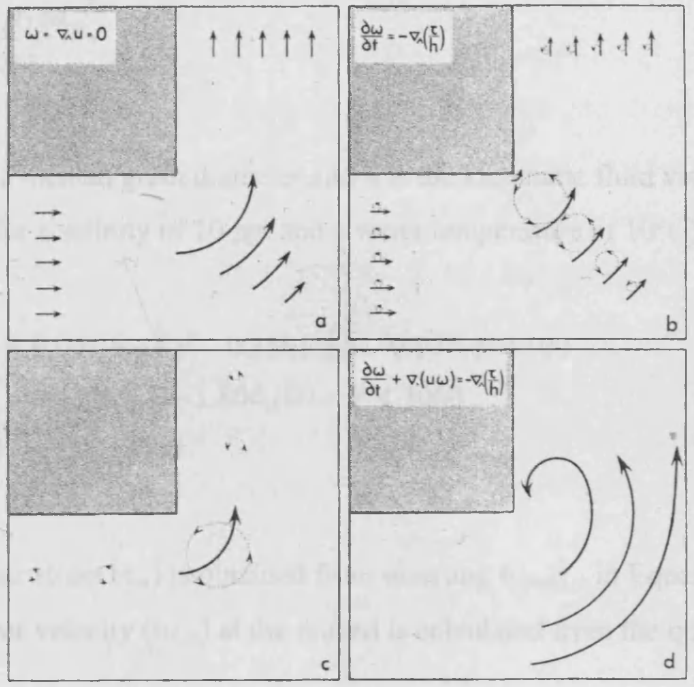

Figure 1.4 Schematic representation of the flow around a promontory (from Pingree, 1979)
(a) Irrotational case (no friction, conservation of depth, no advection and no diffusion)
(b) Introduction of friction and changes in waterdepth, inducing vorticity (dotted circles)
(c) Introduction of advection vorticity due to stretching of the water column
(d) Eddying character of the flow due to the advection of vorticity

1.2.2. Sediment transport in mixed tidal- and wave dominated environments

1.2.2.1. Threshold of sand motion

The sediment begins to move when shear stress of the moving fluid in motion exceeds the gravitational forces and the inter-particular friction which act on individual sediment particles. The dimensionless ratio of force exerted is expressed by the Shields parameter.

$$\theta_{shield} = \frac{\tau}{g(\rho_s - \rho)d} \qquad \text{Equation 1.1}$$

where τ is the bed shear-stress, ρ_s and ρ are the sand grain and water density respectively and d is the grain diameter. The Yalin method's modified by Miller et al., 1977, can be used to compute the dimensionless critical Shields ($\theta_{shield,cr}$) at which sediments start to move. This method relies on the Yalin's parameter, which is easier to measure than Shield's parameter and is defined as follows.

$$Y = \sqrt{\frac{(\rho_s - \rho) g d_{50}^{\ 3}}{\rho \upsilon^2}} \qquad \text{Equation 1.2}$$

Where d_{50} is the median grain diameter and υ is the kinematic fluid viscosity (equal to $1.3 \times 10^{-6} m^2.s^{-1}$ for a salinity of 10 ppt and a water temperature of 10°C).

$$\begin{cases} \log\theta_{shield,cr} = 0.041(\log Y)^2 - 0.356\log Y - 0.977, Y < 100 \\ \log\theta_{shield,cr} = 0.132\log Y - 1.804, 100 < Y \leq 3000 \\ \theta_{shield,cr} = 0.045, Y > 3000 \end{cases} \qquad \text{Equation 1.3}$$

The critical shear stress (τ_{cr}) is obtained from inserting $\theta_{shield,cr}$ in Equation 1.1.

The critical shear velocity ($u_{*,cr}$) at the seabed is calculated from the quadratic law:

$$\tau_{cr} = \rho u_{*,cr}^2 \qquad \text{Equation 1.4}$$

The shear velocity (u_*) at the seabed can be extrapolated to any height above it (u_z) within the boundary layer using the Von Karman-Prandl relation, with the constant K equal to 0.4:

$$\frac{u_z}{u_*} = \frac{1}{K} \ln \frac{z}{z_0} \qquad \text{Equation 1.5}$$

Hence, the critical velocity at the seabed ($u_{*,cr}$) can be extrapolated to one meter above the seabed supposing that the boundary layer extends up to this height, allowing use of the Von Karman-Prandl relation:

$$\frac{u_{cr,100}}{u_*} = \frac{1}{K} \ln \frac{100}{z_0} \qquad \text{Equation 1.6}$$

Where z_0 is the bottom roughness parameter set equal to 5 mm in accordance with values from Pattiaratchi and Collins (1984, 1985), Collins et al. (1995) and Soulsby (1997) selected for similar environments.

1.2.2.2. Estimation of specific sand flux under steady currents

It is difficult to measure sediment transport fluxes in marine environments because of the variety of mechanisms involved (sediment mobilisation and deposition, behaviour of individual sand particles during transport, etc.) and the complexity of the hydrodynamics (turbulence, presence of waves, etc.) (Carmenen and Larroudé, 2003).

As the current speed increases, the mode of sediment transport evolves from primarily bedload (hopping, saltating, sliding or toppling) to suspended load (sediment particles supported by fluid turbulence). Many different formulae are available to estimate transport by steady flows (Dyer, 1986). Attempts to evaluate these formulae in marine environments and more especially in tidal-dominated areas have shown discrepancies between measured and estimated fluxes of up to one order of magnitude (Heathershaw, 1981; Pattiaratchi and Collins, 1984; Pattiaratchi and Collins, 1985). However, amongst all the different approaches, Bagnold's (1963) method has been widely used to estimate bedload flux from current speed because of its simplicity and its physical basis based on the concept that rate of work applied on the sediment particles is proportional to the available stream power. Gadd et al. (1978) reformulated Bagnold's equation into Equation 1.7, and calibrated it with transport rates in the New York Bight.

$$\mathbf{q} = \beta(|\mathbf{U_{100}}| - U_{cr,100})^3 \frac{\mathbf{U_{100}}}{|\mathbf{U_{100}}|} \qquad \text{Equation 1.7}$$

where $\mathbf{q}$ is the transport rate, $\mathbf{U_{100}}$ is the velocity one meter above the seabed and $U_{cr,100}$ is the critical shear velocity one meter above the seafloor calculated from the previous section. Parameter ∃ is an efficiency coefficient ranging between 1.73×10^{-7} to 7.22×10^{-7} kg.cm^{-4}.s^2 (Gadd et al., 1978), and chosen equal to 5.58×10^{-7} kg.cm^4.s^{-2}, following Pattiaratchi and Collins (1985) in the Bristol Channel. The bold styles denote vectors.

1.2.2.3. Combined wave and current sand transport

Supposing waves are monochromatic with a period T_w and wave height H_w, the maximum wave orbital velocity (U_w) and amplitude (A_b) near the seabed (at water depth h), can be calculated using the relation:

$$U_w = \frac{\pi H_w}{T_w \sinh(kh)} \quad \text{and} \quad A_b = \frac{U_w}{\omega} \qquad \text{Equation 1.8 a,b}$$

Where sinh is the hyperbolic sine and k is the wave number computed iteratively from the following dispersion equation:

$$\omega^2 = gk\tanh(kh) \qquad \text{Equation 1.9}$$

where tanh is the hyperbolic tangent, ω is the wave angular frequency (ω=2π/T), g is the acceleration due to gravity.

Methods for estimating sediment transport under the combined effect of waves and currents are still under discussion (Dyer, 1986; Soulsby, 1997). The Grant and Madsen (1986) method remains the most widely used and was used in this work, owing to its extensive empirical verification (Cacchione et al., 1987; Lyne et al., 1990a; Lyne et al., 1990b; Cacchione et al., 1994). Algorithms to compute τ_{cw}, from this method were taken from the freely available SEDTRANS 96 source code (Li and Amos, 2001).

According to Grant and Madsen (1986), a wave boundary layer, with physical similarities to the current boundary layer, develops during the wave cycle. The thickness of the wave boundary layer (δ_{cw}) is defined by the equation:

$$\delta_{cw} = \frac{2Ku_{*cw}}{\upsilon} \qquad \text{Equation 1.10}$$

where K is the Von Karman constant (K=0.4) and u_{*cw} is the shear velocity under the combined wave and current stress which is assumed to be proportional to the wave-only shear velocity (u_{*w}) as follows:

$$u_{*cw} = u_{*w}C_r^{0.5} \qquad \text{Equation 1.11}$$

and

$$u_{*w} = \left(\frac{C_r f_{cw} u_b^2}{2}\right)^{0.5} \qquad \text{Equation 1.12}$$

The wave current factor (f_{cw}) is determined iteratively from the following equation assuming an arbitrary ratio of wave to current C_r initially equal to one:

$$\frac{1}{4f_{cw}^{0.5}} + \log\left(\frac{1}{4f_{cw}^{0.5}}\right) = \log\left(\frac{C_r ub}{\omega z_0}\right) + 0.14(4f_{cw}^{0.5}) - 1.65 \qquad \text{Equation 1.13}$$

As outlined by Grant and Madsen (1986), within the wave boundary layer the following equation governs the near-bed velocity in the case of combined current and wave flows:

$$u_z = \frac{u_{*c}^2}{Ku_{*cw}} \ln\frac{z}{z_0} \qquad \text{Equation 1.14}$$

where u_{*c} is the total current shear.

Above the boundary layer the equation governing the shear velocity is written as follows

$$u_z = \frac{u_{*c}}{K} \ln \frac{z}{z_{0c}} \qquad \text{Equation 1.15}$$

where z_{0c} is the apparent bed roughness experience by the current in presence of waves. By matching the current within the wave boundary layer (Equation 1.14) with the current above the boundary layer (Equation 1.15) at $z = \delta_{cw}$ within the following equation allows to compute u_{*c}

$$u_z = \frac{u_{*c}}{K}\left[\left(\frac{u_{*c}}{u_{*cw}}\right)\ln\left(\frac{\delta_{cw}}{z_0}\right) + \ln\left(\frac{z}{\delta_{cw}}\right)\right] \qquad \text{Equation 1.16}$$

Combining Equations 1.9 to 1.15 with 1.16, allows to evaluate C_r, as follows:

$$C_r = \left[1 + 2\left(\frac{u_{*c}}{u_{*w}}\right)^2 \cos\theta + \left(\frac{u_{*c}}{u_{*w}}\right)^4\right]^{0.5} \qquad \text{Equation 1.17}$$

where θ is the acute angle between the tidal current and the direction of wave propagation. C_r is reinserted in Equations 1.12 and estimates of u_{*c}, u_{*w}, u_{*cw} and f_{cw} are refined until numerical convergence on C_r is reached. Using the Karman-Prandtl relation describing the logarithmic profile of the current, the total shear stress at the bottom (once convergence on Cr as been reached) can be converted to the velocity at one meter above the seabed and inserted in Equation 1.1. Vectorial addition of the current induced shear stress only and the wave induced shear stress is used to obtain the direction of the total shear stress under the combined action of the tidal and wave currents.

1.3. Sand banks

Sand banks are significant features of continental shelves and coastal regions. They can be up to several tens of kilometres in length and have length/width ratios greater than 40 (Amos and King, 1984). Their locations depend generally on the presence of tidal currents strong enough to mobilise sand and the availability of sand. They are found in open seas, mouths of estuaries and adjacent to headlands (Dyer and Huntley, 1999). One of the most accepted explanation for their origin is that they are the product of the interaction between currents and associated sediment transport with a

bathymetric irregularity as the post-glacial sea-level is rising (Berné et al., 1998; Reynaud et al., 2003). These authors suggested that a rapid sea-level rise may lead to the preservation of a sandbank as a "moribund bank". This notion of moribund banks was introduced by Kenyon et al. (1981), who used it to describe sandbanks showing no evidence of active sedimentary transport (such as sand dune migration) and lying in areas of weak currents.

Sandbanks are believed to be maintained by present day local sediment transport regimes (Berné et al., 1998) that could differ from the regimes involved in their formation (Pattiaratchi and Collins, 1987; Dyer and Huntley, 1999). The sand that composes the sandbanks generally originates from the erosion of adjacent coastal or seabed areas. It is generally a relatively well sorted medium to coarse sand (Stride et al., 1982), which in some case can be colonised by an assemblage of benthic communities (Dewicke et al., 2003) or is entirely composed of bioclastic carbonates (Farrow et al., 1984).

Due to the complexity of the environment, confusion has arisen in the terminology related to sandbanks. Dyer and Huntley (1999) have recently tried to reconcile the different terminologies and synthesize previous work. They suggested the following process-based classification recently modified by Kenyon and Cooper (2004) that aims at relating the morphology of the banks to the tidal and wave current regimes and the sedimentary constraints.

1.3.1. Morphology and classification

The three types of sandbanks that Dyer and Huntley (1999) and Kenyon and Cooper (2004) describe in their classification concern banks that occur in open shelf seas, estuary mouths and delta fronts and those associated with headlands. Examples of all these different types of banks can be found along the coasts of the United Kingdom (Pantin, 1991; Kenyon and Cooper, 2004).

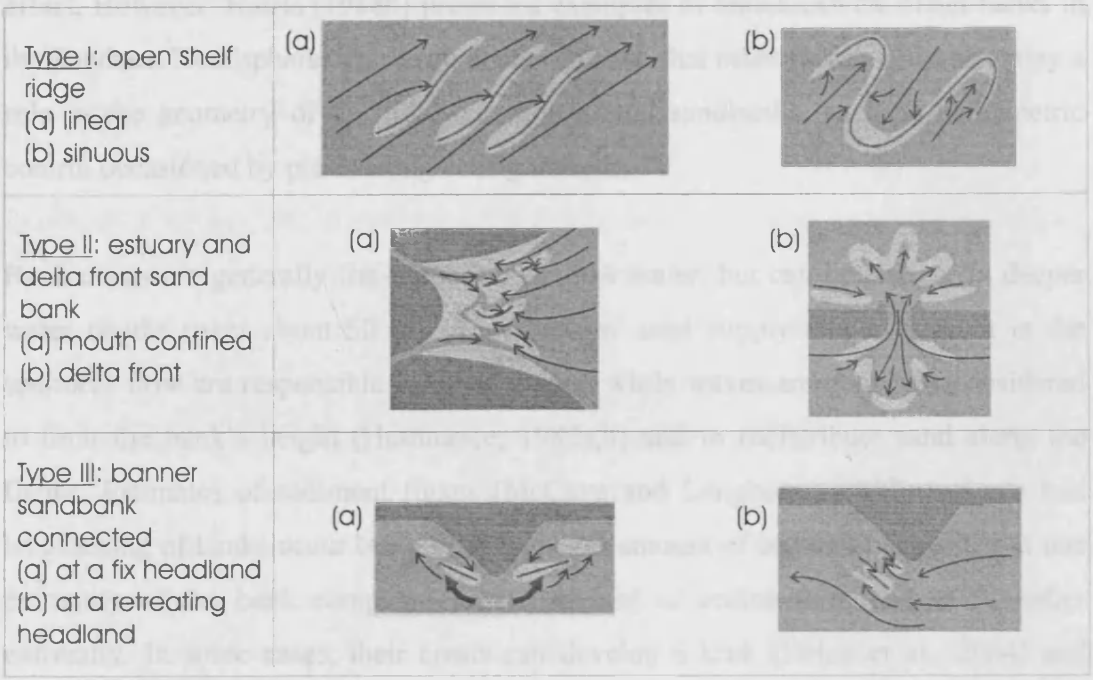

Figure 1.5 Detailed sand ridge classification based on Dyer modified from Kenyon and Cooper (2004)

1.3.1.1. Open shelf ridges

Nearly all shallow tidal seas where currents exceed $0.9 m.s^{-1}$ have sand ridges (Belderson, 1986). These banks were first described by Off (1963). They often appear as groups of parallel sandbanks (Figure 1.5, type I a). Some examples of such open shelf ridges are found in the West English Channel (Berné et al., 1989a), the Norfolk Banks in the North Sea (Caston, 1970; Caston, 1972; McCave and Langhorne, 1982; Collins et al., 1995), the Kaiser Bank in the Celtic Sea (Reynaud et al., 1999a), the Georges Bank and other deposits on the North Atlantic American shelf (Twichell, 1983; Harrisson et al., 2003) or in the Gulf of Cadiz (Lobo et al., 2000).

These ridges are, on average, ~13 km wide, ~80 km long and tens of metres high. Their shapes are asymmetrical, with slopes of ~6° on the steeper side and less than 1° on the gentler side. The long axis of most of them is oriented at an oblique angle to the peak tidal flow direction (30°, on average), generally in an anticlockwise sense (from the major axis of the tidal ellipse) (Kenyon et al. 1981) in the northern hemisphere, suggesting that the Coriolis effect controls this offset. Mathematical modelling (Carbajal and Montano, 2001; Roos and Hulscher, 2003) confirms a preferred anticlockwise orientation of the principal component caused by the Coriolis

effect. However, Harris (1988b) presented examples of anticlockwise offset banks in the Southern Hemisphere. This argument points out that other factors must also play a role in the geometry of the tidal currents around sandbanks, such as bathymetric control occasioned by pre-existing configuration.

Bank crests are generally flat-topped in shallow water, but can be sharper in deeper water depths (over about 50 m). An excess of sand supply and a gradient in the sediment flow are responsible for their growth while waves are generally considered to limit the bank's height (Huthnance, 1982a,b) and to redistribute sand along the flanks. Estimates of sediment fluxes (McCave and Langhorne, 1982) indicate that lengthening of banks occur because of a greater amount of sediment deposited at one extremity of the bank compared to the amount of sediment eroded at the other extremity. In some cases, their crests can develop a kink (Deleu et al., 2004) and become increasingly sinuous (Caston, 1972). Caston (1972) suggested that parallel linear banks may originate from splitting of such sinuous banks (Figure 1.5, type I b).

1.3.1.2. Estuary mouth and delta front ridges

Estuary mouth ridges (Figure 1.5, type II a) are more characteristic of macro-tidal estuaries. The essential differences between this type of bank and the open shelf ridges is that they lie parallel to the flow, the sediment supply can be more limited and that the restriction of the mouth of the estuary induces increasing shear stress near the head of the estuary (Stride et al., 1982). Deltas can also host this type of bank, as they can have a copious supply of sand. However they are often found at the seaward end of the delta while estuary mouth ridges occur closer to the inner part of the estuary (Harris, 1988a).

Examples of estuary mouth ridges are the Cardiff Grounds, Holm Sand, Culver Sand, One Fathom Bank (see section 1.5.3) in the Severn Estuary/Inner Bristol Channel (Harris, 1982; Stride and Belderson, 1991; McLaren et al., 1993). Other examples have been observed from the Thames Estuary (Harris, 1988a), in the Bay of Fundy (Dalrymple, 1984), in the Chesapeake Bay (Perillo and Ludwick, 1984), in the San Fransisco Bay (Rubin and McCulloch, 1980), in the mouth of Moreton Bay (Australia) (Harris, 1988a) and in the Bahia Blanca (Argentina) (Cuadrado and

Perillo, 1997). Intermediate cases between open shelf ridges (section 2.3.1.1) and estuary mouth ridges may be found in straits, such as in the Calais-Dover Strait (Le Bot and Trentesaux, 2004).

Explanation of their occurrence can be found in the inland shoaling and narrowing of macrotidal estuaries resulting in an increase of the tidal range and consequently to large currents and to an increase of the shear stress on the seabed. Major asymmetry between the ebb and flow currents is one of the main hydrodynamic characteristics of estuaries. This can result in net bed load convergence of sediment leading to linear seabed features such as sand ribbons or sandbanks. In the latter case, banks are generally aligned with the flow. Sandbanks may also develop downstream of the bed load convergence, preferably in wide-mouthed estuaries, where the ebb flow is dominant, as in the outer Bristol Channel (Harris, 1988a). Their presence, however, is more usually related to coastal headlands.

1.3.1.3. Banner sand banks

The location of these banks is commonly attributed to the presence of residual current eddies (section 1.2.1) generated by the tidal flow passing a coastal irregularity (Davies et al., 1995) or an island (Wolanski et al., 1984). These sand banks are then likely to appear either directly attached (generally in non-tidal environments) to the obstacle or separated (generally in a tidal environment) by a sediment-swept channel (Figure 1.5, type III a). Also, headland or coastline irregularities change the rate of longshore sediment transport along beaches from waves (Figure 1.6). If the tidal currents are omitted, it can be shown that faster longshore drift is experienced along beaches facing the average wave direction (Ashton et al., 2001). Similarly, little longshore drift is expected for part of the coastline sheltered by the presence of the headland. Hence, variation in the intensity of the flux of sand transport induces sand to accumulate near the headland. Such accumulation of sand is reworked by the strong tidal currents. Hence the role of waves must also be investigated to explain how banner sandbanks are maintained.

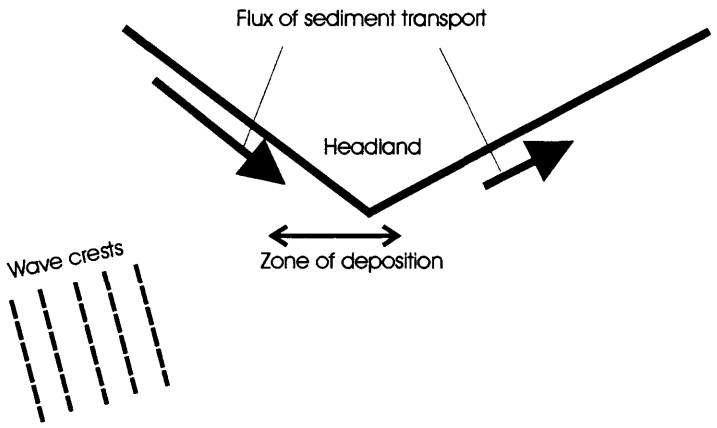

Figure 1.6 Variations of the longshore wave-induced sediment transport flux at the vicinity of a headland. Longshore sediment transport is maximised along the coast facing the average wave direction, whereas it is minimised along the coast sheltered from the wave action by the headland. Hence wave-induced longshore current induces sand accumulation near the headland. This sand accumulation is reworked by the strong tidal currents at the vicinity of the headland.

Numerous examples of banner banks occur around the British Isles, such as the Skerries Bank (Start Point, English Channel), Stanley and North-west Banks (Lundy Island, Bristol Channel), the Devil's Ridge, Tripods and Bastram Shoals (Lleyn Peninsula, Cardigan Bay), the Helwick, Scarweather and Nash Sands, Mixon Shoals (Bristol Channel), the Shambles and Portland Banks (Portland Bill, English Channel), the King Williams, Ballacash, Bahama and Wart Banks (Isle of Man, Irish Sea). Few cases, however, have been studied in detail and reported in the literature. One exception is the Shambles and Portland Banks complex off Portland Bill (Pingree, 1978; Pingree and Maddock, 1979; Signell and Harris, 2000; Bastos et al., 2002; Bastos et al., 2003a,b; Bastos et al., 2004). In that case, and in most tidal cases, two banks are located on both sides of the obstacle, with one of them generally better developed than the other. Sediment transport is in the same sense as eddies generated at the headland (away from the headland in the outer area and towards the headland in the area close to the coast) (Bastos et al., 2002) leading to a linear zone of bedload convergence. This zone of convergence occurs over the crest of the bank.

In the case where the coastal promontory is retreating, the position of the banks will not be fixed. Following headland retreat some banks may develop parallel to the coast (Figure 1.5, type III b). These last types of banks share similar characteristics to open-shelf banks. Examples include the Norfolks Banks in the North Sea (Swift, 1975) or Horns Rev, in Denmark (Kenyon and Cooper, 2004).

1.3.2. Mechanisms of formation and maintenance

The next section will present physical models proposed to explain the formation and the maintenance of sandbanks. They all focus on the causes of gradients in currents and their implications for the initiation and growth of sandbanks.

1.3.2.1. Secondary circulation

The secondary circulation is the pattern of currents measured perpendicular to the main (forcing) tidal current that is created by the interaction of the main current with the irregularities on the seabed. The first observation that tidal currents were altered over a sandbank was suggested by Off (1963) and Houbolt (1968). They measured slower secondary flows over the crest of the sandbank and proposed a model of circulation consisting of two counter-rotating vertical spirals, which converge close to the seabed on the crest and diverge at the top of the water column (Figure 1.7). The common asymmetry of the bank is simply explained by the currents of one of the spirals being stronger than the other. Evidence to support this idea has been found in the current rips observed at the sea surface. Some authors (McCave, 1979; Swift and Field, 1981), however, suggested that, even if these spiral flows exist, and may be responsible for the fining gradient in grain size from the trough to the crest observed on some sandbanks, the strength of these secondary currents is insufficient to create the bank topography. Furthermore, this idea requires the pre-existence of a topographic positive irregularity on the seabed, and thus would not explain how sandbanks originate.

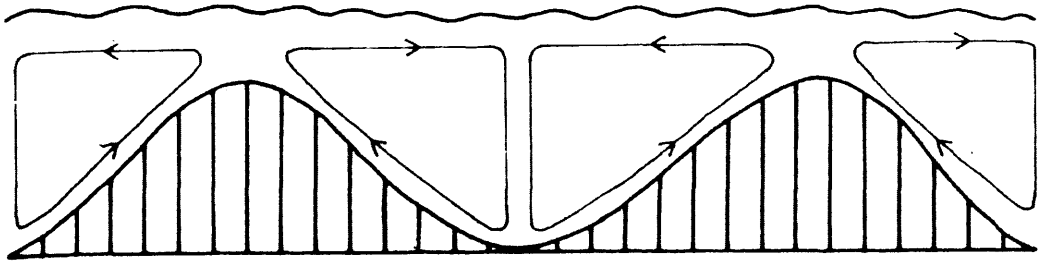

Figure 1.7 Early view of the development of secondary currents over rhythmic sandbanks. Circular convergent secondary currents were interpreted to cause growth and maintenance of these bodies (from Houbolt, 1968)

Smith (1969) showed theoretically that the component of the flow over a seabed feature should create a bed shear stress with a peak that should occur upstream of the feature's highest point. Since the bedload transport flux is related to the shear stress, he asserted that seabed features are eroded upstream of their crests and sediments are deposited downstream of their crests. Thus, once initiated a bedform should migrate downstream. In a tidal flow, the tidally-averaged flow, and thus the sediment flux, on either side of the feature would be towards the crest. Smith (1969) extrapolated this theory from the sand dunes to larger scale features such as sandbanks. Swift and Field (1981) reported a sand grain size distribution consistent with Smith's model. However, Hulscher (1996) proved mathematically that vertical circulation and associated shear stress on the bottom of the type and intensity anticipated by Smith (1969) were relevant at the dune scale or smaller but are irrelevant to bigger seabed features, as a purely advective sand transport approximation does not hold at this scale under oscillating tidal flows. Hence Smith's theory cannot hold for sandbanks, though it can have a role in the sand grain size distribution over the bank and the geometry of superimposed dunes.

1.3.2.2. Stability models

One of the major shortcomings of the models described in the previous section is that they considered the currents to be the main cause of occurrence of seabed features but without considering how these currents would vary with the changing topography caused by the sediment transport. A new approach (Huthnance, 1982a,b) was to consider both the sediment transport and the hydrodynamics. His model consists of an equation representing depth-averaged currents and a simple bedload transport equation, with the flux a function of current speed and bed slope. The model was used to show how a growing bedform interacts with the current flow. Some conclusions from this model are worth mentioning: (1) the orientation of the axis of the sandbank with respect to the tidal flow is predicted to be ~30° anticlockwise (as generally observed for open shelf ridges) due to seabed friction and (2) the optimum wavelength of the growing perturbations is predicted to be ~250 times the mean water depth. As a result of friction it was also suggested that the along-bank component of the tidal current should slow down whereas, due to conservation of current discharge, the across bank component should speed up (Figure 1.8). Therefore Huthnance's

(1982a,b) results suggested that vorticity is essentially due to bed friction and that the Coriolis effect is relatively small (compared to bed friction), a result that should be especially true for coastal sandbanks where the current speed is high.

According to Huthnance's model a current inclined to the axis of the bank turns towards the crest as the flow approaches the crest of the bank because of the stronger torque induced by the increasing bed friction. This results in a crestward oriented sediment transport. On the downstream side of the bank, the flow speed is reduced due to flow expansion. Therefore the flow experiences less friction and thus is subject to a weaker torque. For a reversing tidal flow there will be convergent sediment transport towards the crest of the bank (Figure 1.8). The asymmetry of the sandbank is then explained by the asymmetry of the tidal currents. Huthnance suggested that sandbank growth is limited by the stirring action of waves on the seabed, putting sediment in suspension and enhancing transport over the crest, as observed by Houthuys et al. (1994) and Vincent et al. (1998). In other banks their height may simply be limited by the availability of sand.

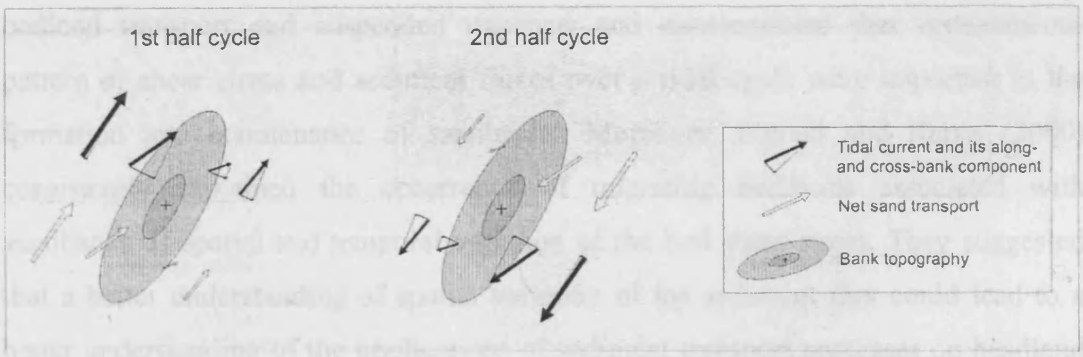

Figure 1.8 Representation of the Huthnance model (1982a, b) for sandbank growth under tidal currents

Despite the fact that these models give insight into the relative importance of the growing and maintaining processes of open shelf sandbanks, their application to banner sandbanks is unclear because of the complexity of the flow interacting with both the headland and the bank (Dyer and Huntley, 1999).

1.3.2.3. Implication of tidal eddies generated at headlands

Eddies generated by vorticity from the tide passing a headland has been described Section 1.2.1 and has been related with the occurrence of sediment deposits (Pingree, 1978; Pingree and Maddock, 1979; Pattiarchi and Collins, 1987; Park and Wang, 2000; Bastos et al., 2002). Pingree (1978) proposed the 'tidal stirring concept' to explain the formation and maintenance of banner sandbanks. Using a depth-averaged model of the tidal currents near Portland Bill (Bastos, 2002) he observed that the anticlockwise residual (tidal currents average on several cycles) eddy located on the eastern side of Portland Bill was associated with Shamble Bank, while a clockwise residual eddy system was associated with the Portland Bank on the west of the headland. He suggested that sand deposition occurs at the centre of the residual eddies and explained the difference of growth of each bank as a function of the relative influence of the Coriolis effect and inertial and gravitational forces (Zimmerman, 1981).

However, a transient characteristic in the flow associated with instaneous eddies generated at the headland and the influence of the changing topography of the sandbank were omitted in Pingree's concept (Signell and Geyer, 1991; Bastos et al., 2002). Signell and Harris (2000) numerically tested Pingree's model both for a bedload transport and suspended transport and demonstrated that instantaneous pattern of shear stress and sediment fluxes over a tidal cycle were important in the formation and maintenance of sandbanks. Moreover, Signell and Harris (2000) consistently explained the occurrence of migrating bedforms associated with sandbanks as spatial and temporal variation of the bed shear stress. They suggested that a better understanding of spatial variation of the sediment flux could lead to a better understanding of the implications of sediment transport processes on headland associated sandbanks.

1.4. Sand dunes and their significance

The occurrence of sand dunes in various environments (rivers, estuaries, and down to the outer shelf) has led to an early interest in these features and a large volume of research. The main features of sand dunes that have been extensively studied are: their morphology, their internal structure, their nature and the quantity of the sediment that composes them, their relation to the flow, their stability in response to

environmental constraints and their migration. There has, however been confusion in the terminology in terms arising from different approaches used to study them (Ashley, 1990).

Sand dunes on the seabed show a hierarchical organisation related to the flow shear velocity (Figure 1.1). Flow-transverse high to medium sand dunes commonly occur on sandbanks (Figure 1.1, Table 1.1) and may be covered by smaller dunes. The morphology of sand dunes superimposed on sand banks is commonly interpreted to reveal the sediment transport direction and infer aspects of the hydrodynamic environment. Numerous authors have used their plan-view orientations and sense of asymmetry to interpret sediment transport paths around sandbanks (Table 1.1). Dunes commonly are evident on the flanks of the banks, while they are usually absent on the crest.

Author	Location	Water depths	Dune characteristics	Survey method
Smith (1969)	Middle Ground, US Atlantic coast	Between 11 m and 16 m	Opposite sense of asymmetry on alternate sides of the bank	Historic datasets and singlebeam echo-sounder
Caston (1970)	Norfolk banks, southern North Sea	Up to 48 m	Clockwise circulation of sand derived from dune asymmetry.	Sidescan and singlebeam echo-sounder
McCave and Langhorne (1982)	Western end of Haisborough Bank, southern North Sea	Between 25 m to 5 m	Asymmetrical dunes (average height 3.2 m and 116 m spacing) becoming smaller at the crest of the bank (reported as megarriples)	Sidescan and singlebeam echo-sounder
Twichell (1983)	Georges Bank, US Atlantic coast	From 70 m to 5 m	Dunes perpendicular to the bank crest on its flanks, becoming parallel and smaller as they approach the bank crest	Sidescan and singlebeam echo-sounder
Lanckneus et al. (1994,1995)	Middelkerke Bank, southern North Sea	Between 22 and 9 m	Straight to slightly sinuous dunes (1.5 m to 2 m high on average) with opposite asymmetry on both flanks. Symmetric dunes are present on the crest.	Sidescan and singlebeam echo-sounder
Collins et al. (1995)	Broken Bank, southern North Sea	Between 18 and 40 m	2-4 m high	Sidescan, singlebeam echo-sounder and seismic records
Reynaud et al. (1999a)	Kaiser Bank, southern Celtic Sea	140 to 170 m	Transverse dunes on the flanks showing opposite asymmetry, becoming smaller and discontinuous on the crest of the bank.	Multibeam sonar
Mallet et al. (2000)	Saint Georges Bank, Gironde Estuary	From 20 m to 1 m (MLWS)	Opposite sense of asymmetry becoming symmetrical towards the crest of the bank	Sidescan and singlebeam echo-sounder
Bastos (2000,2002)	Shamble Bank	Up to 35 m	5-10 m high showing convergent sand transport toward the crest	Sidescan, Hydrographic chart

Table 1.1 (previous page) Selection of reported studies detailing active sandbanks showing superimposed migrating sand dunes.

1.4.1. Morphological descriptors

Dunes are spatially repetitive seabed features, which range in height from several centimetres to 25 m (Mosher and Thomson, 2002) and spacing from several centimetres to 1000 m (Allen, 1982). They are commonly characterised by their amplitude or height and wavelength or spacing (Figure 1.9). A genetically significant morphological classification of transverse subaqueous dunes can be found in Berné et al. (1989b) and Ashley (1990) which is now widely adopted and will be used here. They suggested that the same processes form all flow transverse bedforms, so that they should all be classified as dunes. Their different sizes and shapes are simply the result of local effects of the flow on the sediments.

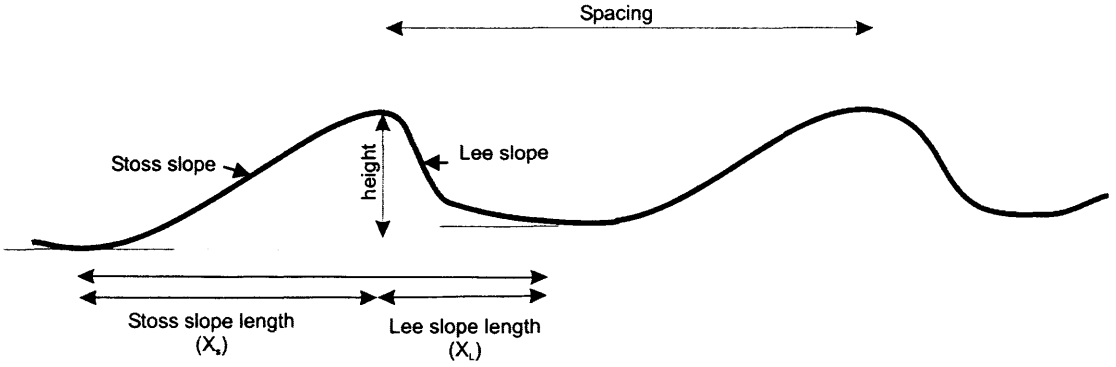

Figure 1.9 Definition diagram for sand dunes

First order descriptors of dune geometry				
	Small	*Medium*	*Large*	*Very large*
Height	0.075-0.4 m	0.4-0.75 m	0.75-5 m	>5m
Spacing	0.6-5 m	5-10 m	10-100 m	>100 m
Shape	2-dimensional or 3-dimensional			
Second order descriptors			**Third order descriptors**	
Superposition (ripples over small dunes) *sediment characteristics* (size and sorting)			*bedform profile* (angle of the stoss and the lee slopes) *Local characteristics of the flow, history of the dune migration*	

Table 1.2. Sand waves descriptors following Ashley et al (1990)

In cross-section, the degree of asymmetry is determined by the ratio of the horizontal distances of the dune stoss slope (X_S) to lee slope (X_L) (Allen, 1980a), (i.e. X_S/X_L). Asymmetric sand dunes are generally associated with unidirectional flow or asymmetric tidal currents. In the latter case, their morphology is characterised by the presence of a rounded crest (McCave, 1970; Langhorne, 1982; Berné, 1993), also known as in "cat-back profile". In reversing tidal currents, it has been assumed that the steepest flank indicates the orientation of the strongest current.

Some sand dunes are covered with dunes of smaller size also called ripples (McCave, 1970; Dalrymple, 1984), which range from several centimetres to several meters in height and are typically tenths of meters in spacing. According to Rubin and McCulloch (1980), the presence of superimposed dunes is due to the development of a boundary-layer induced by the host dune, in which the small dunes are in equilibrium. They cover the stoss flank of the hosting dune rather than the lee side, as the flow detaches over the lee side, inducing the development of a boundary layer (McLean, 1989). Carling et al. (2000a) and Whitehouse et al. (2000) emphasise their role in the sediment transport. McCave (1971), Terwindt (1971) and Rubin (2000) observed that their migration towards the crest of the host dune was accompanied with an increase of their amplitude.

In plan-form, sand dunes can be classified as two-dimensional (linear crested) or three-dimensional (sinuous crested). Costello and Southard (1981) attributed the development of three-dimensionality in tidal areas to the strength of the current. Terwindt and Brouwer (1986) suggested that the variability of the flow direction and hence the sediment transport determine whether dunes are 2D or 3D. Differential migration of the crest (crest flexing) due to gradients in the across-dune celerity of the current has also been argued to create 3D dunes (Dalrymple and Rhodes, 1995).

1.4.2. Relation of the dune with tidal flows and sediment transport

The stability of sand dunes has been investigated by McLean (1989). He demonstrated that shear stress acting on the stoss side tends to increase towards the crest of the dune due to the acceleration of the flow associated with constriction over

the dune crest. A strong deceleration occurs beyond the crest as water depth increases along the lee slope. If the lee slope is more than 1/15 (~1°), the flow detaches at the crest and reattaches at a point on the stoss flank of the downstream dune. In the area of detachment, the flow is turbulent (Bennett and Best, 1995). In some cases a counter-current may exist which moves sediment up the lee side of the dune (Dyer, 1986). However the details of sediment transport in the turbulent area are still not very well understood and in reversing flows the feedback between topography and flow is even less well understood (Seminara, 1998). Nevertheless various authors have tried to find empirical relationships between the geometry of transverse dunes and the characteristics of the flow as they all clearly observed a relation between hydraulic form roughness (occasioned by the dune morphology), flow condition and sediment transport. Hence relations between the maximum height (H_{max}) and corresponding spacing (L) of dunes have been investigated. An empirical power-law relationship was provided by Flemming (2000):

$$H_{max} = 0.0677L^{0.8098} \qquad \text{Equation 1.18}$$

Figure 1.10, presents a scatter plot incorporating the data used by Flemming to compute Equation 1.18 trend. These data are representative of flume experiments, riverine and marine (subject oscillatory currents such due to the tides and waves) environments. Hence this relation reflects a mean global trend and serves as a reference against which local trends can be compared.

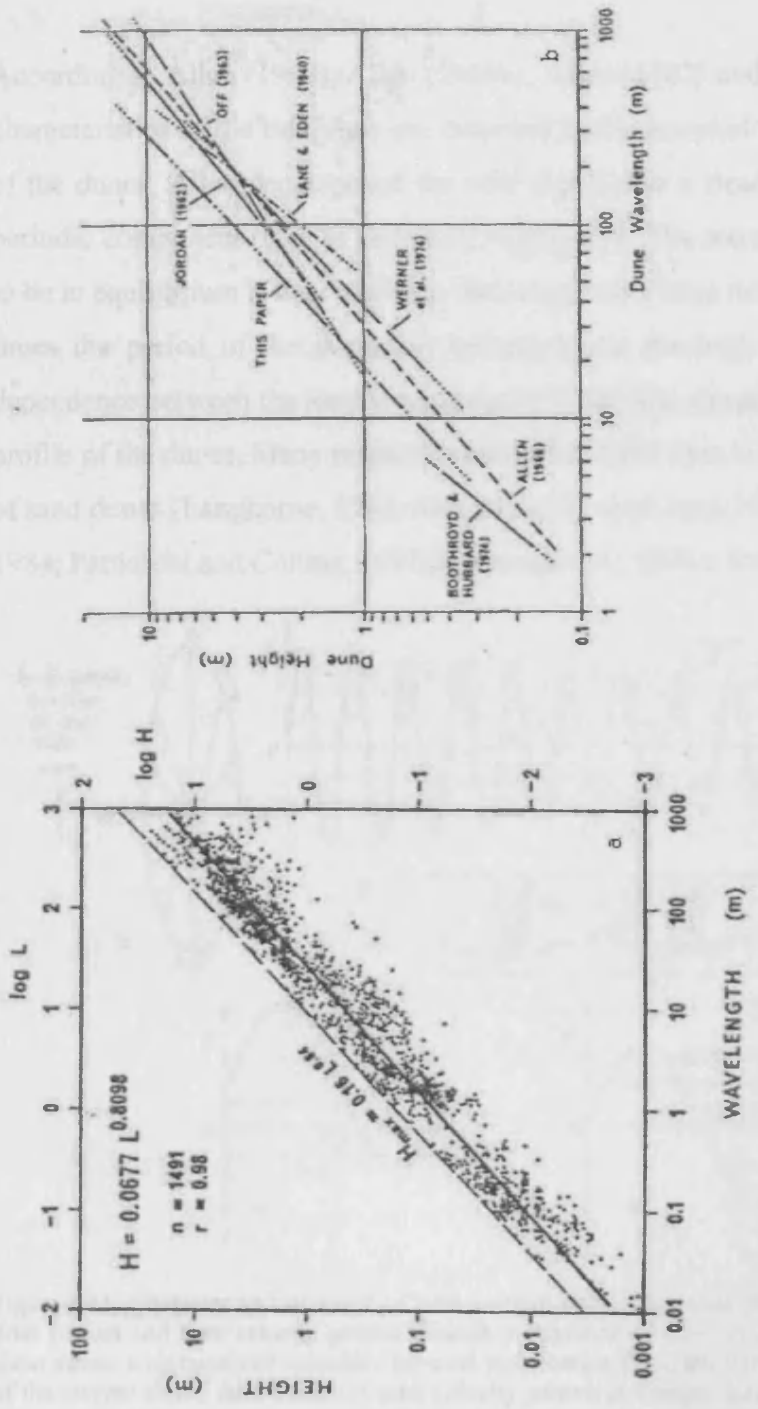

Figure 1.10. Dune height versus dune spacing (Flemming, 1978 and 2000). (a) Scatter diagram incorporating data from flumes and various natural environments. (b) Flemming's mean trend compared with previous studies.

The formation and migration of sand dunes in rivers and in the marine environment is generally attributed to bedload sand transport (Jonhson et al., 1982). However, flow separation often occurs over the lee side (Bennett and Best, 1995), where some sand can be transported in suspension. Reattachment of the flow occurs on the stoss side of the next dune. In some cases a large amount of suspension load may inhibit the growth of sand dunes (Mohrig and Smith, 1996; Carling et al., 2000b) as sand is carried away.

According to Allen (1968), Allen (1980b), Allen (1982) and Berné et al. (1989b) the characteristics of the tidal flow are recorded in the morphology and internal structure of the dunes. Allen decomposed the tidal signal into a steady component (U_s) and a periodic component (U_p), as shown in Figure 1.11. The morphology of a dune is said to be in equilibrium if they maintain their shape on a long time scale (typically several times the period of the dominant hydrodynamic forcing). Allen demonstrated the dependence between the steady component of the tidal signal (U_s) and the equilibrium profile of the dunes. Many researchers have used this idea to interpret the morphology of sand dunes (Langhorne, 1982; McCave and Langhorne, 1982; Perillo and Ludwick, 1984; Pattiarchi and Collins, 1987; Reynaud et al., 1999a; Knaapen et al., 2001).

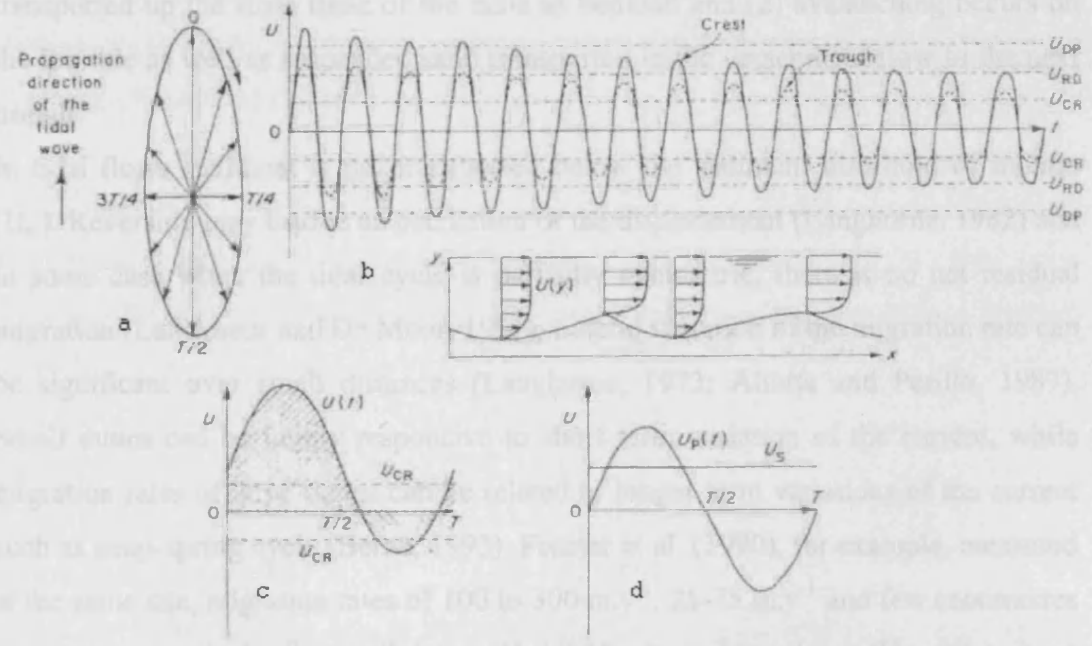

Figure 1.11. Character and structure of tidal currents over sand dunes (from Allen, 1980b). (a) Rotary tidal current and time velocity pattern through a sequence of tides, in the direction of the maximum shear stress, with threshold velocities for sand mobilisation (U_{cr}). (b) Vertical variation of speed profile of the current above sand dunes (c) time velocity pattern in a single tidal cycle. (d) Decomposition of the time velocity pattern into a steady (U_s) and periodic components (U_p).

Less investigation has addressed the relation between the plan-view morphology of the dunes and the flow. Werner and Kocurek (1997), however, examined the terminations of dunes and postulated that their number is a function of the dune-field orientation with respect to the average flow direction. By imposing a change of orientation of the flow, Werner observed an increase of the number of terminations in the dune field, more bifurcations and the appearance of intercalated smaller dunes. He

showed that this number decreases as the dunes crest will re-orient normal to the average flow direction. Hence, it can be argued that plan-view complexity can arise from the changes in flow direction over tidal cycles.

1.4.3. Migration and mutual interaction of dunes in plan-form

Migration rates of sand dunes range from quasi-immobile to up 700 $m.y^{-1}$ (Wever, 2003). Maximum migration rates are generally observed in unidirectional flows. This wide spectrum of celerity can be related to environmental factors such as the strength of the tidal current (Seminara, 1998; Blondeaux, 2001) or the avaibility of sand and its grain size (Allen, 1984). Dune migration generally occurs as: (1) sediment is transported up the stoss flank of the dune as bedload and (2) avalanching occurs on the lee side as well as suspended sand transported in the detachment flow to the next trough.

In tidal flows sediment is not transported below the sediment threshold of motion (U_{cr}). Reversing may lead to an oscillation of the displacement (Langhorne, 1982) and in some case when the tidal cycle is perfectly symmetric, there is no net residual migration (Lanckneus and De Moor, 1991). Lateral variation of the migration rate can be significant over small distances (Langhorne, 1973; Aliotta and Perillo, 1987). Small dunes can be highly responsive to short term variation of the current, while migration rates of large dunes can be related to longer term variations of the current such as neap-spring cycle (Berné, 1993). Fenster et al. (1990), for example, measured at the same site, migration rates of 100 to 300 $m.y^{-1}$, 25-75 $m.y^{-1}$ and few centimetres per year, respectively, for small dunes ($H < 0.25$ m), medium dunes ($H = 0.5$ to 3 m) and large dunes ($H > 3$ m). According to Langhorne (1982), morphologic changes during a single neap-spring cycle can be limited to the crests of very large dunes. In the case of composite dunes, the host dune generally migrates slower than the superimposed smaller dunes (Dalrymple, 1984). However, Carling et al. (2000a) showed that composite dunes migrate more slowly than simple dunes of the same volume.

1.4.4. Estimation of sediment transport associated with dune migration

Study of dune movements in the Mississippi (Harbor, 1998), Idle (Crickmore, 1967), Sacramento (Dinehart, 2002), Fraser (Kostaschuk and Villard, 1996), Rhine and some Dutch rivers (Van den Berg, 1987; Ten Brinke et al., 1999; Carling et al., 2000a,b; Wilbers and Ten Brinke, 2003) demonstrated that dune tracking is a useful method for determining sediment transport fluxes. Two methods are employed to detect bedform movement with echo-sounders. The first consists of recording the bed elevation at a fixed point, where the passage of a bedform appears as a waveform of changing elevation (Nordin and Algert, 1966). By using a second recorder, separated by approximately a dune wavelength, celerity of the bedform can be measured. This method is especially suited for studies in flumes (Engel and Lau, 1980). The second method, most commonly used in natural environments, is based on the correlation of bedforms recorded at different times.

The development of theoretical principles for the estimation of the specific volumetric sediment transport flux is based on the work of Engel and Lau (1980). The continuity equation (Equation 1.19) representing the conservation of sand mass (Allen, 1997) is first introduced as follows:

$$\frac{\partial Q_{bf}}{\partial x} + \frac{\partial z}{\partial t} = 0 \qquad \text{Equation 1.19}$$

where Q_{bf} is the specific volumetric transport flux (m^3/m/unit of time) equal to the mass transport flux (kg/m/unit of time) divided by sand bulk dry density. This equation represents how spatial increase in Q_{bf} (positive $\frac{\partial Q_{bf}}{\partial x}$) leads to erosion (negative $\frac{\partial z}{\partial t}$).

Kinetic equation for the propagation of the dune (Equation 1.20) is also presented:

$$\frac{\partial z}{\partial t} = -c.\frac{\partial z}{\partial x} \qquad \text{Equation 1.20}$$

This relation is representing how local erosion rate ($\frac{\partial z}{\partial t}$) depends on the speed of the migration of the dune (c) and the local bed gradient ($\frac{\partial z}{\partial x}$)

Equations (1.19) and (1.20) are combined, leading to :

$$\frac{\partial Q_{bf}}{\partial x} = c\frac{\partial z}{\partial x} \qquad \text{Equation 1.21}$$

Supposing a constant migration of the dunes, integration of Equation 1.21 leads to:

$$Q_{bf}(x) = c(z(x) - z_0) \qquad \text{Equation 1.22}$$

Over an entire wavelength, the average flux represented by dune migration is:

$$Q_{bf} = \frac{c}{L}\int_0^w (z(x) - z_0)dx \qquad \text{Equation 1.23}$$

Defining the specific volume of the dune (V_{bf}), which can also be seen as the cross-sectional area of the dune as follows:

$$V_{bf} = \int_0^W z(x)dx \qquad \text{Equation 1. 24}$$

If the origin of z is taken to coincide with the troughs, $Q_{bf}(z_{trough}) = 0$, which is equivalent to supposing that the flux of sediment transport goes to zero at the troughs.

$$Qbf = \frac{c}{L}.V_{bf}$$

which can be written as follows:

$$Q_{bf} = f.c.H \qquad \text{Equation 1.25}$$

considering that f is the shape factor defined as $f = \frac{V_{bf}}{HL}$.

This specific sediment flux is generally considered as the bedload sediment transport rate. However suspended or bypassing sediment may be included in the calculation (Rubin and Hunter, 1982), hence biasing the estimate of the transport occurring only as bedload. The main assumption behind the method described in this section is that dunes migrate without changing shape. The identification of such dunes in successive echo-sounding surveys can be difficult because of morphological changes such as combination or splitting. To overcome this strong assumption the shape factor of each of the matched dunes (with relatively similar shape) was averaged and used in Equation 1.25. In tidal environments where dunes migrate in both directions with the flow the method gives an estimate of the net sediment transport vector. Furthermore, the method may not represent any transport parallel to the dune crest, such as might occur from wave currents.

1.5. The Bristol Channel and sand transport paths

1.5.1. Physical description of the Bristol Channel

The Bristol Channel is a funnel shaped embayment open to the Atlantic Ocean and converging eastward into the Severn Estuary (Figure 1.12). The southern coast is straight from Bull Point until it turns in the Severn Estuary. The northern coast contains two bays (Carmarthen and Swansea Bays). The Channel narrows to ~20 km immediately east of Nash Point. Water depths in the central channel (the Breaksea Valley) located a few kilometres north of the southern coast range between 60 m to 10 to 20 m below chart datum. This valley probably originates from the flowing of the Severn River during times of lower sea-level. Apart from this valley, the seafloor slopes gently.

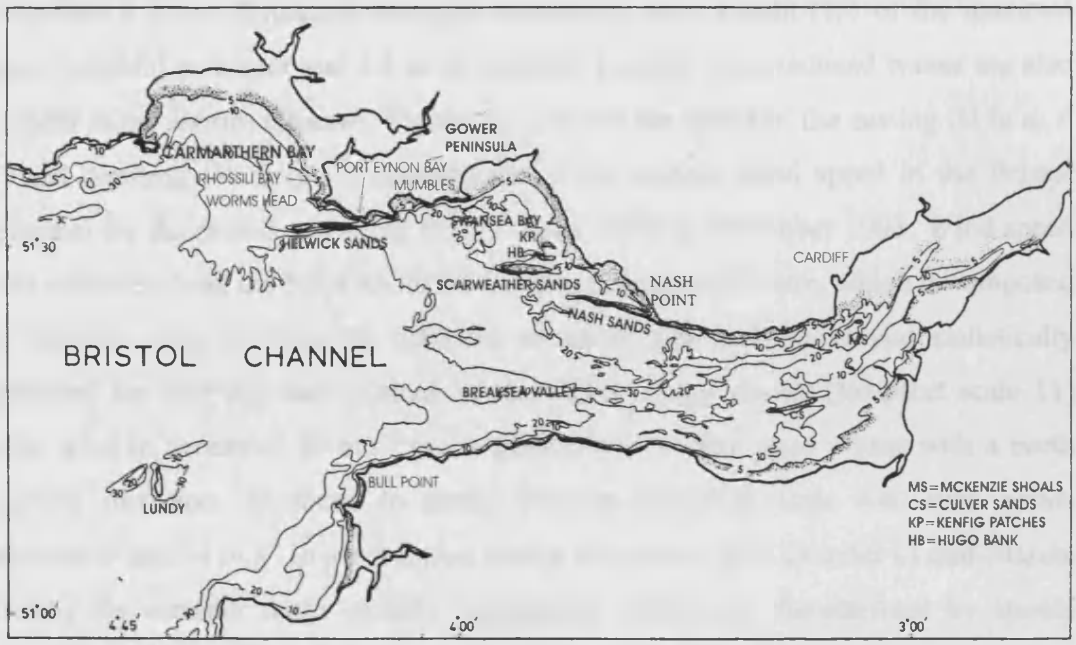

Figure 1.12. Physiographic map of the Bristol Channel and Severn Estuary (modified from Harris, 1988)

Owing to its funnel shape, the Bristol Channel experiences a large tidal range reaching a maximum of 11.4 m, at spring tide and 5.5 m at neap tide at Swansea. The resonant period induced by the morphology of the Celtic Sea/Bristol Channel system, which is around 10 hours (Heath, 1981), contributes to the strong intensity and asymmetry of the tidal flow. The macrotidal regime results in strong and essentially rectilinear currents, reaching velocities in excess of 2 $m.s^{-1}$ during spring tides. Drifter movements (Collins and Ferentinos, 1984) indicate a residual current oriented towards the east in the middle of the Channel, while an opposite residual current has been tracked along the coasts. Complex patterns of the residual circulation arise in bays or at coastal promontories (Ferentinos and Collins, 1980). However, residual currents are more relevant to sediment transported in suspension rather than sediment transported as bedload.

Swell and storms affect the Channel. In particular, storm waves can reach up to 10 m high in the Outer Bristol Channel (Collins, 1987). A 6000 km fetch is available for the swell originating from the North Atlantic, attenuated by the shallow shelf in the last 450 km (Pattiaratchi and Collins, 1987) to reach the northern coasts of the embayment, while the southern coast is more protected. Annual variation of the wave regime measured by satellite altimeter was reported by Woolf et al. (2003) who

described a 2.5 m 3-months averaged significant wave height (1/3 of the maximal wave heights) in winter and 1.2 m in summer. Locally wind induced waves are also present in the Bristol Channel. Figure 1.13, shows the speed of the easting (U in $m.s^{-1}$) and northing (V in $m.s^{-1}$) components of the surface wind speed in the Bristol Channel for the period extending from January 2001 to December 2003. Wind speed was extracted from the NOAA/CIRES Climate Diagnostic Centre, which is composed of climatic data provided by different countries and institutions and statistically analysed for outlying data (Kalnay et al., 1996). Large storms (Beaufort scale 11) with wind in excess of 30 $m.s^{-1}$ occur generally in winter, once a year with a north easterly direction. Moderate to strong breezes (Beaufort scale 4-6) with winds between 6 and 14 $m.s^{-1}$ in are frequent during the period from October to mid-March. During the summer north easterly propagating winds are characterised by speeds below 7 $m.s^{-1}$. On occasions the direction of the wind changes to a westerly direction.

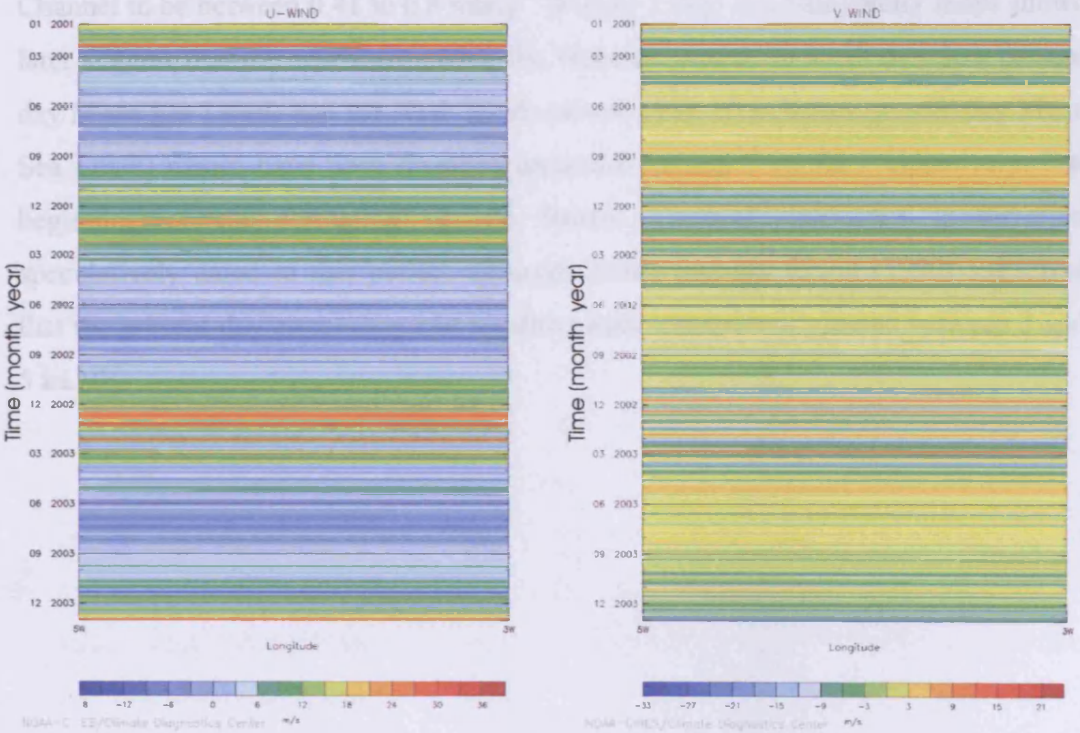

Figure 1.13 U (easterly) and V (northerly) components of the wind speed along the transect 50N 5W to 50N 3W for the period ranging 01/01/2001 to 01/12/2003 (Data extracted from the NOAA-CIRES/Climate Diagnostic Centre Database).

1.5.2. Geological framework and post-glacial sea-level history

Because this thesis is concerned with recent sediment deposits, a complete description of the stratigraphy and the tectonic events affecting the Bristol Channel will not be provided. The interested reader is referred to North (1964) or Tappin et al. (1994) for such details. Exposed bedrock in the Channel is generally of Jurassic and Triassic age (Evans, 1973). Early glacial sedimentary deposits dated from around 150 ka B.P. have been attributed to the combined effect of the Welsh and Irish Sea ice sheets (Britton, 1978; Harris, 1982). During the next inter-glacial (Ipswichian) stage, the mean sea-level rose to 17 m higher than the present day level (Allen, 2002). The Last Glaciation Maximum occurred between 16 and 20 ka B.P. and led to new sediments being deposited (Harris, 1982). During the Flandrian transgression, the sea-level reached its present level between 3 to 5 ka B.P. From this time to the present days Haslett et al. (1998) and Jennings et al. (1998) estimated the rate of sea level rise in the Bristol Channel to be between 0.41 to 0.8 $mm.y^{-1}$ (Figure 1.14). The bathymetry maps shown later suggest that the area surrounding the Helwick (about 20 to 30 m below present day Mean Sea Level) and the Nash Sands (about 10 to 15 m below present day Mean Sea Level) would have been drowned around 8 ka and 7 ka BP, respectively. The beginning of the formation of the Bristol Channel sandbanks is therefore speculatively dated to this period, although Stride and Belderson (1990) suggested that the present day circulation and resulting sand transport originated between 3 and 5 ka BP.

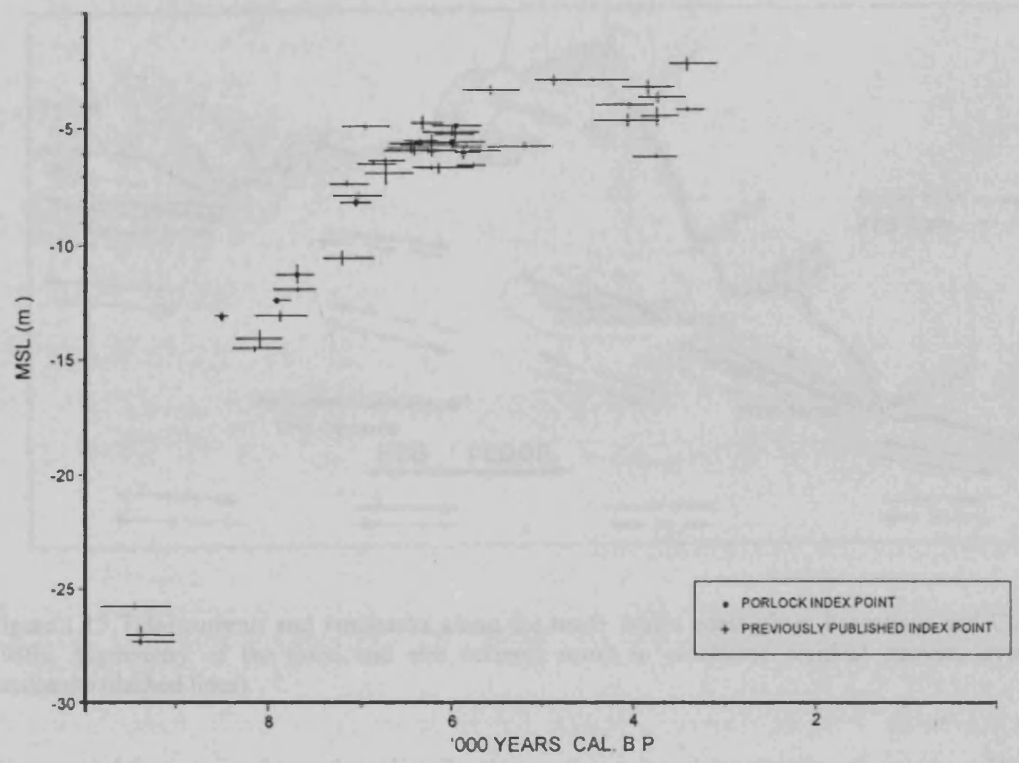

Figure 1.14 Relative sea-level index points from the Bristol Channel (from Jennings, 1998).

1.5.3. Sediment transport

The glacial-supplied sand and to a lesser extent sediment supplied from rivers (Collins, 1987) were mobilised by the present day tidal and wave currents to produce the Bristol Channel scattered sand deposits. Various authors (Belderson and Stride, 1966; Ferentinos and Collins, 1980; Harris, 1982; Harris and Collins, 1984; Pattiarchi and Collins, 1987; Harris, 1988a; Harris and Collins, 1991; Stride and Belderson, 1991; McLaren et al., 1993) have analysed the morphology and distribution of these sediment deposits. They attributed the distribution of deposits to the availability of sediment and pattern of convergence of the sand transport pathways. Figure 1.15 illustrates how the differing flood and ebb currents produce a circulatory residual current over the banner bank.

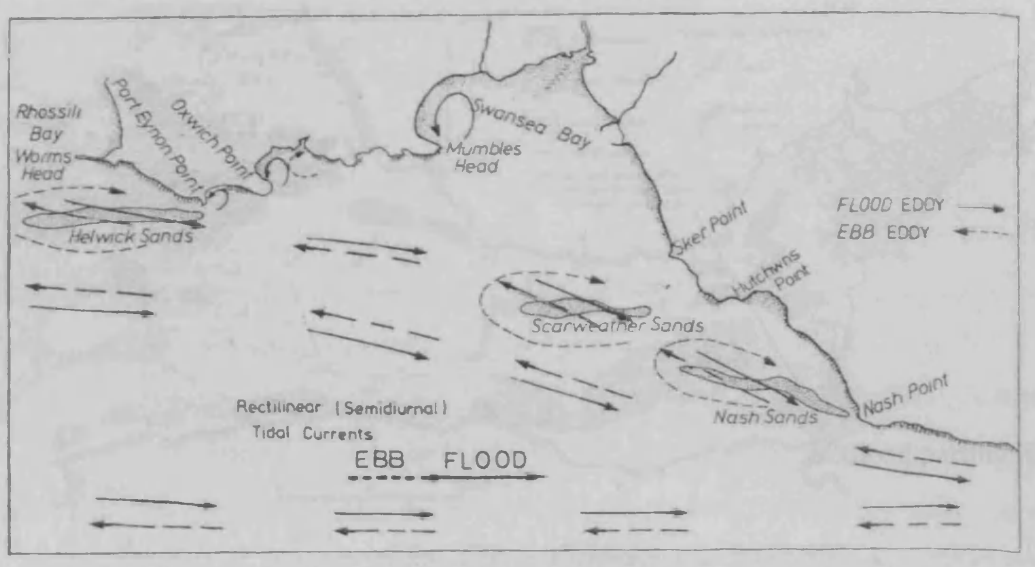

Figure 1.15 Tidal currents and sandbanks along the south Wales coast (from Ferentinos and Collins, 1980). Asymmetry of the flood and ebb currents result in clockwise residual currents over the sandbanks (dashed lines).

Figure 1.16 summarises the distribution of sandy deposits in the inner Bristol Channel. Harris (1982) and Harris (1988a) noticed, in the lower estuary end (west of a line from Worms Head to Bull Point), that sand deposits are concentrated in the peripheral near-coastal areas. From the extensive work of Harris (1982), Harris (1984), Harris (1988a) and Harris (1991), sand dunes are found in association with the sandbanks and as sand dune fields in the entrance of the Channel. Sand ribbons are distributed in the centre of the channel where sand is scarcer, grading from elongated sand dune trains to linear ribbons (Kenyon, 1970). Small dunes have not been extensively reported because of the resolution of the surveying equipment. In several areas, especially in the central part of the Channel, scouring induced by the strong tidal currents has resulted in exposure of bedrock.

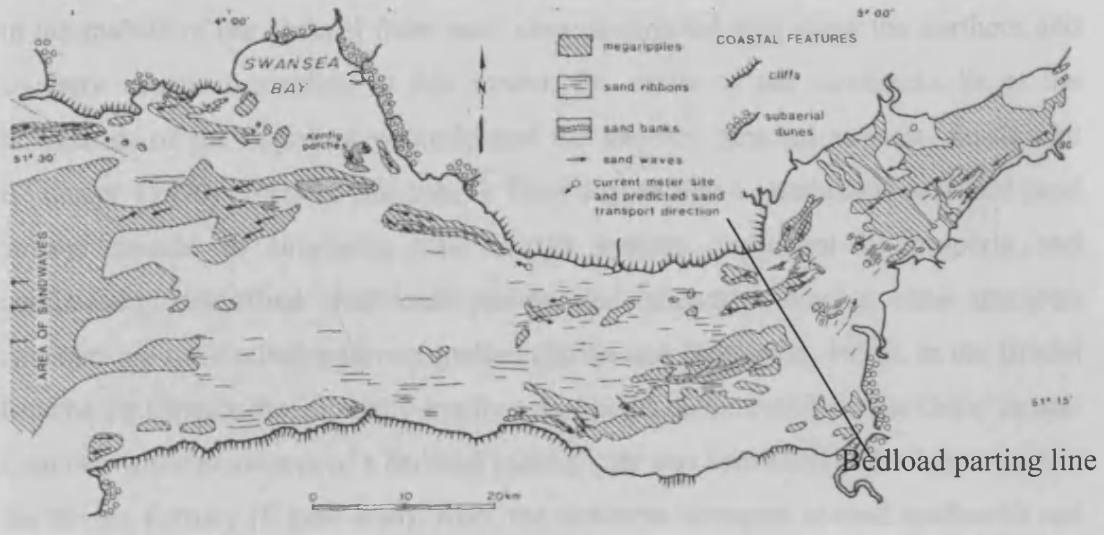

Figure 1.16 Distribution of sedimentary deposits and areas of bare or thinly sedimented bedrock (white) in the Bristol Channel (From Harris, 1982). Approximate position of the bedload parting line is located according to information collected in the literature (see text for details).

The distribution of bed shear stress in the Bristol Channel has been investigated by Uncles (1983) and correlated with the sediment transport pattern inferred from bedforms. The analysis of the distribution of sand deposits and more especially the sense of asymmetry of dunes suggest that a bed-load parting (Stride, 1963; Belderson and Stride, 1966; Harris et al., 1995) occurs in the Bristol Channel. The accurate position and geometry of this bedload parting area is still under discussion (Stride and Belderson, 1990; Harris and Collins, 1991; Harris et al., 1995), hence only a straight line representing its approximate position is shown in Figure 1.16. West of this bed-load parting line the flood-tidal current is dominant over almost the entire width of the Bristol Channel, whereas east of this line sediment movement is directed towards the east leaving the Severn Estuary sand-congested.

Harris and Collins (1988) estimated the annual bedload sand flux in the estuary due to the tidal currents. From grain size measurements and current meter data they estimated fluxes in and out the channel along a transect originating from Nash Point. They showed that the inward (flood dominated) flux of 64.5×10^5 $t.y^{-1}$ was almost balanced by an outward (ebb dominated) flux of 63.7×10^5 $t.y^{-1}$. Areas of net eastward flux were inferred along the northern coast of the estuary while areas of net westward flux were observed along the southern coast and along the Breaksea Valley. From these calculations, Harris and Collins (1991) presented "a mutually evasive sand transport pattern" conceptual model for the Bristol Channel and Severn Estuary, with longitudinal shore-parallel boundaries separating the westerly directed sand transport

in the middle of the channel from sand streams directed east along the northern and southern coasts. According to this model, the crests of the sandbanks lie at the boundaries of the opposing westerly and the easterly directed streams. Stride and Belderson (1990) criticised this model. They argued that a continuous eastward sand stream capable of supplying sand to the system could not be properly and continuously identified. Bed-load parting and mutually evasive sand transport concepts are not exclusive of one another (Stride and Belderson, 1991). In the Bristol Channel, it appears that mutually-evasive sand paths occur mainly in the Outer Bristol Channel, while evidences of a bedload parting area was identified in the Upper part of the Severn Estuary (Figure 1.16). Also, the sediment transport around sandbanks and its role in the overall system is still questioned (Pethick and Thompson, personal communication).

1.6. Presentation of the new datasets and the structure of the thesis

This chapter has related how instantaneous and residual currents in the lee of a promontory, have been used to explain the origin and maintenance of banner sandbanks. However, how the banks, now grown, maintain themselves attached to the coastline has not been addressed in full detail. Furthermore, no study of the sediment dynamics has focused on the immediate connection of the banks with the shore.

Previous studies of the morphology and dynamics of sedimentary deposits have been generally undertaken using sidescan sonar. This type of equipment permits a qualitative description of the marine seabed. Modern multibeam sonar technology (also known as swathe bathymetry) provides, however, a way to quantitatively characterise the geometry of these sedimentary deposits both in plan-view and in height. Moreover this study will demonstrate that repeated surveys of these deposits permit the quantification of their morphological changes and sand dynamic. Data presented here will allow determination of wether either side of the bank are in balance and discussion of how much sand is presumably transported across the bank to maintain sand volumes. Hence, the present work constitutes the first document describing the acquisition and interpretation of repeated swathe bathymetry surveys of banner sandbanks used to infer the dynamics of local sand transport. Two sites have

been investigated in the Bristol Channel, Helwick and Nash Sands (Chapters 3 and 4), for their difference in hydro-dynamic characteristics (wave and tide). In both case the dune kinematics and the inferred sand transport fluxes (from the comparison of quasi-annually repeated surveys) are compared with calculated sand flux from grain size, wave and tidal current data. The study of the Nash Sands (Chapter 4) also includes the migration of dunes over a short time scale (19 days). The extent of the bathymetric datasets acquired for this study are introduced in the following two sections.

1.6.1. Helwick Sands

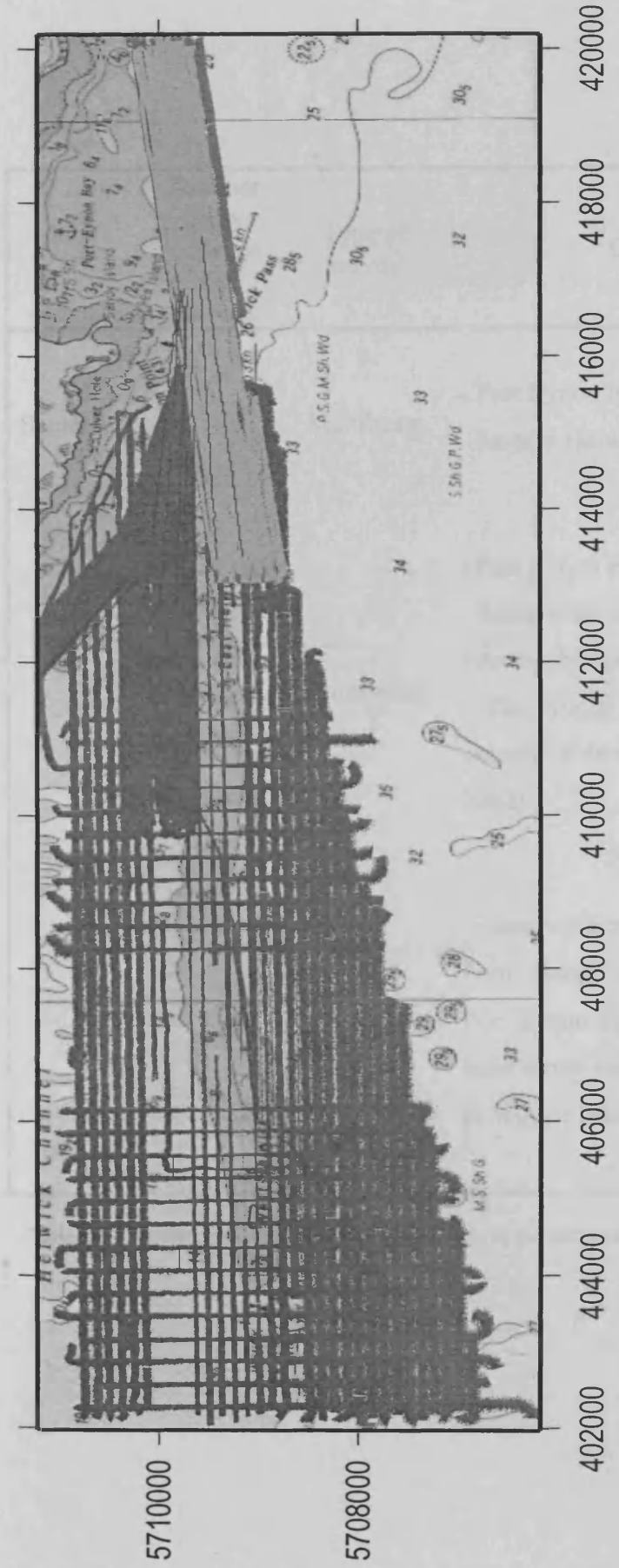

Figure 1.17 Surveys undertaken in the Helwick Sands area plotted over the Admiralty Chart 1165 (water depth in meters). Dark grey shows the extent of the 2002 multibeam survey only. Light grey shows the area covered by both 2001 and 2002 surveys. 2003 Single-beam tracks are represented by black lines. For this map and all the subsequent maps of the Helwick and Nash Sands, map coordinates are in UTM zone 30. Easting and Northing distances are in m.

Date	Number of days between the surveys	Type of survey	Geographic extent
26 September 2001	328	Multibeam	- Port Eynon Bay - Eastern Helwick (mainly south flank)
20-26 August 2002	278	Multibeam	- Port Eynon Bay - Eastern Helwick (north and south flank) - Along the coast towards Worms Head - The whole bank with 150 m by 350 m spacing (between the 22 and the 26 of August 2002)
25 May 2003		Singlebeam	-Eastern Helwick (2 lines from Port Eynon Point along the southern flank, 5 lines from Port Eynon Point along the northern flank, 3 lines along the coast from Port Eynon Point to Worms Head)

Table 1.3 Repeated bathymetric datasets collected for the purpose of this thesis around Helwick Sands

1.6.2. The Nash Sands

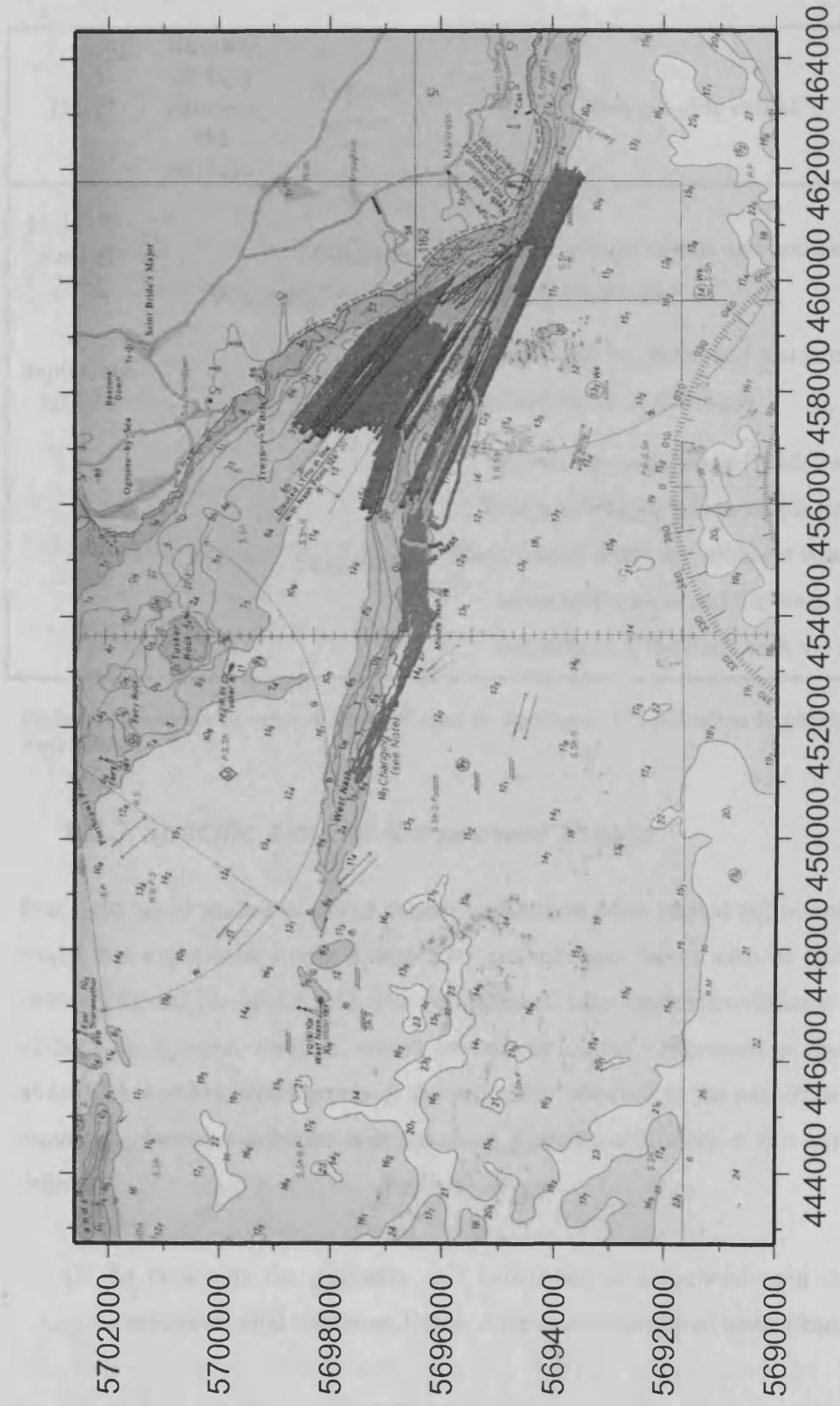

Figure 1.18 Surveys undertaken in the Nash Sands area plotted over Admiralty Chart 1165 (water depth in meters). Dark grey shows the extent of the first multibeam survey only. Medium grey shows

the extent of the second multibeam survey only. Light grey shows the area covered by both surveys. 2003 Single-beam tracks are represented by black lines.

Date	Number of days between the surveys	Type of survey	Geographic extent
16-17-19-August 2002	19	Multibeam	-Eastern Nash (northern and southern flanks and along the coast).
4 September 2002	263	Multibeam	-Eastern Nash (northern and southern flanks) -Southern flank of mid Nash
25 May 2003		Singlebeam	-8 lines along the coast (Nash Point to Trwyn-y-Witch), 5 lines on the northern flank, 6 lines along the southern flank, 6 lines between the bank and the coast at the connection of the bank with the shore

Table 1.4 Repeated bathymetric datasets collected for the purpose of this thesis at the connection of the Nash Sands

1.6.3. Specific aims of the present thesis

Few field based studies of linear banner banks have been carried out in areas of the world that experience strong mixed tidal currents and waves such as those in the Bristol Channel (Section 1.5.1). The two selected sites experience different intensity of the hydrodynamic forcings, which are morphologically expressed on the seafloor and which enabled investigation of the processes involved in the movement of sand around the banner sandbanks near the shore. Specific objectives of this study are as follows:

(i) To determine the geometry and kinematics of associated sand dunes and characterise sand migration fluxes at the nearshore end of banner banks.

(ii) To asses whether the sand flux derived by dune tracking are compatible with data on the tidal and wave currents and grain size characteristics.

(iii) To asses whether the characterized fluxes are balanced on either side of each bank

(iv)To compare and contrast Nash and Helwick Sands to see if their different water depths, tidal currents and wave climates lead to different sand fluxes and morphology.

1.6.4. Structure of the thesis

Chapter two: "time lapse bathymetric surveys: acquisition, comparison and interpretation method"

As this thesis strongly relies on the interpretation of high resolution bathymetric data, this chapter presents the equipment and the processing methods that were used. Also, a new method for characterising uncertainties between repeated surveys is presented prior to discussing the significant changes due to sediment erosion/deposition in the next chapters. Finally, this chapter presents a method based on the application of the autocorrelation function and directional variograms to the multibeam data in order to characterise the geometry of sand dunes. Such data are then discussed along with relationships to flow properties.

Chapter three: "Helwick Sands" and Chapter four: "Nash Sands"

These two chapters describe observations of the banks and the distribution and geometrical properties of associated sand dunes. Then dune kinematics (migration rates and calculated sand fluxes) are presented from the comparison of the surveys. These observations are then discussed with the aim of characterising the environmental factors involved in sediment transport at the nearshore end of these banks. These two chapters will have a similar structure to enable a comparison between the sites.

Chapter five: (Discussion) "Comparison of the Nash and the Helwick connection with the shore and their relation to the general Bristol Channel sediment transport"

This chapter compares the morphology and dynamics of these two banks. These are discussed along with the difference in tidal regime (stronger for the Nash) and wave power (stronger for the Helwick) at both banks. The findings of this thesis are discussed in the context of other banner sandbanks. Limitations and suggested work will also be presented.

Chapter six: "Conclusion"

This last chapter summarises the findings of this work.

Chapter 2.

Time lapse bathymetric surveys: acquisition, comparison and interpretation method

2.1. Introduction

Bathymetric data constitute the main dataset of this study. Other types of data that support the observations and interpretations will be introduced in subsequent chapters. Bathymetric data have been acquired with modern acoustic echo sounders. However, various uncertainties occur related to the equipment used and the survey conditions. It is therefore essential to present how these data were acquired and assess uncertainties before any interpretation.

The objectives of this chapter are:

1. To provide an overview of the data acquisition techniques, broadly discuss their limits and describe basic processing methods applied;
2. To present a new method aimed at assessing the relative vertical accuracy between repeated bathymetric surveys. The rationale of this part is to evaluate the accuracy of sand dune change and sediment transport between the surveys, which will be used in Chapters 3 and 4.
3. To present an innovative method for characterizing sand dune height, orientation and spacing based on the calculation of the autocorrelation function and semi-variogram from high-resolution multibeam bathymetric data. This section aims to characterize quantitatively the geomorphology of dunes, which can be used to study systematic trends in the datasets.

2.2. Bathymetric data acquisition and processing

2.2.1. Acquisition

Sound waves propagate in the water column. Celerity of the sound in water (V) is between 1450 $m.s^{-1}$ and 1550 $m.s^{-1}$, depending on the salinity and the temperature which affect the density and the elastic modulus of the medium. Reflection occurs at the seabed due to the difference of impedance between the water column and the seabed material. The time needed for the acoustic pulse to travel in the water column, to be reflected at the seafloor and return to the transducer is known as the two-way travel time (TWTT). At vertical incidence the water depth is calculated from the sound wave celerity (V) and the TWTT as follows:

$$z = \frac{Vt}{2}$$ Equation 2.1

where t is the TWTT measured by the echo-sounder.

A piezo-electric transducer transforms an electric signal into an acoustic pulse. The acoustic pulse is created at the transducer. Because of reciprocity of the piezo-electric component the returning signal, also received at the transducer, is turned into an electric signal, amplified and recorded. Uncertainties are induced by multiple reflection, propagation losses, variations of the sound velocity in the water column (Lurton, 2002). Horizontal positioning is generally provided by a Differential Global Positioning System (DGPS). A depth measurement is hence fully qualified by coupling the horizontal position (x,y) and depth under the sounder (z).

2.2.1.1. Instrumentation

2.2.1.1.1. Single beam echo sounder

Single beam echo sounders collect discrete depth measurements along the vessel's track. The transducer points vertically, below the vessel (Figure 2.1a). The TWTT is measured when the time at which the sharp leading edge of the first returning acoustic peak is detected. This method is also known as amplitude detection. The resolution of an echo-sounder defines its detection capabilities. This is a function of the pulse duration, the angle of incidence of the acoustic wave with the target, the nature of the target and the beamwidth. Modern transducers transmit pulses of typical duration of 10^{-4} to 10^{-3} s in a beam of angular aperture of the order of 5-30°.

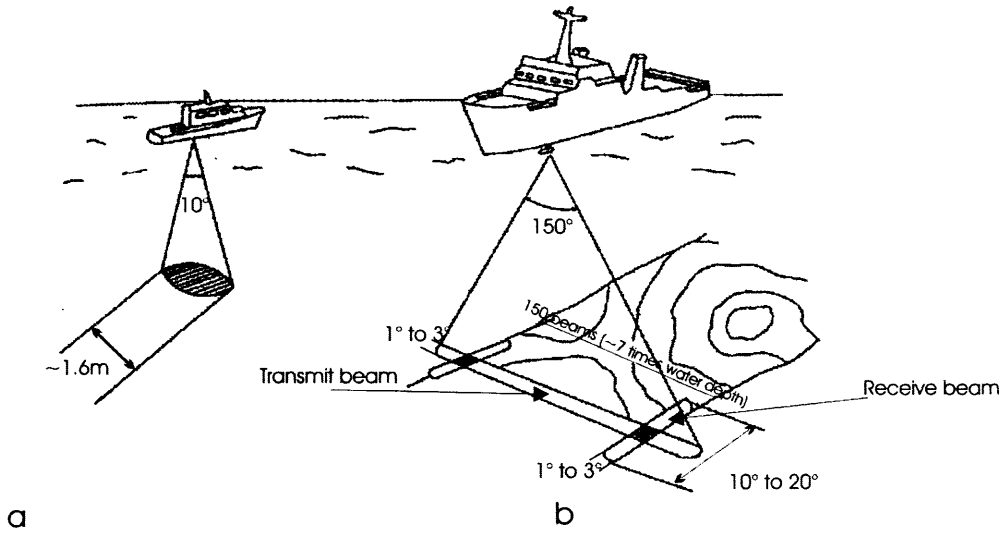

Figure 2.1 Geometry of acquisition of bathymetric data (modified after Kerleguer (1992)). Footprint dimensions are given for a water depth of 10 m.
a) singlebeam echosounder
b) multibeam echosounder (see text for details).

2.2.1.1.2. Multibeam sonar

The multibeam echo-sounder is essentially an extension of the single-beam echo sounder. Instead of transmitting and receiving a single vertical beam, however, the multibeam sounder transmits and receives a fan of beams with small individual widths (1 to 3°) across the axis of the ship. The fan of beams is formed by the "mills cross" principle described as follows. The multibeam sonar head consist of one transmitting array (along the axis of the head) and one receiver array (perpendicular to the axis of the head), each of which are generally composed of ceramic transducers. The transmitting array emits a wide across-track and narrow along-track beam (typically 150 to 170° by 1° to 3° for shallow water equipment depending on the manufacturer). The receiver array generates a series of fan-shaped receiving beams that are in planes parallel to the ship's direction of travel (typically 1° to 3° in the across track direction, and 10° to 20° in the along track direction). These beams are either physically or electronically steered ("beam-steering"). The system then detects echoes from the narrow areas of the seafloor that are formed by the intersection of the transmitting and receiving beams (Figure 2.2). For convenience, the intersection of the transmitting beam and the receiving ones are known as individual beams.

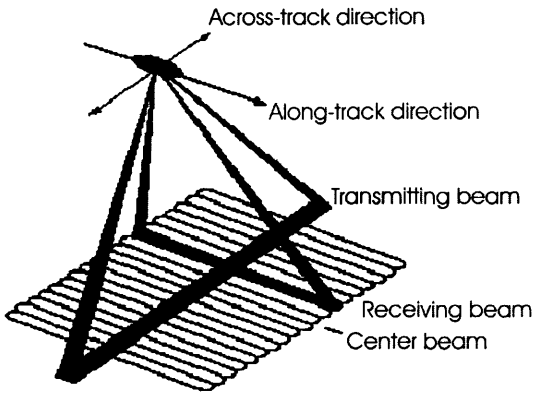

Figure 2.2 Geometry of multibeam sonar data acquisition (modified from Grant and Schreiber (1990))

Bathymetry measurement by a multibeam sonar corresponds to the determination of the couple (y_h,z_h) where y_h is the horizontal distance and z_h the vertical distance of the footprint on the seafloor relative to the sonar head. This couple is computed from the measurement of the couple (t, θ_R) as follows (Farr, 1990):

$$\begin{cases} y_h = \frac{Vt}{2}\sin\theta_R \\ z_h = \frac{Vt}{2}\cos\theta_R \end{cases} \qquad \text{Equation 2.2}$$

where θ_R is the angle of the transmitting beams with the nadir. Sound velocity varies between 1400 m.s^{-1} and 1800 m.s^{-1} with the salinity, the temperature and the pressure. In unevenly mixed water, the celerity profile may change rapidly, with a direct impact on the geometry of the acoustic path (ray) in the water column, especially for oblique beams. The ray of beams at oblique angles must be reconstructed using a ray-tracing algorithm (Kammerer, 2000) with an accurate knowledge of the sound velocity profile in the water column. The accuracy of the measurement of the arrival time is also dependant on the bottom detection method employed by the system. Generally multibeam sonars use two modes of bottom detection. The amplitude detection, described earlier for single-beam echo-sounders (Section 2.2.1.1.1) is efficient for near-nadir beams (see Figure 2.3a). For increasing grazing angles, the echo loses its sharp leading edge and the accurate determination of depth with the amplitude detection method, becomes more difficult as illustrated in Figure 2.3a. An alternate solution is to use the phase detection method, illustrated in Figure 2.3b. This method consists of measuring the TWTT when the phase difference between two nearby beams pointing in the same angular direction is null (De Moustier, 1998). The phase

differences between the two received time series are computed at each instant. The time of null phase difference corresponds to the arrival of a signal from a target in the beam axis. Both amplitude and phase detection methods are performed on each beam on many modern multibeam sonars, including the Reson 8101 used for the present study. The system software uses a weighted function to compute the mean TWTT determined by both methods (RESON, 2001).

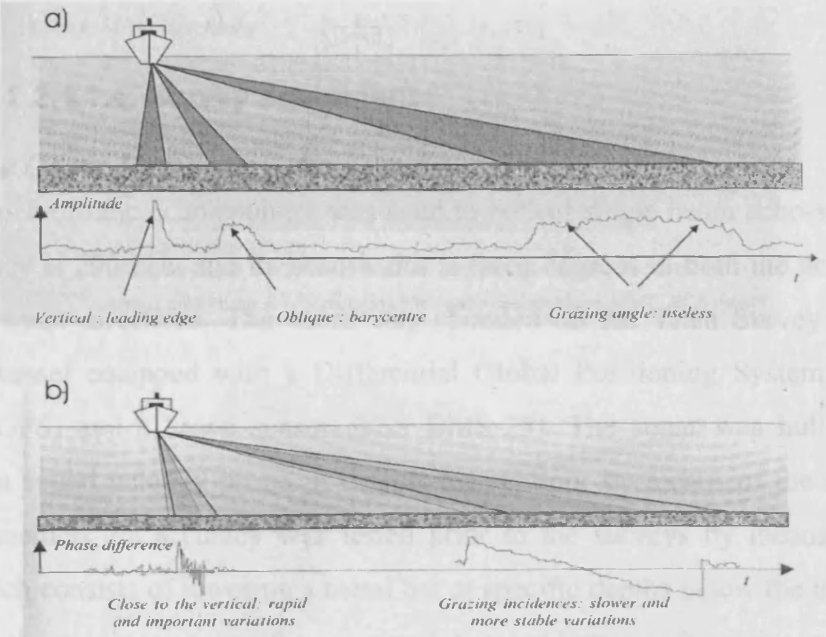

Figure 2.3 Amplitude (a) and phase (b) detection methods (from Lurton (2002)).

2.2.1.1.3. Position and motion of the platform

As multibeam sonar determines the angle and range of echoes within beams relative to the sonar head, corrections allowing for the vessel orientation and position must be applied to the angle and range couple to project them into a geographical frame. Hence, both the vertical and horizontal accuracies of the soundings are easily degraded by poor quality of positioning and orientation. Vessel orientation is monitored by measuring the roll, pitch, yaw and heave with a motion system physically attached to the boat (generally as close as possible to the centre of gravity). Especially roll and, to a lesser extent, pitch, yaw and heave also affect the estimated position of the impact of the acoustic beam on the seafloor. Modern systems (such as the Reson system) solve this problem by using a motion sensor with an accuracy of 0.05° or better (TSS, 1999) and using the angular roll data to steer the sounder's beam

towards the correct direction instantaneously (roll compensation). Bathymetry measurement errors induced by the position and motion of the platform can hence be either biased by, for example, the angular misalignment of the sonar head, which is considered to be stable and predictable or by random fluctuations (jitter) in the angular measurement of the platform, which are characterised by a high frequency and are unpredictable.

2.2.1.1.4. Survey equipment

The Odom Hydrotrac echo-sounder

The Odom Hydrotrac echo-sounder was used to collect single beam echo-soundings. Its frequency is 200 kHz and its beamwidth is three degrees in both the across-track and along-track directions. The sonar was operated on the Titan Survey company Surveyor vessel equipped with a Differential Global Positioning System (Trimble AG132 DGPS) and a heave sensor (TSS DMS-25). The sonar was hull mounted alongside a sound velocity probe. It detects the seafloor by means of the amplitude detection method. Its accuracy was tested prior to the surveys by means of a bar check, which consists of lowering a metal bar at specific depths below the transducer, comparing the readings against the measured distance between the sonar and the bar. The specification of this echo-sounder are detailed in Table 2.1.

Frequency	200 kHz
Range resolution	0.01 m
Minimum depth	0.2 m
Maximum depth	300 m
Maximum ping rate	20 Hz

Table 2.1 Odom Hydrotrac single beam echo-sounder characteristics

The Reson 8101 system

The Reson Seabat 8101 multibeam operates at 240 kHz, generates 101 beams per ping across an angular sector of 150°. The usable angular sector in shallow water is limited to ~130°. In shallow waters, the sonar is hence capable of providing a swath coverage of about 5 times the water depth. However multiple paths (reflection of the signal on the air/sea and seabed interfaces) may limit the coverage down to 3.5 times the water-depth. The maximum ping rate for the 8101 system is 30 pings per second. The beam widths in both the fore-aft and port-starboard directions are 1.5°, and are of equal angular size regardless of whether they are at the nadir or the outer beams. The design of the Seabat 8101 utilizes a curved receive array. The curved array allows the system to generate beams that are orthogonal to the face of the array. The 8101 is capable of both amplitude and phase detection methods. The Applanix POS-MV220 was used to measure the position and motion of the survey vessels on which the sonar was mounted. Sound velocity was measured alongside the sonar head. Because the water-column was supposed to be well mixed by the strong tidal and wave currents, sound velocity profiles were recorded only occasionally (every two to three days of survey). Some of the most important physical characteristics of the equipment are summarised in Table 2.2.

Frequency	240 kHz
Range resolution	1.25 cm
Minimum depth	0.5 m
Maximum depth	500 m
Number of beams	101
Transmit beamwidths (across-track x along-track)	170° x 1.5°
Receive beamwidths (across-track x along-track)	1.5° x 15°
Maximum horizontal coverage	150°
Maximum ping rate	30 Hz
Pulse length	21 to 225 μs

Table 2.2 Reson 8101 multibeam echo-sounder characteristics

2.2.1.2. Limitations of echo-sounders' ability to record sand dunes

Sand dunes are finite three-dimensional objects with sizes ranging from ~5 cm to 20 m in height, 10 cm up to 1000 m spacing and extending along crest by a few metres to few hundreds meters (see Allen (1982), Ashley (1990) and Section 1.4). Since singlebeam echo-sounders only provide one dimensional profiles, the lateral continuity of the bedform cannot be investigated without interpolation between the surveyed tracks. Voulgaris and Collins (1991) also discussed the apparent geometrical distortion of the dunes cross-sections which can occur depending on the orientation of the survey tracks relative to the transversal direction of the bedforms. However, single beam echo sounders provide a cost-effective solution for tracking bedform changes over time. For the purpose of this work, this type of sonar was used to track dunes located first in the multibeam surveys.

Theoretically, the ability of multibeam sonar to detect bedforms depends on the across-track and along-track resolution of the sonar, as well as the density of soundings. Across-track resolution is equal to across-track transversal beamwidth 2_T projected onto the seafloor:

$$\delta y = \frac{z\theta_T}{\cos 2\theta} \qquad \text{Equation 2.3}$$

Along-track footprint size is equal to the distance of the seabed from the sonar head times the along-track beamwidth (θ_L):

$$\delta x \approx \theta_L R \qquad \text{Equation 2.4}$$

Hence the footprint size on the seafloor at 10 m for a Reson 8101 sounder is 0.2 cm x 0.2 cm (along-track x across-track) at the nadir, and 0.4 cm x 0.5 cm at a 45° grazing angle. Supposing such geometry of the surveys, a speed of 8 knots and a typical pinging rate of 30 Hz, provides a density of footprints on a flat seabed as shown on Figure 2.4.

Practically, however, due to the precision of the differential GPS system used in these surveys (constant broadcast from Nash Point), the horizontal data resolution was around 1 m.

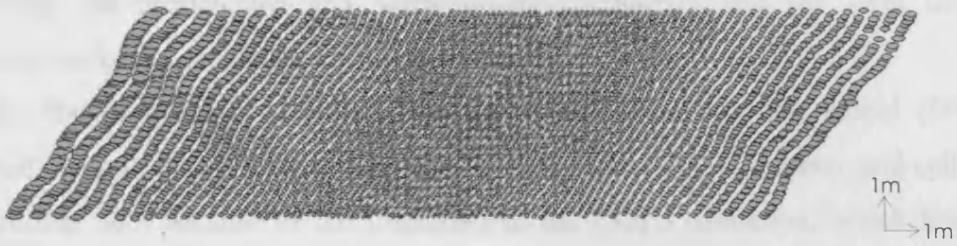

Figure 2.4 Footprint density pattern for the Reson 8101 at 8 knots, with a ping rate of 30 Hz for a waterdepth of 10 m over a flat seafloor.

The vertical resolution of a multibeam echosounder is defined as the minimum depth difference that can be determined between adjacent acoustic returns. This resolution is essentially a function of pulse length. Shorter pulse allows greater resolution in the angle and amplitude measurements to be achieved (Lurton, 2002). With the specification of both the Hydrotrack and Reson 8101 echosounders, the manufacturers claim that the sonars can resolve features vertically separated by 2 cm in the water depths surveyed here.

2.2.2. Processing

Before any meaningful Digital Elevation Model (DEM) is created, erroneous data must be removed and environmental corrections must be applied. Figure 2.5 presents the different steps of the processing workflow. Erroneous measurements or outliers for each of the sensors are first removed (i.e. sonar, positioning and motion sensors). This has been done manually, using the CARIS HIPS software, which allows visualising each of the sensors individually in order to assess the data quality. Travel time and beam angle are then recalculated to true vertical and horizontal distance from the sonar allowing for refraction of the acoustic ray in the water column using independently measured vertical profile of the sound velocity.

A procedure called "patch-test" involving repeat surveying of particular areas of seabed in different speeds and directions is carried out prior to the surveys in order to work out angular and timing offsets between the motion sensor unit and the sonar head (Hare et al., 1995). These calibration values are then applied when the measurements of the sonar corrected for refraction and from the other sensors (DGPS, motion sensors and tidal signal) are then merged together. During this step the

soundings are recalculated and geographically projected, and sea level heights measured at local tidal gauges are applied.

Finally, the bathymetric data are used to form a digital terrain model (DTM). Fluctuations (noise) are averaged out within each grid cell. A one meter grid cell size was chosen here because of the limitation of the DGPS resolution, which had the coarser spatial resolution. Hence the DTM is created as a grid of cells in which the soundings are averaged. Single beam surveys are displayed as along-track profiles.

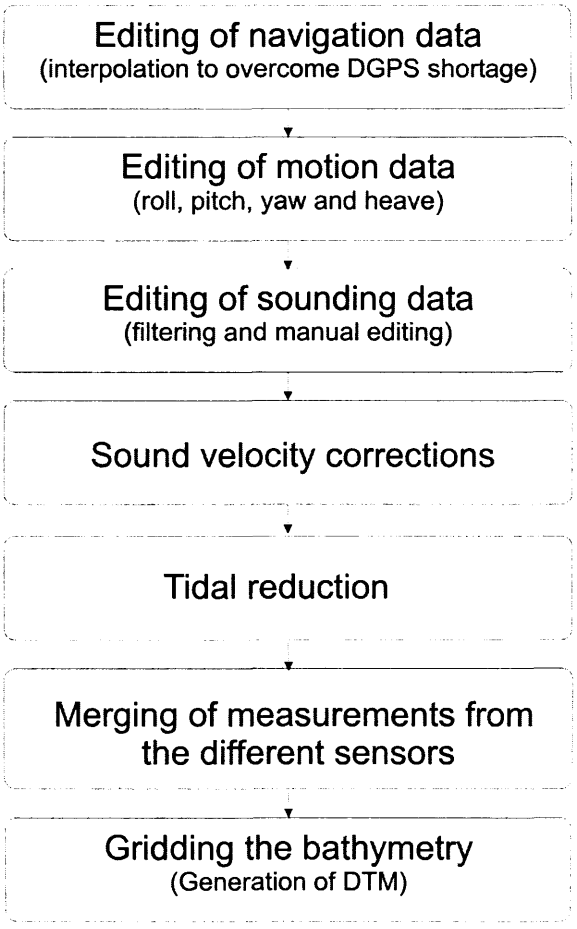

Figure 2.5 Multibeam data processing workflow

2.2.3. Tidal height prediction method

In order to make valid comparison of the different datasets, it is essential that the datasets are corrected to a common vertical reference datum. However, the different datasets have been collected at different stages of the tide and tidal levels were not always collected in the immediate vicinity of the survey. The following paragraphs will present a scheme that was elaborated in order to correct tide measurements recorded at a permanent gauge at the Mumbles for the different time and amplitude of

the tide in the Helwick area. This method relies on the comparison of a tidal heights record, concomitantly acquired at the Rhossili Beach during the 2002 multibeam survey of the Helwick (courtesy of Longdin and Brownig Ltd.) and at the Mumbles. The justification for using such a method is based on Uncles (1983) who presented the variation of the phase and the amplitude of the tidal signal in the Bristol Channel. He showed that these two characteristics vary primarily along the estuary rather than across it.

The method of comparison consists of finding values of the amplitude scale factor (A_0) and phase shift (t_0) minimizing the root-mean-square difference between the two tide measurements (after applying an amplitude scale factor and a phase shift to one of them) so that Equation 2.5 can be equated.

$$H_2 = A_0(H_1(t - t_0)) \qquad \text{Equation 2.5}$$

where H_2 is the Rossili tide measurement (used as reference), H_1 is the Mumbles tide measurement, A_0 is the amplitude multiplier and t_0 is the time offset.

The amplitude multiplier was iterated from 0 to 0.2 in steps of 0.01 and the time phase shift was iterated from 0 to 10 minutes in steps of 30 seconds. RMS differences between the corrected Mumbles and Rhossili measurements show a minimum for an amplitude coefficient of 0.1 and time offset of 7 minutes (Figure 2.6). The RMS difference at this point is 0.5 m. Figure 2.6a shows an example of the match between the two tide records with these values of A_0 and t_0.

a)

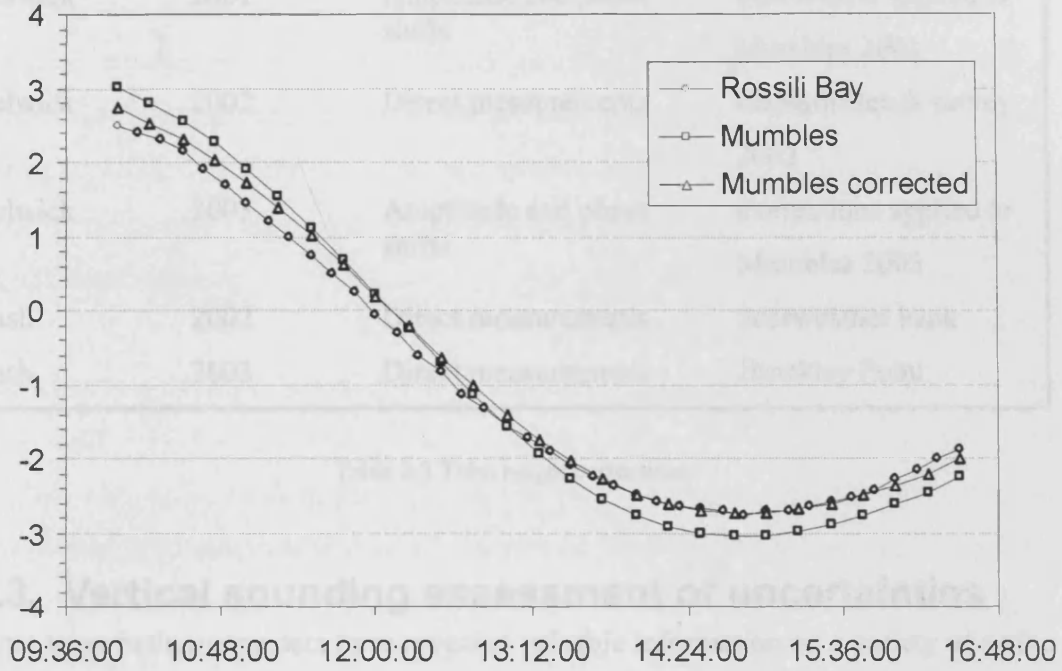

b)

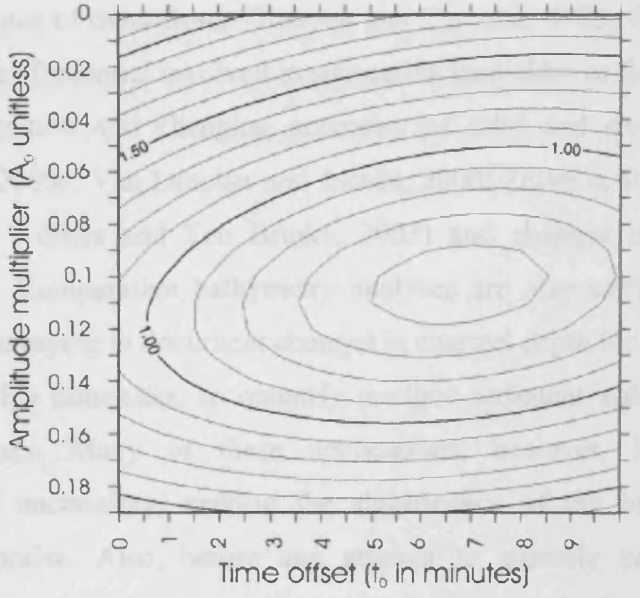

Figure 2.6 Amplitude factor and phase shift determination between Rhossili and Mumbles tidal heights records. (a) Example of records at both sites on the 28/08/2002. (b) RMS difference (m) between the Rhossili tide signal and the Mumbles signal corrected as a function of time offset and amplitude multiplier. Best time offset and amplitude multiplier to extrapolate the Mumbles tide to Rhossili is given for the minimum RMS difference (see text for details). Extrapolated Mumbles tide records for amplitude scale factor and phase shift (found for a minimum RMS difference) is also plotted on (a).

For the Nash Sands surveys tide gauges at Scarweather Sands and Hinkley Point provided adequate corrections (Table 2.3).

Survey	Date	Tide correction method	Tide gauge used
Helwick	2001	Amplitude and phase shifts	Corrections applied to Mumbles 2001
Helwick	2002	Direct measurements	Rhossili Beach survey 2002
Helwick	2003	Amplitude and phase shifts	Corrections applied to Mumbles 2003
Nash	2002	Direct measurements	Scarweather bank
Nash	2003	Direct measurements	Hinckley Point

Table 2.3 Tidal height corrections

2.3. Vertical sounding assessment of uncertainties

Time-lapse bathymetric data have revealed valuable information on a variety of active earth science processes such as the spatial distribution of erupted lava (Fox et al., 1997), the advance of delta fronts (Kenyon and Turcotte, 1985; Pirmez et al., 1998), the mobilization of material involved in submarine landslides or floods (Urgeles et al., 2002), the migration and changing geometry of tidal and river bed sand dunes (Carling et al., 2000a; Van Lancker and Jacobs, 2000; Zeiler et al., 2000; Villard and Church, 2002; Wilbers and Ten Brinke, 2003) and changes in beach shorefaces (Komar, 1998). Comparative bathymetry analyses are also carried out in practical hydrographic surveying to document changes in channel depth for navigational safety, to monitor dredge dumpsites, to quantify dredged sediment volumes and sediment transport budgets. Many of these applications, however, have not included assessments of uncertainty, making the significance of the bathymetric changes difficult to appraise. Also, before any attempt to quantify bathymetric changes induced by sediment transport around the Helwick and the Nash sandbanks, it is important to assess the level of relative vertical accuracy of the data collected. Various environmental factors induce systematic or non-systematic vertical errors on bathymetric data. We subdivide vertical inaccuracies into systematic bias and non-systematic uncertainties. Systematic bias, causing a general depth offset between surveys, includes errors in measuring sonar mounting height, but can also include variations of long timescale, such as tidal correction errors or vessel draft, if they

occur over a period typically longer than the time needed to survey an individual line (typically greater than few minutes). This bias is easily removed by finding the mean vertical offset between two datasets, but the uncertainties of shorter spatial and temporal wavelengths are more difficult to assess and can have large magnitudes. Short-wavelength uncertainties are related to the intrinsic noise resulting from the technology, such as ambient noise and motion sensor error. Although not easy to remove, the quantification of their characteristics allows determination of the limits of significant change.

The common practice has been to assess the intrinsic accuracy of each survey individually knowing the instrument characteristics and the conditions under which the data were acquired (Van der Wal and Pye, 2003). However, the full error budget is often difficult to assess as individual component uncertainties are poorly known. We instead take an approach of deriving relative uncertainties more directly from the data. The method is based on a graph presented in Dunn et al. (2001), who calculated the difference of bathymetry collected in two surveys over the East Pacific Rise. They derived a series of histograms of depth differences between the two surveys, with each histogram calculated with data filtered over a different spatial scale. The variability of depth differences was then shown to decay with increasing filter size as expected if differences were spatially uncorrelated random noise and hence there was no resolvable change. In this section, we extend this technique to show how spatially correlated noise can be characterized and then use the results to produce maps of uncertainties and significant seabed change. This method is qualitatively analogous to that of Goff and Kleinrock (1991) who resolved spatial characteristics of co-located bathymetry using the data covariance.

2.3.1. Quantifying vertical uncertainties between co-located bathymetric data

2.3.1.1. Method

Using data from an immobile area of seabed (the "benchmark"), the bathymetry data were convolved with a boxcar filter (moving average). The spatial size of the filter was progressively increased so that the decrease in small-scale fluctuations with

increasing filter width could be studied. A maximum value for uncorrelated fluctuations is then revealed at small filter size, while the way in which variability declines with increasing filter size at broader scales reveals the influence of spatially correlated noise.

Any difference remaining after very large-scale filtering (defined as 100 m scale here) then provides an estimate of the systematic bias between the surveys. The method assumes that the positioning data are perfect because during the fieldwork experiments differential GPS corrections supplied by coastal broadcasts provided ~1 m accuracy (hence the smallest scale of filtering used here). Any larger positioning uncertainty over rugged seabed terrain will cause an artificial depth uncertainty and make the method more difficult to implement.

The method is carried out in four steps:

(1) Filter the co-located bathymetric survey profiles or surfaces separately.

(2) Difference the filtered datasets.

(3) Plot the distribution (histogram) of height differences.

(4) Increase the size of the spatial filter

Re-iterate steps (1) to (4) until the size of the filter is half of the profile length or the seabed area.

Figure 2.7 illustrates the types of graphs used to present the results, where grey coding represents the number of occurrences within a vertical difference by filter length bin. The distribution characteristics are: (1) the convergence of the height difference distribution towards a single height difference class for wide filters, of value interpreted as the systematic bias; (2) a wide distribution for small-size filters, where the distribution width represents the short-scale non-systematic uncertainties.

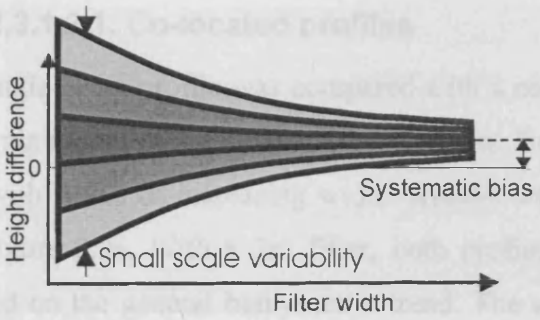

Figure 2.7 Interpretative scheme of graphs of height difference distributions versus increasing filter size. For a given filter width, the difference distribution is plotted along a vertical line with histogram counts in gray (darkness increasing with number of occurrences). Successive distributions show the change in variability with increasing filter size. Systematic bias is the error remaining after small-wavelength variability is removed by filtering (i.e. statistical mean). Small-scale variability is estimated from the width of the distribution at small filter size.

2.3.1.2. Application to bathymetric data collected with different types of sonar

The method was tested on datasets acquired in the vicinity of Helwick Sands, over an area of bedrock supposed not to have been affected by any erosion or sedimentation between the surveys. Therefore differences measured between the datasets are only due to intrinsic uncertainties related to the equipment and the survey conditions. The comparison was done using the two multibeam surveys collected in September 2001 and August 2002 and the single-beam profiles collected in 2003. Track lines and areas used are displayed on Figure 2.8.

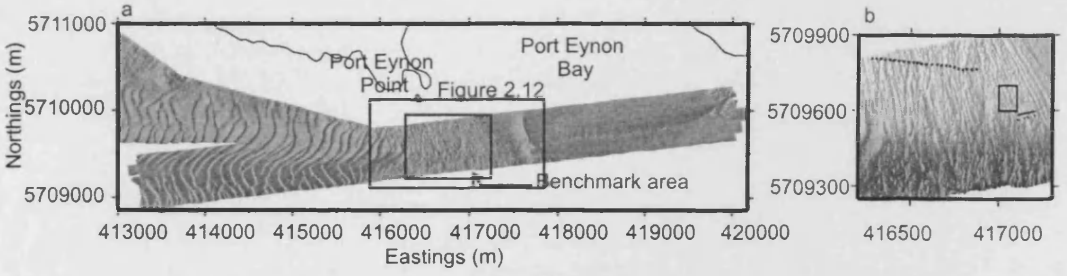

Figure 2.8 Test area. (a) Shaded relief image of the 2002 survey bathymetry. (b) The benchmark area supposed not to have changed over the period between surveys. Superimposed are the singlebeam track (long dashed line); the multibeam area (rectangle) used for comparison, and also multibeam nadir (plain) and off nadir (dotted) beams.

2.3.1.2.1. Co-located profiles

The 2003 single-beam profile was compared with a co-located profile extracted from a digital terrain model of the 2002 multibeam data. The two co-located profiles were convolved with filters of increasing width. Results with 2, 50 and 150 m filters are shown in Figure 2.9a. With a 2m filter, both profiles show small scale variations superimposed on the general bathymetric trend. The unimodal distribution of height differences (Figure 2.9b, left) has a mode at –0.3 m. Its bell shape shows that small-scale fluctuations are distributed almost normally with a 0.28 m standard deviation, suggesting that the vertical uncertainties are mostly due to uncorrelated noise between the surveys. With wider filters, the general trend of the profiles can be observed (Figure 2.9a) but small scale variations are smoothed. The height difference distribution tends towards a peak at -0.2 to -0.3m (Figure 2.9b, middle and right).

In order to show this change in a more general way revealing the transition, the difference distribution was computed for filter widths from 2 m to 300 m. The resulting graph (Figure 2.9c) shows a large variability at small filter widths (broad grey region), which decreases with increasing filter width. The maximum height difference between the surveys at large width (300 m) is centred on -0.2 to -0.3 m, representing the systematic bias (suspected to be partly due to unrecorded changes in vessel draft with fuel expenditure and also to the accuracy of the tide height).

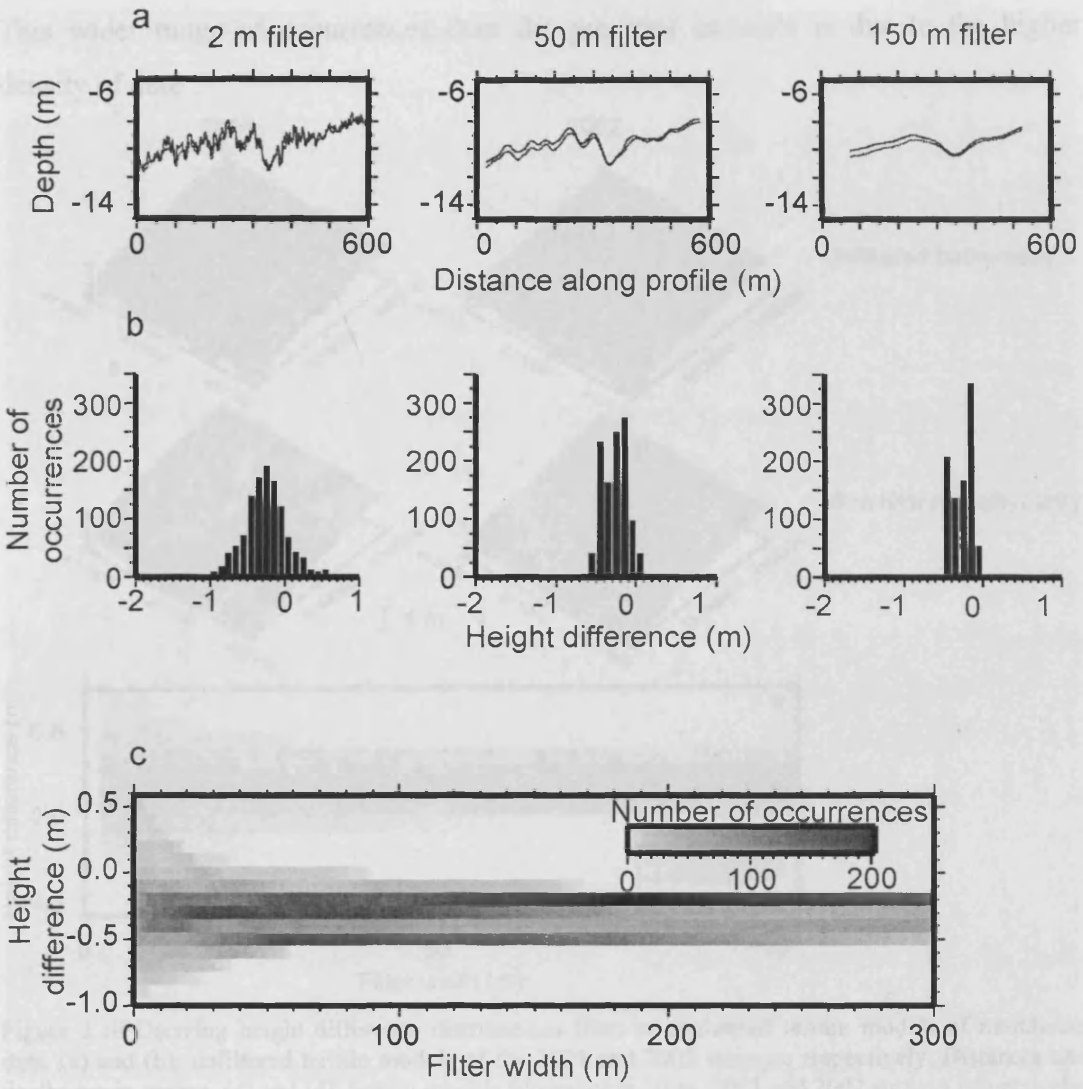

Figure 2.9 Height difference analysis using co-located single-beam and multi-beam soundings. (a) Bathymetric profiles filtered with a 2 m, 50 m and 150 m width (1-3, respectively). (b) Corresponding height difference distributions binned in 0.1 m intervals. (c) Distribution of height differences with increasing filter width. Each of the rectangles represents a 0.1 m difference in height. Occurrences of height differences are grey coded.

2.3.1.2.2. Co-located surfaces

The method can also be applied to surface data e.g. from multibeam surveys. In this case the filter has a circular shape, with an increasing diameter according to the size of the filter. Figures 2.10a and 2.10b show a representative 100 m by 100 m area of bedrock from the terrain models computed from the 2001 and 2002 multibeam surveys (see Figure 2.6 for location). Filtering out the small scale features leaves the general trend surface of the area (Figures 2.10c and 2.10d). Height differences were measured for increasing filter widths, from 0 to 100 m with a 2 m step. Classes of height difference are 0.1 m wide. The grey coding ranges from 0 to 3500 occurrences.

This wider range of occurrences than the previous example is due to the higher density of data.

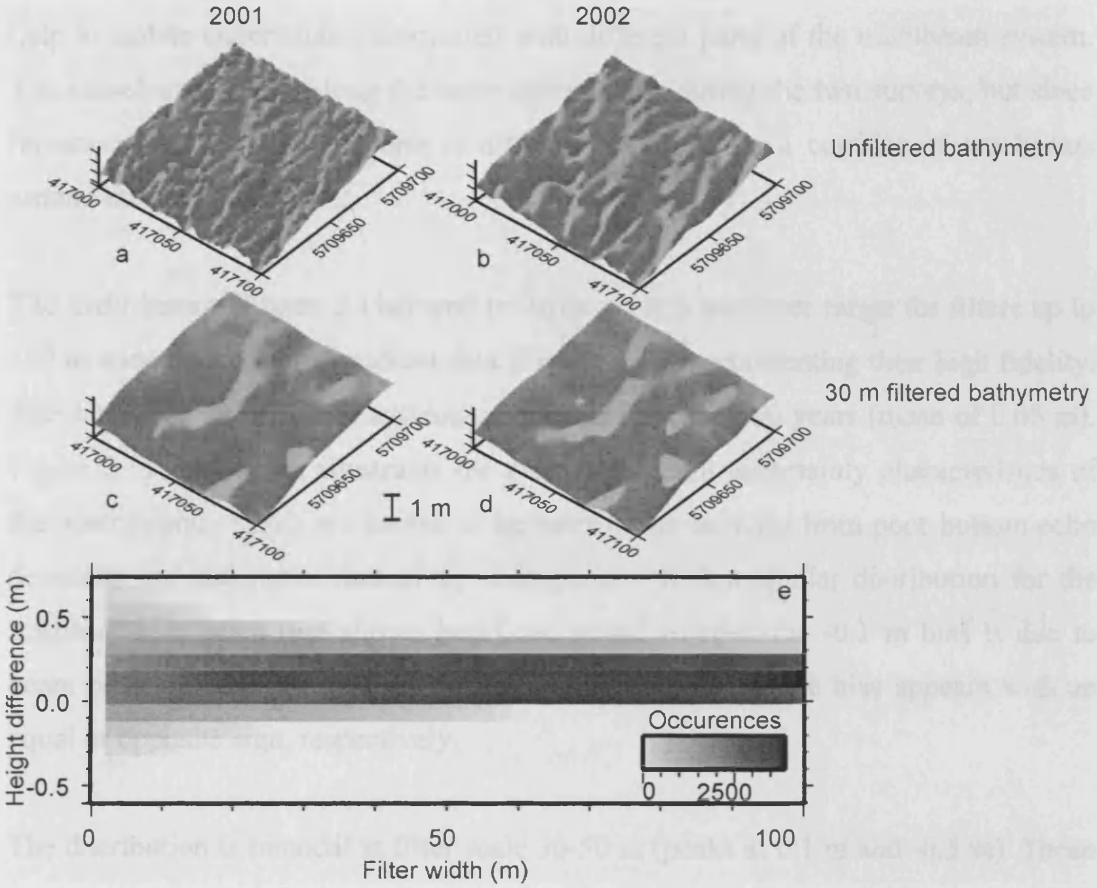

Figure 2.10 Deriving height difference distributions from co-registered terrain models of multibeam data. (a) and (b): unfiltered terrain models of the 2001 and 2002 surveys, respectively. Distances and depths are in meters. (c) and (d): terrain models filtered over 30 m, 2001 and 2002 surveys respectively. (e) Height difference distribution.

Figure 2.10e presents similar characteristics to Figure 2.9c and can be interpreted in a similar way. The two surfaces compared for large filter size (~100 m) show a narrow distribution of height difference classes with a peak of occurrences around 0.15 m, slightly positively skewed. This distribution peak shows a relatively small vertical bias between the surveys. This indicates that the tidal corrections (section 3.3.2.2.1) have reduced tidal error to within 0.15 m. Small scale variability, illustrated on the left side of Figure 2.10e ranges within a standard deviation of 0.329 m about a mean at + 0.1 m. The slow decay in the range of the difference of height distribution suggests an influence of spatially correlated noise in one or both surveys.

2.3.1.2.3. Beam-to-beam comparison

The method was extended to compare soundings for specific beams because this can help to isolate uncertainties associated with different parts of the multibeam system. The vessel was steered along the same survey track during the two surveys, but since repeating exactly the same line is difficult, we compare a corridor of ten beams around the studied beam.

The nadir beams (Figure 2.11a) tend towards a much narrower range for filters up to 100 m wide than with the gridded data (Figure 2.10e), representing their high fidelity. The data show only a small systematic bias between the two years (mean of 0.05 m). Figure 2.11b, however, illustrates the more significant uncertainty characteristics of the outer beams, which are known to be more prone to noise from poor bottom echo detection and roll meter inaccuracy. Comparison with a similar distribution for the starboard side beam (not shown here) can reveal whether the -0.1 m bias is due to beam pointing error or a roll offset, depending on whether the bias appears with an equal or opposite sign, respectively.

The distribution is bimodal at filter scale 30-50 m (peaks at 0.1 m and -0.3 m). These modes may be related to a known irresolvable roll artefact in the 2001 survey. Thus the data standard deviation (2σ), illustrated by the dotted lines in Figure 2.11, decreases more slowly with increasing filter size than expected if the variability were uncorrelated random noise, which is modelled by the continuous lines in Figure 2.11. The latter was calculated by assuming that the filtered data noise σ_{th} should decline with $1/\sqrt{N}$, where N is the number of data encompassed by the filter, in turn proportional to the spatial scale of the filter. Hence the theoretical decay of the uncorrelated noise standard deviation with increasing filter width follows the law $\sigma_{th} = \sigma_0 / \sqrt{w}$, where σ_0 is the unfiltered uncorrelated noise and w the filter width. The standard deviation decreases slowly for the outer beam (Figure 2.11a). Since heave error affects the nadir and outer beams equally, this slower decrease suggests that a roll effect must be responsible for it.

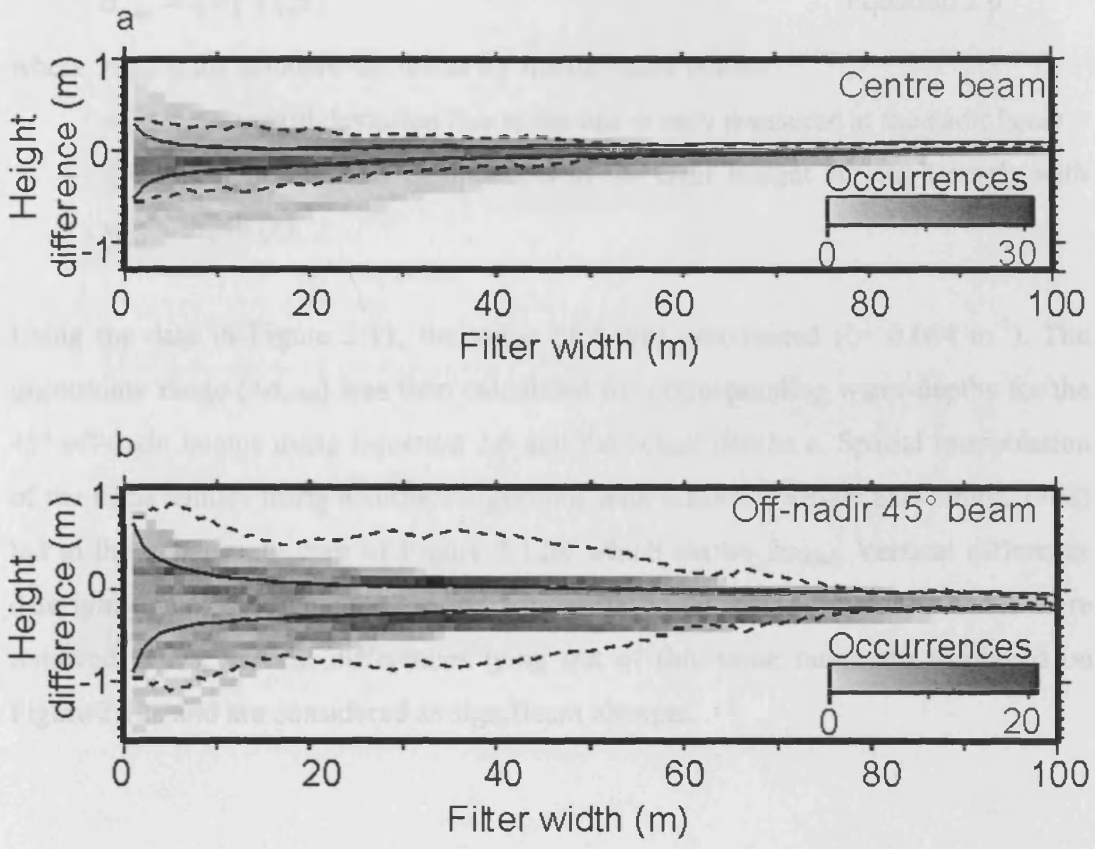

Figure 2.11 Analysis for individual beams. (a) Height comparison of the nadir beam. (b) Height comparison of the 20th beam at 45° from the nadir. Superimposed is (continuous curves) the decay of the 2σ expected theoretically if variability were caused by spatially-uncorrelated Gaussian-distributed random noise. As the 2σ of the data (dashed lines) reduces more slowly than the random noise model, the presence of spatially correlated noise is interpreted.

2.3.2. Uncertainty and significant change maps

The next step is to use the uncertainty analysis results to estimate the significant change between the bathymetric data to be compared. An example of such a significant change map is given in Figure 2.12. This figure encompasses the area of bedrock used as the benchmark along with the western subtidal component of Port Eynon Bay and an area of mobile sand forming the eastern Helwick Sands, west of the headland. The difference data 2σ range was measured from the results of Figure 2.11, at a filter width of 20 m for both the nadir beam (2σ = 0.7 m) and the off-nadir 45° beam (2σ = 1.2 m) for a water-depth of 15 m. Assuming that the heave and other components of the uncertainty budget (i.e. mainly roll) are uncorrelated and that the nadir beam is subject to heave error only, which affects the vertical accuracy of the soundings independently of water depth, then an off-nadir beam uncertainty can be modeled as follows:

$$\sigma_{total} = \sqrt{\sigma_h^2 + (\xi z)^2} \qquad \text{Equation 2.6}$$

where σ_{total} is the standard deviation for the off-nadir beam

σ_h is the standard deviation due to the heave only measured at the nadir beam

ξz represents the other components of the error budget varying linearly with water-depth (z).

Using the data in Figure 2.11, the value of ξ was determined (ξ= 0.064 m^{-1}). The uncertainty range ($\pm\sigma_{total}$) was then calculated for corresponding water-depths for the 45° off-nadir beams using Equation 2.6 and the actual depths z. Spatial interpolation of the uncertainties using a surface algorithm with tension (Wessel and Smith, 1998) led to the uncertainty map of Figure 2.12b, which shows $2\sigma_{total}$. Vertical difference data lying within the $2\sigma_{total}$ range are considered to be insignificant and hence were removed. Thus, vertical differences lying out of this same range are displayed on Figure 2.12c and are considered as significant changes.

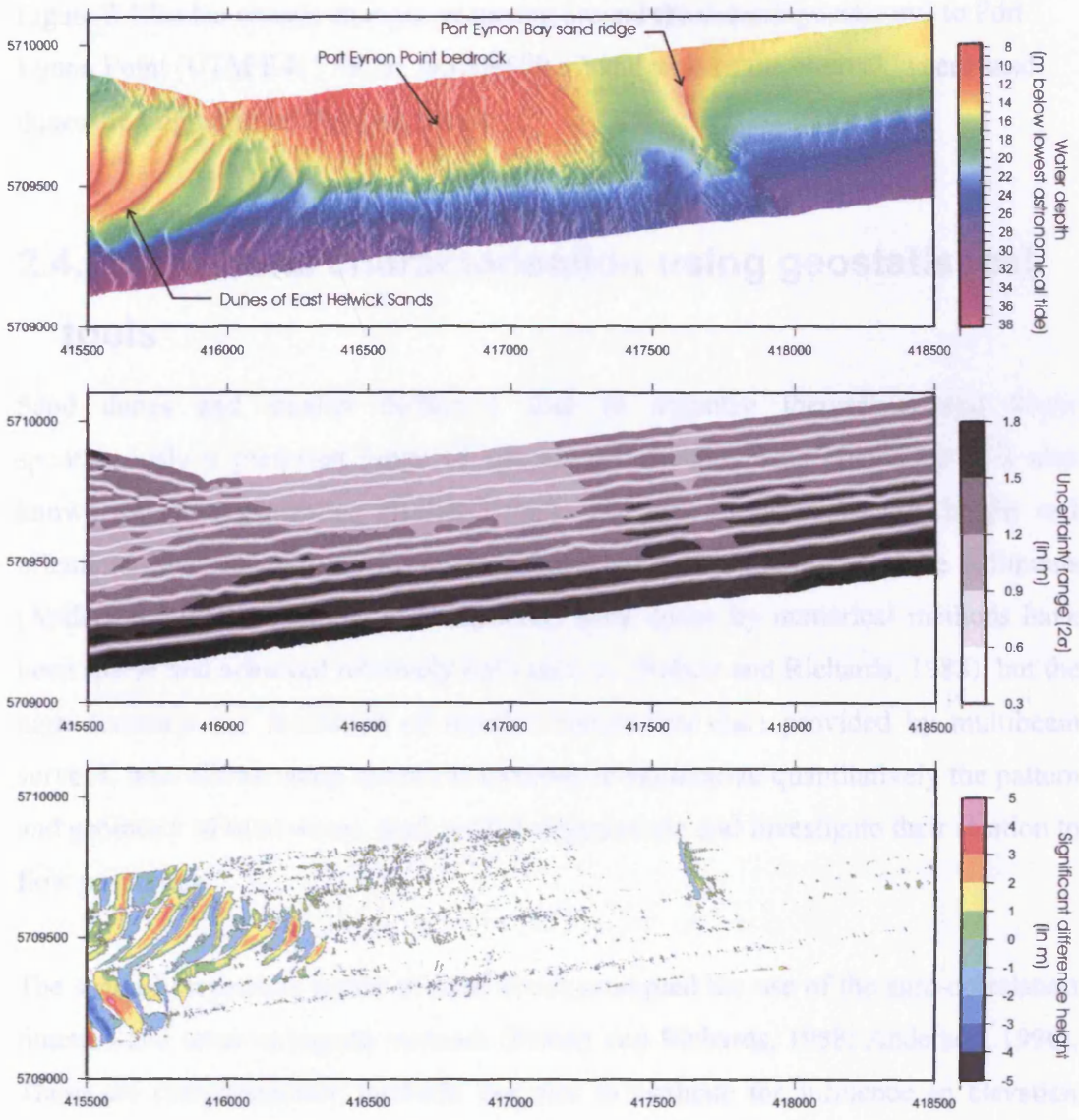

Figure 2.12. Significant changes map of the bedrock area (benchmark) and its neighbouring sedimentary deposits.
a) Bathymetric map of the area (2002 multibeam survey)
b) $2\sigma_{total}$ range calculated at the nadir and 45° off-nadir beams for a 20 m filter width and interpolated.
c) Significant changes map. Difference map between the 2002 and 2001 multibeam surveys, censored using the results from the uncertainty map.

Figure 2.12c shows some significant change over the bedrock. These might seem inconsistent but the $2\sigma_{total}$ uncertainty range still allows for 5% of the Gaussian noise to appear to be significant. As a significant part of the error budget is due to the heave artifact from the 2001 survey, some of the erroneous significant change in Figure 2.12c is aligned across-track. Also, the alignments of many of these changes with bedrock strata may imply that the variability can originate from sediment deposits between strata, seaweed or acoustic artifacts.

Figure 2.12c also reveals changes occurring around the sand ridge adjacent to Port Eynon Point (UTM E417700 m, N5709500 m) and west of the bedrock where sand dunes are migrating on Helwick Sands.

2.4. Sand dune characterisation using geostatistical tools

Sand dunes and smaller bedforms tend to organize themselves and adopt spontaneously a preferred range of spacing and height. This phenomenon is also known as self-organization (Hallet, 1990). The characteristic spacing, height and orientation may relate to environmental characteristics of the flow and the sediments (Anderson, 1990). Attempts to characterise sand dunes by numerical methods have been sparse and achieved relatively little success (Robert and Richards, 1988), but the high accuracy and resolution of modern bathymetric data provided by multibeam surveys, now allows using statistical methods to summarize quantitatively the pattern and geometry of sand dunes, their spatial-organisation and investigate their relation to flow properties.

The spatially repetitive nature of sand dunes prompted the use of the auto-correlation function and semi-variogram methods (Robert and Richards, 1988; Anderson, 1990). These are complementary methods that aim to evaluate the influence an elevation Z(x,y) has on a neighbouring elevation Z(x+i, y+j) (where i and j are the easterly and northerly components defining the lag vector **h**). The objective of this section is to describe these two geostatistical tools and to illustrate their ability to characterise quantitatively the spatial characteristics of sand dunes.

2.4.1. Definitions and properties of the autocorrelation function and semi-variogram

2.4.1.1. The autocorrelation function

The degree to which close neighbours of a surface share similar properties can be characterised by spatial autocorrelation. The autocorrelation function (ACF), measures the correlation between two points separated by a distance called the 'lag'. The ACF can be easily understood as a measure of the similarity between a signal and its copy, one sliding with the lag distance with respect to the other. The function is normalised so that it varies between -1 and 1. A positive autocorrelation means that points separated by the specified distance lag have similar values and are spatially correlated (e.g. successive crests of a dune field); negative autocorrelation means they have opposite values or are spatially anti-correlated (e.g. crests and troughs). A null autocorrelation means that there is no spatial correlation.

Mathematically, the autocorrelation function is the covariance function (covar($Z(r_0)$, $Z(r_0+h)$) of the spatial process (Z) at a position $r_0(x,y)$ with itself at a lag distance (**h** being the lag vector) divided by its variance (Var($Z(r_0)$)), such as:

$$ACF(h) = \frac{\text{covar}(Z(r_0), Z(r_0 + h))}{\text{var}(Z(r_0))} \qquad \text{Equation 2.7}$$

In two dimensions, it is defined in full as follows:

$$\text{ACF}(i,j) = \frac{\sum_{i=1}^{n}\sum_{j=1}^{n}\left(\left(Z(x,y)-\bar{Z}\right)\left(Z(x+i,y+j)-\bar{Z}\right)\right)}{\sqrt{\sum_{j=1}^{n}\left(Z(x,y)-\bar{Z}\right)^2}} \qquad \text{Equation 2.8}$$

where Z(x,y) here is a bathymetry value at the point described by its easting (x) and northing (y). Z(x+i, y+j) defines the bathymetry at the location x+i, y+j, $\bar{Z}$ represents the mean of Z(x,y). To prevent any edge effect, the summation and $\bar{Z}$ are calculated over the area defined from the intersection of the tested area and its lagged copy. The algorithm used to compute the ACF in two dimensions is presented in Annexe A.1.

This method has been used in image analysis (Gonzalez and Woods, 1992). Akal and Hovem (1978) first adapted it to the analysis of seabed roughness. Since then it has been used to quantify the morphology of the Mid-Atlantic Ridge (Herzfeld, 1993), abyssal seamounts (Shaw and Smith, 1990) and seafloor oceanic transects (Goff and Jordan, 1988; Goff et al., 1991). Limited work, however, has been published on using the ACF to perform spatial analysis of repetitive sedimentary bedforms such as marine sand dunes.

2.4.1.2. The semi-variogram

The semi-variogram (Journel and Huijbregts, 1978; Isaaks and Srivastava, 1990; Davis, 2002) also represents the degree of spatial correlation among observational data as a function of the distance between observational data points, but the Z(x,y) are instead differenced. It is defined (Davis, 2002) as:

$$2\gamma(h) = Var[Z(x_0 + h) - Z(x_0)] \qquad \text{Equation 2.9}$$

which in fully developed form is:

$$\gamma(h) = \frac{1}{2N(\mathbf{h})} \sum_{N(\mathbf{h})} [Z(x_0 + h) - Z(x_0)]^2 \qquad \text{Equation 2.10}$$

where h is the lag distance and N(**h**) is the number of pairs of points separated by the lag vector **h.** The term variogram is used for the rest of this chapter to refer to the semi-variogram which is a common practice (Gringarten and Deutsch, 2001). The variogram is a one dimensional function which increases when the studied spatial series Z(x) is uncorrelated and decreases when the series is correlated (Figure 2.13).

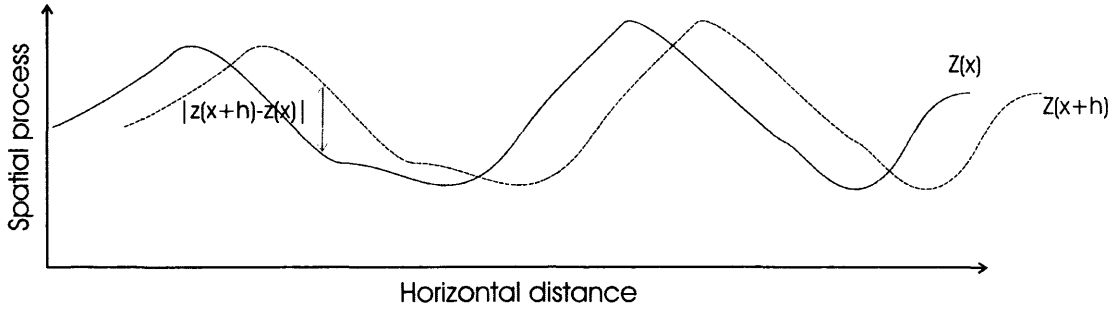

Figure 2.13 Variable used in the calculation of the variogram of sand dune cross-section. This diagram illustrates that the variogram function increases when the spatial series are uncorrelated (large differences between the two series) and decreases when the series are correlated (small differences between the series, when crests and troughs coincide).

The use of variograms to characterize morphological patterns was introduced by Oliver and Webster (1986). Roberts and Richard (1988) used the variogram to characterise small sand dunes (ripples about 30 mm high, produced in flume). They showed that the method was useful because of its relatively simple interpretation (Figure 2.13) and its statistical meaning compared to other methods such as zero-crossing, time-series and spectral analysis. The method requires second-order stationarity, which means that the mean exists and is constant and independent of location and that the covariance exists, and is only dependent on the distance between any two values, and not on their locations. Variograms were calculated from the topography of ripples created in a hydrodynamically-controlled flume. These variograms were modelled with simple mathematical functions (exponential and sine) which were physically interpreted to obtain geometrical properties of the seabed features, which were then related to the flow characteristics. To date, however, the variogram technique has not been applied to naturally occurring dunes.

2.4.2. Application to the geometry of sand dunes

For illustration, three types of surface were used. The first two are synthetic surfaces, whereas the last one is a sample of seabed DTM. A sinusoidal synthetic model of the seabed was selected for its similarity to the dunes and its deterministic nature. Figure 2.14 shows this surface with its crest oriented at an angle of 45°W, a spacing of 100 m and wave height of 4 m. Figure 2.15 shows a random topography characterised by a normal distribution around a 0 m mean, a 2 m^2 variance and horizontal size of the features of 10 m created using a function outputting normal random values (Wessel and Smith, 1998). Figure 2.16 is a 300 m by 300 m area of the bathymetric data collected in 2002 on Helwick Sands. The spatial resolution is 1 m in both axes. Transverse dunes are observed superimposed on the general south-westerly sloping trend of the southern flank of the bank. Before application of the geospatial methods (ACF and variogram), the data were de-trended to fulfil the condition of stationarity. The trend was removed from the bathymetry by subtracting a quadratic surface fitted by least squares to the data (Figure. 2.17).

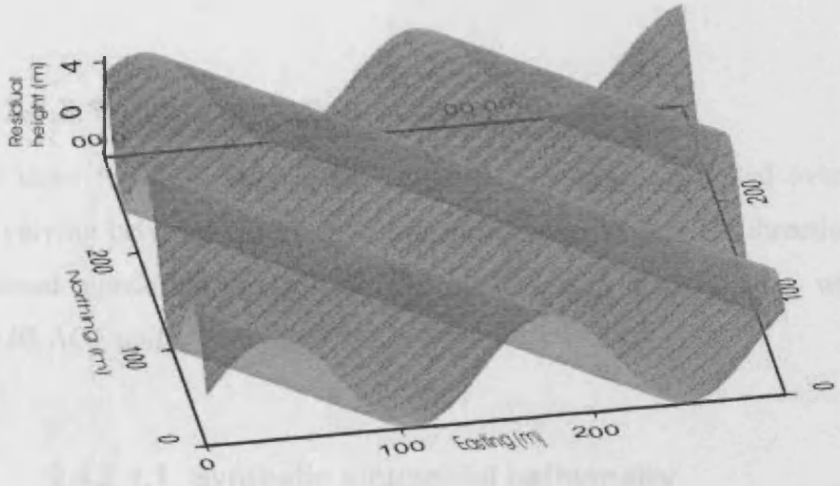

Figure 2.14 Artificial sinusoidal seabed surface simulating 4 m high, 100 m symmetric sand dunes with their crest oriented at an angle of N45°W

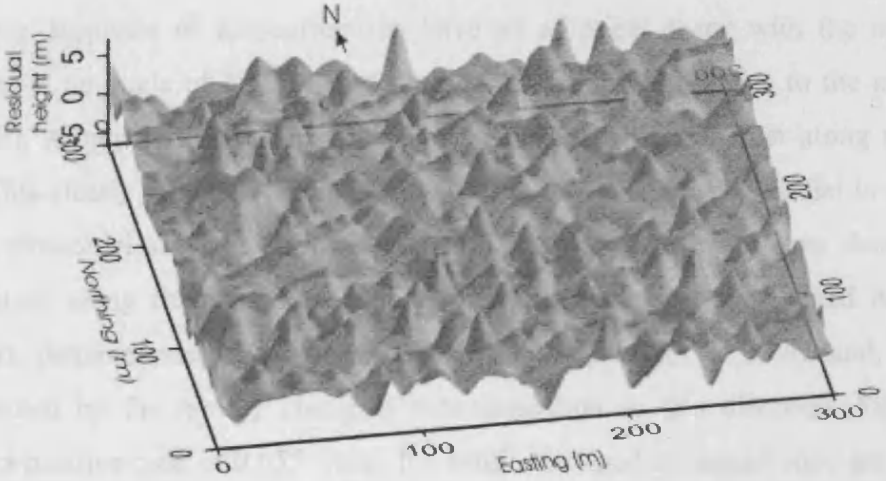

Figure 2.15 Artificial random surface characterised by a normal distribution with 0 mean and 2 m^2 standard variation.

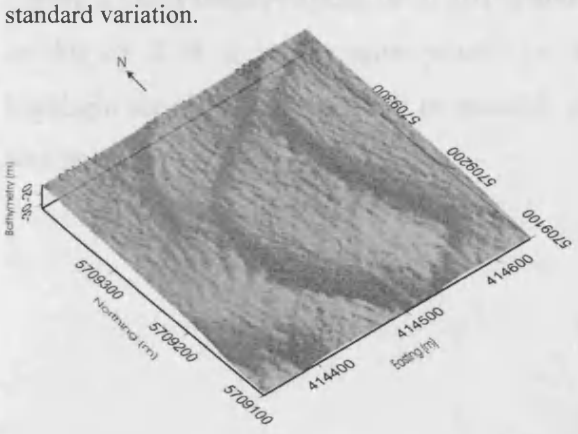

Figure 2.16 Sun illuminated bathymetry of the experimental area

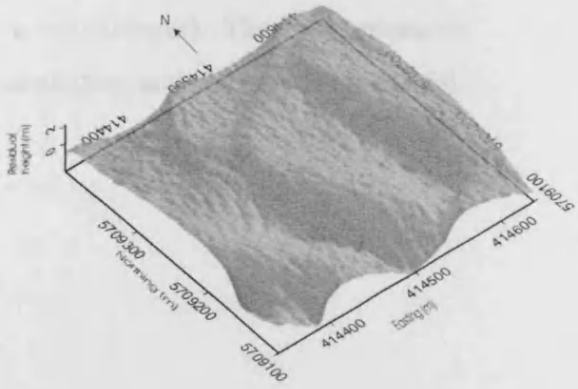

Figure 2.17 Residual bathymetry of the experimental area, after removing a quadratic surface fitted to the data in Figure 2.16 by least squares.

2.4.2.1. Interpretation of the ACF

For the three types of seabed, the autocorrelation was calculated over a range of offsets varying between -150 m and 150 m in both EW and NS directions. The two dimensional autocorrelation surface was plotted as a contour map, with isopleths every 0.05 ACF units.

2.4.2.1.1. Synthetic sinusoidal bathymetry

The ACF calculated from the sinusoidal bathymetry of Figure 2.14 is presented in Figure 2.18. It shows a succession of positive and negative peaks along a N45°E direction. Isopleths of autocorrelation have an elliptical shape with the major axis oriented at an angle of N45°W and the minor axis at right angles to the major axis (N45°E). Along the minor axis, the correlation decays faster than along the major axis. This clearly indicates the spatial anisotropy of this dataset. Parallel to the crests of the sinusoidal surface, the bathymetry is constant; hence the slow decay of the correlation along this direction is due to the censoring of the lagged dataset. In contrast, perpendicular to the crests, the bathymetry varies as a sinusoid, which is represented by the rapidly changing autocorrelation in this direction. Figure 2.18 shows a positive peak of 0.655 where the bathymetry and its lagged copy are in phase. The distance between this peak to the central peak corresponds to one wavelength on Figure 2.14. A negative peak of -0.801 is shown on Figure 2.18, where the topography on Figure 2.14 is in opposite phase (i.e. half a wavelength). These observations highlight the ability of the ACF to quantify the orientation and spacing of sinusoidal-like features.

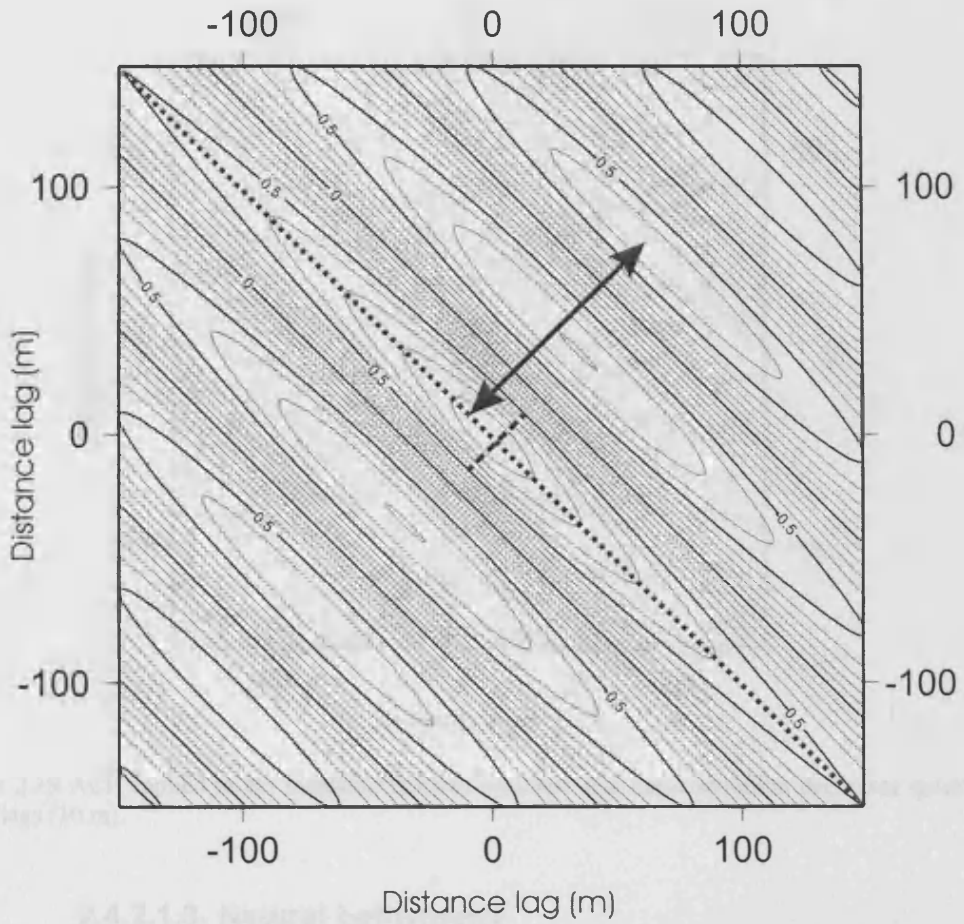

Figure 2.18 ACF function applied to the sinusoidal seafloor. The dotted lines show the axes of the ellipses of same isopleth. The double arrowed line is the measure between two positive correlation peaks.

2.4.2.1.2. Synthetic random bathymetry

The ACF calculated from the synthetic random bathymetry of Figure 2.15 is shown on Figure 2.19. The sharp peak at the centre of the figure, showing the maximum autocorrelation, decays rapidly towards 0, within a distance of ~10 m in all directions, showing a very poor spatial correlation. No directional anisotropy can be detected from the contour-map. Variations out of the central region vary around 0 from 0.1 down to -0.146, but with no specific orientation. This corresponds with the characteristics of the surface presented in Figure 2.15 where the features have a horizontal size of 10 m.

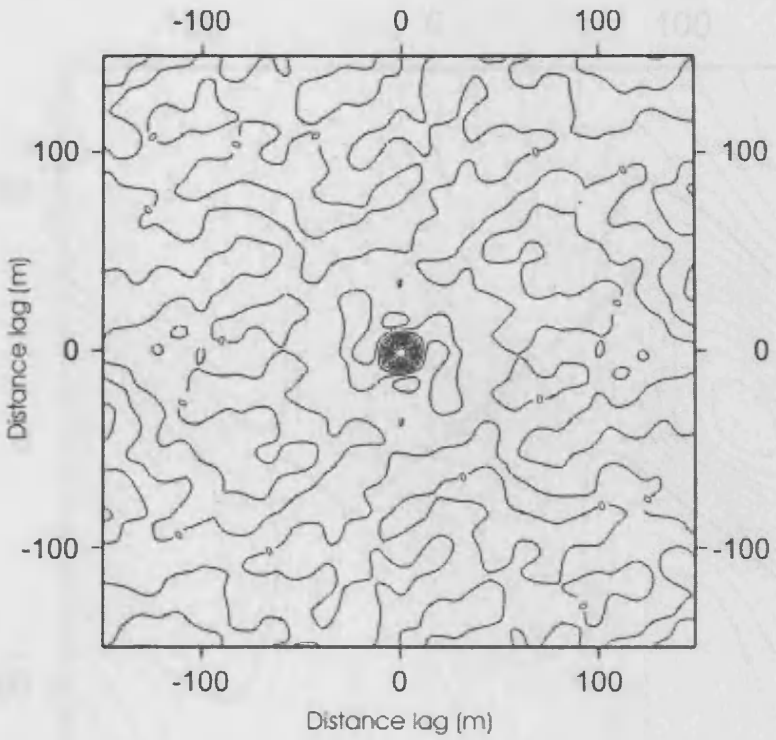

Figure 2.19 ACF applied to the synthetic random seafloor. The autocorrelation decreases quickly for small lags (10 m).

2.4.2.1.3. Natural bathymetry

Figure 2.20 shows the ACF calculated from the residual natural bathymetry (Figure 2.17). The contour map is characterised by three maxima. On both sides of the largest maximum (centre of the plot), two other peaks occur with a positive autocorrelation of 0.491. The peaks are separated by minima of -0.275. The contour lines about the peaks encompass elliptical shapes. Hence, the residual bathymetry shows evidence of spatial correlation. However, the shapes of the contour lines are not perfect ellipses. This highlights the more three-dimensional component of the bathymetry and the influence of relief smaller than the sand dunes.

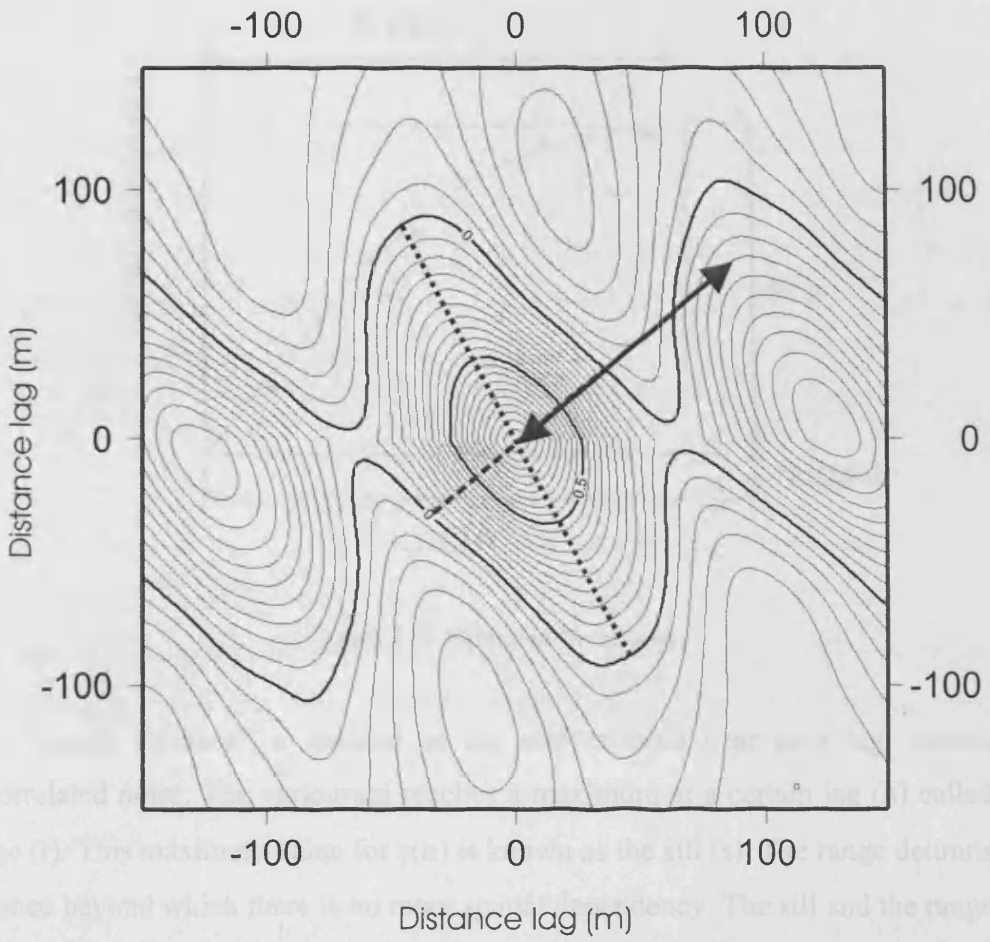

Figure 2.20 ACF function applied to the residual bathymetry of the experimental dataset. The dotted lines shows the axes of the ellipse of the isopleth 0.5. The double arrowed line is the measured distance between two adjacent positive correlation peaks.

The longer axis (long dashed line on Figure 2.20) represents an average trend of the dune crests, estimated from Figure 2.20 to be N027°W. The smaller axis (short dashed line) is oriented N049°E. The distance between the peaks (double-headed arrow in Figure 2.20) is ~120 m, which is considered to be a good estimator of the dune spacing.

2.4.2.2. Interpretation and modelling of the variogram

Before describing the calculated variograms, a few terms are defined here for describing them (Figure 2.21) following Journel and Huijbregts (1978). Some of the geometric models (Oliver and Webster, 1986) are also introduced.

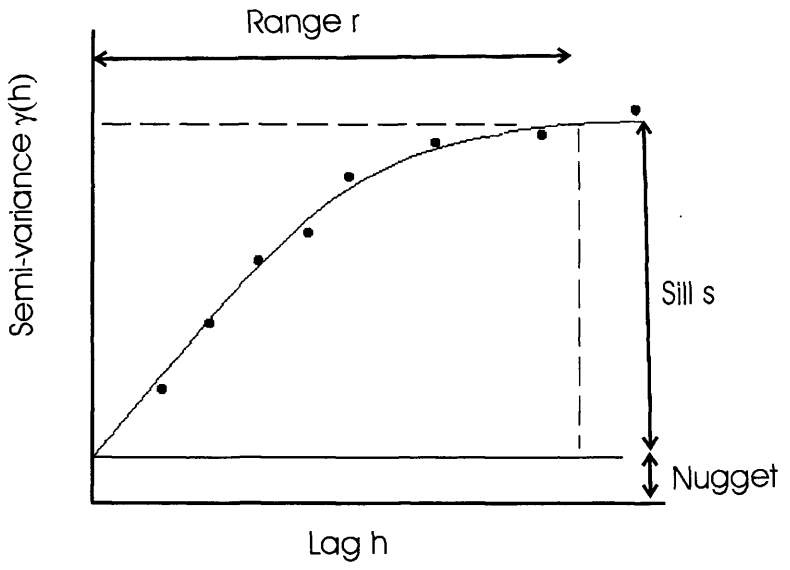

Figure 2.21 Variogram definitions

The "nugget variance" is defined as the semivariance near zero lag, caused by uncorrelated noise. The variogram reaches a maximum at a certain lag (h) called the range (r). This maximum value for $\gamma(h)$ is known as the sill (s). The range delimits the distance beyond which there is no more spatial dependency. The sill and the range are marked on Figure 2.21.

Oliver and Webster (1986) and Robert and Richards (1988) suggested that exponential and periodic functions can be used to model variograms of landforms or bedforms to represent their stochastic and periodic components, respectively. Robert and Richards (1988) represented a ripple field variogram using a linear combination of these two functions as follows:

$$\hat{\gamma}(h) = \gamma_1(h) + \gamma_2(h) \qquad \text{Equation 2.11}$$

where $\gamma_1(h)$ is an exponential function representing the stochastic variation:

$$\gamma_1(h) = s\left[1 - e^{\frac{-h}{r}}\right] \qquad \text{Equation 2.12}$$

and $\gamma_2(h)$ is a periodic function, which represents the deterministic (periodic) variation of the bathymetry:

$$\gamma_2(h) = a\left[1 - \cos\left(\frac{2\pi h}{l}\right)\right] \qquad \text{Equation 2.13}$$

The constants s and r are the sill and the range. The parameter l in the periodic function represents the wavelength of the sinusoid and a controls its amplitude.

A set of parameters (s, r, a and l) can then be calculated from the experimental variograms by minimizing the square of the difference between the model and the data (Williams and Kelley, 1998).

2.4.2.2.1. Purely sinusoidal bathymetry

The variogram computed from the synthetic sinusoidal bathymetry perpendicular to wave crests (i.e. N45°E) is presented in Figure 2.22. The variogram is a sinusoidal function with a maximum of 16 m^2 and wavelength of 100 m. The variogram is modelled solely by the periodic function (plain line on Figure 2.22) with the following equation:

$$\hat{\gamma}(h) = 8\left(1 - \cos\left(\frac{2\pi h}{100}\right)\right) \qquad \text{Equation 2.14}$$

Equation 2.14 can be seen to follow from the geometry of the sinusoidal features in Figure 2.22 because the wavelength of the modelled variogram matches the wavelength of the sinusoid on Figure. 2.22 in the N45°E (i.e. 100 m) direction and their amplitude is twice the root squared amplitude of the sine function (i.e. 4 m from Equation 2.17).

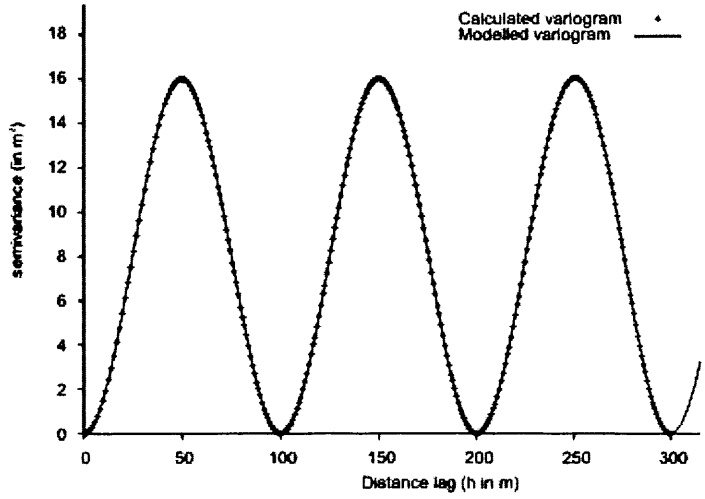

Figure 2.22 Directional variogram and its model of the sinusoidal seabed (Figure 2.14), calculated in the N45°W direction (across crest direction determined from the ACF method)

2.4.2.2.2. Random model bathymetry

Since no directional trend was observed, the variogram of the synthetic random bathymetry was computed arbitrarily in the N45°W direction. The variogram (Figure 2.23) increases rapidly to reach its sill of ~2.5 m^2. The range is of the order of ~10 m. Beyond this range, the semivariance varies erratically around 2.5 m^2. The variogram is modelled as a linear combination of an exponent component and a periodic component:

$$\hat{\gamma}(h) = 2.5\left(1 - e^{\frac{-h}{11}}\right) + 0.09\left(1 - \cos\left(\frac{2\pi h}{100}\right)\right)$$

Equation 2.15

Equation 2.15 highlights the dominant exponential component, which represents the stochastic (random) nature of the studied bathymetric profile. Its main characteristics are a 2.5 m^2 sill and 11 m range. The measure of the range agrees with the 10 m size of the features defined when creating the synthetic bathymetry.

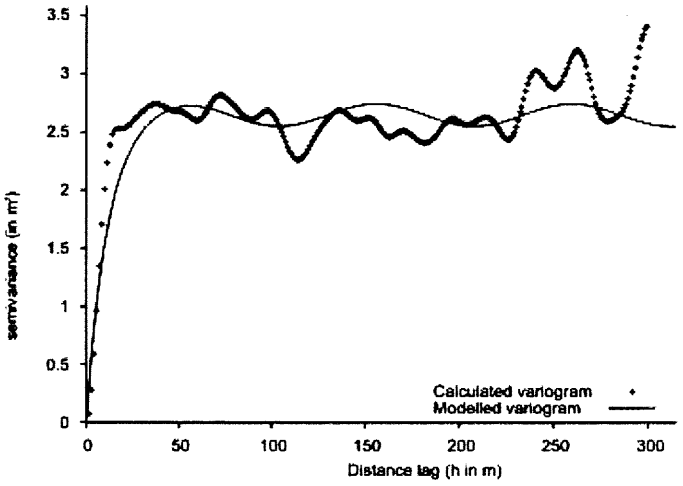

Figure 2.23 Directional variogram and its model of the random seabed (Figure 2.15), calculated in the N45°W direction (determined arbitrarily)

2.4.2.2.3. Natural bathymetry

The variogram in Figure 2.24 was calculated in the direction of the axis of periodicity (N85°E) interpreted from the ACF map (Figure 2.20). The variogram has a sinusoidal trend ranging between 0.2 to 1.02 m^2. The plain line on Figure 2.24 fits the calculated variogram with the following model:

$$\hat{\gamma}(h) = 0.2427\left(1 - e^{\frac{-h}{18.4047}}\right) + 0.3941\left(1 - \cos\left(\frac{2\pi h}{137.056}\right)\right)$$

Equation 2.16

The exponential and the periodic components have similar weights, reflecting the fact that this natural surface has mixed periodic and random components. Variogram modelling with exponential and sinusoidal functions is thus useful for quantifying the relative importance of random and deterministic components of the dune fields.

From Equation 2.16, the geometry of the sand dunes can be interpreted. First, the wavelength (137 m) of the periodic component indicates the spacing of the dunes. Second, the dune height ($\tilde{H}$) is defined after Robert and Richards (1988), as:

$$\tilde{H} = 2\left(a^{1/2} + s^{1/2}\right) \qquad \text{Equation 2.17}$$

Thus the dune spacing in the test area (Figure 2.16) is 137 m, which agrees with the estimation from the ACF method (120 m) (Figure 2.20). The dune height estimate is ~2 m from Equation 2.17, with a = 0.2 and s = 0.4, which is in broad agreement with observations (Figures 2.16 and 2.17).

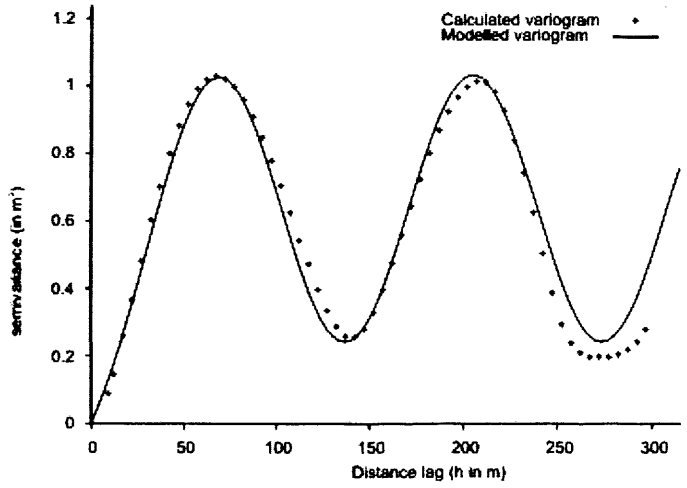

Figure 2.24 Directional variogram and its model of the natural seabed dataset (residual bathymetry Figure 2.17), calculated in the N85°E direction (in the across crest direction determined by the ACF method)

2.4.3. Relationship of dune geometrty to flow parameters

The ACF and the variogram have been demonstrated to be complementary useful statistical tools to characterise spatial patterns such as sand dunes. They benefit from simple implementation and ease of their interpretation compared to other statistical methods used previously. Unfortunately neither the ACF nor the variogram permit a quantification of the asymmetry of the dune which is an important descriptor (Ashley, 1990).

Harms (1969), Yalin (1977) and Allen (1983) have shown that the degree of spatial regularity of sand dunes and ripples relates to the flow velocity and can have an inverse relation to the water depth. These considerations lead Robert and Richards (1988) to investigate the relationship between the spatial regularity measured from the variogram and parameters of the controlled flow in their flume experiment with small dunes (ripples H = 0.2 m). They defined a regularity parameter (R_p) derived from the variogram modelling as follows:

$$R_p = \frac{s^{1/2}}{r} \qquad \text{Equation 2.18}$$

This parameter represents the influence of the exponential component in the variogram model relative to the sinusoidal component. It is apparent from Equation 2.12 and Robert and Richards (1988) observations that the stochastic component tends to zero value as R_p tends to zero (with r tending to large values), leaving the variogram's variation to be represented only by γ_2 (Equation 2.13). Robert and Richards (1988) pointed out that an inverse relationship between the Froude number and the regularity parameter could be seen within their data. Hence, a power law relation was fitted to their data by least square regression (Figure 2.25).

$$Fr = 0.1484 Rp^{-0.4258} \qquad \text{Equation 2.19}$$

The dashed line in Figure 2.25 fits the relation between $\log_{10}(Fr)$ and $\log_{10}(Rp)$ with a correlation coefficient of R^2=0.81. Although it is not known how medium and large sand dunes agree with this relation, this suggests that the variogram of sand dunes in unidirectional currents could be interpreted in terms of the flow Froude number. A physical interpretation of this relation is that higher velocity flows (large U), lead to more turbulence in the flow, which in turn dictates the distribution and geometry of the dunes (Figure 2.25). Unfortunately it is unclear, quantitatively, what influence unsteady or reversing flows have on the dune geometrical parameters. The reverse current may tends to flatten dune crests (Berné, 1993). Oscillations due to surface waves in shallow water, also, may tend to transfer sand from the crest to the troughs (Mei and Liu, 1993) enhancing the stochastic character of the dune morphology. Therefore, R_p for a marine dune may be higher than for a dune created in unidirectional flow and Equation 2.19, may over-estimate Fr. Nevertheless, it is suggested that there is a tendency for R_p to decrease with increasing U and with decreasing water depth (z).

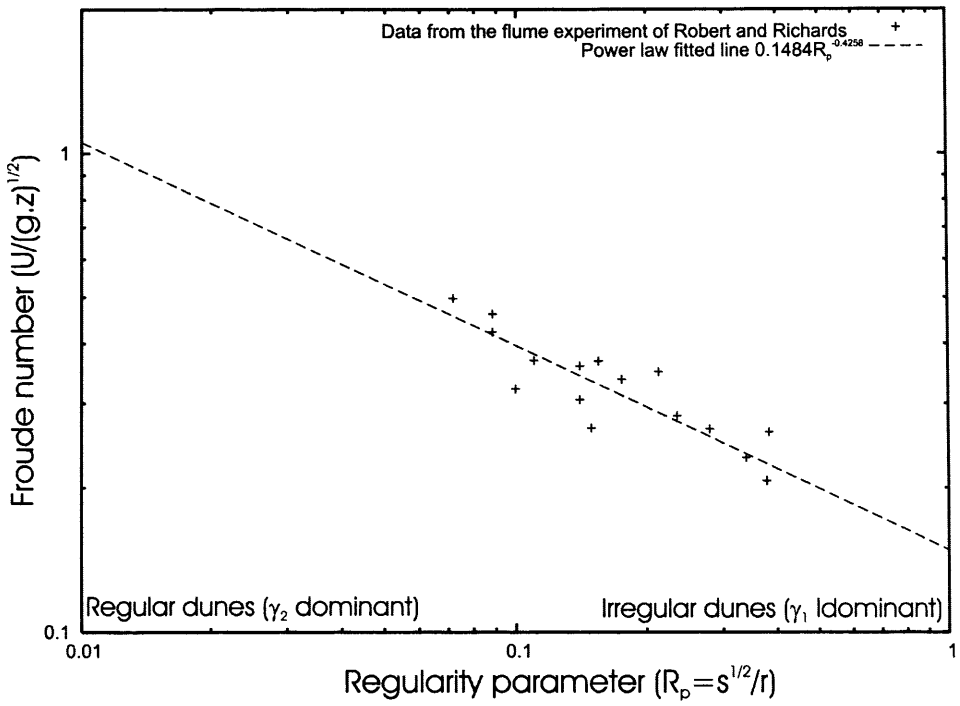

Figure 2.25 Relation between the regularity parameter and the Froude number from the flume experiment of Robert and Richards (1988). Power law was fitted by linear regression with a coefficient of correlation of R^2=0.81.

2.5. Summary

High resolution bathymetric data were acquired using singlebeam and multibeam sonars. The data accuracy is known to be affected by external environmental factors, in particular, tide correction errors resulting from the high tidal range in the Bristol Channel. Incorporation of local beach tidal survey data, as well as sound velocity data and the removal of erroneous recorded data formed the main processing stage. The accuracy of the data must be known in order to map significant changes between surveys induced by sedimentary processes. A method for quantifying uncertainties in repeat bathymetric surveys (bias and short-wavelength variability) has been presented. The method consists of filtering two co-located bathymetric datasets to be compared with a simple moving-averaging window of increasing spatial scale and displaying the height differences versus the size of the filter. In contrast to other techniques, this method derives bias and variability directly from the compared datasets, rather than from estimates of the surveying conditions.

Morphologic classification tools have been described in the last part of the chapter. The autocorrelation function of an area of seabed was used to estimate dune

orientation. Modelling of the variogram of across-crest profiles taken perpendicular to dune crests was used to separate the deterministic sinusoidal component from the random component. These parameters allow estimation of the spatial distribution and vertical geometry of the dunes. Earlier work on small dunes in a controlled unidirectional flow, although not strictly applicable to oscillating flows, suggests that a relation between the estimators derived from the analysis of the variogram (regularity) and flow parameters such as the Froude number can be ascertained.

Chapter 3.

Morphology and sediment dynamics at the approach of Helwick Sands with Port Eynon Point Headland

3.1. Introduction

Helwick Sands is the westernmost of the linear banner banks studied here (Figure 1.12). Its westerly location results in more exposure to south-westerly waves originating from the Atlantic (swell and storms) (Woolf et al., 2003), less intense tidal currents (Uncles, 1983; Lin and Falconer, 2001) and greater water depths at its base than for the other sandbanks in the Bristol Channel (Figure 1.12). Strong sediment transport is expected there, but somewhat weaker than further east were tidal currents are known to be stronger. This chapter presents the first time-series bathymetric datasets collected near the connection of Helwick Sands with the shore using multibeam and singlebeam sonars. Associated dunes were discovered running obliquely across the crest of the bank. In some cases continuity of these dunes could be observed. Moreover, dunes on opposite flanks of the bank were observed to migrate in opposite direction. Hence the connection of the dunes above the crest of the bank results in an uncommon geometry, which is interpreted here as a feature of the wave climate with waves propagating parallel to the dune crests, causing along-dune sand movements. Sediment transport fluxes derived by dune tracking are compared with fluxes computed using sand transport formulae from tide, wave and sediment grain size data acquired in the same area.

3.2. Large-scale morphology of the area around Helwick Sands

Figure 3.1 presents a shaded relief image of the multibeam sonar data collected in 2002. Along with a full coverage of the easterly area where the bank connects with the shore (Figure 3.4), the west and the centre of the bank was surveyed opportunistically with a track offset of 150 m (N) by 350 m (E) (Figure 3.1) leaving some gaps. The bathymetric data were processed using the workflow shown in Figure 2.4 to produce a grid with a 1 m resolution. Tidal corrections were applied as mentioned in Section 2.3.3. Comparing this dataset with the 2001 multibeam survey data using the method detailed in Section 2.3 indicates an irresolvable uncertainty in depth difference over the bedrock which forms Port Eynon Point of $2\sigma = 0.3$ m for a spatial-scale of 20 m. (Figure 2.10e) and a mean offset of 0.15 m.

The area of principal interest (Figure 3.1 and 3.2), was repeatedly surveyed as tabulated in Table 1.3. It encompasses three key morphological features: Helwick Sands (Figures 3.1 to 3.4), the bedrock submarine extension of Port Eynon Point headland (Figure 3.5) and the subtidal part of Port Eynon Bay (Figure 3.6a).

3.2.1. Helwick Sands

The bathymetric data in Figure 3.1 range between 8 and 45 m. The bank is attached to a bedrock submarine extension of Port Eynon Point and extends linearly to the west (N95°E). It is separated from the coast to the north by a flat floored depression constituting the Helwick Channel and Helwick Passage. The breaks in the slope at 20 m water-depth on the northern side and at 35 m water-depth on the southern side mark its northern and southern limits, respectively. The bathymetric gradient, calculated from the 2002 multibeam data spatially-averaged using a 150 m averaging filter to smooth out the effect of the superimposed sand dunes (Figure 3.3), shows a varying across-bank asymmetry. The southern flank reaches a typical gradient of 4°, which is steeper than the maximum of 1° on the northern flank. Subtle variations in both the asymmetry of the bank and water-depth of the crestline reflect the weak sinuosity of the crestline. Across-bank profiles change from an asymmetric section with a steeper southern slope at the East Helwick, to a more symmetrical profile at the Swatch where a subtle kink in the bank crestline can be observed (Figure 3.2), to an asymmetric profile again with a steeper southern slope at the West Helwick.

Large sand dunes (wavelength ~100 m, height from 2 to 7 m) are superimposed on the bank (Figure 3.1). They extend further north (in the Helwick Channel depression). Published data (Harris and Collins, 1984) shows that they also extend further south (beyond the surveyed area). Artificial illumination of the bathymetric terrain model from the west in Figure 3.1 highlights the dunes and reveals their asymmetry. On the southern side of the bank, their lee sides face west, whereas on the northern side they face east. Smaller dunes (less than 60 cm high and a few tenths of meter spacing) can be observed on the stoss side of some larger dunes in higher resolution images not shown.

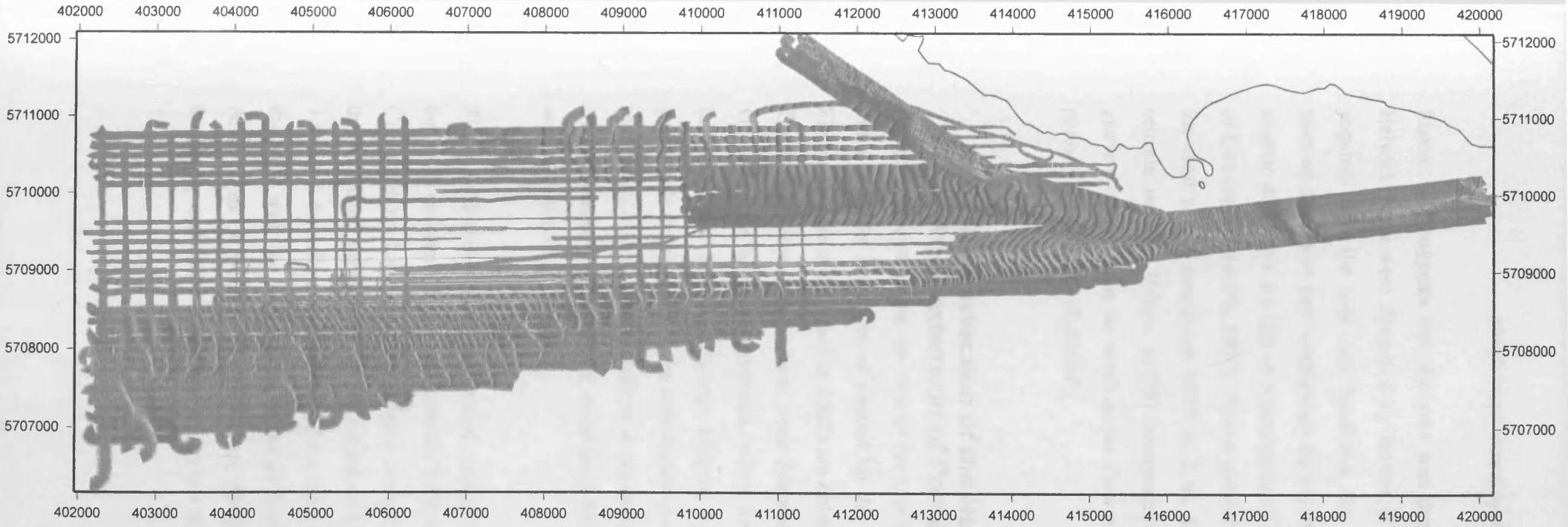

Figure 3.1: Morphology of the Helwick Sandbank and local area.
The bathymetric terrain model was constructed from multibeam survey data collected in 2002. Tracks are 125m by 250m (northing, easting respectively) spacing for the non-full coverage part of the survey
The coordinates are in UTM zone 30 (projected using the WSGS84 ellipsoid).

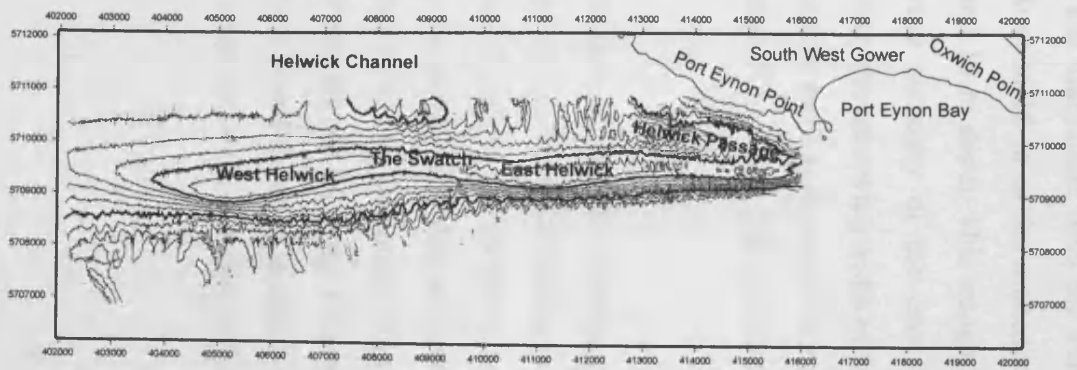

Figure 3.2: Physiographic map of the Helwick Sandbank and Port Eynon Bay. Depth contours are displayed each 3 meters below Chart Datum with 10 and 25 meters deep in bold.

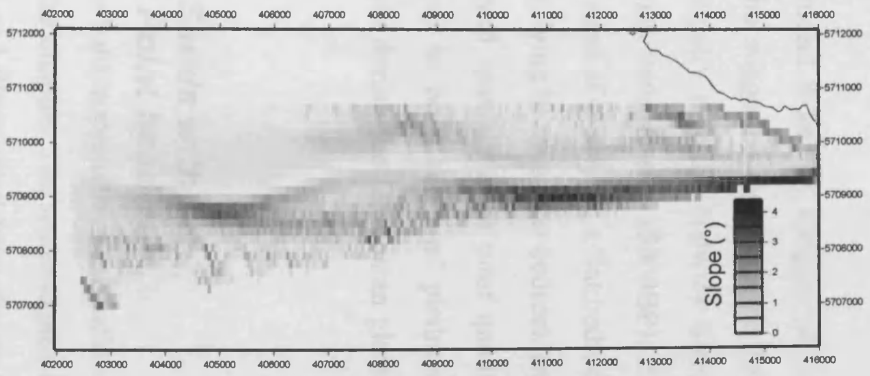

Figure 3.3 Slope angle computed for an interpolated grid of the bathymetry. Grid cells are 150m by and 40m (northing, easting respectively).

Figure 1.14 suggests that the area was drowned around 8 ka BP. Origins of the Helwick Bank were discussed by Britton (1978), who suggested from seismic data acquired over the bank and boreholes dug in its vicinity that the Helwick Sands reached its present day morphology during the Flandrian transgression (5000BP). His seismic data show a width of a maximum of 40 m of sand of overlying a flat bedrock of Lias origin (Neville, 1970). Gravel and till deposits, lying between the bedrock and the sand with a maximum width of 2 m, are observed sparsely from poor quality seismic records. Britton (1978) interpreted this layer to be a relict of piedmont glaciers extending as far south as the Gower Peninsula during the Devensian glacial period (70,000BP to 10,000BP).

3.2.2. The connection of the Helwick Sands with the bedrock extension of Port Eynon Point headland

Figure 3.4 shows a close-up view of the area where the bank approaches the headland; this will be the main area of interest for the rest of the chapter. The water-depths in Figure 3.4a (data collected in 2002) are colour coded and illuminated from the west. These data show that the bank crest deepens from 10 m to 18 m in the immediate vicinity of the headland extension, which lies at around 10 m depth. This trough is known as the Helwick Passage (Figure 3.1). A weak sinuosity of the crest is perceptible despite gaps in the bathymetric data (caused by the narrowing width of the multibeam swath towards shallow water-depth). The across bank asymmetry created by the steeper southern flank, mentioned earlier (Section 3.2.1), can also be clearly seen in Figure 3.4a.

Figure 3.4b provides an interpreted map of the distribution of subtidal outcrops of bedrocks and sand dunes based on the 2002 multibeam survey. Subaerial outcrops of Carboniferous Limestone are located around Port Eynon Point, to the north-west of this headland, along the coast and off Oxwich Point, on the easternmost side of Figure 3.4. Sand deposits cover the rest of the area. Sand dunes extend to the connection of the bank with the bedrock extension of Port Eynon Point (in the Helwick Passage Area: UTM E416000 m, N5709500 m). Small dunes (less than 1 metre in height) are frequently associated with larger dunes (on their stoss sides) except at the crest of the

bank. The spatial characteristics and the kinematics of the sand dunes in this area will be addressed in more detail in Section 3.3.

Barchanoid-shaped sand dunes (UTM E412000 m, N5710500 m) and associated ripples occur along the coast extending from Port Eynon Point towards Worms Head. The crest of these dunes are oriented NNE-SSW, perpendicular to the coast and their asymmetry (lee slope facing SSE) suggests sand transport from the NNW to the SSE.

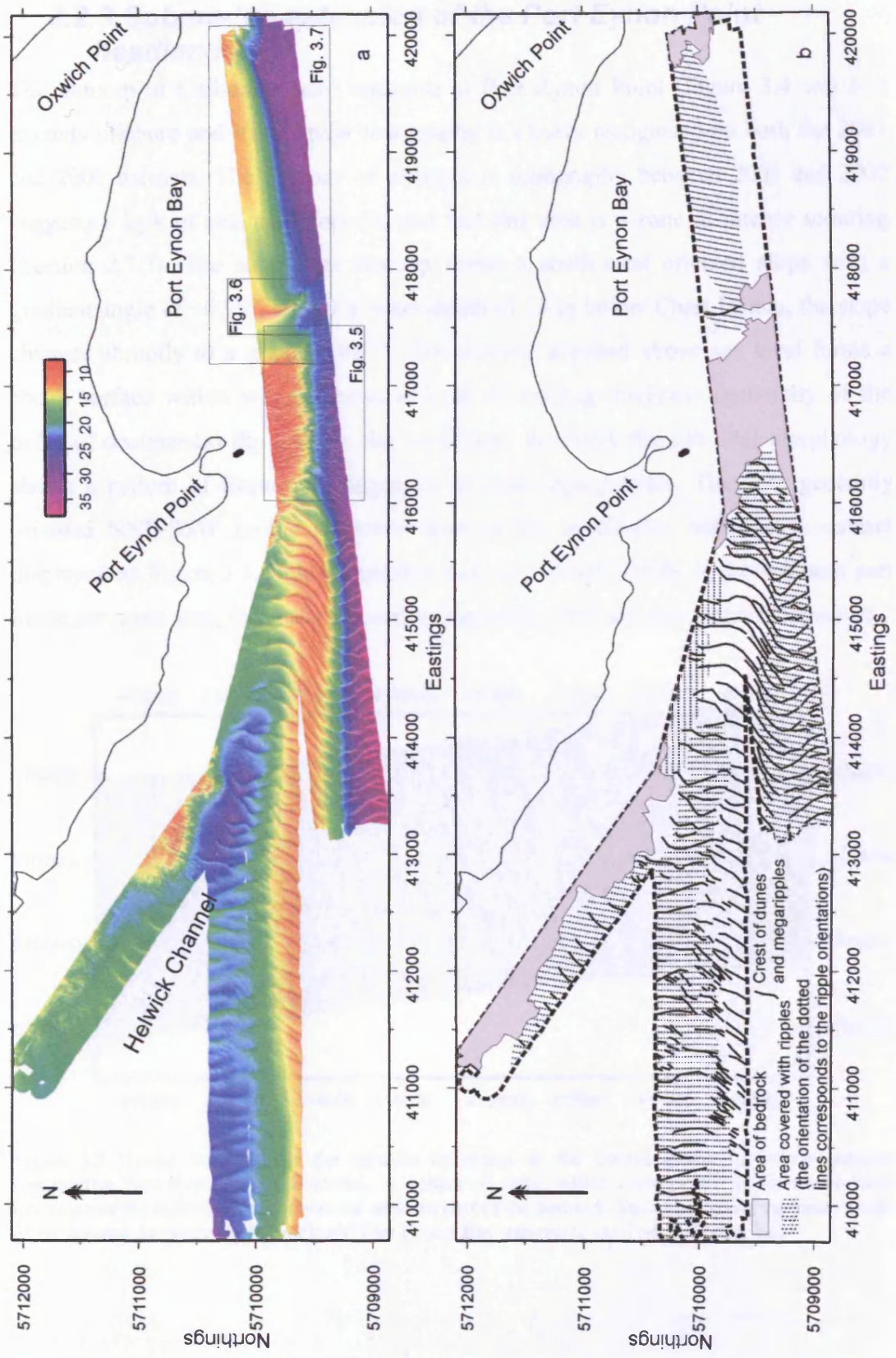

Figure 3.4 (a) 2002 multibeam bathymetric survey (UTM zone 30) of the eastern Helwick Sands. Colour scale refers to water-depth in metres below chart datum. The artificial illumination is from the west. (b) Interpreted structural and sedimentary features.

3.2.3. Submarine extension of the Port Eynon Point headland

The outcrop of Carboniferous Limestone at Port Eynon Point (Figure 3.4 and 3.5) extends offshore and its irregular topography is clearly recognised on both the 2001 and 2002 datasets. The absence of changes in topography between 2001 and 2002 suggests a lack of sediment deposits and that this area is a zone of intense scouring (Section 2.3.3). The submarine outcrop forms a south-west oriented slope with a gradient angle of ~0.95°. Below a water-depth of 15 m below Chart Datum, the slope changes abruptly to a gradient of 3°. The outcrop exposed above sea level forms a rough surface within which limestone beds of varying thickness (generally of the order of decimetres) dip ~45° to the north-east. Similarly the sub-tidal morphology shows a pattern of lineations suggestive of outcropping strata. They are generally oriented NNE-SSW in the shallower part of the multibeam bathymetric dataset displayed on Figure 3.5. Below approximately 10 m water-depth, in the southern part of the surveyed area, the surface becomes smoother, with less pronounced lineations.

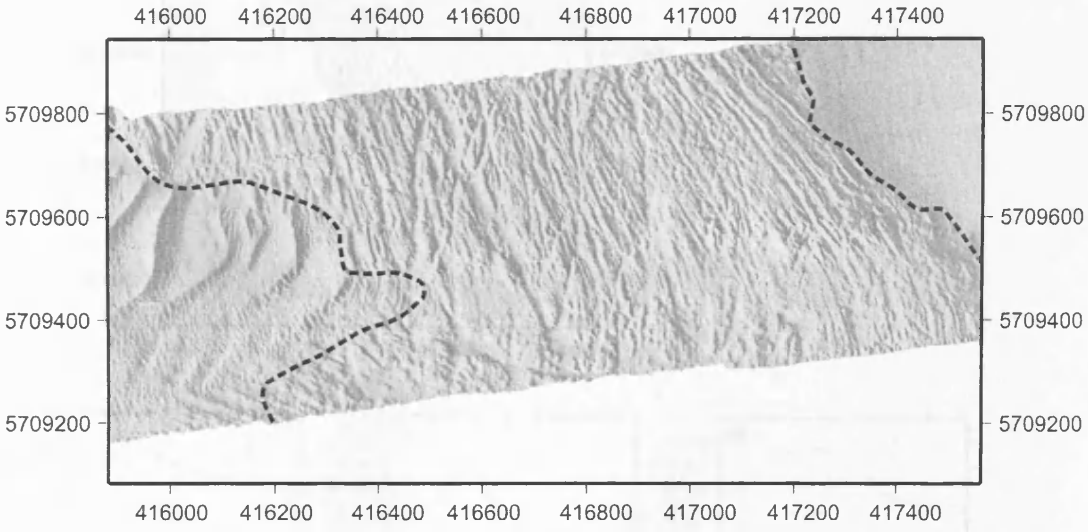

Figure 3.5 Dotted line outlines the subtidal extension of the Carboniferous Limestone outcrop constituting Port Eynon Point headland. A veneer of sand, which corresponds to the easternmost extension of the Helwick bank covers the western part of the bedrock. Sand also covers the eastern side of the outcrop, between the bedrock and Port Eynon Bay transverse sand ridge (Figure 3.6)

3.2.4. Port Eynon Bay

Port Eynon Bay lies east of Port Eynon Point (Figure 3.2) and can be described as a crenulated-bay as defined by Finkelstein (1982). The bathymetric datasets collected in 2001 and 2002 covered part of the sub-tidal part of the bay, extending from Oxwich Point outcrop (to the east) to Port Eynon Point outcrops (to the west) and between ~10 m to ~30 m water-depth (Figure 3.4).

In the western end of the bay, a transverse ridge (Figure 3.6a), with a crest slightly concave (towards the east) lying approximately north-south, overlies an isolated outcrop of the Carboniferous Limestone, to the east of the main outcrop constituting Port Eynon Point (Figure 3.5). The presence of a small rocky outcrop underlying the ridge (Figure 3.6) may suggest that the ridge is primarily topographically controlled.

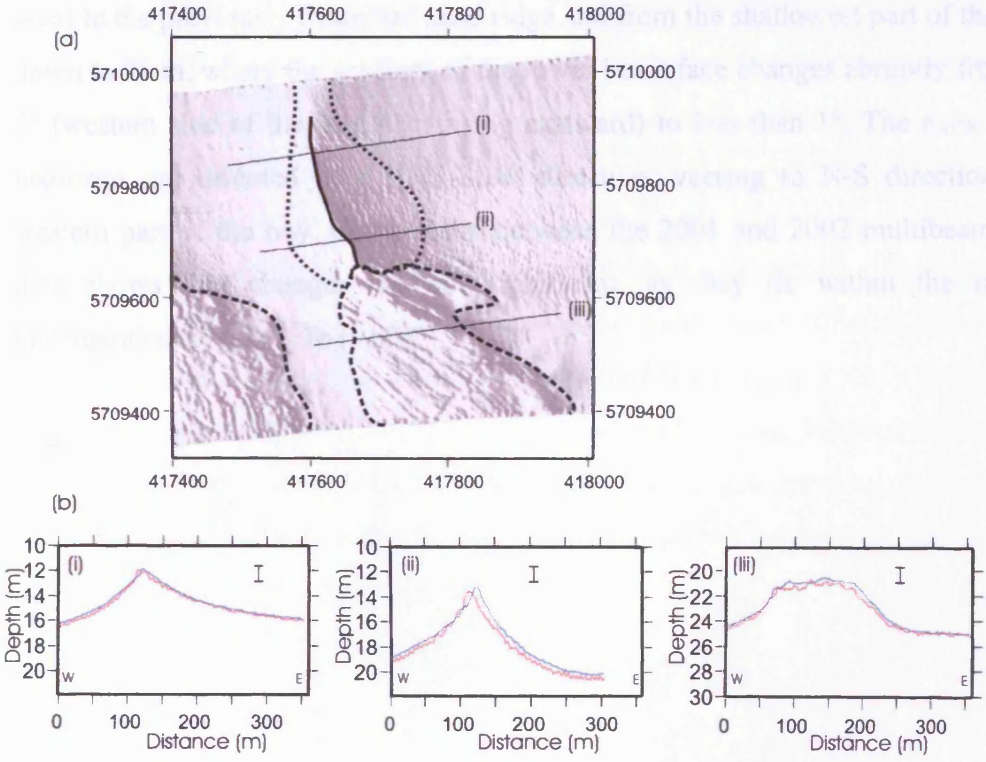

Figure 3.6 (a) Extension of Port Eynon Bay transversal ridge (short dotted line, crest in plain line) and location of outcrops of Carboniferous Limestone (long dotted lines) within the western part of Port Eynon Bay.
(b) Morphological changes of the ridge between the 2001 (blue) and 2002 (red) multibeam surveys. Length of error bars are scaled to the 2σ uncorrelated uncertainty in depth difference quantified in Section 2.2 for a 25 m spatial filter scale.

The crest of this sedimentary feature has a maximum height of 6.5 m and is roughly parallel to the adjacent rock outcrop. It has a relatively symmetric trochoidal shape in section with varied steepness. Cross-sections change from an almost flat shape in the north to a sharp ridge with slopes of a minimum of ~2° in the south (Figure 3.6b, second profile). Ripples are observed in both years' data on the western side of the ridge parallel to its crest. The profiles of the 2001 and 2002 datasets suggests that vertical changes occurred but in practice these are unresolved (the 2σ uncertainty bars represent depth difference uncertainty determined using the benchmark method in section 3.2 with a filter width of 25 m).

Further east, the rest of the bay is characterised by features commonly found in the sub-tidal domain of beaches, such as a small sand dune field (H = 0.5 m, L = 30 m). This field extends laterally from the Oxwich Point outcrop (north east of the surveyed area) to the previously described sand ridge and from the shallowest part of the survey down to 25 m, where the gradient of the lower beachface changes abruptly from up to 5° (western side of the bay, decreasing eastward) to less than 1°. The axes of these bedforms are oriented in a NNE-SSW direction, veering to N-S direction in the western part of the bay. Comparison between the 2001 and 2002 multibeam survey data shows that changes are not significant, as they lie within the range of uncertainties (Figure 3.7b (i-iii)).

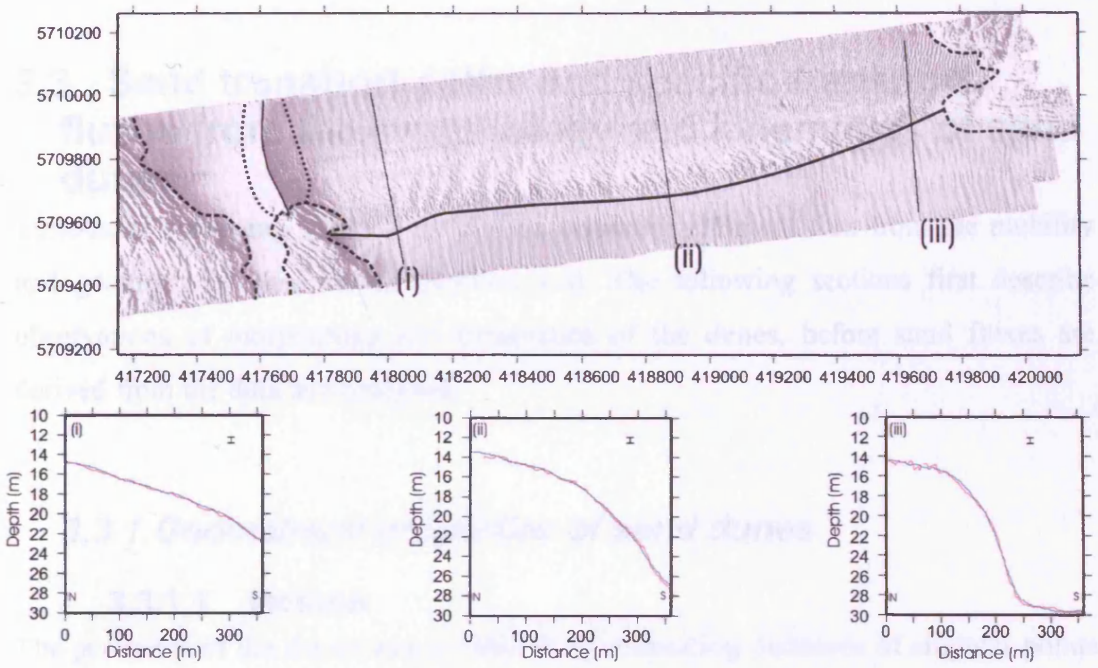

Figure 3.7 Morphological characteristics of the subtidal area of Port Eynon Bay.
(a) Shaded relief of the data collected in the bay with interpretation of the extent of the Carboniferous Limestone outcrop (dashed line), the transversal sand ridge (doted line) and the subtidal part of Port Eynon beach (north of bold line).
(b) Cross-sections (blue:2001, red:2002) showing insignificant changes in the shoreface beach profile. Length of error bars represents the 2σ uncorrelated uncertainty quantified in Section 2.2 for a 25 m filter spatial scale.

Port Eynon Bay can be considered as an independent sedimentary cell as previously suggested by Harris and Collins (1988) because of the orientation of the bedforms (ridge and small sand dunes), the lack of resolvable changes of the sub-tidal beach profiles and uncorrelated temporal variation of sand volume between the bank and across-shore transects (Brampton, 2002). However, some transient movements of sediment from Oxwich Bay and the Helwick Sands to Port Eynon Bay during extreme storm forcing can not be completely ruled out.

3.3. Sand transport paths and specific transport fluxes from the morphology and kinematics of sand dunes

Time-lapse surveying offers a method of assessing sediment flux from the mobility and geometry of sand dunes (Section 1.4). The following sections first describe observations of morphology and kinematics of the dunes, before sand fluxes are derived from the data and analysed.

3.3.1. Geometrical properties of sand dunes

3.3.1.1. Method

The geometry of the dunes was quantified by measuring distances of singular points such as their troughs and crests along across-crest profiles from the "mobile dune layer" (Figure 3.8). This layer represents the thickness of sand affected by dune migration. To resolve it, dune troughs were digitised from cross-sections and a surface was fitted to them using a continuous curvature gridding algorithm, with maximum tension (Smith and Wessel, 1990). This surface was then subtracted from the bathymetry, leaving only the mobile dune layer.

Dune spacing (defined as the horizontal distance between consecutive crests), dune height (defined as the vertical distance between the crest and the average of the adjacent troughs) and dune asymmetry (quotient of the horizontal length of the lee and stoss slopes) were computed (see Figure 1.9 for definitions). These morphological characteristics were measured along the same profiles as those used to compute the base of the "mobile dune layer" which were oriented roughly perpendicular to the crest of the dunes (parallel to the bank crest).

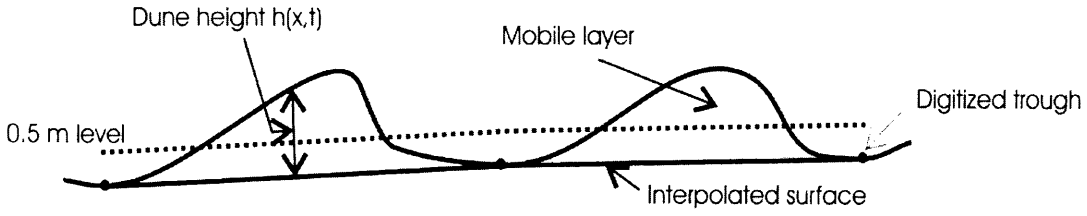

Figure 3.8 Definition of the mobile dune layer. The residual height, h(x,t), above the interpolated surface passing through the digitized troughs constitutes this layer. The h(x,t)=0.5 m level represents the height below which low shear strength induces little sand displacement in the trough. It also represents the limit to which the mobile layer can be defined well because of digitising and interpolation errors. Hence the mobile layer is plotted for h(x,t) > 0.5m in Figure 3.11.

3.3.1.2. Results

Dune height (Figure 3.9a)

Dunes with height greater than 2 m occur on the southern flank below the 15 m contour line and can attain a maximum height of 3.5 m to 4 m. Smaller dunes are found intercalated between bigger ones at the foot of the flank. As the seabed shallows above the 15 m contour-line, dune height decreases. In some areas, dunes are absent (UTM E413400 m, N5709300 m). Over the crest of the bank, dunes are present but their height generally reaches less than 1 m. At the inflexion point (location where a dune crest's curvature in plan view changes sense) dune height is at its minimum.
As water-depth increases across the northern flank, dune height increases, reaching up to 3 m. The terminations of dunes are clearly identified where heights decrease. Gentle dune termination (where the dune height decreases progressively) are commonly recorded (UTM E414100 m, N5710000 m). Abrupt terminations, however, occur where dunes meet with the bedrock (UTM E416000 m, N5709600 m). Dune heights near the headland bedrock (UTM E415500 m, N5709700 m) are relatively uniform at 2.5 m.

Dune spacing (Figure 3.9b)

Dune spacing is relatively uniform for the studied area with an average value of 110 m. Dunes with a smaller spacing than the average are located at the foot of the southern flank of the bank, where bifurcation of dune crests occurs. There (UTM E414000 m, N570900 m) spacing is around 60 m. Spacing tends to increase towards the crest of the bank to 190 to 200 m.
Along the northern flank (UTM E414500 m, N5709800 m) the typical dune spacing of 200 m is slightly greater than along the southern flank. However, at the vicinity of the connection with the headland, dune wavelength ranges between 40 and 80 m.

Dune asymmetry (Figure 3.9c)

Dune symmetry index was computed as defined in Section 1.4.1. Symmetric profiles (index close to 1) are located at the inflexion points of the dune crests and on the northern side of the bank near its connection with the subtidal bedrock outcrop of the headland (UTM E415500 m, N5709700 m). These dunes have a 1° slope gradient. Easterly facing lee side dunes occur on the northern flank of the bank. Their lee and stoss slopes reach on average respectively 2.2° and 0.7°. Westerly facing lee side dunes occur on the southern flank with their steep slopes ranging between 1.5° and 2° and gentler stoss slope lying between 0.5° and 1°. At the foot of the bank extreme gradients are observed. The lee slopes reach between 4° and 7° whereas stoss slopes vary between 2° and 3°.

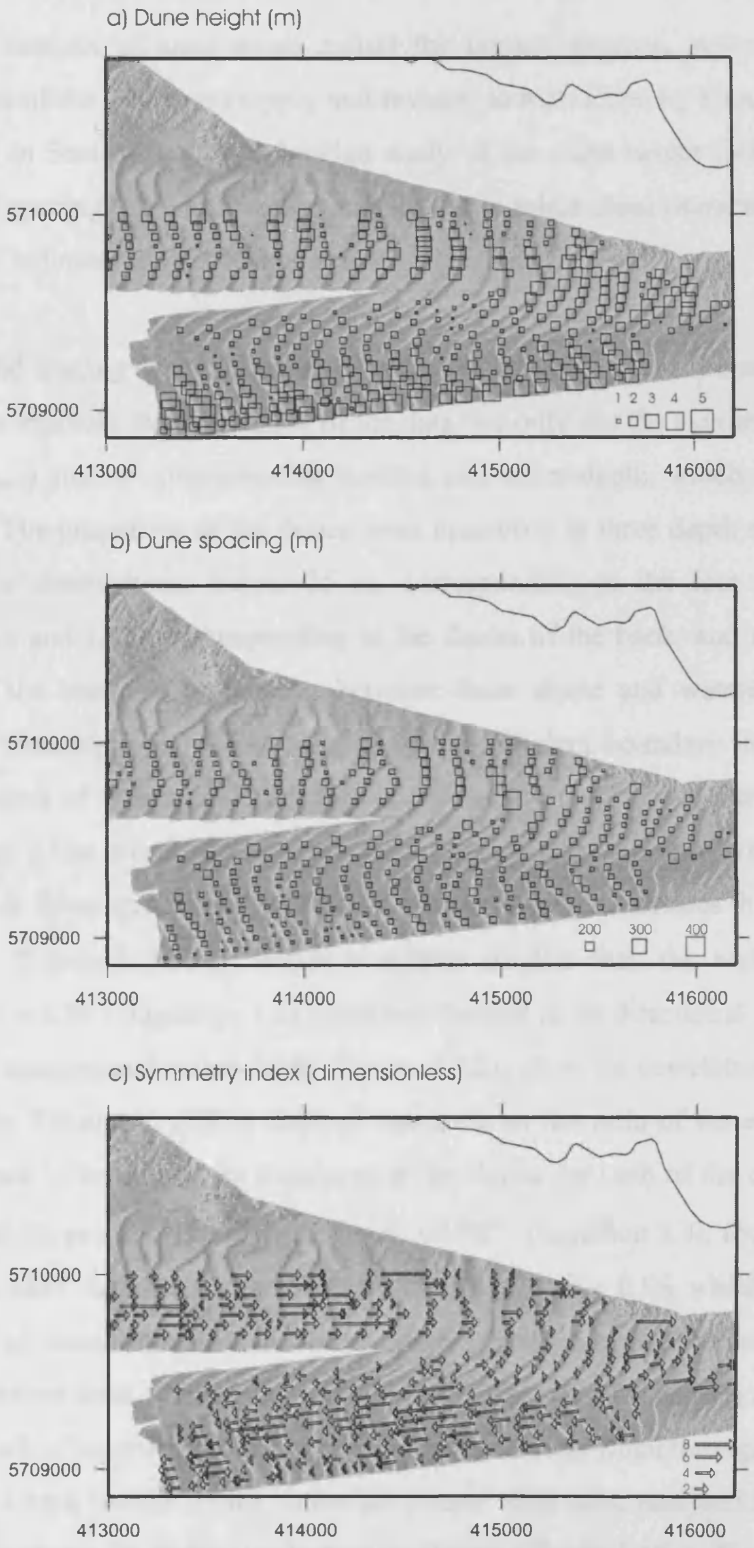

Figure 3.9 Geometrical characteristics of dunes in the area of repeated surveys.
Dune height, spacing and asymmetry have been measured from profiles constructed from the gridded 2002 multibeam data parallel to the sandbank crest.
(a) Dune height measured from crests to the base of the mobile layer (m).
(b) Dune spacing measured between consecutive troughs (m).
(c) Dune symmetry index (Section 1.4.1) representing the sense and magnitude of the asymmetry of the medium sized dunes (ratio of the horizontal length of the stoss side to the length of the lee side)

Geometrical features of sand dunes reflect the current strength, wave regime and characteristics of the sediment (supply and texture) as mentioned by Flemming (2000) and reported in Section 1.4.2. A detailed study of the dune height (H), crest water depth (z) and spacing (L) was therefore carried out to relate these characteristics to the conditions of sediment transport found in other studies.

The height and spacing of the dunes show some variation along crestlines (Figure 3.9a and 3.9b). To suppress this dispersion of the data, we only use the maximum height of the dune (H_{max}) and its corresponding spacing and water-depth, which are shown in Figure 3.10. The properties of the dunes were measured in three depth regions based on the above observations: below 25 m, corresponding to the foot of the bank, between 25 m and 15 m, corresponding to the flanks of the bank, and from 15 m to the crest of the bank. A correlation between dune shape and waterdepth can be expected as waterdepth can affect the size of the turbulent boundary layer and limit the development of wakes and turbulences on the lee side of the dunes (McLean, 1989). Figure 3.10a clearly shows that sand dune height increases with increasing water-depth. A linear trend fitted to the data by least-squares indicates that on average $H/z = 0.11$ (Equation 3.120), which is a little smaller than the widely accepted relation $H/z = 0.167$ (Equation 3.2) for dunes formed in unidirectional flows (Yalin, 1992). Dune spacing and water-depth (Figure 3.10b) show no correlation, as spacing varies weakly. Flemming (2000) defined steepness as the ratio of dune height to its spacing. Figure 3.10c shows the steepness of the dunes for each of the depth groups. Flemming (2000) proposed a relation $H = 0.0667L^{0.8}$ (Equation 3.3), found by power regression of 1491 data, with a coefficient of correlation, R = 0.98, which represents a global trend of dunes in both fluvial and marine environments. Flemming's results provide a baseline with which local trends can be compared (Wienberg and Hebbeln, 2005). For each of the dune groups, power regressions were fitted through the data. At the foot of the bank (below 25 m), dunes are steeper than those analysed by Flemming (2000), while above 25 m the dunes tend to flatten (Figure 3.10c). The tendency to flatten could arise from one or more effects: (1) increasing suspension and bedload movements by surface waves which are likely to intensify towards shallow water and with proximity of the water surface; (2) the tidal current intensifying as it is

concentrated through a narrower depth extent as proposed for flattening of sand banks at larger scale (Huthnance, 1982a); and (3) the effect of shallow water reducing the vigour of lee-side eddies (Kostaschuk, 2000).

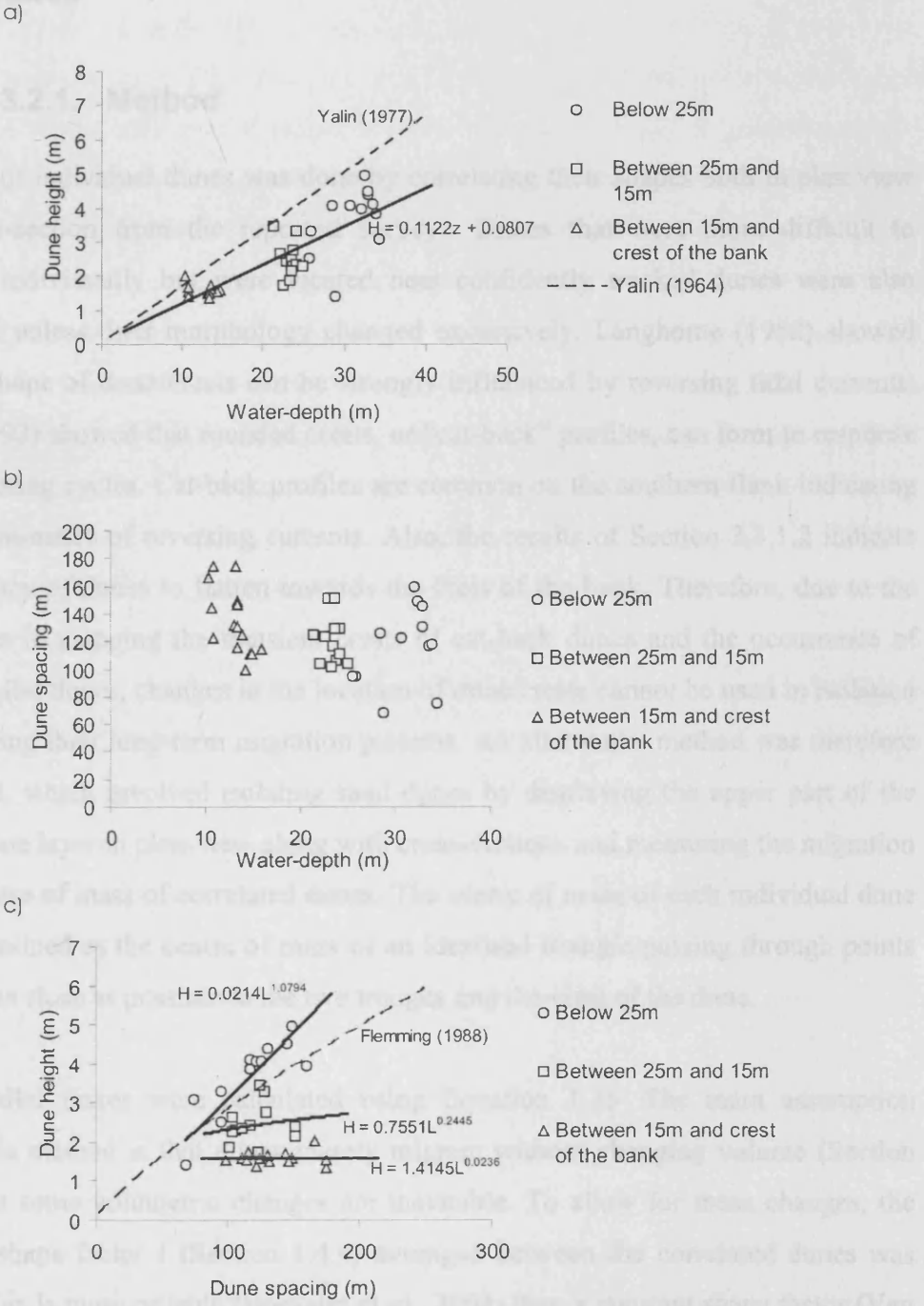

Figure 3.10 Interrelationships between the dune geometrical properties. Measurements were made where each dune reached its maximum height. Dune height (a) and hence dune flatness (c) are depth dependant while dune spacing (b) is not. Dune flattening at the crest of the bank suggests active wave-induced erosion.

3.3.2. Bank-parallel migration of dunes and their implied fluxes

3.3.2.1. Method

Tracking of individual dunes was done by correlating their shapes both in plan view and cross-section from the repeated surveys. Dunes that were more difficult to correlate individually but were located near confidently tracked dunes were also correlated unless their morphology changed excessively. Langhorne (1982) showed that the shape of dune crests can be strongly influenced by reversing tidal currents. Berné (1993) showed that rounded crests, or "cat-back" profiles, can form in response to neap-spring cycles. Cat-back profiles are common on the southern flank indicating the predominance of reversing currents. Also, the results of Section 3.3.1.2 indicate the tendency of dunes to flatten towards the crest of the bank. Therefore, due to the difficulties in mapping the transient crests of cat-back dunes and the occurrence of relatively flat dunes, changes in the location of dune crests cannot be used in isolation for resolving their long-term migration patterns. An alternative method was therefore developed, which involved isolating sand dunes by displaying the upper part of the mobile dune layer in plan-view along with cross-sections and measuring the migration of the centre of mass of correlated dunes. The centre of mass of each individual dune was determined as the centre of mass of an idealised triangle passing through points digitised as close as possible to the two troughs and the crest of the dune.

Bank-parallel fluxes were calculated using Equation 1.25. The main assumption behind this method is that dunes merely migrate without changing volume (Section 1.4.4), but some volumetric changes are inevitable. To allow for these changes, the use of a shape factor f (Section 1.4.4) averaged between the correlated dunes was used, as this is more reliable (Hoekstra et al., 2004) than a constant shape factor (Van den Berg, 1987). Volumetric sediment transport was then converted to a specific mass by multiplying the volumetric sand flux by $(1-\varepsilon)\rho_s$, where ρ_s is the dry density of sand grains (typically 2650 kg.m^{-3} for quartz) and ε is the deposited sand porosity which is chosen equal to 0.4 for a typically packed and sorted sand (Soulsby, 1997).

3.3.2.2. Results

3.3.2.2.1. Sand dune migration

Figures 3.11 and 3.12 show an example of how confidently dunes can be tracked between the surveys. In the 2001 survey data, tracked dunes are referred to as A to M along the southern flank of the bank and 1 to 15 along the northern flank. Apostrophes are applied to the 2002 data. Changes in cross-sectional area and migration rates for tracked dunes are given in Table 3.1. The dunes migrated with similar displacements forming trains during the 11 month period separating the surveys, with a mean average of 22 m (10 m standard deviation) along the southern profile, compared with 34 m (13 m standard deviation) on the northern profile. The tracked dunes migrated in the directions expected from dune asymmetry (Figure. 3.9c). Amongst 11 dunes, 8 show a volume change of less than 25%, meaning that migration occurred with little erosion or deposition (Mohrig and Smith, 1996). The geometrical similarity of dunes in plan-form and cross-section between the two surveys (Figures 3.11 and 3.12) is therefore interpreted as the product of primarily bedload transport leading to dune migration (Van den Berg, 1987).

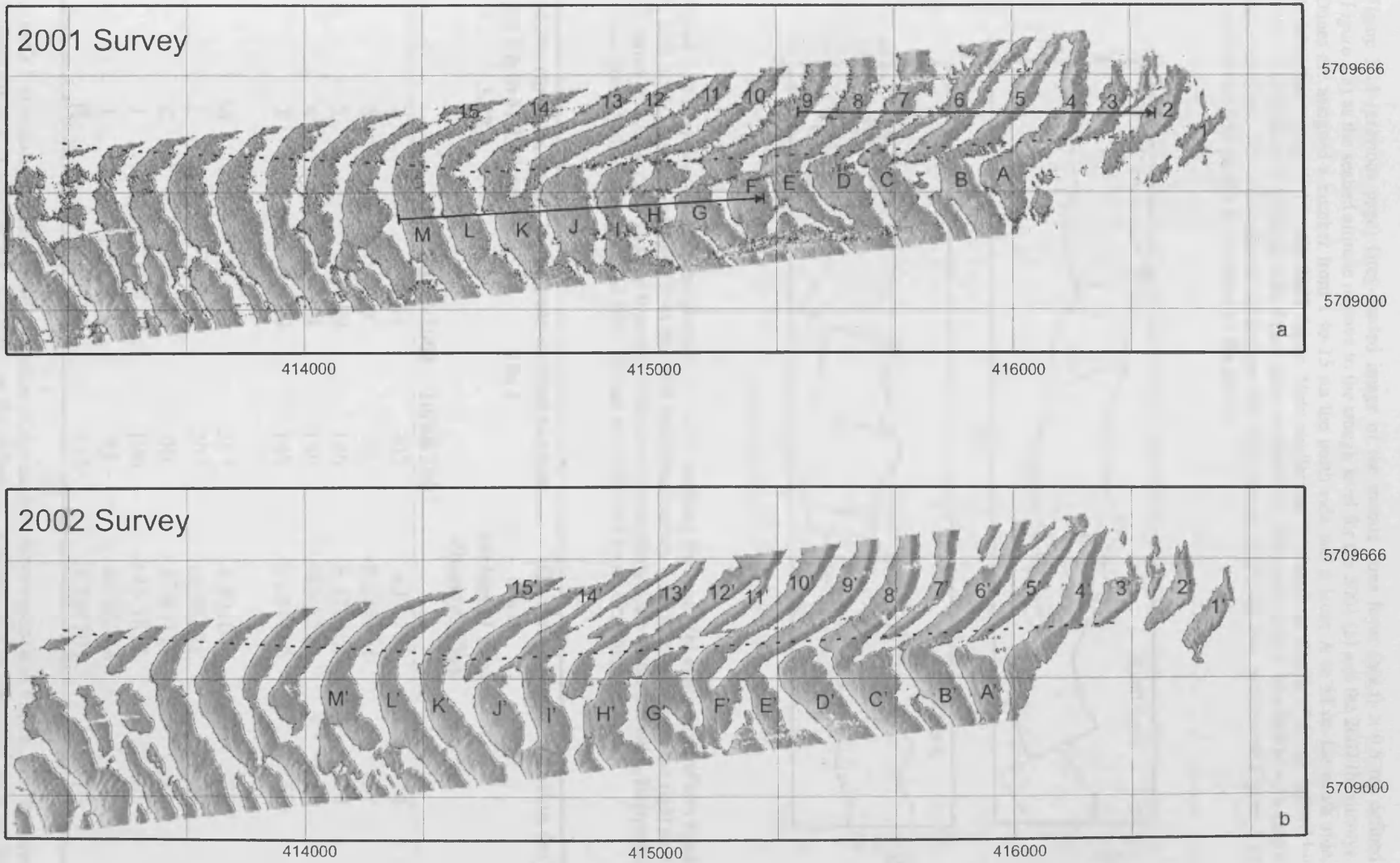
2001 Survey
15
14
13
12
11
10
9
8
7
6
5
4
3
2
1
M
L
K
J
I
H
G
F
E
D
C
B
A
a
5709666
5709000
414000
415000
416000
2002 Survey
15'
14'
13'
12'
11'
10'
9'
8'
7'
6'
5'
4'
3'
2'
1'
M'
L'
K'
J'
I'
H'
G'
F'
E'
D'
C'
B'
A'
b
5709666
5709000
414000
415000
416000

Figure 3.11 (previous page) Grey-shaded image of the mobile dune layer (h(x,t) > 0.5 m) defined (Figure 3.8) as the seabed altitude relative to the trough level for the 2001 (a) and the 2002 (b) surveys. Dunes are assigned a number from 1 to 15 on the north side and a letter A to M on the south side. Apostrophes are applied for the 2002 dunes. Note similarities in plan-form shapes of dunes defined by the h = 0.5 m level suggesting that dunes have migrated by relatively simple translation with minor shape changes. The solid arrows plotted on the 2001 survey mark the two profiles of Figure 3.12 (orientation of the profile is indicated by the arrow)

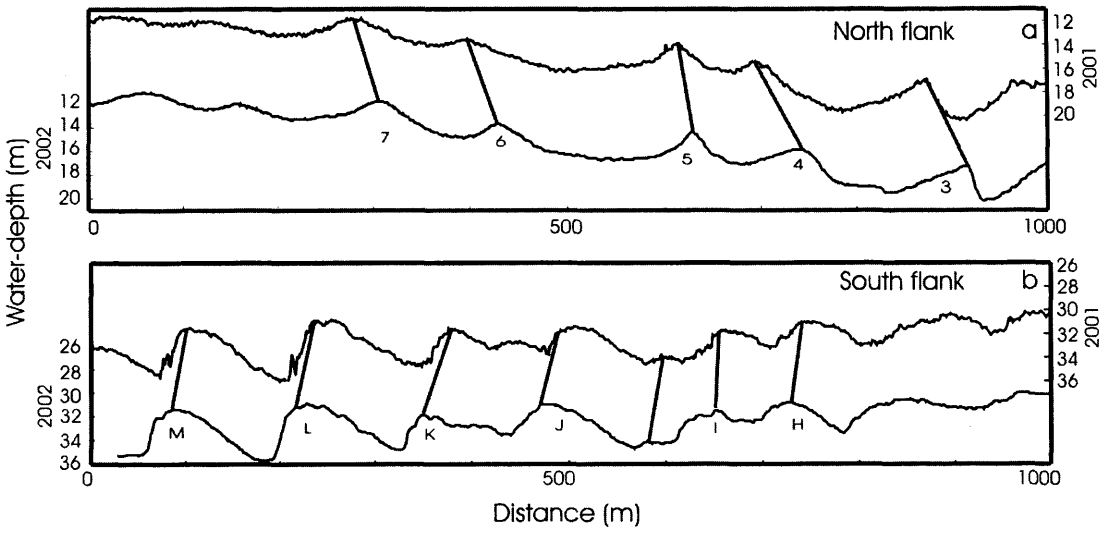

Figure 3.12 Examples of collocated profiles (a) on the northern flank and (b) along the southern flank. In each figure, the data extracted from the 2001 multibeam survey (waterdepth scale on the right side) are shown above the data extracted from the 2002 survey (waterdepth scale on the left side). Interpreted similar dunes both in plan-form and cross-section are connected by tie-lines between crests.

Dune (as referenced on Figures 3.11 and 3.12)	Cross-sectional area (m^2)		Relative cross-sectional area changes (%)	Migration (m)
	26/09/2001	20/08/2002		
7	151	202	+33.77	34
6	97	88	-9.278351	29
5	159	146	-8.176101	14
4	118	169	+43.2203	44
3	190	149	-21.57895	50
M	279	267	-4.301075	32
L	281	295	+4.98221	28
K	109	90	-17.43119	30
J	135	196	+45.1852	25
I	112	57	-49.10714	8
H	122	115	-5.737705	10

Table 3.1 Morphologic variation and migration of the tracked dunes reported in Figure 3.13. Relative cross-sectional area changes are calculated as the difference between the cross-sectional areas of the 2001 and 2002 tracked dunes divided by the cross sectional area measured in 2001.

From Figure 3.11, the splitting of dunes can be observed. For example, dune D on the southern side of the bank was connected in 2001 with dune 7 on the northern side. In 2002, dune D' has migrated eastward (Figures. 3.11a and 3.11b). As defined by the h = 0.5 m contour, it is clearly disconnected from dunes to the north. Dune 7 migrated eastward and may have connected with dune C' temporarily in the period between the two surveys, but was disconnected from dune C' by the time of the 2002 survey. At this time dune 8' was laterally connected with dune C'.

Merging of dunes can also be observed. For example, dune H was split in two parts and barely connected with dune 10 in the 2001 survey (Figure 3.12a). In the time between the surveys, the southern part of dune H migrated faster than the northern part. In 2002, the northern part of dune H' merged with dune 12' to form a single laterally continuous dune from one side of the bank to the other. In some cases, dunes have also amalgamated. For example, dune 6 presents a "X" plan-form on the 2001 survey. In 2002, both southern legs of the "X" shape are amalgamated and form dune 6' which is laterally connected to dune B'.

Further information concerning the migration of the dunes was extracted from a comparison between the 2001 and 2002 multibeam surveys along with the 2003 single-beam echo-sounder survey. Dune cross-sections extracted from the mobile dune layer for each bathymetric survey are plotted along with the 2003 single-beam data deliberately collected parallel to the crest of the bank (shown in the insert of Figure 3.13). Lateral continuity of the dune crests is represented on Figure 3.13 by lines connecting the crests of the 2002 survey mapped dunes. Arrows show confidently tracked dunes permitting a measurement of displacement.

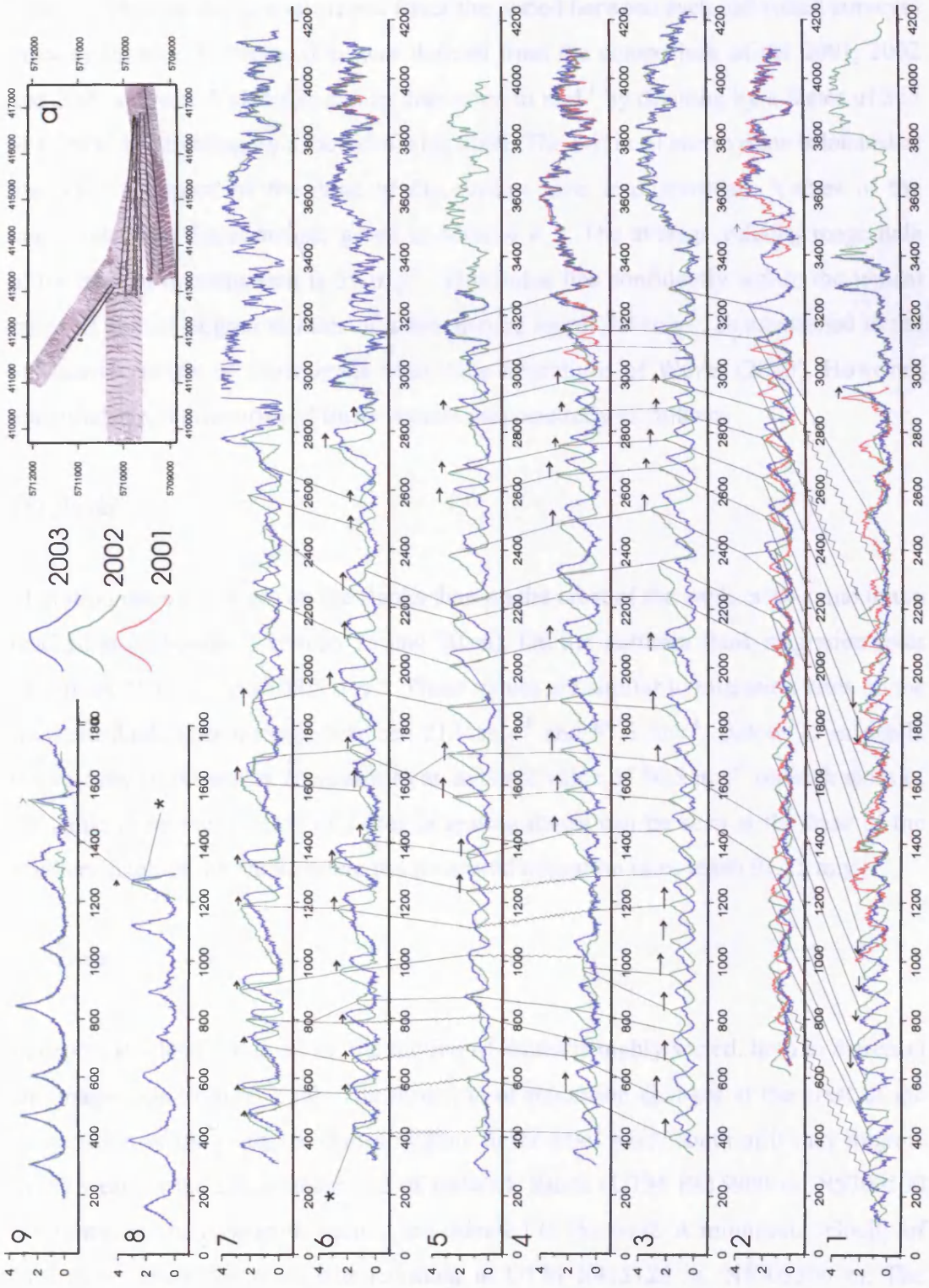

Figure 3.13 Time-series of profiles of sand dunes. Bathymetry from the 2001 and 2002 multibeam and 2003 single-beam echo-sounder surveys relative to the dune trough level (i.e. the mobile dune layer) are plotted along the 2003 survey tracks (insert, origin of the profile is located at the reference number location). Continuous lines between dune crests connect dunes recorded on adjacent lines, as interpreted from the 2002 survey (jagged lines represents supposed continuity). Discrepancy between the heights of bedrock between the surveys may be an artefact of the dune trough digitising method.

Figure 3.14 plots the time-averaged (over the period between each individual surveys) velocity (in $m.y^{-1}$). Vector field was derived from the comparison of the 2001, 2002 and 2003 surveys. Velocities can be converted to $m.d^{-1}$ by dividing by a factor of 365 or to $m.s^{-1}$ by dividing by a factor of 31536000. The origin of each vector is located at the centre of mass of the dune at the earliest time it is recorded. Values of the magnitudes and directions are given in Annexe A.2. The average velocity magnitude in the area of investigation is 55 $m.y^{-1}$. This value lies confidently within the typical range of annual migration rates of a few meters up to 700 $m.y^{-1}$, as mentioned in the exhaustive review of subaqueous sand dune migrations of Wever (2003). However, magnitudes and directions of these vectors vary spatially as follows.

The flanks

Migration rates are larger on the flanks than on the crest of the bank, with a maximum reached at mid-slope (between 15 and 20 m). On the northern flank migration rates vary from 21.9 $m.y^{-1}$ to 109.5 $m.y^{-1}$. These values are similar to migration rates on the southern flank, which range between 21.9 $m.y^{-1}$ and 87.6 $m.y^{-1}$. Below 25 m depth, the velocity of the dunes decreases to an average value of 36.5 $m.y^{-1}$ on both sides of the bank. However a patch of faster migrating dunes can be seen at the base of the southern flank of the bank, where the measured migration rates reach 91.25 $m.y^{-1}$.

The crest

In depths shallower than 12 m, the motion of dunes is highly varied, both in direction and magnitude (Figure 3.14). The direction of migration changes at the crest of the bank. North of the crest, the dunes migrate to the east; while south of it they migrate to the west. In the easternmost end of Helwick Sands (UTM E415900 m, N5709500 m), however, the migration vectors are oriented to the west. A minimum velocity of 21.9 $m.y^{-1}$ along the crest was recorded at UTM E415125 m, N5709500 m. The maximum migration velocity of 75 $m.y^{-1}$ was found at the vicinity of the headland bedrock.

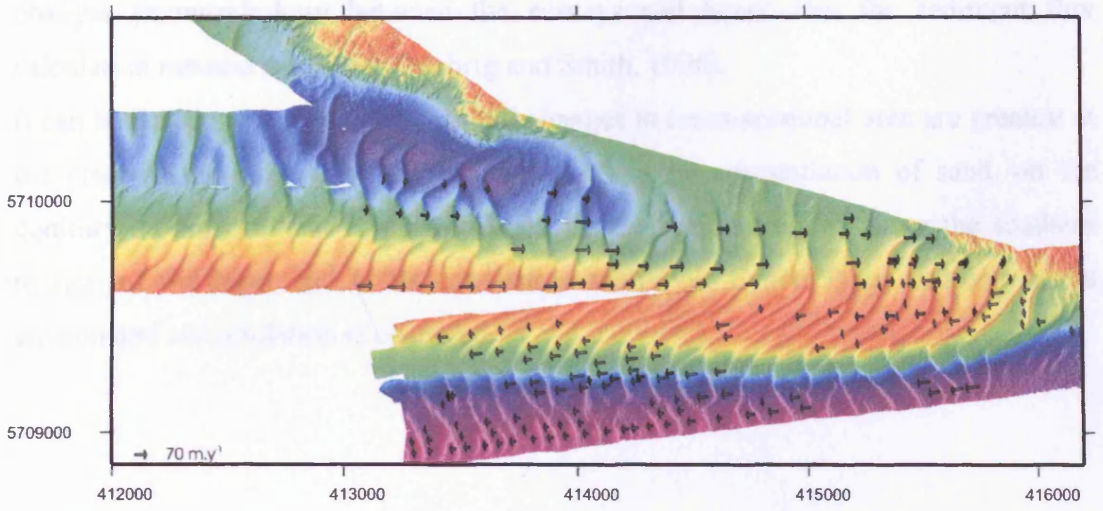

Figure 3.14 Dune velocity vector field. Displacement of the dune were measured from the comparison of the 2001 with the 2002 multibeam surveys (Figure 3.11) and the comparison of the 2002 multibeam data with the 2003 singlebeam data (Figure 3.13). Migration velocity is annually time-averaged. Values of migration velocity are reported in the Annexe A.2.

3.3.2.2.2. Pattern of erosion and deposition

The relative change in cross-sectional area (m^2 across unit of width) of paired dunes indicates their changes from erosion or deposition processes. Relative cross-sectional change can be calculated as follows:

$$\frac{A_2 - A_1}{A_1} \qquad \text{Equation 3.4}$$

where A_1 is the cross-sectional area of a reference dune and A_2 is the cross-sectional area of its migrated counterpart.

Figure 3.15 shows relative cross-sectional changes between the 2001 and 2002 multibeam surveys and between the 2003 singlebeam survey and the 2002 multibeam survey computed from Equation 3.4. Column height is proportional to the percentage of change and is plotted at the crest of each reference dune. Dunes exposed to net erosion (negative relative change between the surveys) are plotted in blue while those affected by net deposition (positive relative change between the surveys) are plotted in red. Dunes that show a net erosion lost on average 19% of their cross-sectional area, while those affected by deposition gained on average 21.5% of their cross-sectional area. This illustrates that the migration of the dunes occur without major

changes in morphology between the surveys and hence that the sediment flux calculation method is reliable (Mohrig and Smith, 1996).

It can be noted, however, that erosional changes in cross-sectional area are greatest at the crest of the bank than over its flanks. Relative accumulation of sand, on the contrary, is predominant along the flanks. In the region situated along the southern margin of the bank and at its connection with Port Eynon Point bedrock mixed erosion and accumulation is observed.

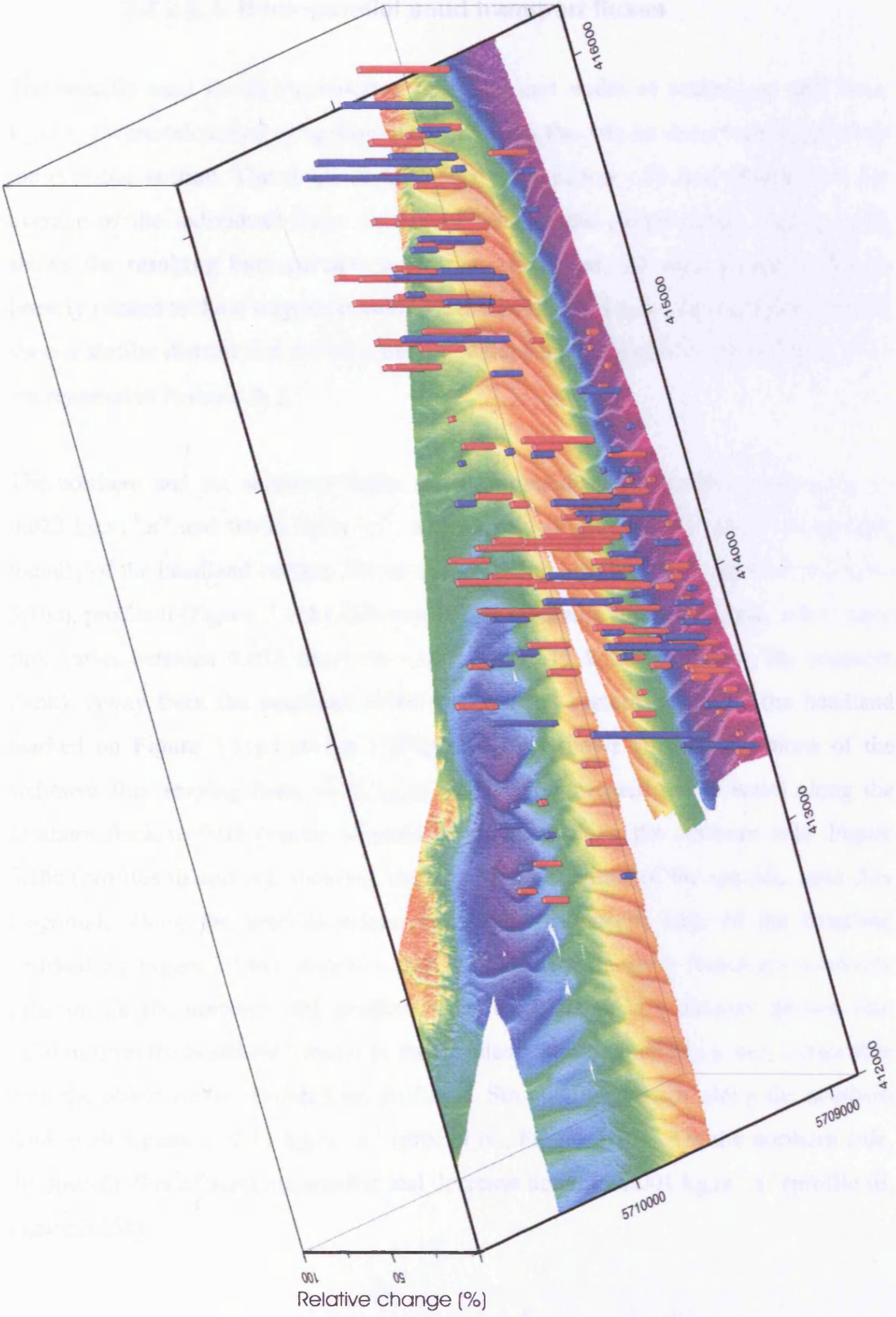

Figure 3.15 Relative cross-sectional changes between paired dunes (between 2001 and 2002 and between 2002 and 2003). Red columns represent net deposition, while blue columns represent net erosion. Relative cross-sectional changes less than 5% are not shown.

3.3.2.2.3. Bank-parallel sand transport fluxes

The specific sand fluxes (transported mass per unit width of seabed per unit time: $kg.m.s^{-1}$) were calculated using Equation 1.25 from the data on dune velocity given in the previous section. The shape factor f used in Equation 1.25 was estimated as the average of the individual shape factors of each of the paired dunes. Figure 3.16a shows the resulting bank-parallel sand transport fluxes. As sand transport flux is linearly related to dune migration velocity, the field of sediment transport flux vectors show a similar distribution and orientation. Values for these specific sand flux vectors are reported in Annexe A.2.

The northern and the southern flanks show comparable average flux magnitudes of 0.023 $kg.m^{-1}.s^{-1}$ and 0.026 $kg.m^{-1}.s^{-1}$, respectively (Figure 3.16b). At the immediate vicinity of the headland (within 250 m of the easting headland limit marked on Figure 3.16a), profile ii (Figure 3.16b) indicates strong gradients across the bank, where sand flux varies between 0.018 (near the crest) and -0.11 $kg.m^{-1}.s^{-1}$ (along the southern flank). Away from the headland (1500 m from the eastern border of the headland marked on Figure 3.16a) profile i (Figure 3.16b) shows smaller variations of the sediment flux varying from -0.03 $kg.m^{-1}.s^{-1}$ (vector oriented to the west) along the southern flank to 0.03 (vector oriented to the east) along the northern side. Figure 3.16c (profiles iii and iv), showing bank-parallel variations of the specific sand flux magnitude along the profiles originating from the eastern limit of the headland (marked on Figure 3.16a), indicates that the sediment transport fluxes are relatively constant for the northern and southern sides of the bank at a distance greater than 1000 m from the headland. Nearer to the headland, strong gradients occur, compatible with the observations recorded on profile ii. Strong fluxes occur along the southern flank with a peak of 0.11 $kg.m^{-1}.s^{-1}$ (profile iv., Figure 3.16c). On the northern side, the specific flux of sand are smaller and decrease down to 0.001 $kg.m^{-1}.s^{-1}$ (profile iii, Figure 3.16c)

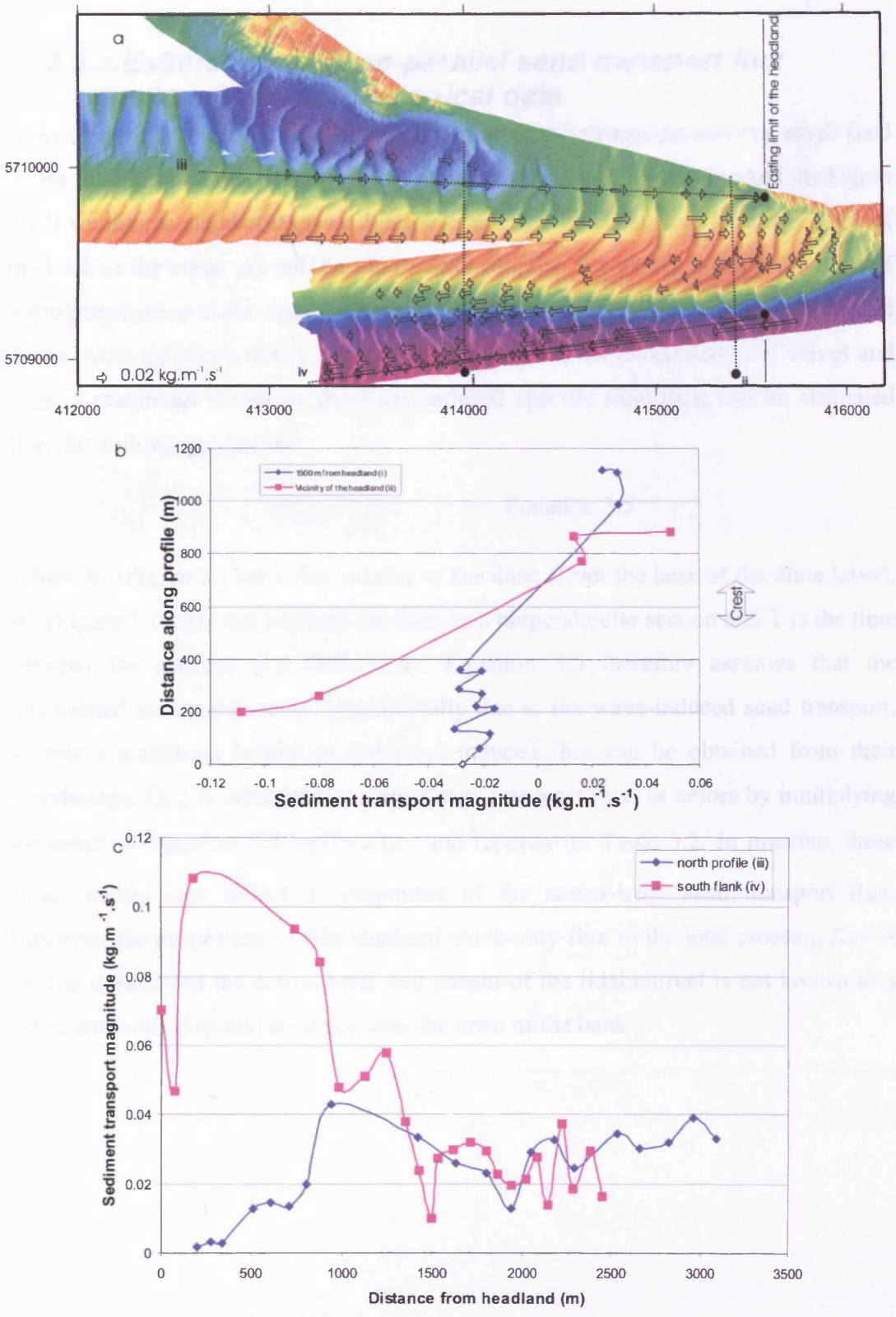

Figure 3.16 Sand transport flux calculated from the dune celerity (Figure 3.14) and morphology (Figure 3.9) using Equation 1.25. See Sections 1.4 and 3.3.2.1 for details of the method used and assumptions. Across- (b) and along-bank (c) profiles show the spatial variations as a function of the distance from the headland bedrock. The origin of the profiles is marked by a black dot on (a). Positive values on (b) represent west to east directed fluxes.

3.3.3. Estimation of dune-parallel sand transport flux maxima from morphological data

Comparison of the survey data show that, in the time between the surveys, small sand dunes (about 0.5 m) have formed at the crest of the bank. These (marked on Figure 3.17) are intercalated between sand dunes crests that are continuous from one flank of the bank to the other. As will be shown later (Section 3.4.4), the average direction of wave propagation at the crest of the bank is parallel to the crest of these intercalated dunes. Although these dunes may have formed by the combined action of waves and tides, a maximum bound on the wave induced specific sand flux, can be estimated from the following equation:

$$Q_{b,w} = \frac{V_c}{t.W_c} \qquad \text{Equation 3.5}$$

Where V_c (Figure 3.17a) is the volume of the dune (from the base of the dune layer), W_c (Figure 3.17a) is the width of the dune in a perpendicular section and T is the time between the surveys (i.e. 328 days). Equation 3.5 therefore assumes that the intercalated dunes grew only longitudinally due to the wave-induced sand transport, so that a maximum bound on the wave-induced flux can be obtained from their morphology. $Q_{b,w}$ is converted to a mass sand transport flux, as before by multiplying the result of Equation 3.5 by $(1-\varepsilon)\rho_s$ and reported in Table 3.2. In practice, these dunes should also reflect a component of the across-bank sand transport flux. However, the proportion of this idealised wave-only flux in the total crossing flux is hard to quantify as the across-bank component of the tidal current is not known to a sufficient level of spatial accuracy near the crest of the bank.

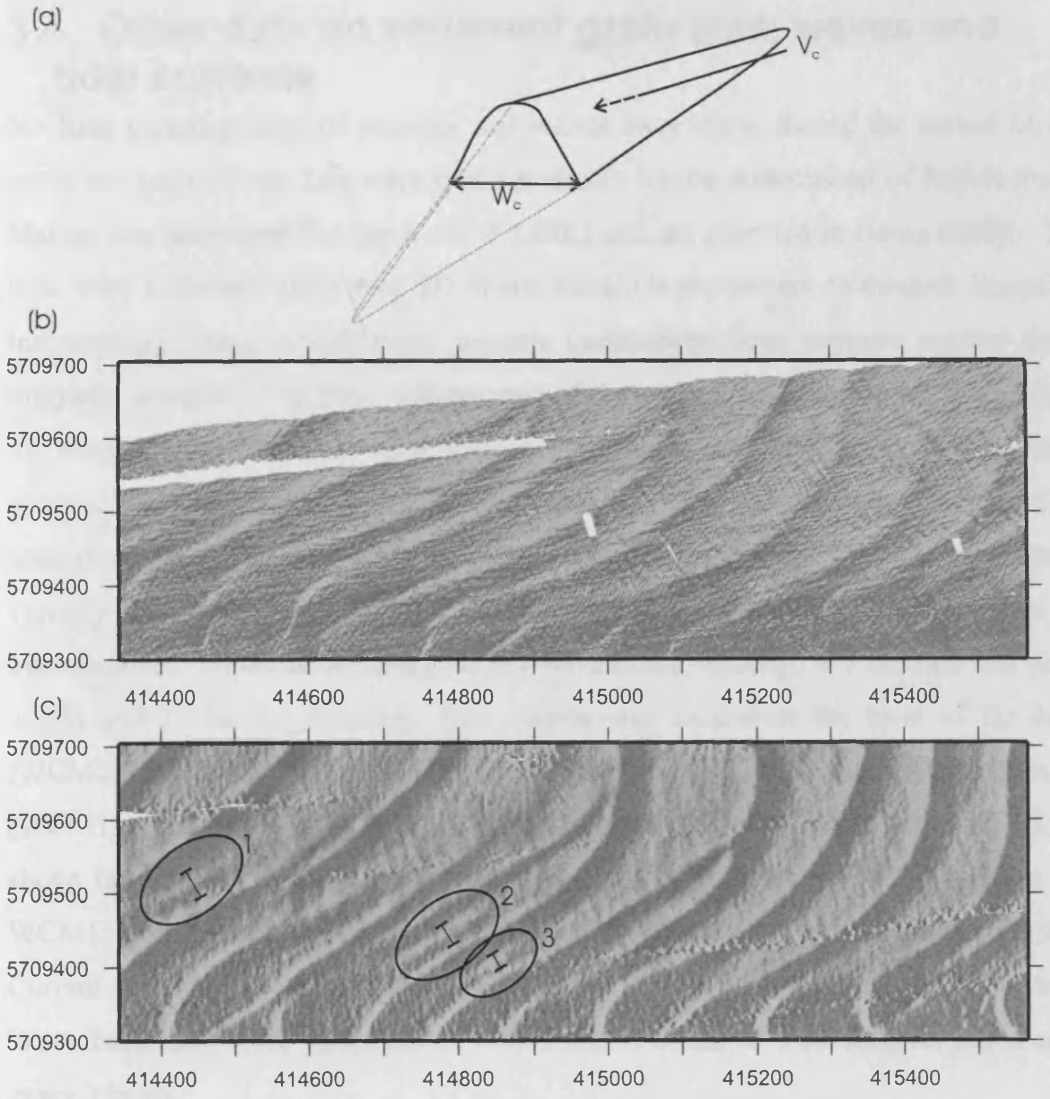

Figure 3.17 Interpretation of intercalated dune (circled on c) formed within the dune field at the crest of the bank between the 2001 (b) and 2002 (c) multibeam surveys. An extreme estimate (maximum bound) on the sand flux due to wave currents parallel to dune crests can be obtained using the geometry in (a). The sand forming the volume V_c is assumed to have passed through the width W_c. This is a maximum bound as it ignores movements caused by tidal currents.

Dune	V_c (m^3)	W_c (m)	$Q_{b,w}$ ($kg.m^{-1}.s^{-1}$)
1	360	32	9.3×10^{-4}
2	665	69	9.0×10^{-4}
3	99	23	4.0×10^{-4}

Table 3.2 Along-dune specific sand flux estimates assuming transport by surface wave currents only. See text for the method of calculation.

Average across-bank flux from the measurements taken from the three dunes yields a value of 7.33×10^{-4} $kg.m^{-1}.s^{-1}$.

3.4. Other data on sediment grain size, waves and tidal currents

No field measurements of currents and waves were made during the period of the study but some recent data were made available by the Association of British Ports, Marine Environmental Research (ABP MER) and are reported in Haine (2000). The data were collected using two 3D-Wave current/wave meters (Falmouth Scientific Instruments). These include eight acoustic transducers, three pressure sensors and a magnetic compass. The three components of the current velocity are measured from the acoustic echo frequency shift (Doppler) within at least three of the non-collinear acoustic paths (Gilboy et al., 2000). The wave spectrum and direction are derived by combining measurements from the three pressure sensors and the vertical Doppler velocity (McComb et al., 2001). Flow characteristics are measured, according to the manufacturer, within an accuracy of 2% for current velocity, ± 3 mm for the wave height and 2° for the direction. One station was located at the crest of the bank (WCM2, UTM E415294 m, N5709617 m) and the other one in the Helwick Passage (WCM1, UTM E415315 m, N5710139 m) (Figure 3.18a). Both were deployed 0.85 m above the seabed, which corresponds to a depth of 9 m for WCM2 and 18 m for WCM1. Both probes started logging on 16/6/1998 and were recovered on 9/8/1998. Current velocity data were measured twice for an average of 2 minutes every hour. Wave burst data were collected for 9 minutes at a rate of 5.36 samples per second every 3 hours.

ABP MER also provided sediment texture information for the area. Surficial grab samples were collected between 25/7/1998 and 5/8/1998 in the East Helwick area with a sampling grid spacing of ~500 m (Figure 3.17a).

3.4.1. Sediment grain size

Sand at the vicinity of the East Helwick Sands and Port Eynon Bay is generally fine to medium (0.2 mm < d_{50} < 0.5 mm) (Figure 3.18.a), well sorted to very well sorted and slightly skewed to symmetrically skewed. Grain-size characteristics for four sub-regions (Port Eynon Beach, northern and southern flank, crest of the bank) are given in Table 3.3.

Morphologic area	*Median*	*Sorting*	*Skewness*
South (n=12)	1.21 (0.43mm)	0.94	0.66
North (n=20)	1.45 (0.36mm)	0.59	0.51
Crest (n=26)	1.51 (0.35mm)	0.49	0.07
Port Eynon (n=44)	1.66 (0.31mm)	1.23	1.08

Table 3.3 Grain size characteristics for different morphologic regions of the Helwick Sands and the adjacent Port Eynon Bay. Grain size units are N ($N=-\log_2$(grain size in mm)).

Port Eynon Bay sand differs from the rest of the dataset in that it is finer, more poorly sorted and strongly positively skewed. This may be due to the weaker sorting effect of the tidal currents in the bay compared to the bank area (Ferentinos, 1978; Ferentinos and Collins, 1980). On the bank, grains are on average coarser than in the bay. Finer sand tends to segregate on the crest and on the northern flank, while coarser sand is found along the southern flank. The data show a better sorting on the crest relative to both flanks. Table 3.3 demonstrates a trend towards more positively skewed populations from the crest to the flanks.

Figure 3.18.b shows the critical shear velocity of the flow at one meter above the seabed for the initiation of sand grain motion. This value was calculated using the method of Yalin modified by Miller as described in Section 1.2.2.1. As expected from the median grain size (Figure 3.18.a), the highest values of $U_{cr,100}$ are predicted to occur in the south-eastern part of Figure 3.18b, and in particular in the southern part of Port Eynon Bay below 15 m, with $U_{cr,100}$ values of up to 0.28 $m.s^{-1}$. In the vicinity of Helwick Sands, the sand is more easily mobilised. Subtle variations appear between the different morphological areas characterising the bank. Along the southern flank, the maximum value of $U_{cr,100}$ is 0.24 $m.s^{-1}$. On the crest, the northern flank and the nearshore area above 15 m along the coastline $U_{cr,100}$ is uniform with a value of 0.2 $m.s^{-1}$. In the depression between the bank and the coastline below 15 m, $U_{cr,100}$ values are slightly higher than in the previous area with a maximal value of 0.24 $m.s^{-1}$.

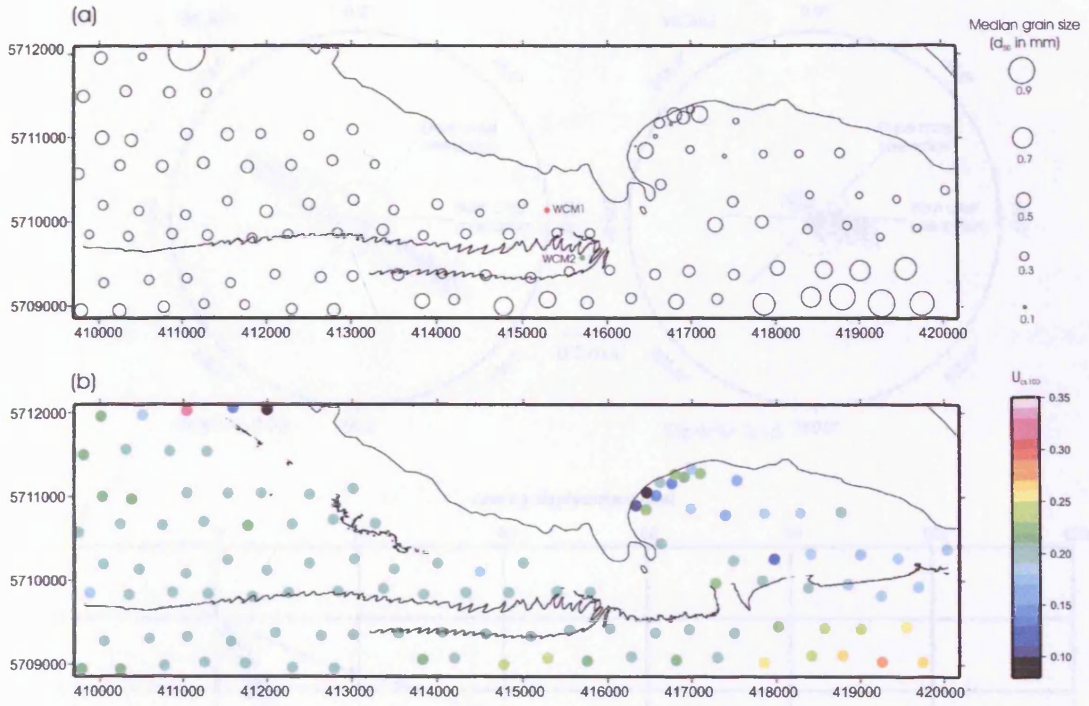

Figure 3.18 Grain sizes in the vicinity of the East Helwick Sands and Port Eynon Bay area. The contour line is the 15 m water-depth contour.
(a) Median grain size (d_{50} in mm) of the seabed samples (data from Haine (2000)). The two current/wave meters (WCM1 and WCM2) are also displayed by red and green dots respectively.
(b) Derived critical bedload threshold speed at one meter above the seabed ($U_{cr,100}$) calculated using the method of Yalin modified by Miller (see Section 1.2.2.1) and supposing that the current boundary layer lies within the first meter above the seabed and has a logarithmic velocity profile.

3.4.2. Near bed tidal currents

During the period of measurement, which corresponds to a succession of four neap-spring cycles, a reversing north-west to south-east current was observed (Figure 3.19a). The progressive vector diagram of Figure 3.19b, plotted over one neap-spring cycle, exhibits flood oriented residual currents.

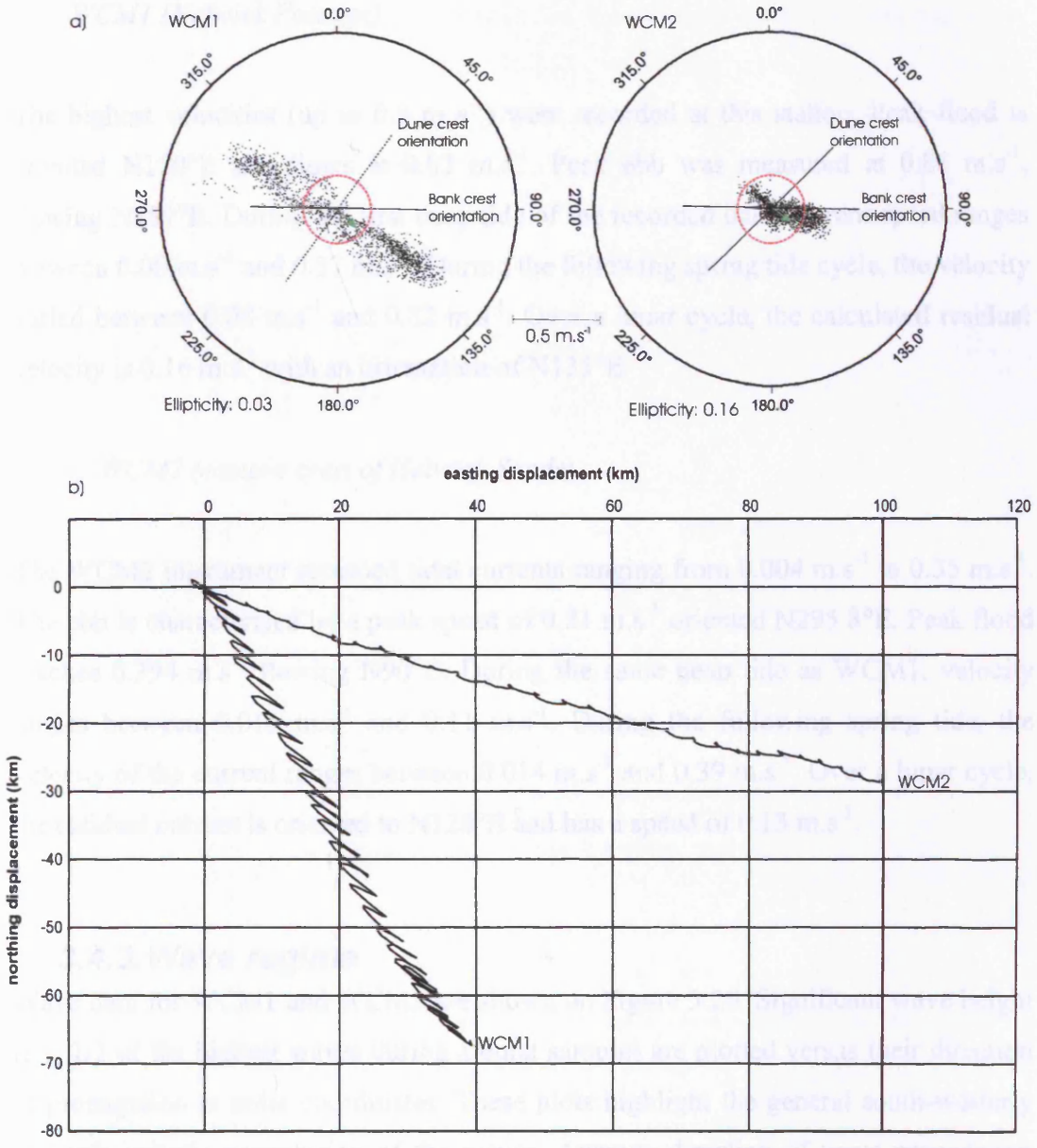

Figure 3.19 Tidal flow regime in the Helwick Passage (WCM1) and in the eastern crest of Helwick Sands (WCM2). (a) Direction and velocity for both records at one meter above the seabed during the period 16/6/1998 to 09/08/1998. Critical shear velocity $U_{cr,100}$ for 0.3 mm diameter sand is plotted as the red dotted circles. Green arrow is the averaged current vector over a complete lunar cycle. Orientation of the bank crest and dune crests is also shown. (b) Progressive vector diagrams for a neap-spring cycle (18/06/1998 to 17/07/1998), showing the residual flood component for both records. Derived from data from Haine (2000). Ellipticity was calculated as the ratio of the RMS distances (residual between the axis and the data point) of data points from the minor and major tidal ellipse axis. The long axis was determined by fitting a line by regression through the data. The short axis is perpendicular to the long axis.

WCM1 (Helwick Passage)

The highest velocities (up to 0.8 m s^{-1}) were recorded at this station. Peak flood is oriented N120°E and flows at 0.82 $m.s^{-1}$. Peak ebb was measured at 0.81 $m.s^{-1}$, flowing N281°E. During the first neap tide of the recorded data, current speed ranges between 0.08 $m.s^{-1}$ and 0.37 $m.s^{-1}$. During the following spring tide cycle, the velocity varied between 0.08 $m.s^{-1}$ and 0.82 $m.s^{-1}$. Over a lunar cycle, the calculated residual velocity is 0.16 $m.s^{-1}$ with an orientation of N135°E.

WCM2 (eastern crest of Helwick Sands)

The WCM2 instrument recorded tidal currents ranging from 0.004 $m.s^{-1}$ to 0.35 $m.s^{-1}$. The ebb is characterised by a peak speed of 0.21 $m.s^{-1}$ oriented N295.8°E. Peak flood reaches 0.394 $m.s^{-1}$ flowing N90°E. During the same neap tide as WCM1, velocity ranges between 0.016 $m.s^{-1}$ and 0.11 $m.s^{-1}$. During the following spring tide, the velocity of the current ranges between 0.014 $m.s^{-1}$ and 0.39 $m.s^{-1}$. Over a lunar cycle, the residual current is oriented to N128°E and has a speed of 0.13 $m.s^{-1}$.

3.4.3. Wave regime

Wave data for WCM1 and WCM2 are shown on Figure 3.20. Significant wave height (Hs, 1/3 of the highest waves during a burst sample) are plotted versus their direction of propagation in polar coordinates. These plots highlight the general south-westerly to north-easterly propagation of the waves. Average direction of wave propagation (calculated as the tangent of the ratio of the average of the northing component by the easting component) at WCM1 is N84.03°E and N45.82°E at WCM2. Figure 3.20a shows that the waves in Helwick Passage were propagated only slightly anticlockwise of the orientation of the bank's crest. Interestingly, Figure 3.20b shows waves at WCM2 propagating parallel to the local dune crest orientation (N46°E). The difference in the direction of propagation can be explained by the refraction over the shallow crest of the bank at WCM2. The standard deviation of wave orientation about the average direction of propagation was calculated to represent the dispersion of the wave regime. Respective values for WCM1 and WCM2 are 11.88° and 10.94°.

Maximum and average values of the significant wave height are reported respectively in Tables 3.4 and 3.5. The two sites experienced similar wave statistics, with the Helwick Passage being slightly more energetic, as average wave periods differ by less than 5% and significant wave height by less than 25%.

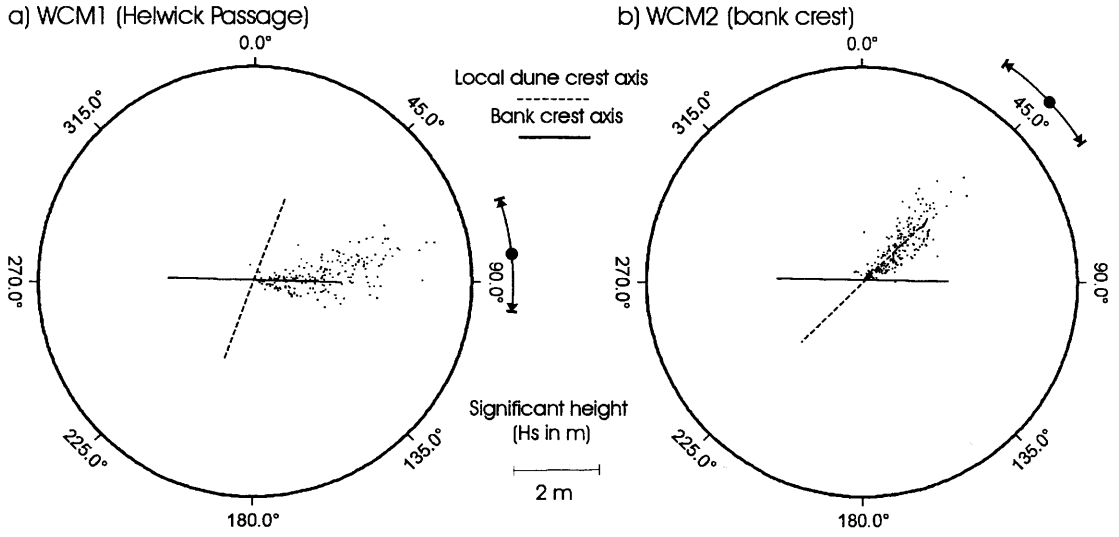

Figure 3.20 Significative wave height vs. direction of propagation (derived from data from Haine (2000)). Average direction is represented by the black dots (see text for details of the calculation). One standard deviation from the average is displayed by double arrowed lines (see text for details). Note the similarity between the orientations of the local dune crests and the wave propagation direction at the crest of the bank for WCM2.

	Mean period (s)	Significant wave height (m)	Calculated near bed orbital velocity ($m.s^{-1}$)
Maximum	9.63	4.25	0.92
Average	6.31	1.57	0.28
Standard deviation	0.90	0.92	

Table 3.4 Wave regime statistics for WCM1. Mean period and significant wave height were derived from the data of Haine (2000). Orbital velocity was calculated at 10 m from Equation 1.8a.

	Mean period (s)	Significant wave height (m)	Calculated near bed orbital velocity ($m.s^{-1}$)
Maximum	9.77	3.39	0.73
Average	6.02	1.17	0.21
Standard deviation	0.90	0.68	

Table 3.5 Wave regime statistics for WCM2 station. Mean period and significant wave height were derived from the data of Haine (2000). Orbital velocity was calculated at 10 m using Equation 1.8a.

Maximum orbital velocity calculated at 10 m below the sea surface (chosen arbitrarily for the purpose of comparison between both sites) using Equation 1.8a is only 25% higher at the WCM1 station. Figure 3.21 shows a comparison of the calculated tidal current velocity and the calculated orbital velocity at one meter above the seabed for both sites. The solid and dashed lines on Figures 3.21a and 3.21b show the calculated moving average of 10 data points (i.e. a period of 90 minutes). Figure 3.21a clearly demonstrates that tidal currents are dominant at the WCM1 station, as the moving average of the tidal velocity is always above the wave orbital velocity moving average. Mixed influence of the currents and the wave are observed on Figure 3.22b as wave orbital velocity is above tidal current velocity on several occasions. By comparing individual data, it was found that tidal current velocity is above maximum wave orbital velocity for 76% of the time at station WCM1 whereas tidal current is greater 50% of the time at WCM2. It can be finally noted that the depth to the wave base (the depth at which the orbital motion is null), defined as half the wavelength, is estimated to lie at 26 m below the water level (calculated with averaged data of WCM1).

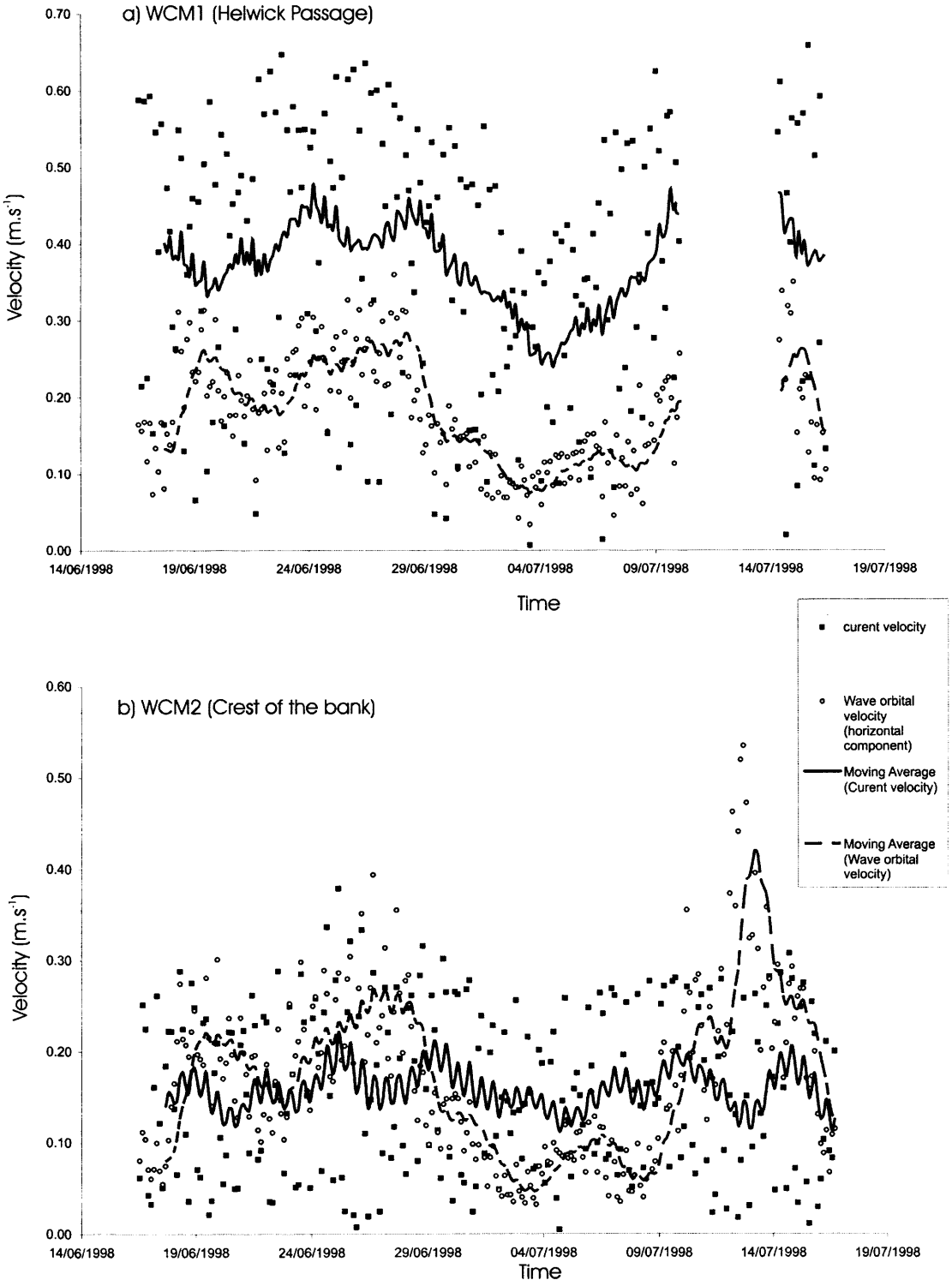

Figure 3.21 Tidal current and horizontal orbital velocity at one meter above the seabed. Current and wave orbital velocity data were averaged over a period of three hours to obtain values for concomitant periods of time. Moving average is calculated for a ten data points window. Derived from data from Haine (2000) using Equation 1.5 for the tidal current and Equation 1.18a.

3.5. Discussion

3.5.1. Pattern of sediment transport and associated processes based on the morphologic and dynamic evidence

Section 3.3.1 showed that sand dunes on the flanks of East Helwick Sands have asymmetrical cross-sections and rounded crests. The rounded morphology (cat back profile) is interpreted to be caused by reversing tidal currents (Berné, 1993). Thus, bank-parallel tidally induced sediment transport occurs on the flanks. Dunes along the southern flank show a net ebb orientation from their asymmetry (Figure 3.9b) and migration (Figure 3.14). This confirms previous observations along the south-eastern flank (Harris and Collins, 1984), that the southern flank is ebb dominated. The asymmetry and migration of dunes (Figure 3.14) along the northern flank show a net flood dominated influence, which is compatible with the tidal current observations at the station WCM1. Such a sediment transport path around sandbanks has been observed on many occasions around other sandbanks (Section 1.3).

As the bathymetry shallows, dune crests veer from about 90° to about 50° relative to the bank's crest and become simultaneously more symmetrical and smaller. Although there are no extensive measurements of the currents one can speculate on their spatial variability from the sinuosity of the dune crests and their morphology. Supposing that dunes are aligned perpendicular to the time-averaged dune-normal transport (Rubin and Hunter, 1987; Rubin and Ikeda, 1990) (i.e. perpendicular to the longer axis of the tidal ellipse in the case of tidal only sediment transport), the veering of the dune crests towards the crest of the bank reflects how topographically induced friction (Section 1.2.1) combined with the eddying nature of the (instantaneous) flow passing the headland (Section 1.2.1) deflects the current across the crest of the bank, with an acceleration up-bank and a deceleration down-bank from the crest. This pattern of water movement and associated sediment transport would be similar to the suggestion of Huthnance (1982a,b) for currents and sediment transport over isolated shelf sand banks (i.e. irrespective of the presence of a headland). However, WCM2 unexpectedly indicates slower currents at the crest of the bank than WCM1 in the deeper water of Helwick Passage. The constriction formed by the proximity of the coastline and the bank, in which WCM1 was positioned, may explain this difference, as the flow

acceleration may occur between the bank and the coastline rather than near the crest of the bank. The lateral compression (funnelling) of the flow in the Helwick Passage is believed to create strong current velocity. The symmetric, less well developed and slowly migrating sand dunes over the crest of the bank suggest lower net sediment transport fluxes and hence weaker residual currents (a weaker asymmetric tidal current was calculated for WCM2 compared with WCM1). This qualitative description of water and sand motion implies a net flood-oriented sediment transport that supplies sand to the easternmost end of Helwick Sands. This transport may be important for maintaining the connection between the bank and the extension of the bedrock from Port Eynon Point.

Importantly, the presence of sand deposits and dunes up to the immediate connection of the bank with Port Eynon Point bedrock is not fully compatible with the residual eddy sandbank maintenance theory (Section 1.3.2.3) because it predicts the presence of an area of intense scouring between the bank and the headland. In the case of Helwick Sands the bank deposits connect to the sub-tidal part of the headland through the Helwick Passage, which has a saddle shape but is not a scouring zone. It is suspected that in addition to the tidally driven sediment transport around the bank, wave driven sand transport induces a cross-bank component, which Pingree did not take into account. Also Pingree's model did not take account of how the bank topography itself would modify the flow. Morphological support of the wave influence on the sediment transport affecting the bank crest is given by the flattening of the sand dunes (Section 3.3.1.2) and Figure 3.20 which shows that waves propagate parallel to the dune crests at station WCM2.

3.5.2. Sediment mobility

Figure 3.19a indicates that the tidal current speed at one meter above the seabed (U_{100}) overcomes the critical threshold speed of the sediment ($U_{100,cr}$) during some parts of the tidal cycle at both station WCM1 and WCM2. The excess of shear velocity (with $U_{cr,100}$=0.2 m.s^{-1}) was used with Equation 1.7 to compute the tidal current induced fluxes of sand transport during a neap-spring cycle (18/06 to 17/07). The calculation was made for both tidal current measurements recorded at station WCM1 and WCM2 and are shown on Figures 3.22a and b, respectively. The components of the currents

were resolved parallel to the major axis of the tidal ellipse (fluxes in the flood direction are considered to be positive, while those in the ebb direction are considered to be negative).

Figure 3.22a shows the results at Helwick Passage site. Tidal current derived sand fluxes show a great variability in magnitude, ranging between 0.47 $kg.m^{-1}.s^{-1}$ and -0.57 $kg.m^{-1}.s^{-1}$. The average calculated over the neap-spring cycle (18/06 to 17/06) is 0.012 $kg.m^{-1}.s^{-1}$. Local flux derived from dune tracking at UTM E413492m, N5710071m

is 0.017 $kg.m^{-1}.s^{-1}$.

Figure 3.22b shows the results at the crest of the bank site. Flood oriented sand fluxes reach a maximum magnitude of 0.037 $kg.m^{-1}.s^{-1}$. Negligible ($1.6x10^{-6}$ $kg.m^{-1}.s^{-1}$) sand is transported in the ebb direction. The average current derived flux is 0.001 $kg.m^{-1}.s^{-1}$. Local value of the dune tracking derived flux at UTM E415203 m, N5709644 m is 0.004 $kg.m^{-1}.s^{-1}$

In both cases, the fluxes derived from the two different methods compare relatively well, as they fall in the same order of magnitude. Discrepancies between both methods may arise due to the assumption employed to compute the fluxes from the dune displacement (Section 1.4.4) or due to the choice of the β parameter in Gadd's method (Equation 1.7). Moreover, differences between the two methods could also be related to processes other than the tidal currents in the sediment transport, such as wave induced currents, as expected near the crest (WCM2 site).

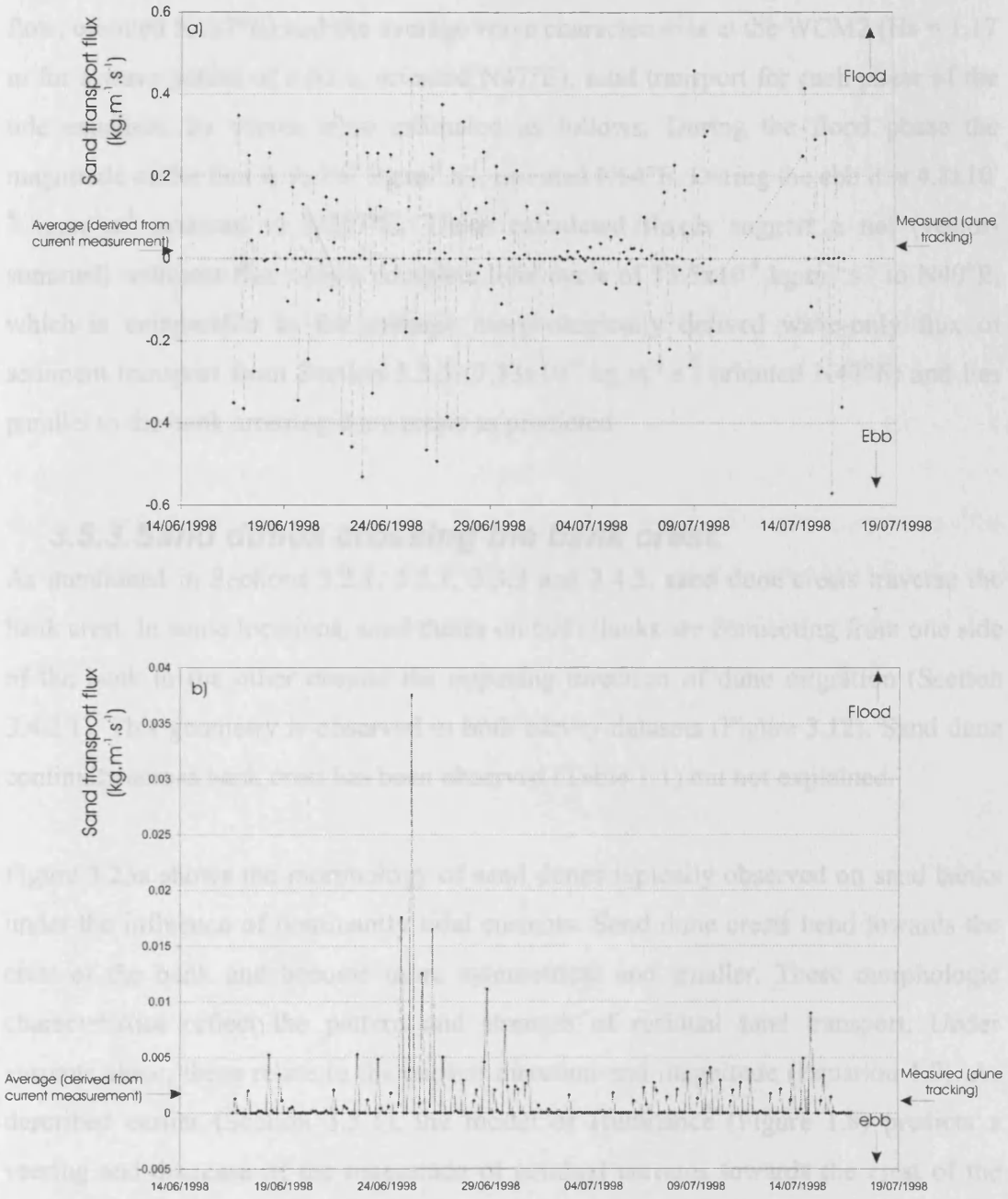

Figure 3.22 Calculated sand transport from the tidal currents using Gadd's formula (Equation 1.7). (a) WCM1 site. (b) WCM2 site. Average of sand fluxes derived from the current measurements over a lunar cycle are compared with the local sand flux derived from dune tracking (see text for details).

Wave-driven transport must be considered at the crest of the bank. Using the method described in Section 1.2.2, the sediment transport flux was estimated for the combined action of tidal currents and waves. An estimate of the mixed tide and wave current sand transport can be calculated considering the average tidal conditions (U_{100} = 0.09

$m.s^{-1}$ during the ebb flow, oriented N207°E and U_{100} = 0.175 $m.s^{-1}$ during the flood flow, oriented N117°E) and the average wave characteristics at the WCM2 (Hs = 1.17 m for a wave period of 6.02 s, oriented N47°E), sand transport for each phase of the tide enhanced by waves were estimated as follows. During the flood phase the magnitude of the flux is $9x10^{-4}$ $kg.m^{-1}.s^{-1}$, oriented N64°E. During the ebb it is $4.8x10^{-4}$ $kg.m^{-1}.s^{-1}$ oriented to N237°E. These calculated fluxes suggest a net (vector-summed) sediment flux over a complete tidal cycle of $13.5x10^{-4}$ $kg.m^{-1}.s^{-1}$ to N40°E, which is comparable to the average morphologically derived wave-only flux of sediment transport from Section 3.3.3 ($7.33x10^{-4}$ $kg.m^{-1}.s^{-1}$ oriented N47°E) and lies parallel to the bank crossing dune crests as predicted.

3.5.3. Sand dunes crossing the bank crest

As mentioned in Sections 3.2.1, 3.3.1, 3.3.3 and 3.4.3, sand dune crests traverse the bank crest. In some locations, sand dunes on both flanks are connecting from one side of the bank to the other despite the opposing direction of dune migration (Section 3.4.2.1). This geometry is observed in both survey datasets (Figure 3.12). Sand dune continuity across bank crest has been observed (Table 1.1) but not explained.

Figure 3.23a shows the morphology of sand dunes typically observed on sand banks under the influence of dominantly tidal currents. Sand dune crests bend towards the crest of the bank and become more symmetrical and smaller. These morphologic characteristics reflect the pattern and strength of residual sand transport. Under currents alone, these relate to the current direction and magnitude (Equation 1.7). As described earlier (Section 3.5.1), the model of Huthnance (Figure 1.8) predicts a veering and decrease of the magnitude of residual currents towards the crest of the bank. Hence the residual sand transport vectors will veer and decrease in magnitude towards the crest of the bank where there lies a zone of bedload convergence. As observed by several authors (Lees, 1983; Houthuys et al., 1994; Vincent et al., 1998; Reynaud et al., 1999a), waves can erode dunes at the crest of banks depending on their direction of propagation with respect to the tidal current, leading to a smooth morphology.

Figure 3.23b presents a conceptual model to explain the bank-crossing sand dunes as the result of the combined effect of tidal and waves currents. As for Figure 3.23a, sand dunes bend towards the crest of the bank in response to the veering tidal currents. Sand transport on the uppermost part of the bank is subject to the mixed influence of tide and wave currents. The net (tidal and waves) sand transport vector for an average tide oriented to N40°E results in elongation of dune crests as shown by the dashed lines on Figure 3.23b (step 1). A wave-induced current channelling effect has been proposed by McCave and Langhorne (1982) to explain small dunes (megaripples, H=0.6 m) crossing the tip of Haisborough Sand in the southern North Sea. Such a mechanism would also promote sand transport parallel to dune crests here because waves propagate parallel to them (Figure 3.20). It is speculated that these mechanisms of both stretching of the dune and channelling sediment transport parallel to sand dunes lead continually to an elongation of dune crests towards the bank crest (step 1) and their connection to dunes on the opposite flank as shown on Figure 3.23b (step 2). In some cases (step 3), sand dunes bifurcate over the crest of the bank which may be a morphological evidence of ongoing connections or disconnections

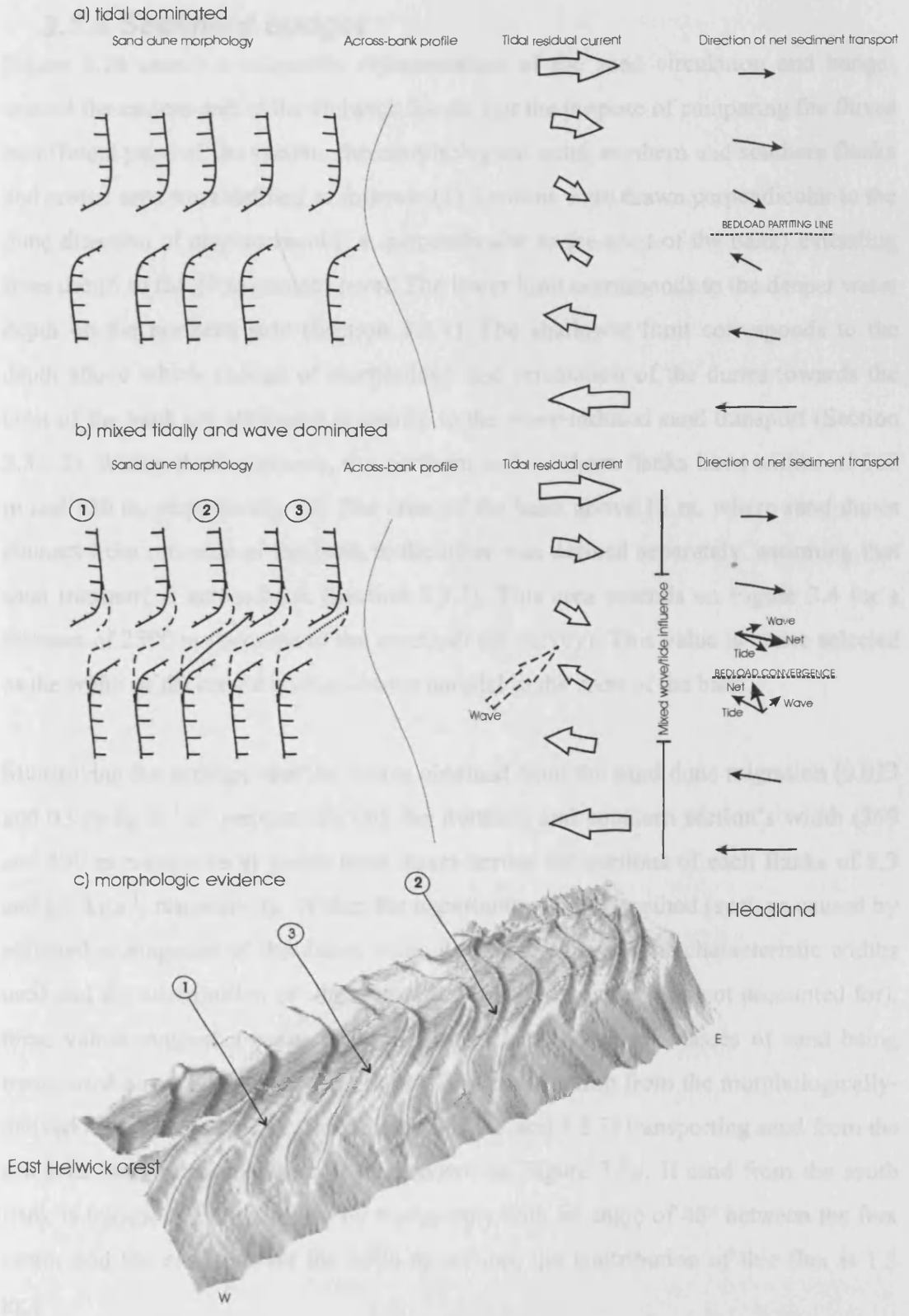

Figure 3.23 Conceptual model for how wave-induced sand-transport leads to dunes crossing over the crest of Helwick Sands. (a) Commonly observed configuration on other sandbanks (barb lines represent the direction of the dune stoss slope). (b) Proposed model for East Helwick Sands. Dashed lines represent the dune crest displacement due to the combined effect of tide and wave on the sediment transport. Dotted lines represent the dune crest stretching induced by channelling effects of the waves. (c) Morphological evidence supporting the model.

3.5.4. Sediment budget

Figure 3.24 shows a schematic representation of the sand circulation and budget around the eastern end of the Helwick Sands. For the purpose of comparing the fluxes in different parts of the system, the morphological units, northern and southern flanks and crestal area were defined as follows. (1) Sections were drawn perpendicular to the dune direction of displacement (i.e. perpendicular to the crest of the bank) extending from the 15 to the 27 m contour level. The lower limit corresponds to the deeper water depth on the northern side (Section 3.2.1). The shallower limit corresponds to the depth above which change of morphology and orientation of the dunes towards the crest of the bank are attributed primarily to the wave-induced sand transport (Section 3.3.1.2). Within these contours, the northern and southern flanks have widths of 360 m and 330 m, respectively. (2) The crest of the bank above 15 m, where sand dunes connect from one side of the bank to the other was defined separately, assuming that sand transport is across-bank (Section 3.5.3). This area extends on Figure 3.4 for a distance of 2500 m (because of the extent of the survey). This value is hence selected as the width of the crestal section drawn parallel to the crest of the bank.

Multiplying the average specific fluxes obtained from the sand dune migration (0.023 and 0.026 $kg.m^{-1}.s^{-1}$ respectively) by the northern and southern section's width (360 and 330 m respectively) yields total fluxes across the sections of each flanks of 8.3 and 8.6 $kg.s^{-1}$, respectively. Within the uncertainties of the method (such as caused by assumed propagation of the dunes without volume changes, the characteristic widths used and the contribution of the suspended load to transport flux not accounted for), these values suggest a balanced sand flux with nearly equal masses of sand being transported along each of the two flanks. The contribution from the morphologically-derived across-bank specific flux (Sections 3.3.3 and 3.5.2) transporting sand from the southern flank to the northern is also shown on Figure 3.24. If sand from the south flank is transported to the north by waves only with an angle of 46° between the flux vector and the crest, across the 2500 m section, the contribution of this flux is 1.3 $kg.s^{-1}$.

From this model and the pattern of sediment transport presented in this chapter, it is therefore argued that the eastern part of Helwick Sands is maintained in dynamic equilibrium by dominantly tidal current sand transport along the flanks of the bank.

Across-bank wave-induced sand transport provides sand from the southern flank to the northern one. However, this contribution in the sand transport must be balanced to maintain the geometry of the bank and prevent the infilling of the Helwick passage. Morphological evidence of sand returning to the southern flank can be seen in the Helwick Passage where the sand dunes tend to strongly veer with their crest nearly parallel to the crest of the bank. This shows the occurrence of the flood oriented dominated transport at the eastern end of the bank having a southerly component as shown on Figure 3.19.

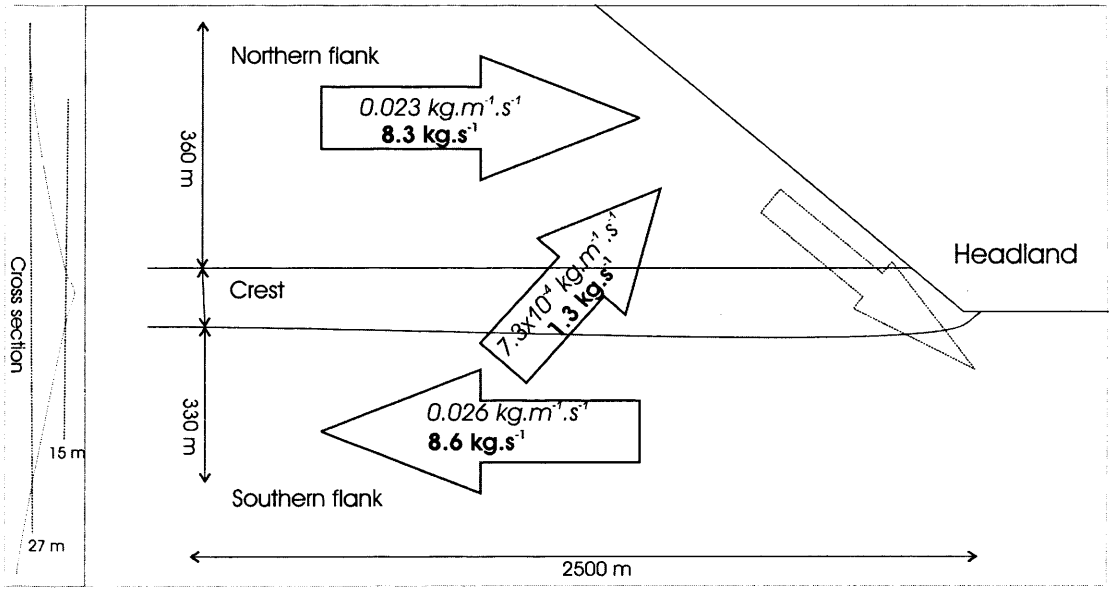

Figure 3.24 Sediment budget near the connection of the bank with the headland. Bold values are averaged specific fluxes (values in italic) multiplied by the width of section of the different morphologic units (northern and southern flank, crest). See text for the measurement of the width of these sections.

3.5.5. Spatial erosion and deposition trends

Spatial variations in transport flux suggest that deposition and erosion must occur to conserve sediment mass as shown by the "continuity relation" (Allen, 1997), given as follows.

$$\frac{\partial z}{\partial t} = -\nabla.\vec{q} \qquad \text{Equation 3.21}$$

where ∇ is the divergence operator $(\frac{\partial}{\partial x}\vec{i} + \frac{\partial}{\partial y}\vec{j})$ and q is expressed as the volumetric sand flux.

Spatial divergence of the sediment transport specific flux derived in Section 3.3.2.2.3 leads to erosion or deposition as shown on Figure 3.25c. This figure was obtained in

two steps. In the first step, the eastern (x-axis) and northern (y-axis) components of the specific sediment flux vector field from Section 3.3.2.2.3 and 3.3.3 were interpolated onto a grid with a 167 m resolution (chosen as the maximum sand dune spacing) using a triangulation interpolation scheme (Wessel and Smith, 1998). This scheme performs a Delauney triangulation, which connect data points by triangles that are as close to equilateral triangles as possible. Interpolated grid data are then linearly calculated between the three data points defining each triangle. In the second step, the x-oriented and y-oriented derivatives of flux were calculated from the interpolated gridded data.

Ninety percent of the rates of change between the data lie between -0.4 and 0.4 $mm.d^{-1}$. The outliers and high spatial variability spatial observed on Figure 3.25c are due primarily to the sensitivity of the derivative to the rapid changes of magnitude and direction of the sediment flux vectors. However this spatial variability is indicative of the transient nature of sand transport and erosion, which may be related to transient features of the flow near Port Eynon Point headland (eddies in the tidal currents such as observed at the lee of Portland Bill by Bastos et al. (2004) and oscillations due to the surface waves). In general, patches of sediment convergence (deposition) can be seen at the crest (+0.1 $mm.d^{-1}$ at UTM E414860 m, N5709506 m), in the eastern limit of the Passage (+0.6 $mm.d^{-1}$ at UTM E415361 m, N5709637 m and 0.22 $mm.d^{-1}$ at E414192 m, N5709768 m), along the southern flank (+0.8 $mm.d^{-1}$ at UTM E415027m, N5709113 m and +1.36 $mm.d^{-1}$ at UTM E413357 m, N5709375 m). Areas of divergence (erosion) are observed between the areas of deposition: at the crest (-0.15 $mm.d^{-1}$ at UTM E415862 m, N5709375 m), along the northern flank (-0.16 $mm.d^{-1}$ at UTM E413524 m, N5709768 m) and in the Helwick Passage area (-0.45 $mm.d^{-1}$ at UTM E416196E, N5709367m) and along the southern flank (-0.3 $mm.d^{-1}$ at UTM E415528 m, N5709375 m). Average erosion in the area chosen for Figure 3.25c is +0.3 $mm.d^{-1}$ compared with the average deposition of -0.2 $mm.d^{-1}$. The average rate of change is +0.04 $mm.d^{-1}$, which confirms the idea that the approach of the bank with the shore is roughly in a state of dynamic equilibrium.

Figure 3.25c can be compared with 3.24b which shows the bathymetric difference between the single-beam dataset provided by Llannelli Sand Dredging Ltd. (sounding locations plotted on Figure 3.24a along with waterdepth contours), undertaken on the 1st of September 2001 and the second multibeam datasets (acquired 354 days later).

Each of the bathymetric datasets was first block-averaged (within an area of 167 m x 167 m, chosen to allow the comparison with Figure 3.25c). Triangular interpolation was also used to create regular spaced grids of the block-averaged bathymetry datasets. To allow a comparison with the divergence map (Figure 3.25c), the difference grid was divided by the number of days between the surveys to provide a grid of daily changes. Average erosion for the considered area is 0.47 $mm.d^{-1}$ while average deposition is 0.33 $mm.d^{-1}$. Figure 3.25b shows a general pattern of positive difference (deposition) at the crest of the bank with an average rate of +0.3 $mm.d^{-1}$ above the 10 m water-depth contour line. An area of sand deposition was also observed in the Helwick Passage with changes of +0.2 $mm.d^{-1}$ (UTM N416196 m, E5709637 m). Areas of negative differences (erosion) are observed along both feet of the bank with typical values of -0.5 $mm.d^{-1}$.

Figure 3.25d shows the residual grid computed from the difference between the grids computed for 3.25b (daily averaged bathymetric difference) and 3.24c (daily averaged changes computed using the continuity equation and the measured fluxes). The relative difference in magnitude (absolute value) of bathymetric changes in the grids of Figures 3.25b and c, rarely differs by more than 10%. However some major differences between the two grids are observed primarily in areas where it was not possible to track sand dunes and where interpolation led to undefined results, as near the crest of the bank at UTM E414200 m, N5709600 m or near the eastern end of the south flank at UTM E 414600 m, N5709200 m. In areas where it was possible to track sand dunes, differences in the distribution of patterns of deposition and erosion can be partly explained by the accuracy of the method used to track the dunes and to compute the associated sand flux. The variation in the volume of the sand dunes, due partly to sand bypassing the dunes (negative difference) or deposition from suspended load (positive difference), which was neglected by the dune tracking method (Section 1.4.4) can also be a reason of the difference between 3.25b and 3.25c. Negative differences (Figure 3.25d) are observed along the flanks of the bank (-0.3 $mm.d^{-1}$ at UTM E413524 m, N5709899 m on the north; -0.5 $mm.d^{-1}$ at UTM E413691 m, N5709113 m on the south), while positive residue is observed at the crest of the bank (+0.3 $mm.d^{-1}$ averaged for values above the 10 m water depth contour). Figure 3.15, presenting the relative cross-sectional changes between paired dunes, shows some similarities with Figure 3.25d. In both case, positive values are essentially observed near the crest of the bank down to 10 to 15 m, negative values are primarily observed

near the eastern end of the crest of the bank in the Helwick Passage and in the southwest corner of the surveyed area. These similarities suggest that gain or loss of volume of individual sand dunes between the surveys is the major source of errors in the determination of sand dune associated transport fluxes.

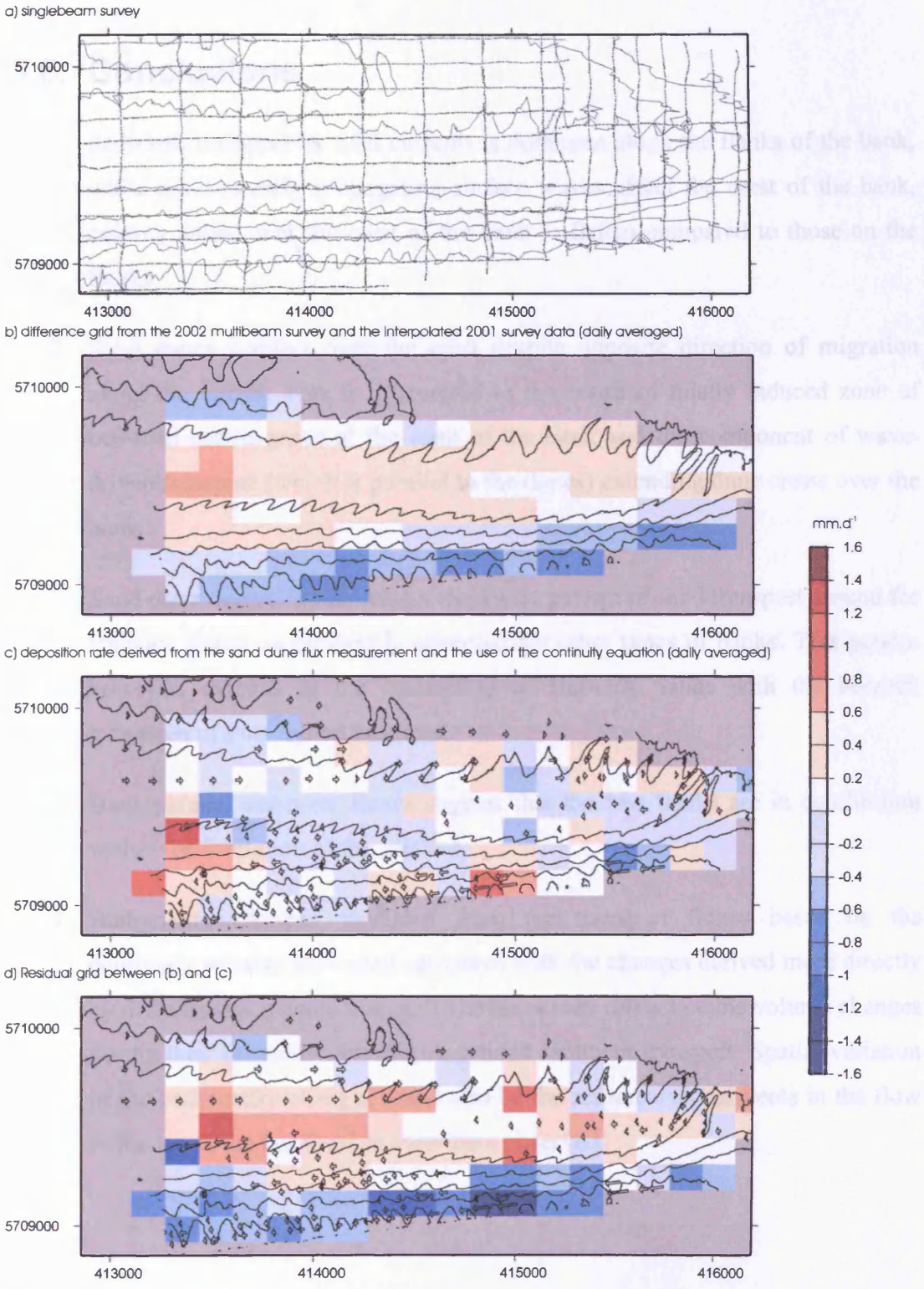

Figure 3.25 Comparison of erosion and deposition rates computed from the difference of bathymetric data grids (b) with rates computed using the continuity equation from the specific flux of sediment transport (c). Grid in (b) was computed from the difference of the 2002 multibeam survey data (Figure 3.2) and 2001 Singlebeam survey data (provided by Llannelli Sand Dredging Ltd.). Soundings location and interpolated 10, 15, 20, 25, 30 and 35m water-depth contour lines are represented on (a).Vectors on (c) and (d) represent sand fluxes reproduced from Figure 3.16. Grey areas denote the absence of data. Contour lines of the East Helwick Sands are displayed at 10, 15, 20, 25, 30 and 35 m on (b), (c) and (d).

3.6. Conclusions

1. Sediment transport by tidal currents is dominant along the flanks of the bank, while north-easterly propagating surface waves affect the crest of the bank, causing dunes over the crest of the bank to flatten compared to those on the flanks.

2. Sand dunes connect over the crest despite opposite direction of migration along the flanks. This is interpreted as the result of tidally induced zone of bed-load convergence at the crest of the bank and the component of wave-driven transport (which is parallel to the dunes) extending dune crests over the bank.

3. Sand dune migrations indicate a clockwise pattern of sand transport around the Helwick Sands as previously observed for other types of banks. This pattern however, extends to the connection of Helwick Sands with the bedrock extension of Port Eynon headland.

4. Bank-parallel sediment fluxes suggest that the two flanks are in equilibrium within the limitation of the method.

5. Bathymetry changes predicted from the transport fluxes based on the continuity relation are varied compared with the changes derived more directly by differentiating two surveys. Differences may relate to dune volume changes during their migration and the suspended sediment transport. Spatial variation of the bathymetry changes could also be the response to transients in the flow in the lee of the headland as elsewhere observed.

Chapter 4.

Morphology and sediment dynamics of East Nash Sands

4.1. Introduction

Owing to its easternmost location (Figure 1.12), Nash Sands is subject to stronger tidal current and smaller waves than the other linear banner banks of the Bristol Channel. However, its shallower bathymetry also leads to an enhanced role of the tidal and wave currents than might otherwise be expected. These environmental conditions confer on Nash Sands an intense sand transport setting (Pethick and Thompson, 2002). Following a similar approach to the previous chapter, this chapter will present dune morphological and kinematic evidence from repeated bathymetric surveys (Figure 1.18) showing how tides and waves transport sand around East Nash.

4.2. Large scale morphology of Nash Sands

Nash Sands is a 13.7 km long sand bank. Its crest runs WNW (average orientation N285°E) from the sub-tidal outcrop of Nash Point (Figure 1.18). In plan view, Nash bank can be divided into three sectors: East Nash, Middle Nash and West Nash. The crestal orientation of the three different parts varies from N297°E for East Nash, N261°E Middle Nash and N285°E for West Nash. The bank is widest in the middle sector (1.2 km). In cross-section, the bank is asymmetrical particularly in the eastern sector. Here, the southern slope is steepest where it coincides with the southward convex axis of the bank.

Figure 4.1a shows the bathymetry of the studied area (grey shaded image). The image represents data from two surveys acquired in 2002 (16-17-18 August 2002 and 4 September 2002, see Section 1.6.2). Water depths range between 15 m below chart datum to 3 m above chart datum. A depression between the coast and the bank defines the northern limit of the bank. The relatively flat seabed, including several outcrops of bedrock at the southern border of the surveyed area (Figure 4.1b), defines the southern limit of the bank. The adjacent bedrock platform at Nash Point is exposed during low tide and comprises Jurassic strata (Bourne and Willemse, 2001) which probably continue under Nash Sands. Limited sub-bottom profiling data (Turner, 1976) suggests that the underlying bedrock structure does not determine the position of the bank. Turner (1976) suggested that Nash Bank formed during the Holocene marine transgression, but considering the elevation of the sub-Holocene surface, it is more likely that the area became submerged at around 7000 years BP (Figure 1.13). Based

on geochemical and micro-paleontological data, Culver (1976) and Hamilton et al. (1979) argued that the sand was probably winnowed from glacial tills during the Holocene marine transgression. Hence, the bank may have originated and grown during the deceleration of sea level rise, as the water depths and tides became progressively established post 7000 years BP (Figure 1.13).

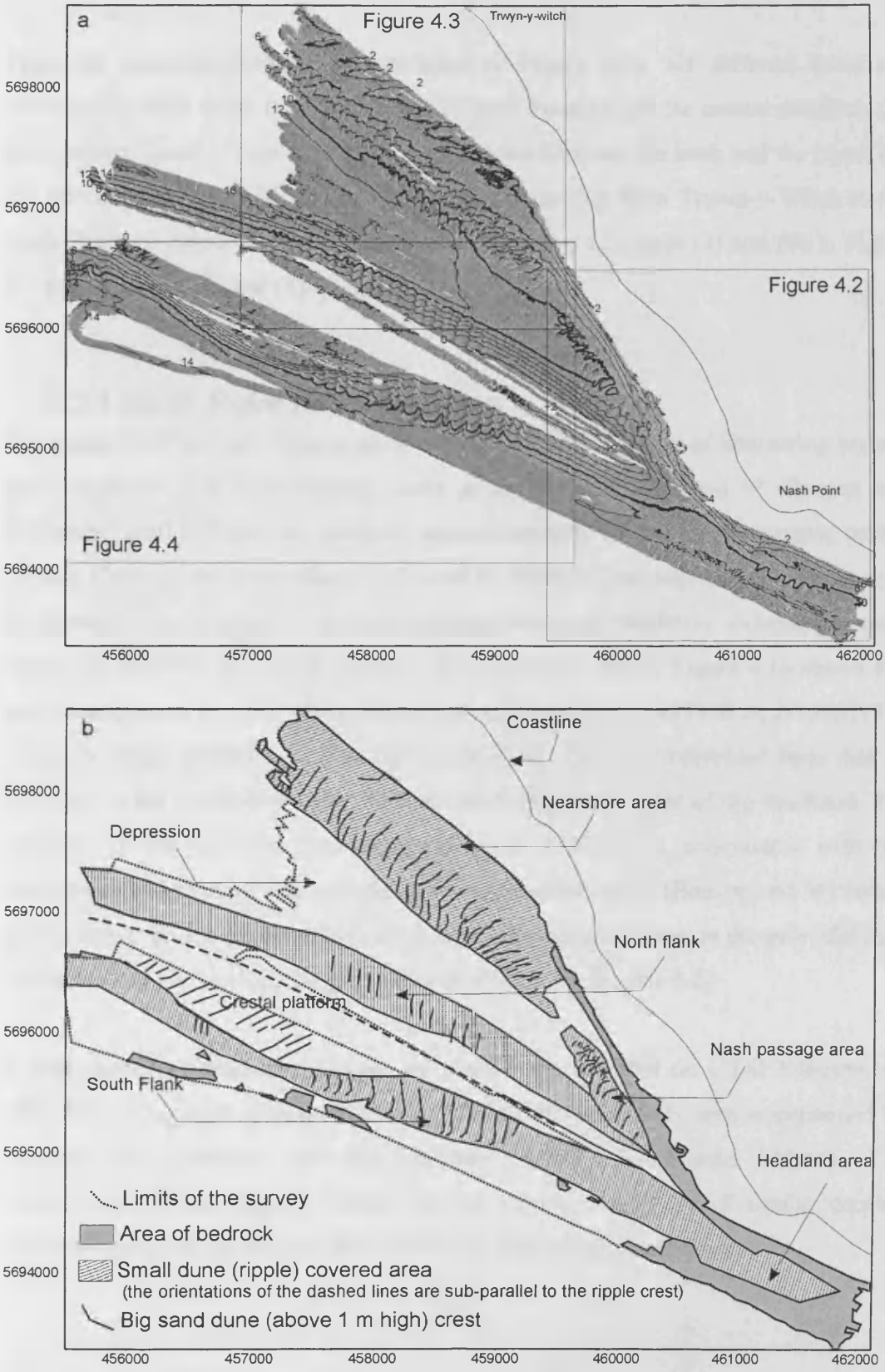

Figure 4.1 Large-scale morphology of East Nash. (a) Gray shaded multibeam survey (composite of the two surveys undertaken in 2002). Water-depth is given at the extremities of the contour lines. They are referred to as below the Chart Datum, otherwise above Chart Datum if marked with "+" sign. (b) Morphological summary.

From the geomorphological interpretation of Figure 4.1b, six different areas are defined: (1) Nash Point headland area, (2) Nash Passage, (3) the crestal platform, (4) the southern flank, (5) the bathymetric depression between the bank and the coast, (6) the northern flank and (7) the nearshore area extending from Trywn-y-Witch to the Nash Passage. Areas (1) and (2) are shown in Figure 4.2, areas (3) and (4) in Figure 4.3 and areas (5), (6) and (7) in Figure 4.4.

4.2.1. Nash Point headland area

The coastal cliff at Nash Point is composed of ~1 m thick layers of alternating beds of grey limestone and shale dipping south at an angle of less than 5° (Bourne and Willemse, 2001). These are shallow marine deposits of the lower Jurassic period (British Geological Survey Sheet 51°N–04°W, Bristol Channel). The inter-tidal zone is characterised by shallow seaward-dipping wave-cut platforms extending over a horizontal distance of ~100 m (Bourne and Willemse, 2001). Figure 4.1a shows that they extend down to ~8 m below Chart Datum (from UTM E459500 m, N5696713 m to E462024 m, N5693911 m to the south). The edges of individual beds can be followed in the multibeam sonar data obtained from both sides of the headland. The thickness of the sub-tidal beds ranges between 1 and 2 m, comparable with bed thicknesses observed in the inter-tidal and supra-tidal zones (Bourne and Willemse, 2001). However, the extent of the wave-cut platforms is narrower in the sub-tidal zone than in its sub-aerial zone, ranging between 30 to 60 m (Figure 4.2).

A thin veneer of sand to the south of Nash Point (centred on UTM E461096 m, N5693993 m) occurs at water-depths of 8 to 12 m. This sandy area is contained by southern and northern wave-cut platforms within the Liassic bedrock. The morphology of the bedding within these platforms, which are of similar dipping direction and gradient, suggest their continuity beneath the sand veneer.

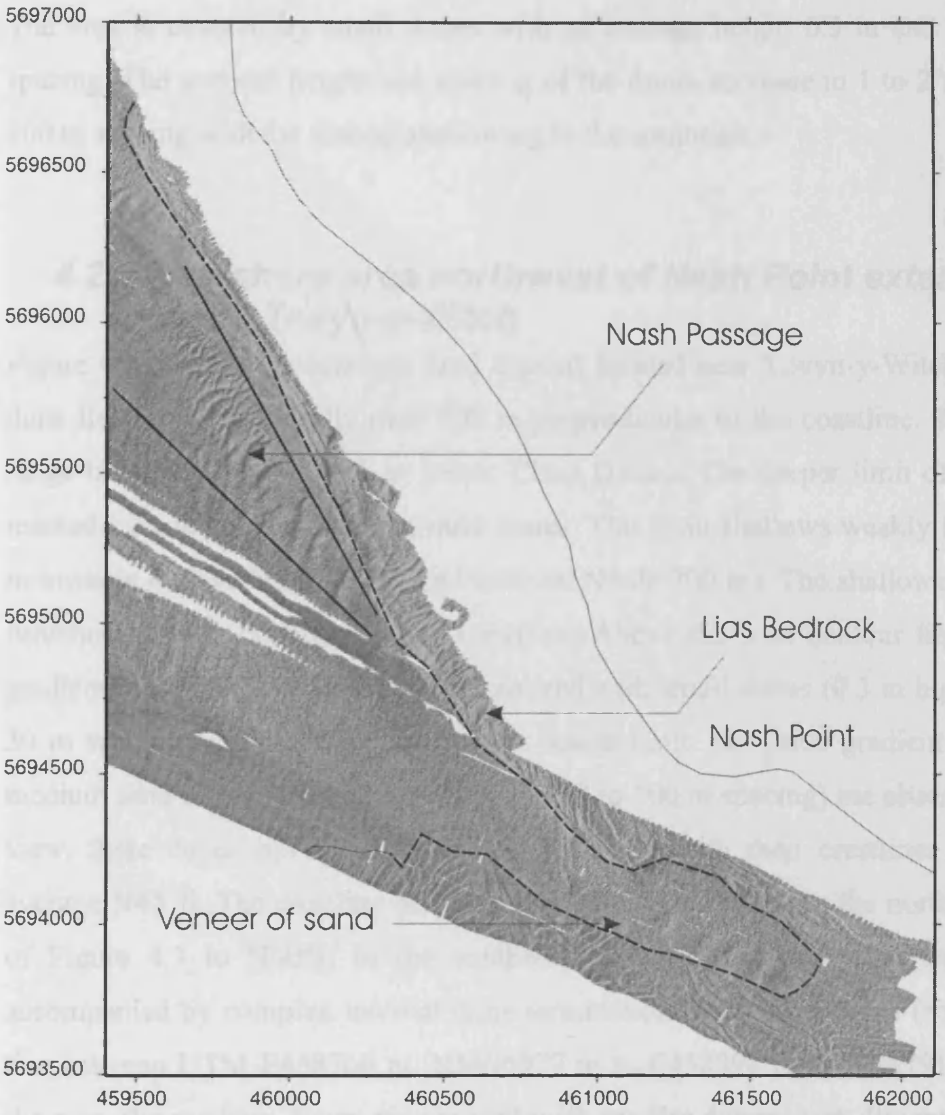

Figure 4.2 Shaded relief of the Nash Point headland and associated outcrops (delimited by dashed lines) and Nash Passage (enclosed by the two solid straight lines).

4.2.2. Nash Passage

Nash passage is funnel shaped. It narrows from northwest to southeast and is bounded by the northern flank of Nash Sands to the southwest and by the coastline to the northeast. Its lateral extent (between the bank and the limit of Lias outcrops) narrows from 300 m at its northern border (UTM E459460 m, N5695734 m to E459735 m, N5696075 m) to 60 m at its southern border (E460132 m, N5695171 m to E460295 m, N5695272 m). Simultaneously, the bathymetry rises from 11 m to 8 m depth along the axis of the passage.

The area is covered by small dunes with an average height 0.5 m and 30 to 50 m spacing. The average height and spacing of the dunes increase to 1 to 2 m and 80 to 100 m spacing with the seabed shallowing to the southeast.

4.2.3. Nearshore area northwest of Nash Point extending towards Trwyn-y-Witch

Figure 4.3 shows the nearshore sand deposit located near Trwyn-y-Witch. This sand dune field extends laterally over 700 m perpendicular to the coastline. Water-depths range between 0 m and ~11 m below Chart Datum. The deeper limit of this area is marked by a depression without sand dunes. This limit shallows weakly from 11 to 9 m towards the southeast (UTM E459500 m, N5696700 m). The shallower part of the nearshore area is bounded by the coastline. Above the 3 m contour line, the slope gradient is low (0.5°) and is densely covered with small dunes (0.3 m high and 10 to 30 m spacing). Below 3 m down to its lower limit, the slope gradient is 1.3° and medium sand dunes (1.5 to 2.5 m high and 50 to 100 m spacing) are observed. In plan view, these dunes have a slight crescentic shape with their crestlines oriented on average N45°E. The crestline orientations rotate from N38°E in the northwest corner of Figure 4.3 to N60°E in the southwest corner. This change in orientation is accompanied by complex internal dune terminations and bifurcations (southeast of a line between UTM E458766 m, N5696977 m to E458898 m, N5696791 m). Within the area, the medium dunes are covered with smaller dunes, with dimensions similar to those observed at depths above 3 m. Below 11 m, these medium sand dunes and their associated smaller dunes terminate abruptly.

4.2.4. Bathymetric depression between the bank and the coast

This area (Figure 4.3) is characterised by a relatively featureless seabed where water depth ranges between 10 and 14 m. It is located between the nearshore sand dune field (previously described) and the northern flank of Nash Sands. Limited occurrences of bedrock outcrops (UTM E459567 m, N5696082 m) are visible in the deepest part of this area. To the east, this area shallows (10 m) towards Nash Passage.

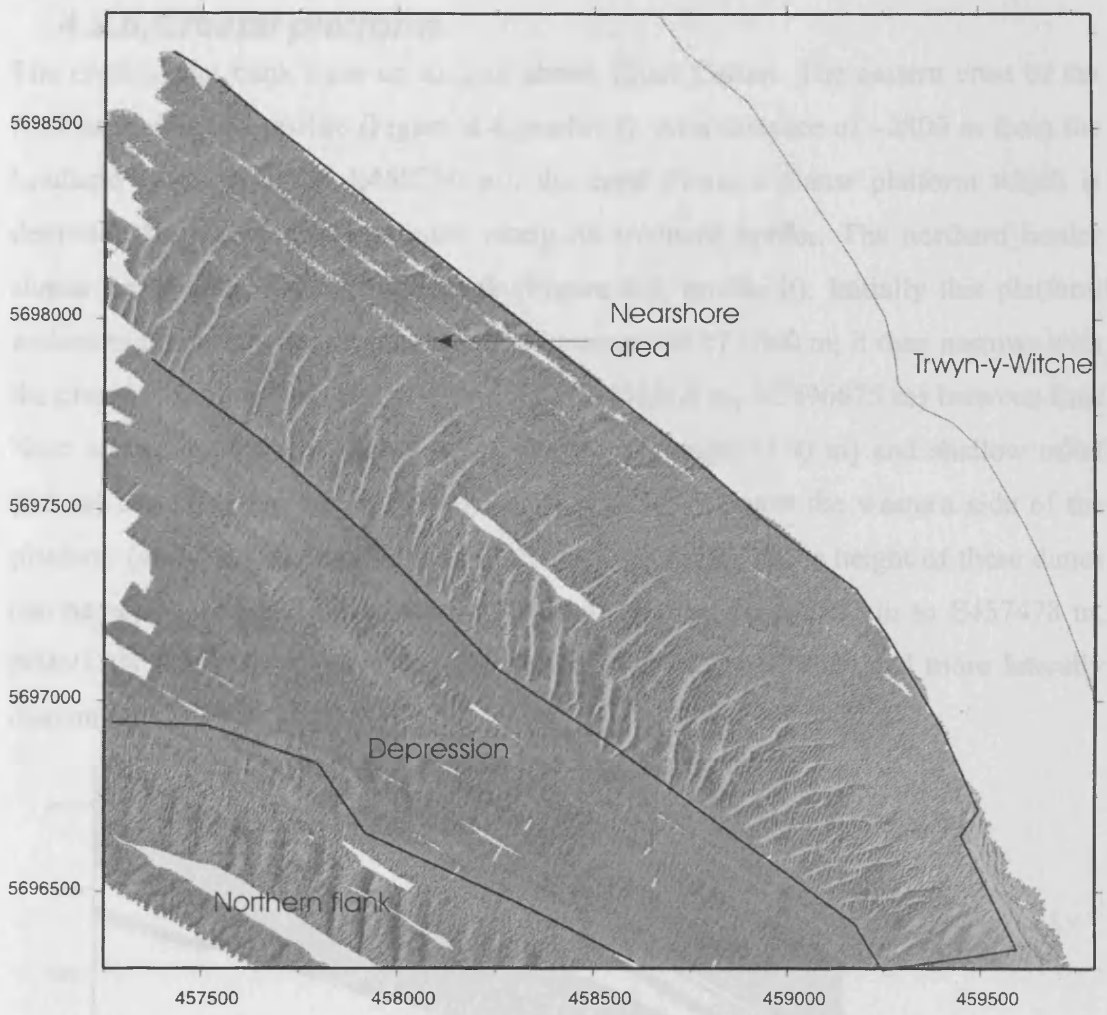

Figure 4.3 Nearshore sand dune fields near Trwyn-y-Witch and Nash Passage, separated from the north flank of East Nash by a featureless depression showing limited occurrences of bedrock outcrops.

4.2.5. Northern flank of East Nash

North of a crestal platform (which will be described in the next Section) the bathymetry of the bank deepens gently. The upper limit (also the southern limit of the area) is defined by a progressive increase in the slope gradient from 0.5° (at the crestal platform) to 2°. Small and medium (1 to 2 m high and 90 to 120 m spacing) sand dunes cover this flank. The dune crests are orientated on average N10°E. The northern flank of Nash Sands extends down to depths of about 12 m. The limit between the flank and the depression is defined by the change of texture of the seafloor, where small dunes tend to smooth out and disappear.

4.2.6. Crestal platform

The crest of the bank rises up to 2 m above Chart Datum. The eastern crest of the bank is rounded in profile (Figure 4.4, profile i). At a distance of ~2800 m from the headland (west of UTM E458250 m), the crest forms a planar platform which is delimitated by a sharp escarpment along its southern border. The northern border slopes gently onto the northern flank (Figure 4.4, profile ii). Initially this platform widens to the west where it attains a maximum width of ~800 m; it then narrows with the change in orientation of the crest (UTM E455860 m, N5696675 m) between East Nash and Middle Nash (Figure 4.1a). Long wavelength (100 m) and shallow relief (0.5 m) dunes with a NNE-SSW orientation (N50°E) cover the western side of the platform (see cross-section (iii) in Figure 4.4). A change in the height of these dunes can be seen east of a line between UTM E457780 m, N5695893 m to E457478 m, N5695708 m, where these dunes become smaller (0.2 to 0.3 m) and more laterally discontinuous.

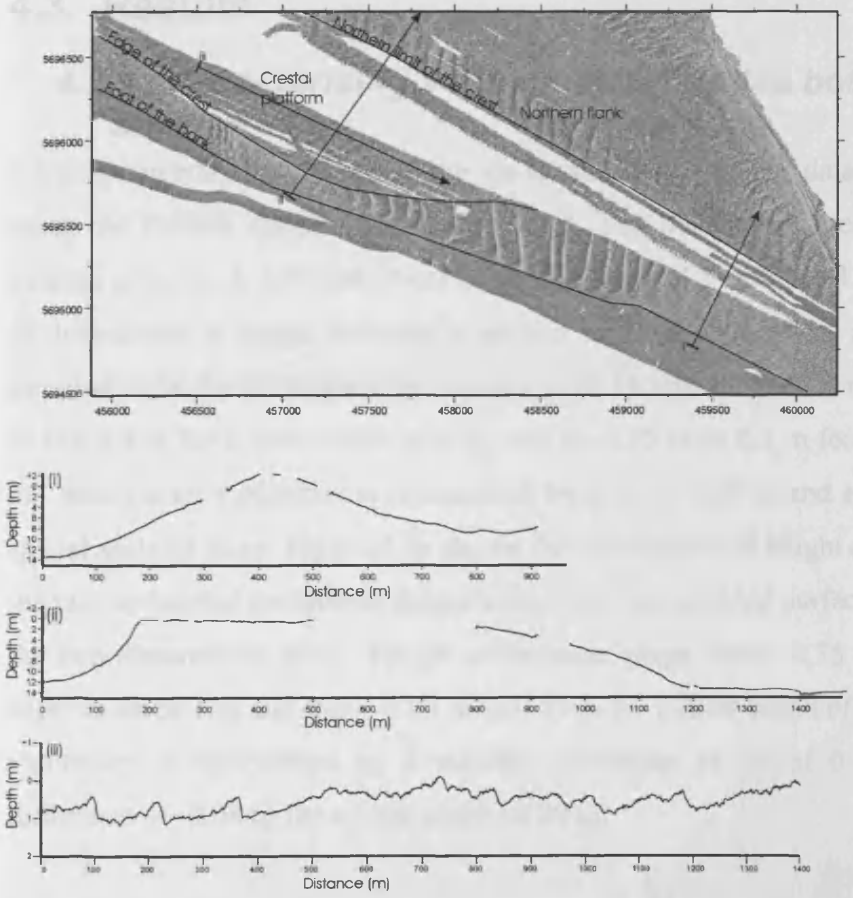

Figure 4.4 Northern and southern flanks of East Nash, together with the crestal platform area. Profiles (i) and (ii) show the morphological changes of the crest with distance from headland. (i) Rounded crest in the vicinity of the headland. (ii) Wide crestal platform at ~2800 m from the headland. Waterdepths are below Chart Datum unless a "+" sign is indicated (representing waterdepths above Chart Datum).

4.2.7. Southern flank of East Nash

The northerly limit of the southern flank is delimited by the edge of the crestal platform. Within 50 m of the edge of the bank the upper flank has an average gradient of 6°. The slope angle diminishes with depth to 2.5°. The southerly limit of the flank lies between 10 and 11 m depth, below which the seafloor becomes flat and featureless. Well-defined large dunes (up to 4 m) together with their associated smaller dunes cover parts of the southern flank. The widening of the crestal platform is associated with a decrease of the height of the large dunes on the southern flank. In some areas, where the crestal platform attains its maximum width, such as near UTM E457500 m, N5695550 m, dunes are absent. On the eastern side of the area, closer to the headland area (UTM E459000 m, N5695000 m), small dunes with heights ranging between 0.2 to 0.4 m and spacing of 20 m cover the southern flank.

4.3. Results

4.3.1. Characterising vertical uncertainties between the surveys

Vertical uncertainties between the co-located bathymetric datasets were assessed using the method detailed in Section 2.3.2. The benchmark area is the submerged outcrop of bedrock off Nash Point (insert of Figure 4.5). Figure 4.5a shows the decay of differences in height between a section of single-beam and a coincident profile sampled from the multibeam bathymetry grid. Height difference ranges between -0.3 m and 0.4 m for a filter width of 1 m, and to -0.05 m to 0.1 m for a filter width of 80 m. Small-scale variability is represented by a 2σ of 0.25 m and a mean of 0.01 for a spatial scale of 20 m. Figure 4.5b shows the distribution of height differences between the two co-located multibeam datasets derived from gridded surfaces of the data using the two-dimensional filter. Height differences range from -0.35 m to 0.45 m for a filter width of 1 m and from -0.05 m to 0.35 m for a filter width of 100 m. Small-scale variability is represented by a standard deviation of 2σ of 0.17 m and a mean difference of -0.08 m for a filter width of 20 m.

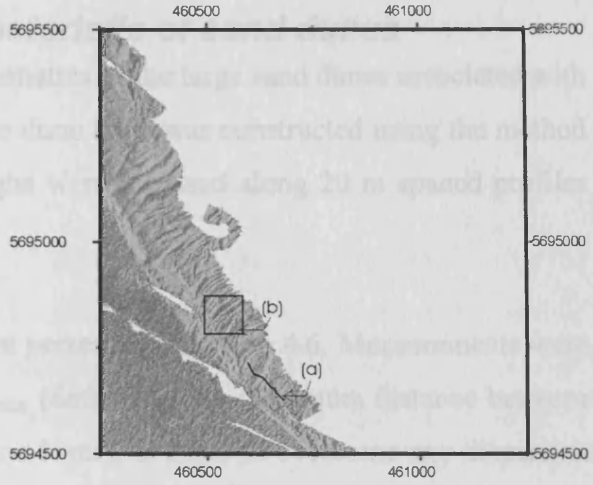

Figure 4.5 Height difference distributions over an area of bedrock outcrop in the vicinity of Nash Point shown on the map. (a) Distribution computed from the 2003 single-beam and a profile obtained by sampling the 2002 multibeam bathymetry grid. (b) Distribution computed from the 17th of August 2002 and 4th of September 2002 multibeam surveys data. The lines on (a) and (b) represent two standard deviations about the mean value.

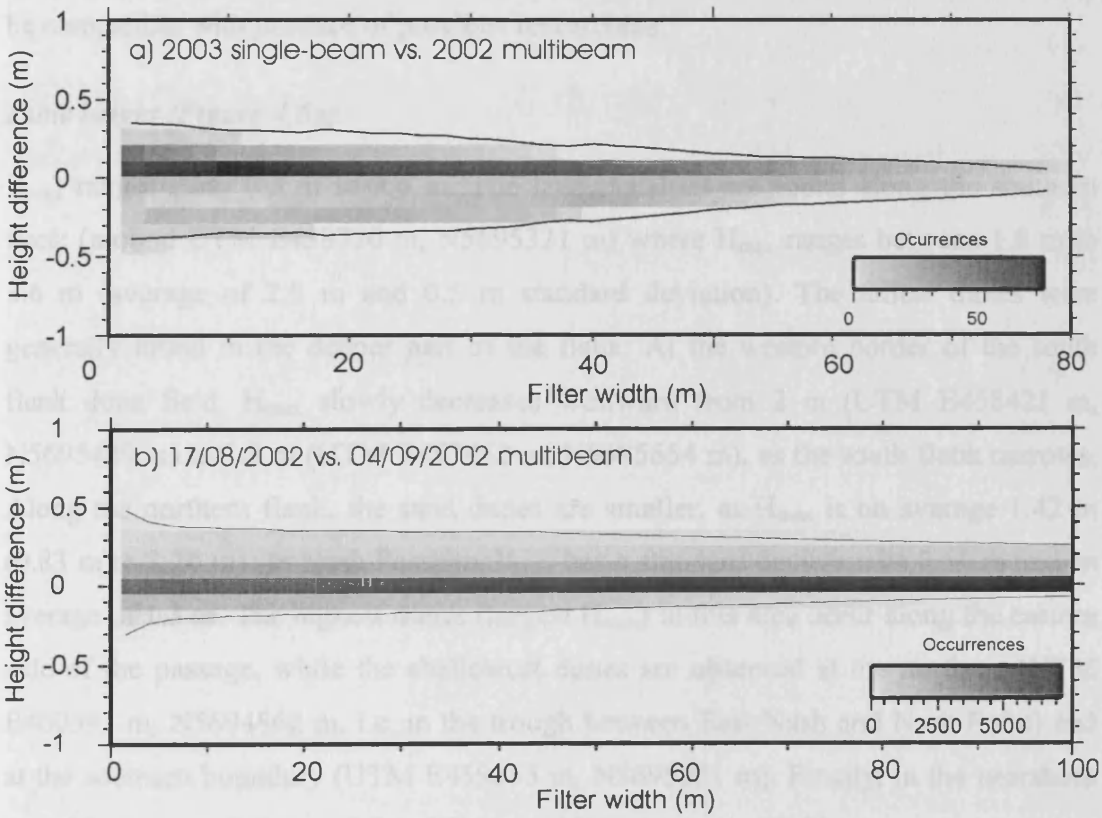

4.3.2. Morphological characteristic of sand dunes

To investigate the morphology and kinematics of the large sand dunes associated with East Nash Sands, the map of the mobile dune layer was constructed using the method described in Section 3.3.1. Dune troughs were digitised along 20 m spaced profiles run perpendicular to the dune crests.

Height, spacing and asymmetry data are presented in Figure 4.6. Measurements were taken at points of maximum height, H_{max} (defined as the maximum distance between the crest and the base of the mobile dune layer), in order to overcome any dispersion of dune characteristics due to the variation of their geometry along their crests and to be compatible with practice of previous researchers.

Dune height (Figure 4.6a)

H_{max} ranges from 0.3 m to 3.6 m. The largest values are found along the southern flank (around UTM E458720 m, N5695321 m) where H_{max} ranges between 1.8 m to 3.6 m (average of 2.9 m and 0.5 m standard deviation). The tallest dunes were generally found in the deeper part of the flank. At the western border of the south flank dune field, H_{max} slowly decreases westward from 2 m (UTM E458421 m, N5695429 m) to 1.8 m (UTM E457452 m, N5695654 m), as the south flank narrows. Along the northern flank, the sand dunes are smaller, as H_{max} is on average 1.42 m (0.83 m to 2.26 m). In Nash Passage, H_{max} has a standard deviation of 0.51 m and an average of 1.3 m. The highest dunes (largest H_{max}) in this area occur along the eastern side of the passage, while the shallowest dunes are observed at the northern (UTM E460391 m, N5694862 m, i.e. in the trough between East Nash and Nash Point) and at the southern boundary (UTM E459655 m, N5695951 m). Finally, in the nearshore area, H_{max} ranges between 0.7 and 3.4 m, with an average of 2.05 m.

Dune spacing (Figure 4.6b)

Dune spacing ranges from 37 m to 200 m. Widely spaced dunes occur along the southern flank, where spacing varies between 66 and 199 m, about an average of 125 m and with a 50 m standard deviation. Along the northern flank, dune spacing ranges between 74 m and 154 m, with an average of 101 m and a standard deviation of 22 m, indicating a relatively uniform spacing. Within the nearshore area, dune spacing

averages 99 m with a 31 m standard deviation. Finally, closely spaced dunes, with an average spacing of 82 m and a 44 m standard deviation, are observed in Nash Passage.

Dune asymmetry index (Figure 4.6c)

The dune asymmetry index (defined in Section 1.4.1) ranges from 0.3 to 6.4. For the dunes along the southern flank, the symmetric index has a maximum of 6.4 and an average of 2.61, indicating a strong asymmetry, which is oriented to the west (N288°E). The average slope angle of stoss faces is 0.87° compared to the average slope angle of lee faces of 2.92°. For the north flank, the asymmetry index is typically 1.44 which indicates somewhat less asymmetric dune profiles, with lee sides facing N111°E. Typical lee face slope angles are 2.15° compared to 0.95° for the stoss slope angles. In Nash Passage, lee faces typically face southeast (N141°E). The average asymmetry index is 1.6, with a maximum of 4.2. Lee and stoss faces have slope angles of 2.7° and 1.5°, respectively. Finally, the nearshore area is characterised by lee faces dipping on average towards N306°E. The asymmetry index increases westward from 0.3 to 6 which indicates an increasing dune asymmetry towards the north. The more symmetrical dune profiles at the southern border of the nearshore area are characterised by lee and stoss slopes angles of 3.17° and 2.31°, respectively. Towards the northern border of the nearshore area the typical strongly asymmetric dune profiles are characterised by a 7.6° lee slope compared to a 1.7° stoss slope angle.

Figure 4.7 shows the relationships between the dune dimensions (H_{max}, L) and their crestal waterdepth (Z) for the four regions of interest. These relationships are essentially indicative of the flow strength and sand supply (Sections 1.4.2 and 3.3.3.2). Figure 4.7a, b, c and d show the relationship between the dune height (H_{max}) and water depth (L). The northern flank data show some agreement with the empirical relation of Yalin (1977), as the empirical linear trend ($H = 0.167Z$ Equation 4.1) lies within the data, but the data do not show the increasing trend. For the south flank and to a lesser extent in the nearshore area, Yalin's relationship slightly underestimates the dune height. Within the Nash Passage area, Yalin's empirical relationship generally overestimates dune heights.

Figure 4.7.e to g shows relationships between dune spacing (L) and crestal water-depth (Z). As with the dune heights, dune spacing was expected to increase with water-depth, as argued by Yalin (1977), who presented a linear relation for this dependency ($L = 6Z$, Equation 4.2). This relationship appears to underestimate the dune spacing for a given waterdepth, except for the Nash Passage. Yalin (1992) and Kostaschuk (2000) argued that turbulent vortices within water flowing over sand dunes are scaled by the waterdepth, which also limits the vertical development of the dunes.

The flatness of the dunes was investigated from the relationship between dune height (H_{max}) and dune spacing (L). Figure 4.7m shows a comparison between the power-law regressions obtained from the datasets (Figure 4.7h to l) and the well established relation of Flemming (2000) ($H_{max} = 0.0667L^{0.8}$) derived from fully developed dunes from marine and river environments (Section 1.4.2). Trends were calculated by least-squares regression of $\log_{10}$(Hmax) on $\log_{10}$(L) (Williams and Kelley, 1998). The summary of these trends on Figure 4.7m shows that Flemming's relation tends to overestimate H_{max} suggesting that sand dunes here have not reached their equilibrium states (Section 1.4.2). Moreover, Flemming (2000) suggested that, in similar riverine and marine conditions, the time needed to attain the equilibrium profile of large or medium dunes takes longer than for small dunes. Thus, the smaller than expected H_{max} could be representative of the finite time taken for dunes to grow as they migrate along the flank, as the trends approach Flemming's relationship for small L.

The exponents in Equation 4.3 indicate the typical flatness of the dunes within each dune field. Flatness increases (steeper to flatter) from the Nash Passage (0.298), to the South flank (0.3603), to the nearshore (0.6449) and to the northern flank (0.9812). Flatter dunes can be the result of wave induced erosion or strong suspended sand deposition. Strongly asymmetric tidal currents, on the contrary, such as those expected along the southern flank and in the Nash Passage (see section 4.5.2) tend to form steeper dunes (Allen, 1968).

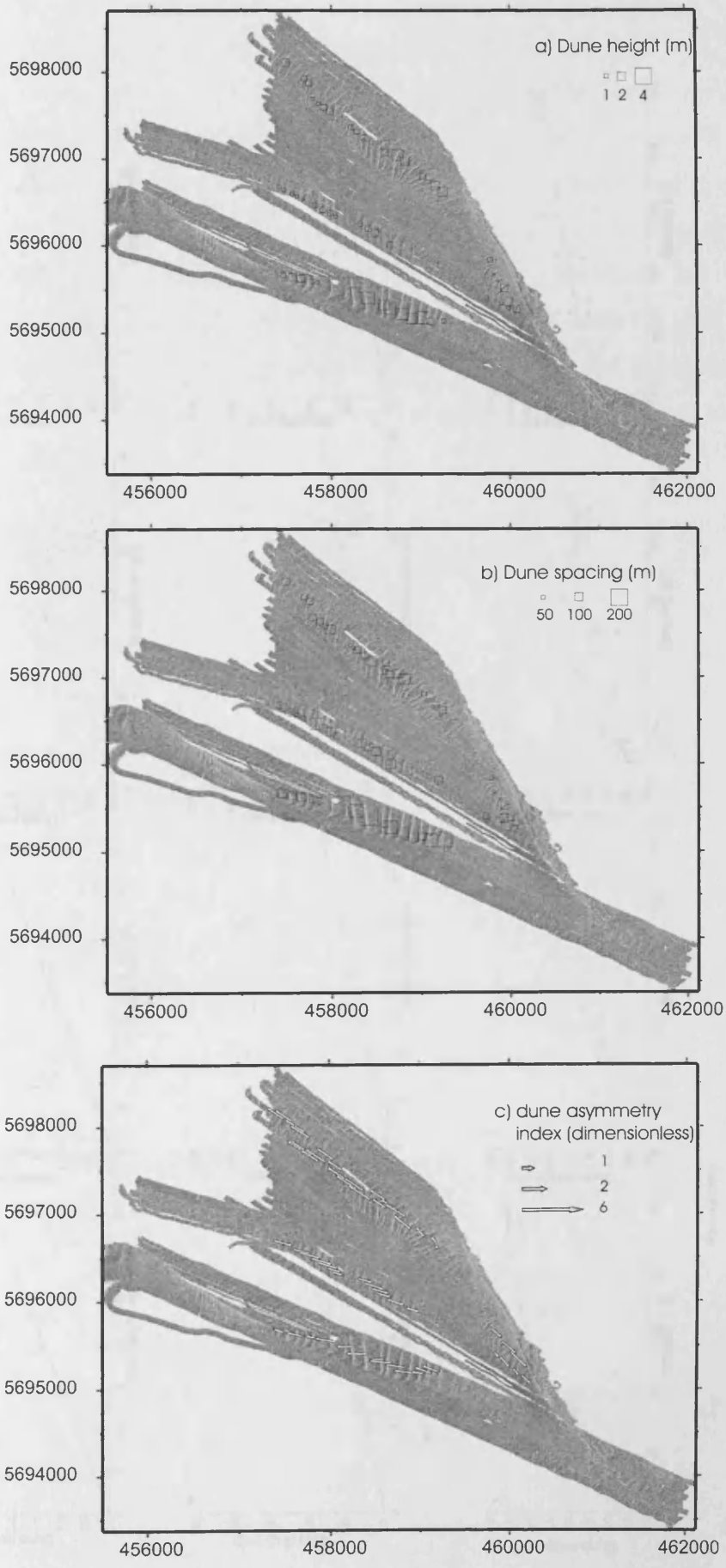

Figure 4.6 Geometrical characteristics of sand dunes. Dune height, spacing and asymmetry index were measured at the highest point of the dune crest in the composite 2002 multibeam survey data
(a) Dune height, defined as the vertical distance between the crest and the base of the mobile layer (m),
(b) Dune spacing, measured between consecutive troughs (m),
(c) Sense and magnitude of the asymmetry of the dunes (ratio of the horizontal length of the stoss side to the lee side). Vectors are plotted in the lee side direction perpendicular to the dune crests.

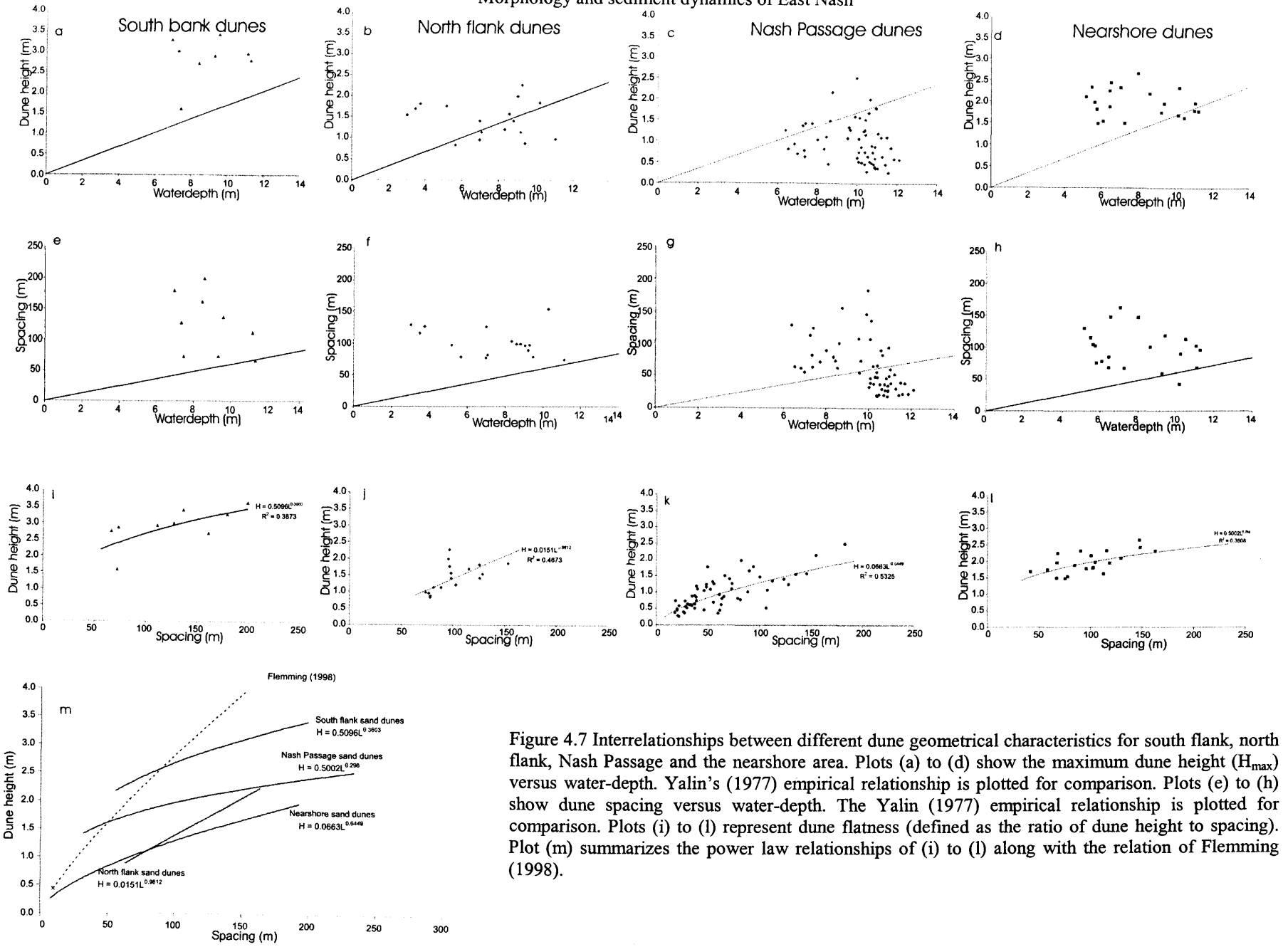

Figure 4.7 Interrelationships between different dune geometrical characteristics for south flank, north flank, Nash Passage and the nearshore area. Plots (a) to (d) show the maximum dune height (H_{max}) versus water-depth. Yalin's (1977) empirical relationship is plotted for comparison. Plots (e) to (h) show dune spacing versus water-depth. The Yalin (1977) empirical relationship is plotted for comparison. Plots (i) to (l) represent dune flatness (defined as the ratio of dune height to spacing). Plot (m) summarizes the power law relationships of (i) to (l) along with the relation of Flemming (1998).

4.3.3. Sand dune migration

The migration of individual sand dunes was measured by comparing successive bathymetric datasets, both in cross-sections and in plan-view. Figure 4.8 shows examples of cross-sections across the four identified dune fields around East Nash. For these profiles, the majority of the dunes preserved their geometry between the two multibeam surveys. The comparison of the 2002 multibeam and the 2003 single-beam datasets was also straightforward with only minor morphological differences between them. The Nash Passage area is an exception. Here the sand dunes are smoothed out and their weak morphological expression did not permit their tracking on an annual basis.

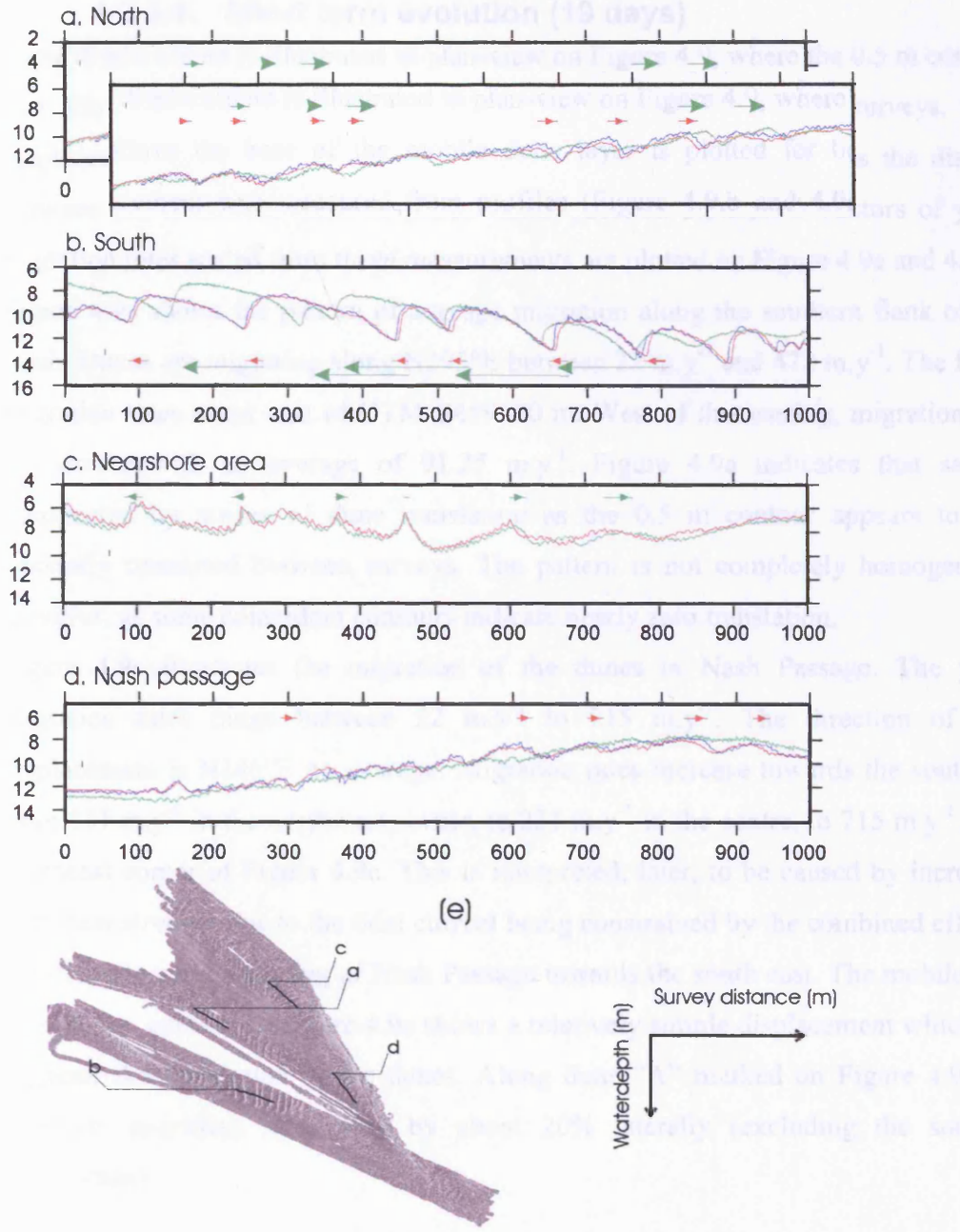

Figure 4.8 Evidence of dune mobility along (a) the northern flank, (b) the southern flank, (c) the nearshore area and (d) Nash Passage from profiles run through the two multibeam surveys and along the single-beam tracks shown on (e) (the lines points to the origin of the profiles). Confidently tracked dunes are marked by arrows in (a)-(d). Vertical uncertainty represents the 2σ standard deviation of height differences for the multibeam data filtered over 20 m.

4.3.3.1. Short term evolution (19 days)

Dune displacement is illustrated in plan-view on Figure 4.9, where the 0.5 m contour-line above the base of the mobile dune layer is plotted for both surveys. Dune displacement was measured from profiles (Figure 4.9.b and 4.9d), as the distance between the centres of mass of paired dunes (Section 3.3.2.2.1). Vectors of yearly migration rates scaled from these measurements are plotted on Figure 4.9a and 4.9c.

Figure 4.9a shows the pattern of average migration along the southern flank of East Nash. Dunes are migrating along N295°E between 22 $m.y^{-1}$ and 472 $m.y^{-1}$. The fastest migration rates occur east of UTM E459520 m. West of this easting, migration rates are slower with an average of 91.25 $m.y^{-1}$. Figure 4.9a indicates that sand is transported by means of dune translation as the 0.5 m contour appears to have generally translated between surveys. The pattern is not completely homogeneous, however, as some coincident contours indicate nearly zero translation.

Figure 4.9c illustrates the migration of the dunes in Nash Passage. The yearly migration rates range between 22 $m.y^{-1}$ to 715 $m.y^{-1}$. The direction of dune displacement is N146°E on average. Migration rates increase towards the south east from 131 $m.y^{-1}$ in the northwest corner, to 231 $m.y^{-1}$ in the centre, to 715 $m.y^{-1}$ in the southeast corner of Figure 4.9c. This is interpreted, later, to be caused by increasing bed shear strength due to the tidal current being constrained by the combined effect of the shoaling and narrowing of Nash Passage towards the south east. The mobile dune layer 0.5 m contour in Figure 4.9c shows a relatively simple displacement which also suggests the translation of the dunes. Along dune "A" marked on Figure 4.9c, for example, migration rates vary by about 20% laterally (excluding the southern termination).

These short-term observations therefore suggest that dune migration rates do not follow the widely accepted tendency that sand dune celerity is anti-correlated with dune amplitude (Fenster et al., 1990; Carling et al., 2000a). Dunes in Nash Passage migrate at a similar rate to those along the southern flank, despite their smaller size (average of 1.3 m high in Nash Passage area compared to 2.9 m high along the southern flank, see section 4.3.2). This is an indicator of a stronger residual current in Nash Passage compared with currents in South Nash.

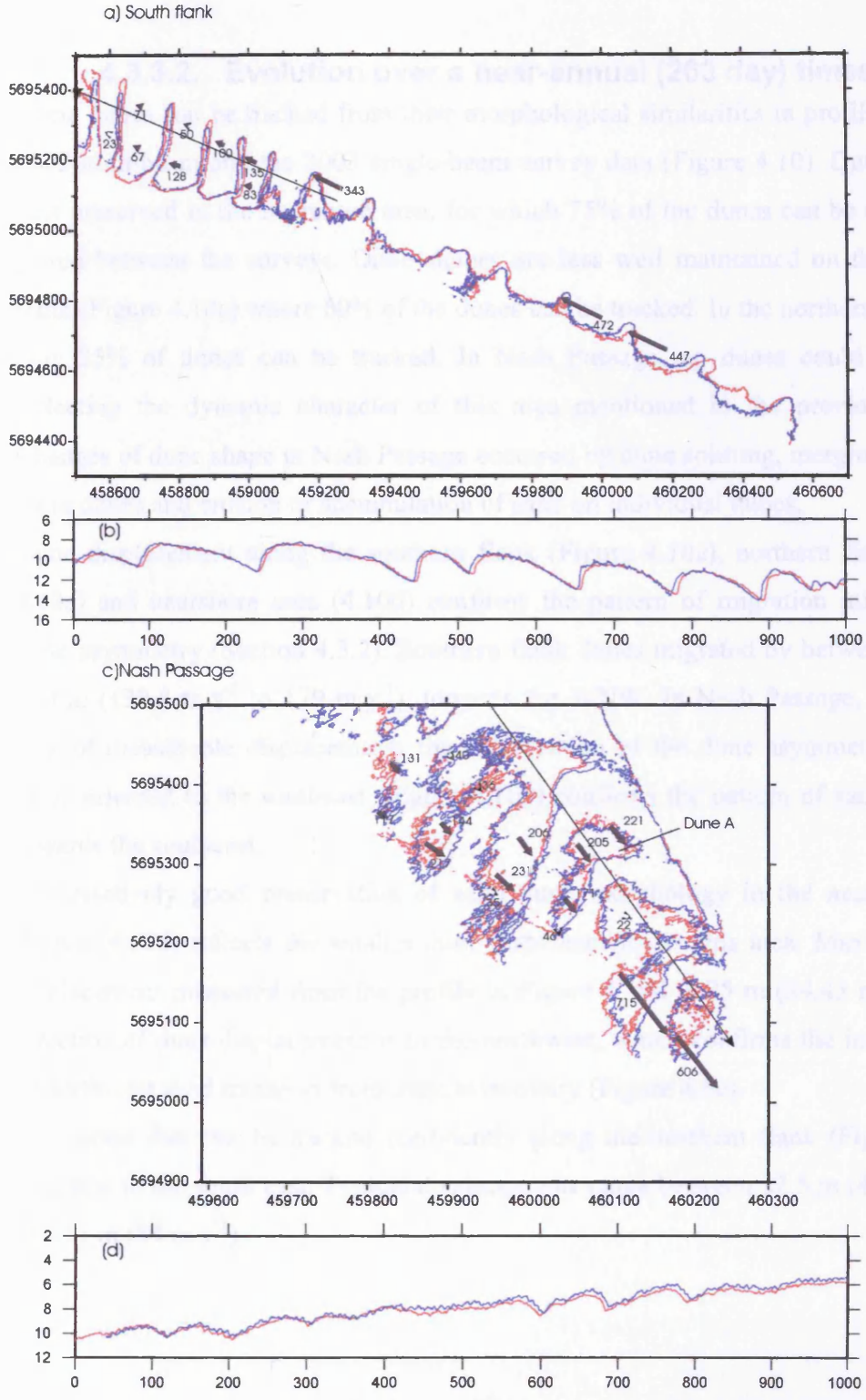

Figure 4.9 Plan view comparison of the 0.5 m contour-line above the base of the mobile dune layer for the two multibeam surveys separated by 19 days (a) along the southern flank and (b) in the Nash Passage. The 0.5 m contour line of the mobile dune layer is plotted in red for the first multibeam survey (16, 17 and 18 August 2002) and in blue for the second survey (4 September 2002). (b) and (d) dune displacement illustrated in cross-sectional profiles located by the fine arrows on the plan views (a) and (c). Bold arrows represent the orientation and magnitude of yearly migration rate ($m.y^{-1}$) vectors obtained by scaling the migration measurements. The base of each vector is plotted at the associated dune centre of mass.

4.3.3.2. Evolution over a near-annual (263 day) timescale

Some dunes can be tracked from their morphological similarities in profile using the 2002 multibeam and the 2003 single-beam survey data (Figure 4.10). Dune shape is best preserved in the nearshore area, for which 75% of the dunes can be confidently paired between the surveys. Dune shapes are less well maintained on the southern flank (Figure 4.10a) where 60% of the dunes can be tracked. In the northern flank area only 25% of dunes can be tracked. In Nash Passage, no dunes could be paired, reflecting the dynamic character of this area mentioned in the previous section. Changes of dune shape in Nash Passage occurred by dune splitting, merging of two or more dunes and erosion or accumulation of sand on individual dunes.

Dune displacement along the southern flank (Figure 4.10a), northern flank (Figure 4.10c) and nearshore area (4.10d) confirms the pattern of migration inferred from dune asymmetry (Section 4.3.2). Southern flank dunes migrated by between 100 and 130 m (138.8 $m.y^{-1}$ to 179 $m.y^{-1}$), towards the WNW. In Nash Passage, despite the lack of measurable displacements the preservation of the dune asymmetry with lee faces oriented to the southeast (Figure 4.10b) confirms the pattern of sand transport towards the southeast.

The relatively good preservation of sand dune morphology in the nearshore area (Figure 4.10d) reflects the smaller dune displacements in this area. Maximum dune displacement measured from the profile in Figure 4.10d is 25 m (34.43 $m.y^{-1}$). The direction of dune displacement is to the northwest, which confirms the interpretation of northwest sand transport from dune asymmetry (Figure 4.6c).

The dunes that can be tracked confidently along the northern flank (Figure 4.10d) migrated to the south east. Typical displacements range between 32.5 m (44.76 $m.y^{-1}$) and 61 m (84 $m.y^{-1}$).

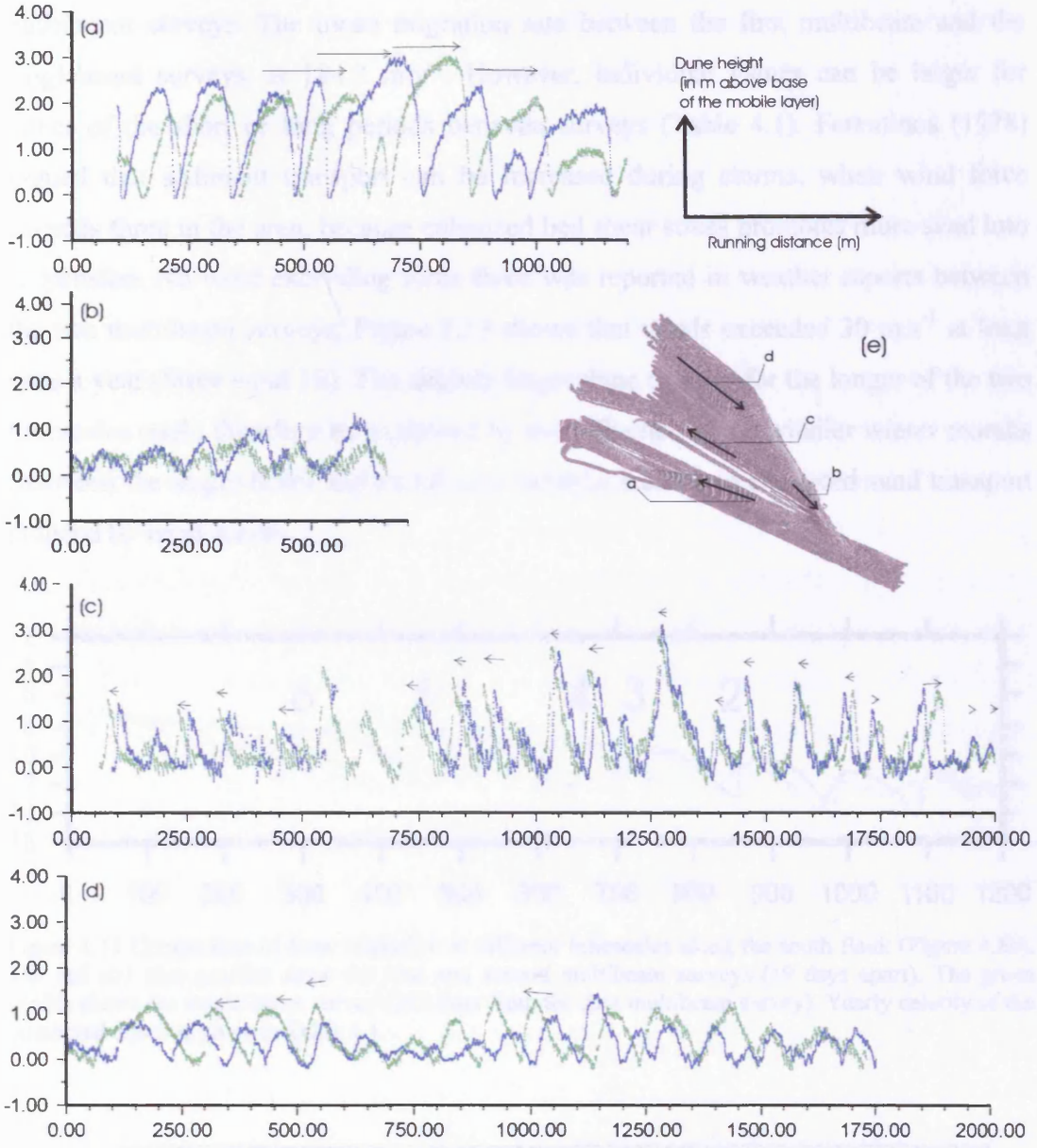

Figure 4.10 Examples of dune tracking between the first multibeam survey (blue profiles) and the singlebeam survey (green profiles) for (a) the southern flank, (b) Nash Passage (c) the nearshore area and (d) the northern flank. Location and direction of the profiles is shown on (e). Arrows in (a) to (d) indicate the confidently tracked dunes.

4.3.3.3. Comparison of dune migration over 19 days and quasi-annual periods

Along the southern flank, where the dunes can be easily tracked within the three surveys, a comparison of the dune displacement over different timescales can be undertaken. Figure 4.11 (which corresponds to a section of Figure 4.8b) and Table 4.1 summarise the displacement of the tracked dunes and the corresponding yearly migration rates. The mean migration rate is 153.3 $m.y^{-1}$ between the first and second

multibeam surveys. The mean migration rate between the first multibeam and the singlebeam surveys, is 184.3 $m.y^{-1}$. However, individual values can be larger for either of the short or long periods between surveys (Table 4.1). Ferentinos (1978) argued that sediment transport can be increased during storms, when wind force exceeds three in the area, because enhanced bed shear stress promotes more sand into suspension. No wind exceeding force three was reported in weather reports between the two multibeam surveys. Figure 1.13 shows that winds exceeded 30 $m.s^{-1}$ at least once a year (force wind 10). The slightly larger dune celerity for the longer of the two timescales could therefore be explained by the influence of the windier winter months (between the single-beam and multibeam surveys) leading to enhanced sand transport induced by wind waves.

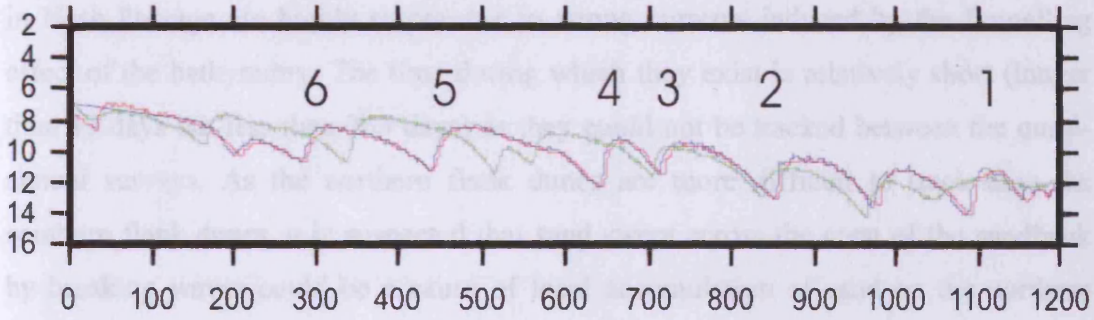

Figure 4.11 Comparison of dune migration at different timescales along the south flank (Figure 4.8b). The red and blue profiles show the first and second multibeam surveys (19 days apart). The green profile shows the single-beam survey (263 days from the first multibeam survey). Yearly celerity of the numbered dunes is given in Table 4.1.

	Between the first and second multibeam surveys	**Between the first multibeam and the single-beam surveys**
Dune 1	200 (+)	177
Dune 2	267 (+)	207
Dune 3	200	220 (+)
Dune 4	111	186 (+)
Dune 5	156 (+)	145
Dune 6	134	170 (+)

Table 4.1 Yearly celerity of dunes ($m.y^{-1}$) measured by dune displacements between the two multibeam surveys (19 days) and between the first multibeam and the single-beam survey (263 days). A plus sign ("+") highlights the larger values.

Figure 4.12 summarises the yearly-averaged migration rates from the comparison of the two multibeam surveys (green arrows) and from comparison of the first multibeam survey with the singlebeam survey (red arrows). Migrations occurred to the west-northwest (N288°E) along the southern flank of the bank and to the east-southeast (N111°E) along the northern flank with a stronger southerly component in Nash Passage (N141°E). Near the coastline, dunes migrated to the north-northwest (N306°E), except at the southern extremity of the nearshore area where some dunes migrated towards the Nash Passage (i.e. towards the southwest).

The bathymetry data along both flanks of the East Nash and in the nearshore area indicate that sand dunes in these areas maintain remarkably stable shapes during migration, as dunes migrated without major morphological changes. However, dunes in Nash Passage are highly responsive to strong currents induced by the funnelling effect of the bathymetry. The time during which they exist is relatively short (longer than 19 days but less than 263 days) as they could not be tracked between the quasi-annual surveys. As the northern flank dunes are more difficult to track than the southern flank dunes, it is suspected that sand swept across the crest of the sandbank by breaking waves could be a cause of local accumulation of sand on the northern flank, which is supported by greater height and spacing of the dunes towards the upper part of the northern flank dune field (i.e. towards the crest, Section 4.3.2), as well as being more difficult to track between surveys (varying morphology).

The overall migration pattern around the flanks of East Nash is consistent with previous studies in the area (Ferentinos and Collins, 1980; Harris, 1982; Brampton, 1999) showing a clockwise transport pattern around the bank. In the nearshore dune field, migration is to the northwest from both dune asymmetry and migration. This locally contradicts conceptual models of sediment transport path in the Bristol Channel, which envision an east directed (flood dominated) sediment transport near the coasts compensating the ebb-dominated (towards the west) transport in the central Bristol Channel (Ferentinos, 1978; Collins, 1987; Harris and Collins, 1988).

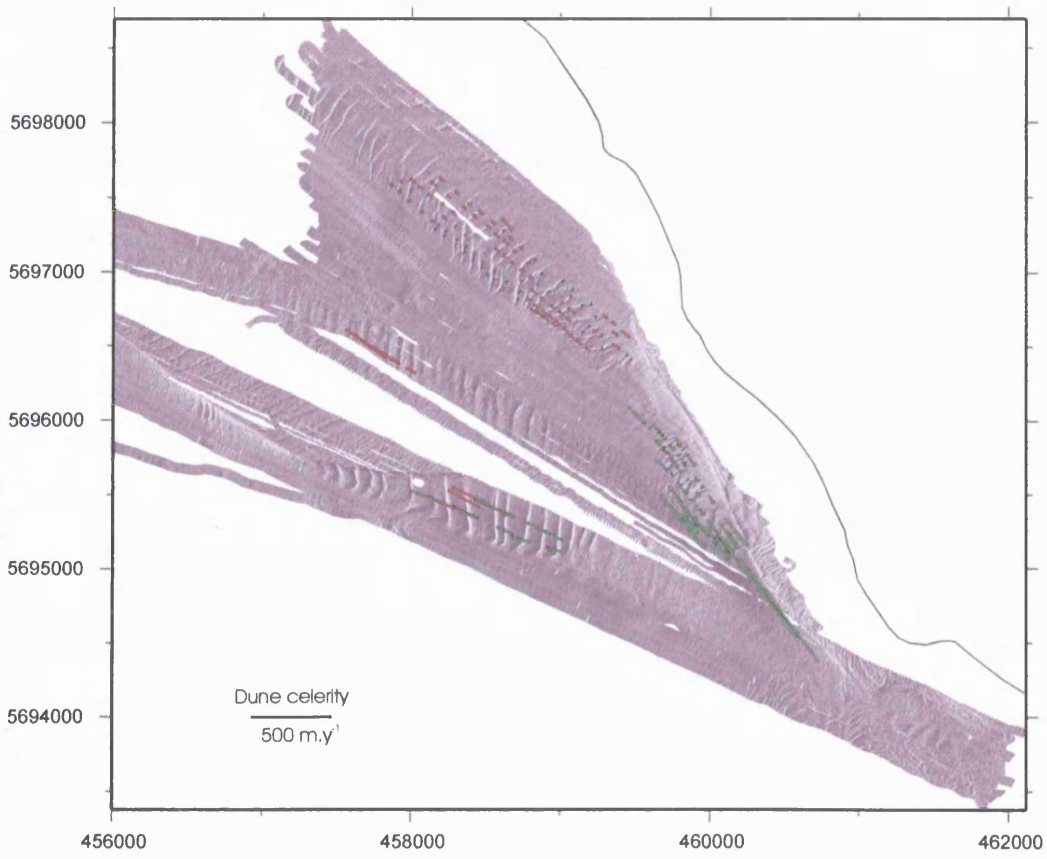

Figure 4.15 Yearly dune migration rate (m.y^{-1}). Green arrows represent the migration measured from tracked sand dunes between the 16-17-18 August 2002 and 04 September 2002 surveys. Red arrows represent the migration measured from tracked dunes between the 16-17-18 August 2002 and the 25 May 2003surveys.

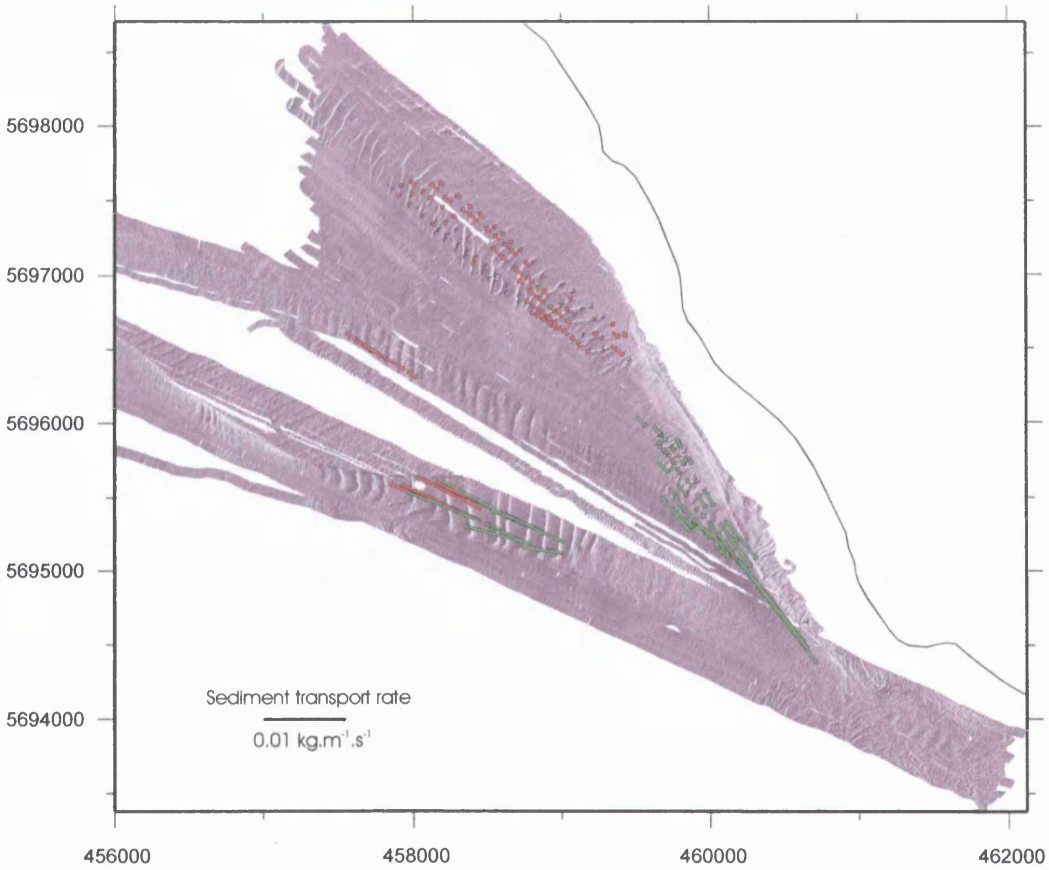

Figure 4.16 Specific flux (in kg.m^{-1}.s^{-1}) of sediment calculated from the migration and the morphology of the sand dunes. Numeric values of the data are given in Annexe A.3.

4.3.4. Estimation of sediment transport flux

Dune-associated specific sand fluxes were calculated using the method introduced in Section 1.4.4. Heights and spacing of the sand dunes were taken from the analysis in Section 4.3.2 and used to compute the average shape factor ('f') for paired dunes. Migration rates of the sand dunes were taken from the analysis in Section 4.3.3. Results of applying Equation 1.25 are reported in Figure 4.13 and values are provided in Annexe A.3. As before, volumetric fluxes were converted to mass fluxes using a porosity ε of 0.4 and a dry sand density ρ_s of 2650 $kg.m^{-3}$ (Section 3.3.2.1).

The directions of specific flux vectors are similar to the directions of sand dune migration (Figure 4.12) from which they are derived. The magnitude of the flux ranges between 0.0009 $kg.m^{-1}.s^{-1}$ and 0.151 $kg.m^{-1}.s^{-1}$. The largest flux magnitude occurs in Nash Passage. However, values as low as 0.002 $kg.m^{-1}.s^{-1}$ also occur in this area. The average value for this area is 0.018 $kg.m^{-1}.s.^{-1}$. The wide range of flux for this area indicates a varied migration of the sand dunes in response to the strong tidal currents in the Passage. Along the north flank, the magnitude of the specific sand flux ranges between 0.013 and 0.038 $kg.m^{-1}.s^{-1}$, with an average value of 0.026 $kg.m^{-1}.s^{-1}$. These values can be compared with specific flux calculated along the southern flank, which ranges between 0.002 and 0.095 $kg.m^{-1}.s^{-1}$ and have an average of 0.051 $kg.m^{-1}.s^{-1}$. Finally, lower values are observed in the nearshore area where the flux magnitude ranges between 0.0009 and 0.017 $kg.m^{-1}.s^{-1}$ with an average of 0.005 $kg.m^{-1}.s^{-1}$.

4.4. Other geological and environmental data

Information on the sediment texture and hydrodynamic data were not collected over the period of the surveys, but such data were made available from limited previous work in the area. Sediment texture data were provided by the ABP MER (Haine, 2000). Current speed and orientation information for the northern flank of East Nash (station T3 in Figure 4.14) and Nash Passage (stations T4 and T5 in Figure 4.14) were retrieved from the work of Turner (1976). Current speed and orientation south of Nash Point (station CM2 in Figure 4.14) along with wave height and period data recorded south of Nash Point (station W1 in Figure 4.14) were provided by the British Oceanographic Data Centre (BODC), collected as part of previous studies directed by Swansea University (Harris and Collins, 1988) and the Institute of Hydraulic Research respectively.

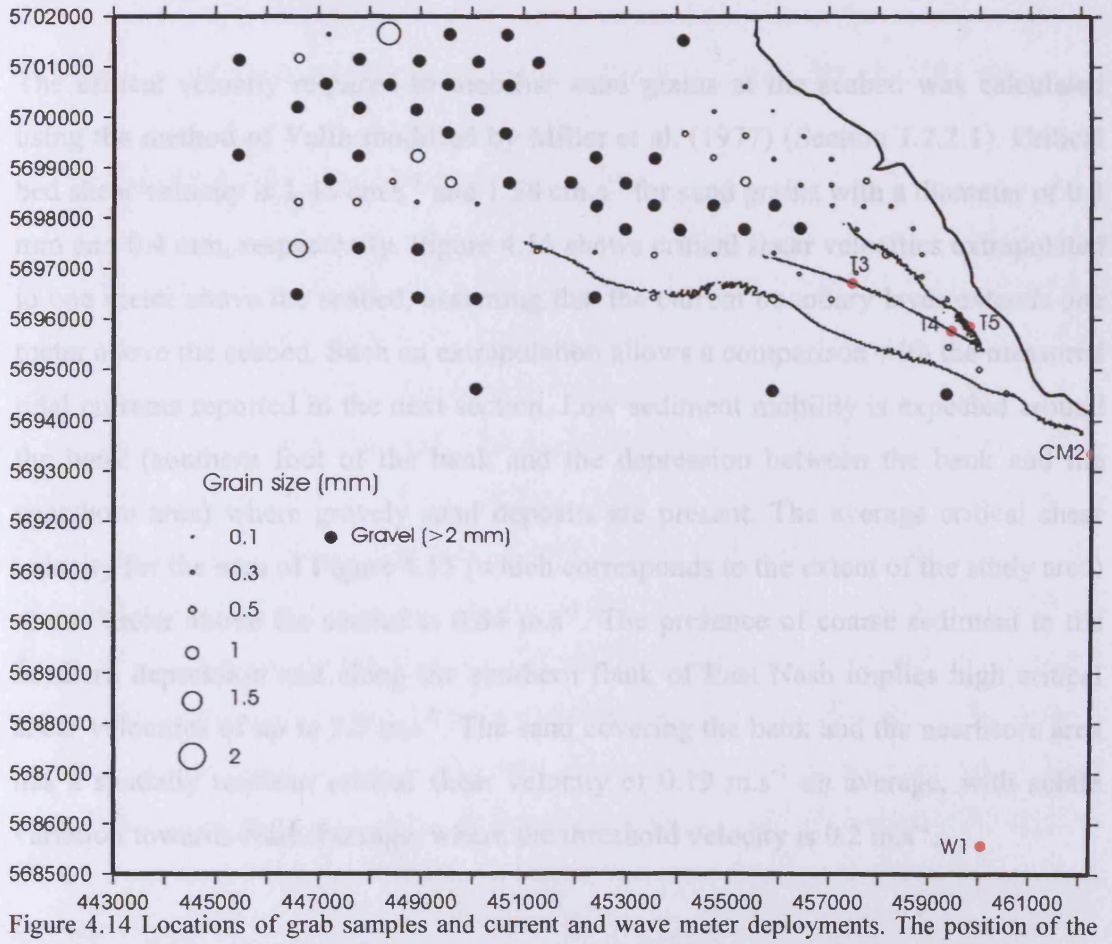

Figure 4.14 Locations of grab samples and current and wave meter deployments. The position of the coastline (thicker line) and the 10 m contour line of the multibeam data are also shown. Sediment information is displayed as the mean grain-size of grab samples collected in April/May 1998 and provided by ABP. Current meters T3, T4, T5 were deployed in 1972 (Turner, 1976). CM2 current meter data were collected by Swansea University scientists in 1983. W1 wave regime data were measured in 1978 by Hydraulic Research Station scientists. Both the last two datasets were provided by the BODC (see text for details).

4.4.1. Sediment texture

Figure 4.14 shows the median grain size (d_{50}) of samples plotted at their grab sampling locations. Sites with a median grain size above 2 mm (gravel) are displayed by the black dots. Figure 4.14 shows that East Nash is surrounded by gravely sand, with occurrences of pebbles (d_{50}=53mm) on occasional sites (UTM E445442 m, N5699254 m). East Nash is covered by sand with a median grain diameter ranging from 0.2 mm to 0.5 mm. Average median grain size diameter within the bathymetric surveyed area is 0.35 mm. In the nearshore area, the crestal platform and the northern flank are characterised by fine median grain size, with an average d_{50} of 0.32 mm. Grains become slightly coarser in Nash Passage with an average median grain size of 0.4 mm. Along the southern flank the average grain size is 0.36 mm, although there are few measurements.

The critical velocity required to mobilise sand grains at the seabed was calculated using the method of Yalin modified by Miller et al. (1977) (Section 1.2.2.1). Critical bed shear velocity is 1.45 $cm.s^{-1}$ and 1.58 $cm.s^{-1}$ for sand grains with a diameter of 0.3 mm and 0.4 mm, respectively. Figure 4.15 shows critical shear velocities extrapolated to one meter above the seabed, assuming that the current boundary layer extends one meter above the seabed. Such an extrapolation allows a comparison with the measured tidal currents reported in the next section. Low sediment mobility is expected around the bank (southern foot of the bank and the depression between the bank and the nearshore area) where gravely sand deposits are present. The average critical shear velocity for the area of Figure 4.15 (which corresponds to the extent of the study area) at one meter above the seabed is 0.64 $m.s^{-1}$. The presence of coarse sediment in the northern depression and along the southern flank of East Nash implies high critical shear velocities of up to 2.5 $m.s^{-1}$. The sand covering the bank and the nearhsore area has a spatially uniform critical shear velocity of 0.19 $m.s^{-1}$ on average, with subtle variation towards Nash Passage, where the threshold velocity is 0.2 $m.s^{-1}$.

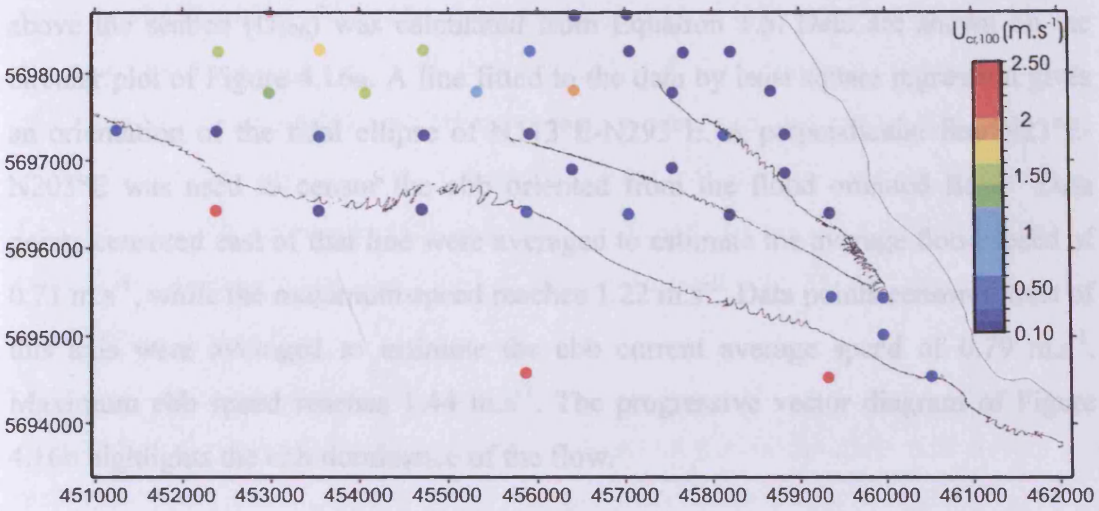

Figure 4.15 Critical shear velocity at one meter above the seabed ($U_{cr,100}$) derived from data of Figure 4.14. These were calculated using the method of Yalin modified by Miller (see Section 1.2.2.1) and supposing the current boundary layer is maintained in the first meter above the seabed and has a logarithmic velocity profile.

4.4.2. Tidal current records from near East Nash Sands

South Nash Point current meter (CM2)

South of Nash Point (Figure 4.14 for location), the University of Wales Swansea scientists moored a self-recording Aanderaa current meter (Harris and Collins, 1988). The data were provided by the British Oceanographic Data Centre, along with a description of the equipment used. The Aanderaa current meter comprises a propeller, which measures the speed of the current from its rotation rate recorded with an electronic counter (with an accuracy of 2%), a vane which aligns the propeller to the flow, a magnetic compass which measures the orientation of the propeller with an accuracy of 5° for currents below 1 m.s^{-1} and 7.5° for currents between 1 m.s^{-1} and 2.5 m.s^{-1} and a quartz clock. The current meter was positioned at 1.5 m above the seabed. Location of the current meter site was determined with an accuracy of ± 30m. Direction and current speed were measured between the 18th of August 1983 and the 3rd of September 1983 at a 10 minutes sampling rate. This period corresponds to a neap-spring cycle.

Assuming a logarithmic profile of current speed up to 1.5 m above the seabed and a seabed roughness of z_0 = 0.5 cm (Section 1.2.2.1) the current speed at one meter

above the seabed (U_{100}) was calculated from Equation 1.5. Data are shown on the circular plot of Figure 4.16a. A line fitted to the data by least square regression gives an orientation of the tidal ellipse of N113°E-N293°E. A perpendicular line N23°E-N203°E was used to censor the ebb oriented from the flood oriented flow. Data points censored east of that line were averaged to estimate the average flood speed of 0.71 $m.s^{-1}$, while the maximum speed reaches 1.22 $m.s^{-1}$. Data points censored west of this axis were averaged to estimate the ebb current average speed of 0.79 $m.s^{-1}$. Maximum ebb speed reaches 1.44 $m.s^{-1}$. The progressive vector diagram of Figure 4.16b highlights the ebb dominance of the flow.

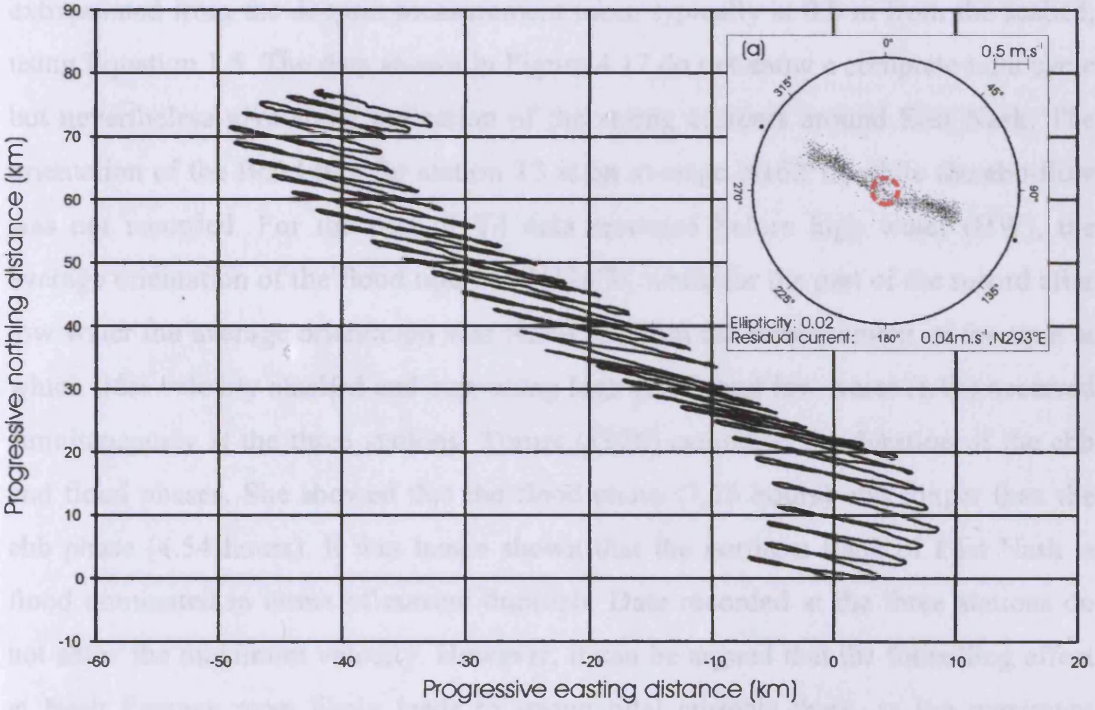

Figure 4.16 Nash Point tidal current data collected over a neap-spring cycle (from 18/08/1983 to 3/09/83). Data were provided by the BODC. (a) Circular plot of U_{100}. Critical threshold speed for grain size of 0.3 mm ($U_{cr,100}$=0.19 $m.s^{-1}$) is represented by the dashed red circle. Estimate of the tidal ellipticity is given as the ratio of the length of the short axis by the long axis of the tidal ellipse (see legend of Figure 3.19 for details). (b) Progressive vector diagram for the whole period of deployment (0,0 corresponds to the 18/08/1983).

North East Nash and Nash Passage current meters (T3, T4 and T5)

T3, T4 and T5 tidal currents data (Turner, 1976) were recorded using a Toho Dentan CM2 current meter. The current was measured by an impellor with an accuracy of ± 0.05 $m.s^{-1}$ (Turner, 1976). The impellor was mounted on a rod, around which it can

rotate freely in the direction of the current. The current direction was measured by a magnetic compass with a claimed accuracy of ± 10°. The meter was lowered in steps of 2 m in the water column and current speed and orientation were read at each step. When the current meter reached the seafloor, it was then pulled back to the surface. This protocol was repeated continuously on 15/06/1972 between 15:29 and 17:39 at station T3, between 21:03 and 23:37 at station T4 and on 16/06/1972 between 09:26 and 11:58 at station T5.

Assuming a logarithmic current speed profile and a seabed roughness of z_0=0.5 cm (Section 1.2.2.1), the current speed at one meter above the seabed (U_{100}) was extrapolated from the deepest measurement taken typically at 0.8 m from the seabed, using Equation 1.5. The data shown in Figure 4.17 do not show a complete tidal cycle but nevertheless give some indication of the strong currents around East Nash. The orientation of the flood tide for station T3 is on average N162°E, while the ebb flow was not recorded. For the part of T4 data recorded before high water (HW), the average orientation of the flood tide was N124°E, while for the part of the record after low water the average orientation was N340°E. From the measurement of the time at which tidal velocity slacked and supposing high (HW) and low water (LW) occurred simultaneously at the three stations, Turner (1976) estimated the duration of the ebb and flood phases. She showed that the flood phase (7.26 hours) was longer than the ebb phase (4.54 hours). It was hence shown that the northern flank of East Nash is flood dominated in terms of current duration. Data recorded at the three stations do not show the maximum velocity. However, it can be argued that the funnelling effect at Nash Passage most likely leads to strong tidal currents there, as the maximum recorded velocity at T4 is 1.17 $m.s^{-1}$ one hour after high water. This can be compared to the maximum speed of only 0.48 $m.s^{-1}$ recorded at T3 two hours after low water.

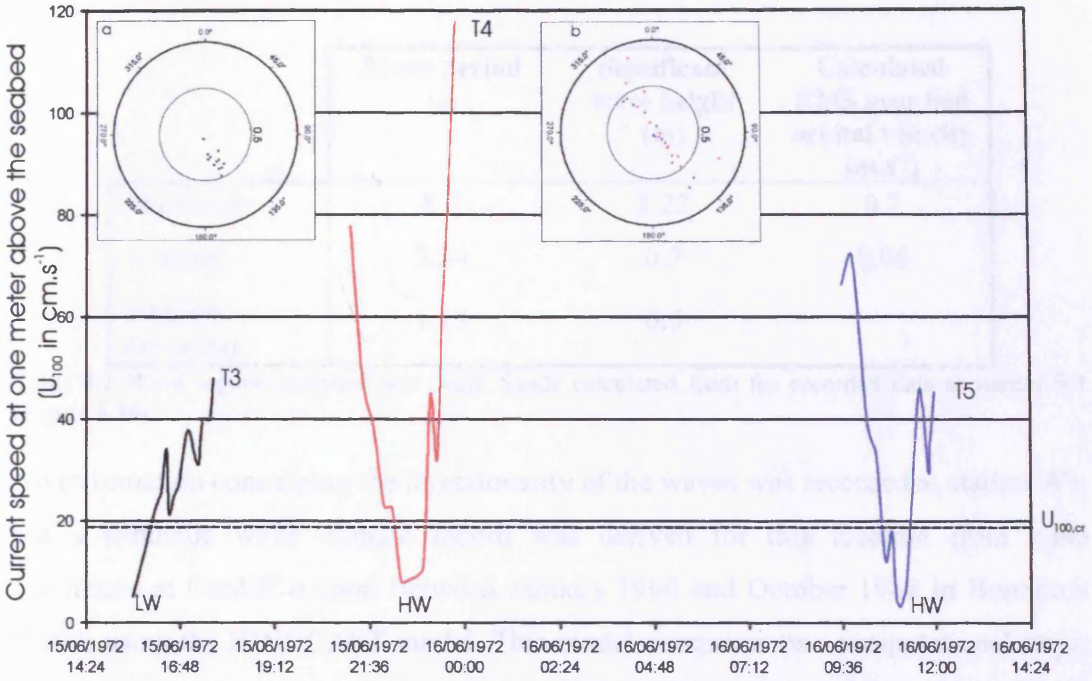

Figure 4.17 Tidal current speed extrapolated to 1 m above the seabed along the northern flank of East Nash (T3) and the Nash Passage (T4 and T5). The dashed line represents $U_{100,cr}$ = 19 cm.s^{-1} for a typical 0.3 mm sand grain size (Figure 4.15). Inserts (a) and (b) show the orientation of the tidal currents. Data are from Turner (1976).

4.4.3. Wave regime

Some wave data were collected in the vicinity of East Nash (W1 on Figure 4.14) by the Hydraulic Research Station between the 10th of April 1978 and the 13th of January 1979, and were provided by the British Oceanographic Data Centre. Measurements were undertaken using a Waverider sensor, which measures the vertical motion of a floating buoy in response to the passing waves (Driver, 1980). Mean period and mean significant wave height data are given in Table 4.2. Near bed orbital velocity for a 10 m water-depth was calculated using Equation 1.8a. Using the averaged data of Table 4.1, the depth of closure (i.e. the depth at which the orbital motion has an insignificant influence on the seabed), estimated to occur roughly at half of the wavelength, lies for average waves 9 m below the water level.

	Mean period (s)	Significant wave height (m)	Calculated RMS near bed orbital velocity ($m.s^{-1}$)
Maximum	8.7	3.22	0.7
Average	3.34	0.7	0.06
Standard deviation	1.18	0.5	

Table 4.2 Wave regime statistics near Nash Sands calculated from the recorded data at station W1 (Figure 4.14).

No information concerning the directionality of the waves was recorded at station W1, but a synthetic wave climate record was derived for this location from wind conditions at Cardiff Airport between January 1960 and October 1988 in Brampton (1999) using the HINDCAST model. This model comprises two computational steps. The first step consisted of applying the JONSWAP equation (Hasselmann et al., 1973), which represents the spectrum of fetch induced wind waves in continental-shelf waters, at evenly spaced directions about the mean direction of the wind direction. In the second step, the average of the component spectra was calculated using a weighted function. The weighting function incorporates the directional spreading of the wind and is of the form of a square cosine centred on the average wind direction (Seymour, 1977). Figure 4.18 was plotted from this synthetic dataset. Higher significant wave height and period for the modelled data compared to the recorded data (Table 4.2) are probably due to the varied effect of shoaling and refraction experienced by the measured waves that were not accounted for in the model (Brampton, 1999). Figure 4.18 suggests that the prevailing wave approach should be from the N240°E-N300°E sector, in which 30% of the occurrence of the modelled wave data was counted. The largest waves are also predicted to approach from the N240°E-N300°E sector. Waves approaching from other directions are predicted to have been smaller and less frequent because of the proximity of the coast and a limited fetch.

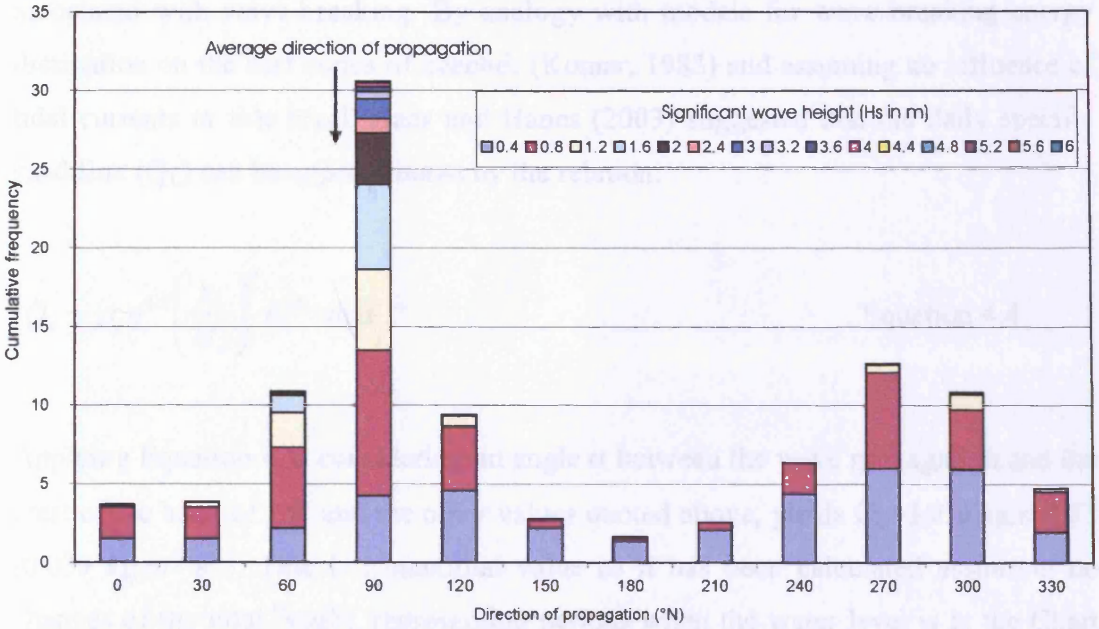

Figure 4.18 Modelled wind-induced significant wave height in the vicinity of Nash Sands (data computed using the HINDCAST model (Brampton, 1999) using wind data recorded at Cardiff Airport, see text for details). Average direction of propagation is N77°E.

4.5. Discussion

4.5.1. Signification of the crestal platform

Breaking waves were observed on Nash Bank (Figure 4.19 and EMU, 1999) during part of the tidal cycle. Plunging or spilling wave breakers are known to strongly influence sediment transport (Yu et al., 1993) because their turbulence induces erosion and maintains sand in suspension while the breaker surges. The criterion for breaking waves was given by Thornton and Guza (1982) as the ratio of wave height (H_s) to water depth, as follows:

$$h_b = \frac{H_s}{0.55} \qquad \text{Equation 4.3}$$

where h_b is the water depth at which wave starts to break. For the average significant wave height $H_s = 0.7$ m measured at site W1 (Table 4.1), Equation 4.4 suggests waves were breaking in water shallower than h_b=1.27 m, for the lowest astronomical tidal height (corresponding to the Chart Datum). This water-depth limit is in close agreement with the southern edge of the East Nash crestal platform, with its lower limit being 2 m below Chart Datum (Section 4.2.6). It can then be argued that the morphology of the crest of East Nash is strongly affected by sedimentary processes

associated with wave-breaking. By analogy with models for wave breaking energy dissipation on the surf zones of beaches (Komar, 1983) and assuming no influence of tidal currents or tide level, Haas and Hanes (2003) suggested that the daily specific sand flux (Q_L) can be approximated by the relation:

$$Q_L = \rho_s g^{1.5} \left(\frac{h_b}{H_s} \right)^3 h_b^{2.5} \sin\alpha \qquad \text{Equation 4.4}$$

Applying Equation 4.5, considering an angle α between the wave propagation and the crest of the bank of 25° and the other values quoted above, yields Q_L=3402 $kg.m^{-1}.d^{-1}$ (0.039 $kg.m^{-1}.s^{-1}$). This is a maximal value as it has been calculated assuming no changes of the tidal height, representing periods when the water level is at the Chart Datum (lowest astronomical tide). Because waves were observed breaking mostly for 1 hour either side of low water 7 days after a spring tide (Figure 4.19), the true value averaged over a lunar month may be closer to 1/6 of the calculated value of Q_L, i.e. 0.0065 $kg.m^{-1}.s^{-1}$. Although no independent data are available to confirm this value, the presence of low-amplitude, long-wavelength sand dunes on the crest of the bank (Section 4.2.6) is compatible with such a type of sediment transport. Flood tidal currents are running transversally to the dune crest (oriented N50°E), as indicated by the asymmetric profiles in Figure 4.4iii., while wave breaking currents (N60°-N120° sector) tend to elongate them longitudinally.

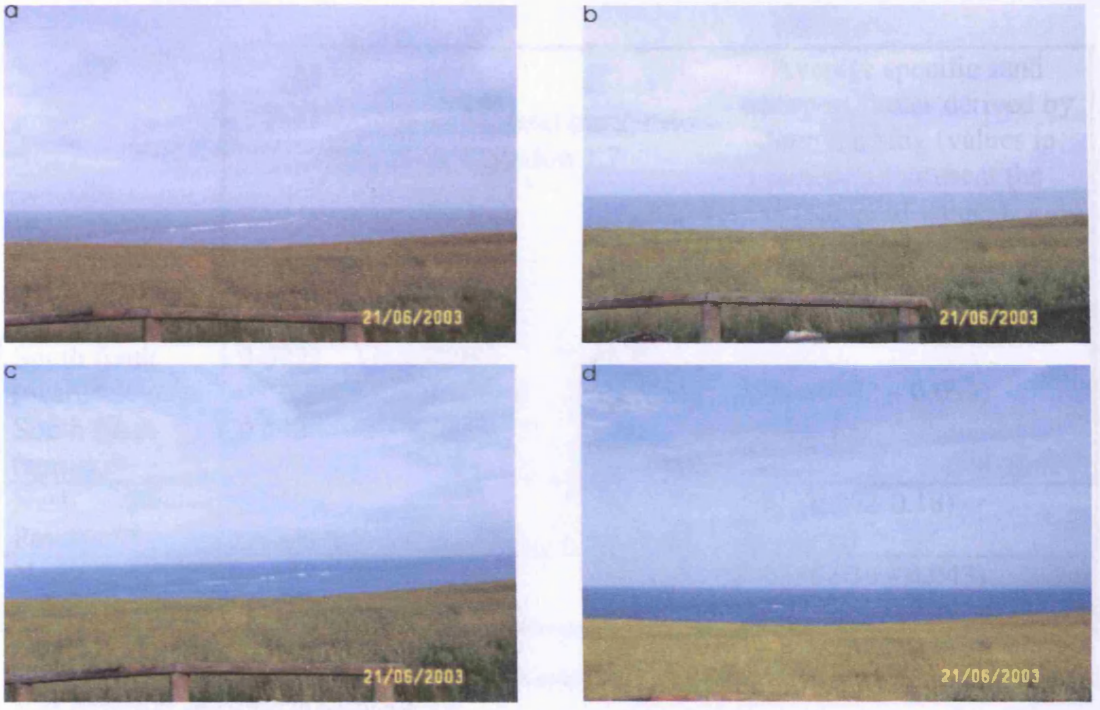

Figure 4.19 Evidence of wave breaking over the crest of Nash Sands. The pictures were taken from Nash Point Lighthouse looking to N270°E on a fair day the 21/06/2003 (i.e. 7 days after a spring tide) (a) at low tide 5:35 BST, (b) 20 minutes after low tide 5:55 BST (c) 1 hour after low tide 6:28 BST and (d) 1 hour and 30 minutes after low tide 7:00 BST.

4.5.2. Sand mobility from tidal currents

Figures 4.16a and 4.17a show that $U_{cr,100}$ is exceeded for 76 % and 92 %, of the T3 (North Flank) and T4 (Nash passage) records, respectively. For current meter CM2, these values are exceeded for 96% and 100 % of the data recorded during the neap and spring tides, respectively. Bedload transport fluxes were estimated using Bagnold's formula modified by Gadd (Equation 1.7) from the excess of tidal velocity above $U_{cr,100}$ (0.19 m.s-1). Characteristics of the predicted fluxes for Nash Passage, the south and north flanks are reported in Table 4.3.

	Predicted specific sand transport flux using Equation 1.7 $kg.m^{-1}.s^{-1}$			Average specific sand transport fluxes derived by dune tracking (values in brackets represent the range of values) $kg.m^{-1}.s.^{-1}$
	Ebb	Flood	Vector sum	
South flank (neap)*	0.0221 (N293°E)	0.0297 (N113°E)	0.0076 (N293°E)	0.05 (0.002 – 0.093) (N288°E)
South flank (spring)*	0.142 (N293°E)	0.251 (N113°E)	0.109 (N293°E)	
Nash Passage**	0.0510 (N340°E)	0.0648 (N124°E)	0.0597 (N123°E)	0.02 (0.002-0.18) (N141°E)
North flank***		0.011 (N162°E)		0.03 (0.016 - 0.043) (N111°E)

Table 4.3 Comparison of measured and predicted specific sand transport fluxes. Dune tracking fluxes were derived as described in Section 4.3.4.
* based on the average of the excess velocity at one meter above the bed (site CM2)
**derived from the maximum of the excess velocity at one meter above the bed for periods HW-1 hour to HW and HW to HW+1 hour from stations T4 and T5
***derived from the maximum of the excess velocity at one meter above the bed (site T3)

Table 4.3 shows that fluxes estimated from the current data are similar to those derived by dune tracking within one order of magnitude. CM2 provides enough information to estimate sand transport during both neap and spring tides. The vector sums of the current-derived fluxes for each phase indicate a consistently ebb-directed net sand flux. The neap tide net flux is an order of magnitude smaller than the flux derived from dune tracking. That for a spring tide is about twice the average of the dune tracking-derived fluxes. The net flux calculated for the neap and spring tides phases can be averaged to indicate the average flux of sediment transported. The magnitude of the resulting ebb-oriented flux (N293°E) is 0.0583 $kg.m^{-1}.s^{-1}$, which is similar to the average dune tracking-derived flux along the south flank which is 0.051 $kg.m^{-1}.s^{-1}$ (Section 4.3.4). Hence, it can be argued that tidal currents alone can explain the sand dune migration and sand transport along the southern flank.

In the case of the North flank and Nash Passage, further assumptions have had to be made due to the incompleteness of the current records and the following interpretation is hence speculative. For T3 (North flank) and T4/T5 (Nash Passage), the maximum excess velocity (calculated using the maximum velocity of the tidal current record) was used. In the case of Nash Passage, the net estimated sand flux is flood-dominated

and greater by three times the averaged rate from dune tracking, but is still smaller than the maximum of those rates.

Although no flux could be calculated for the ebb phase at station T3, the calculated flux (0.011 $kg.m^{-1}.s^{-1}$) for the flood current is smaller than the averaged tracking derived flux (0.02 $kg.m^{-1}.s^{-1}$) by a factor of two. This is primarily due to the lack of extensive data. However, the discrepancy may also reflect the complications of sand supplied by waves breaking over the crestal part of East Nash (Section 4.5.1) which may have affected the dune tracking-derived fluxes.

4.5.3. Sand budget

Using the method described in Section 3.5.4 the net amounts of sand transported along the northern and southern flanks, Nash Passage, the crestal platform and the nearshore area were calculated to represent the sediment budget around East Nash Sands. The fluxes in Figure 4.20 were thus calculated by multiplying the average specific sand flux for each area in Figure 4.13 by the width (perpendicular to transport direction) of each area, estimated as follows. From Section 4.2.6, the southern flank, between the edge of the crest and the foot of the flank, was given an average width of 300 m. The northern flank has an average width of 400 m, between the southern limit of the dune field lying on that side of the bank and the foot of the slope at the 12 m depth contour (Section 4.2.5). The Nash Passage has an average width of 160 m (Section 4.2.2), while the nearshore area has a width of 700 m (Section 4.2.3). The crestal area is 400 m wide on average and can be followed over a longitudinal distance of 2000 m in Figure 4.1.

Figure 4.20 suggests that bank-parallel flux on the southern flank exceeds that of the northern flank by 2 $kg.s^{-1}$. The flux of sand crossing the bank, estimated in Section 4.5.1 (maximum) can be resolved into a purely crest-perpendicular flux and a purely crest-parallel flux (allowing for an acute transport angle with the bank crest of 25°). The calculated parallel component is oriented to the east and has a magnitude of 2.05 $kg.s^{-1}$). The perpendicular component has a magnitude of 3.4 $kg.s^{-1}$. As the sand transported along the northern flank approaches the coast only a small fraction (2.7 $kg.s^{-1}$) appears directed along the Nash Passage, while another fraction (3.5 $kg.s^{-1}$) is

diverted to the nearshore area and may escape the sand circulation system around the Nash Sands.

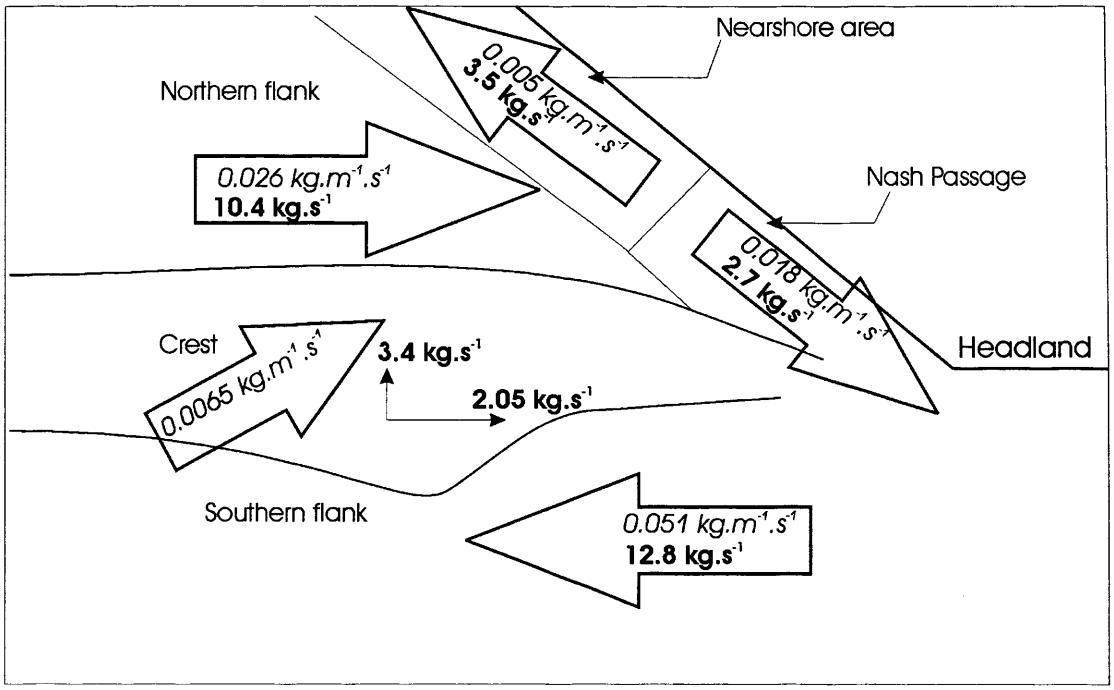

Figure 4.20 Sand budget at the approach of East Nash with Nash Point headland. Bold values are fluxes obtained from the average specific flux of each area (values in italic) multiplied by their widths measured perpendicular to transport directions (in the case of the bank crest resolved parallel and perpendicular to the bank. See text for widths used.

However, morphological evidence for the external input/output of material to the general circulation around the bank is sparse within the confines of the surveyed area. Limited input of sand may occur if the veneer of sand covering the area south of the Nash Point (Section 4.2.1) is mobile. Moreover, Turner (1976) and Pattiarchi and Collins (1987) were not able to show that there was morphological or hydrodynamic evidence of sand being transported between Nash Sands and Scarweather Sands located to the northwest.

Supposing a relatively closed system, this would induce most of the sand provided to the southern flank to pass through the Nash Passage. However the large discrepancy between the fluxes calculated for the south flank area and the Nash Passage is hence difficult to explain. Reasons for such a low value may be found in the definition of the integrating area, the accuracy to track these fast moving sand dunes and the period between the surveys (19 days) extending primarily during a neap tide, leading to individual fluxes being probably underestimated.

4.5.4. Spatial erosion and deposition trends

Using the method described in Section 3.5.5, patterns of erosion and deposition were investigated using the Continuity Equation (Equation 3.5). However, the sand flux data here are sparser than for Helwick Sands and suffer from poor spatial continuity (Figure 4.13). Therefore the divergence of sand flux was instead calculated in one dimension (along cross-sections). Equation 3.5 then simplifies to:

$$\frac{\partial z}{\partial t} = \frac{\partial q}{\partial x} \qquad \text{Equation 4.5}$$

where q is the volumetric specific sand flux and x is the horizontal distance taken along a cross-section. Flux data were first averaged over a spatial scale of 120 m (representing the average dune spacing) along lines passing across the different areas as marked on Figure 4.21d. Applying Equation 4.6 to each averaged flux profile gave the sand deposition/erosion cross-sections plotted in green on Figures 4.21a-4.21c.

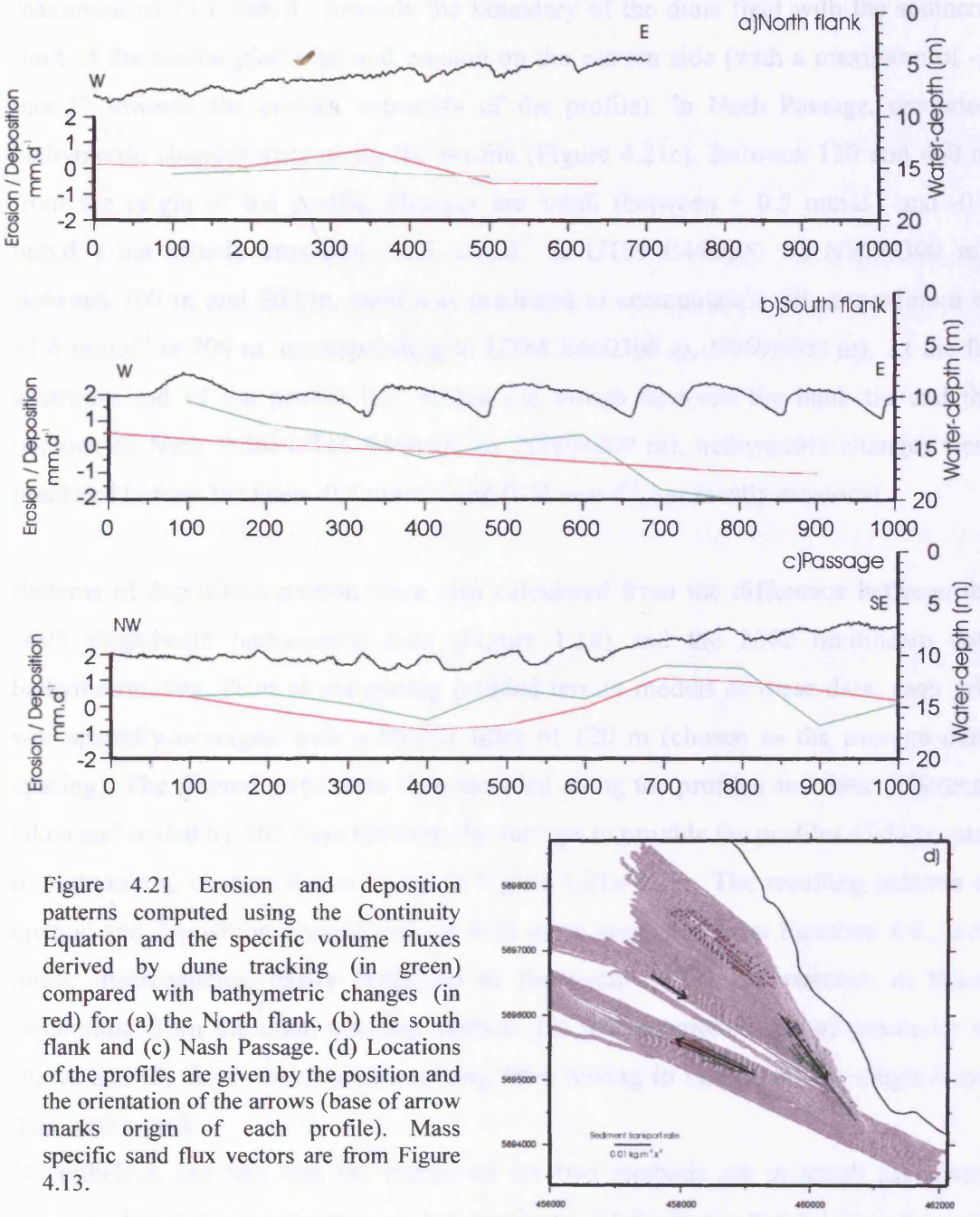

Figure 4.21 Erosion and deposition patterns computed using the Continuity Equation and the specific volume fluxes derived by dune tracking (in green) compared with bathymetric changes (in red) for (a) the North flank, (b) the south flank and (c) Nash Passage. (d) Locations of the profiles are given by the position and the orientation of the arrows (base of arrow marks origin of each profile). Mass specific sand flux vectors are from Figure 4.13.

Sparse specific flux data on the northern side of the bank (UTM E457800 m, N5695800 m to E459000m, N5695200 m) meant that only a limited profile of bathymetric changes could be computed from Equation 4.6. The calculated bathymetric variation (Figure 4.21a) suggests a pattern of relatively constant erosion with an average rate of -0.2 $mm.d^{-1}$ (ranging between -0.1 and -0.3 $mm.d^{-1}$). Along the southern flank (from UTM E457800 m, N5695600 m to UTM E459000 m, N5695200 m), the predicted pattern of bathymetric changes (Figure 4.21b) shows deposition on

the western side of the profile (west of UTM E458400 m, N5695400 m, with a maximum of +1.8 $mm.d^{-1}$ towards the boundary of the dune field with the southern limit of the crestal platform) and erosion on the eastern side (with a maximum of -2 $mm.d^{-1}$ towards the eastern extremity of the profile). In Nash Passage, predicted bathymetric changes vary along the profile (Figure 4.21c). Between 120 and 460 m from the origin of the profile, changes are small (between + 0.5 $mm.d^{-1}$ and -0.5 $mm.d^{-1}$) but mostly erosional (-0.5 $mm.d^{-1}$ at UTM E460000 m, N5695300 m). Between 700 m and 800 m, sand was predicted to accumulate (with a maximum of +1.6 $mm.d^{-1}$ at 700 m, corresponding to UTM E460300 m, N5695000 m). At the far southeast end of the profile (i.e. within the trough between the bank tip and the bedrock of Nash Point UTM E460500 m, N5694800 m), bathymetric changes were predicted to vary between -0.7 $mm.d^{-1}$ and 0.02 $mm.d^{-1}$, but mostly erosional.

Patterns of deposition/erosion were also calculated from the difference between the 2003 singlebeam bathymetric data (Figure 1.18) and the 2002 multibeam data bathymetric data. Prior to comparing gridded terrain models of these data, each grid was spatially averaged with a boxcar filter of 120 m (chosen as the average dune spacing). The filtered grids were then sampled along the profiles and their difference taken and scaled by 263 days between the surveys to provide the profiles of daily rates of bathymetric change shown in red in Figure 4.21a-4.21c. The resulting patterns of erosion and deposition generally agree with those computed from Equation 4.6., with minor discrepancies, easily explained as the result of (1) uncertainties in fluxes originating from the dune tracking method, (2) the incomplete spatial continuity of fluxes and (3) depth uncertainties arising from having to interpolate the single-beam data onto a grid.

Nevertheless, the fact that the results of the two methods are in rough agreement suggests that these uncertainties do not dominate and the fluxes derived from the dune tracking method do indeed represent sand transport around the bank. Some of the largest discrepancies occur along the south flank where the waves breaking may cause some sand to be transported in suspension, which was not accounted for by the dune tracking method (the method implies that the sand dunes migrate as bedload). Also wave-current transport may cause some transverse fluxes. Discrepancies are also observed in Nash Passage, which could be explained by a mis-estimation of the individual fluxes in this area (Section 4.5.3).

4.6. Conclusions

1. The migration rates from dune tracking and orientations of dune lee slopes indicate a clockwise pattern of sand transport around East Nash Sands.

2. Sand transport fluxes derived from dune tracking are broadly comparable with those calculated from current meter data. This correspondence suggests that sand transport along the flanks is dominantly driven by tidal currents.

3. Waves breaking over the crest of the bank control the crestal platform morphology. Cross-bank sand transport fluxes predicted from wave regime measurements (Section 4.4.3) suggest that breaking waves dominate sand transport over the crest.

4. Fast migrating dunes were observed in Nash Passage on the basis of repeated surveys separated by only 19 days. Dunes here could not be correlated from data collected in surveys spaced by 263 days. This is interpreted as the result of the rapid evolution of dune morphology expected from large translations due to strong currents which may have lead to the under-estimation of individual fluxes.

5. The bank parallel flux for the southern flank is almost the same as that for the northern flank (both derived by dune-tracking). Sand is transported from the northern flank to the south flank through Nash Passage, but tracking derived fluxes seem too small to balance the budget.

6. The pattern of bathymetric changes computed from the Continuity Equation (Equation 4.6) using the dune-tracking fluxes is roughly similar to that computed by differencing profiles generated from the multibeam and single-beam data. This is interpreted as suggesting that uncertainties of the method do not dominate the derived flux pattern and that the fluxes derived from the dune tracking do indeed largely represent the movements of sand around East Nash. However some small differences, particularly for the south flank and the Nash Passage could represent a component of suspended transport.

Chapter 5.

Discussion: Comparing Helwick with Nash Sands

5.1. Introduction

The present chapter aims to compare the morphology and sand dynamics of the two banks in order to investigate the potentially contrasting effects of different wave and tidal climate on them and speculate on the banks longer term morphological evolution.

The large-scale morphology of Nash and Helwick Sands sites will first be compared, including historical data (~50 years). Then the relative magnitudes of sand transport flux will be contrasted and discussed along with the tidal current and wave characteristics. How sand dune morphology for each bank responds to differing flow will be assessed based on geo-statistical characteristics computed as described in Section 2.4.

These comparisons along with the results in Chapter 3 and 4 will allow general implications to be drawn on the understanding of the maintenance of banner sandbanks with their respective headland. The chapter will finally conclude by recommending further work and discussing remaining unanswered questions concerning the origin and evolution of banner sandbanks.

5.2. Is the morphology of the Helwick and the Nash Sands indicative of their evolution?

In Figure 5.1, which compares the morphology of East Nash and East Helwick Sands, bathymetry is plotted with depth relative to the Lowest Astronomical Tide (Chat Datum). Mean Low Water Springs (MLWS), which gives an average of the lowest level of the water over a long period (typically two decades), is shown on profiles i to iv for both banks. LAT is the lowest water level under average weather conditions and any combination of Sun-Moon-Earth geometry. Similarly the Highest Astronomical Tide (HAT) is corresponding to the highest water level. LAT and HAT are respectively 0.16 m and 10.54 m at the Mumbles Site and -0.20 m and 12.98 m at the Hinckley Point Site. Thus the western area of the Bristol Channel has a somewhat smaller tidal range (maximum tidal range of 10.38 m at the Mumbles) compared with the eastern area (maximum tidal range of 13.18 m at Hinckley Point).

The eastern ends of the banks are morphologicaly similar in a number of respects. They are both located on the ebb lee side of the headland. At both sites, limited signs of the development of sand deposits were observed on the flood lee side of the

headland (eastern side). Both banks have a swale between the headland and the bank (Helwick and Nash Passage). Their across-bank asymmetric geometry is similar, with steeper southern flank in both cases. The pattern of dune orientation and direction of migration is similar. However, the eastern ends of the banks differ morphologically in some ways. The surrounding area is deeper around the Helwick Sands (30 to 40 m) than around the Nash Sands (15 m). Water-depth is considered to limit the vertical development of sandbanks (Huthnance, 1982b; Harrisson et al., 2003), hence, the Helwick Sands has a height of 30 m compared to 15 m for Nash Sands. The broader and flatter across-section of Nash Sands (Figure 5.1, profiles iii and iv) compared to those of Helwick Sands is suggested to result from the relatively strong cross-bank flux caused by breaking waves (Section 4.5.1) continually moving sand to the northern side of the bank. Despite any formal way to determine the accuracy of the cross-bank estimates of Sections 4.5.1 and 3.3.3, this interpretation is consistent with the more intense cross-bank sand flux across East Nash (0.0065 $kg.m^{-1}.s^{-1}$) compared with East Helwick (0.0007 $kg.m^{-1}.s^{-1}$).

Based on the orientation and migration of dunes on the flanks of both banks, a zone of bed shear stress convergence towards the bank crests is predicted. On the inshore flank of both banks, sand transport is oriented towards the headland, while on the offshore flank sand transport is oriented away from the headland (Figures 3.14 and 4.13). The zone of bed shear stress convergence is most pronounced on Helwick Sands with dune crests veering to be more parallel to the bank along its crest. In both cases, this zone of bed convergence extends to the sub-tidal limit of the headland bedrock. Hence, sand transport occurs as far as the headland bedrock. There, sand transport is intense, most especially for Nash Sands (dune migration-derived flux of up to 0.15 $kg.m^{-1}.s^{-1}$, Section 4.3.4).

The general pattern of sand transport around both the Nash and the Helwick Sands agrees with observations from banner and non-banner sand banks elsewhere (Caston, 1972; Kenyon et al., 1981; Pattiarchi and Collins, 1987; Collins et al., 1995; Lanckneus and De Moor, 1995; Bastos et al., 2002).

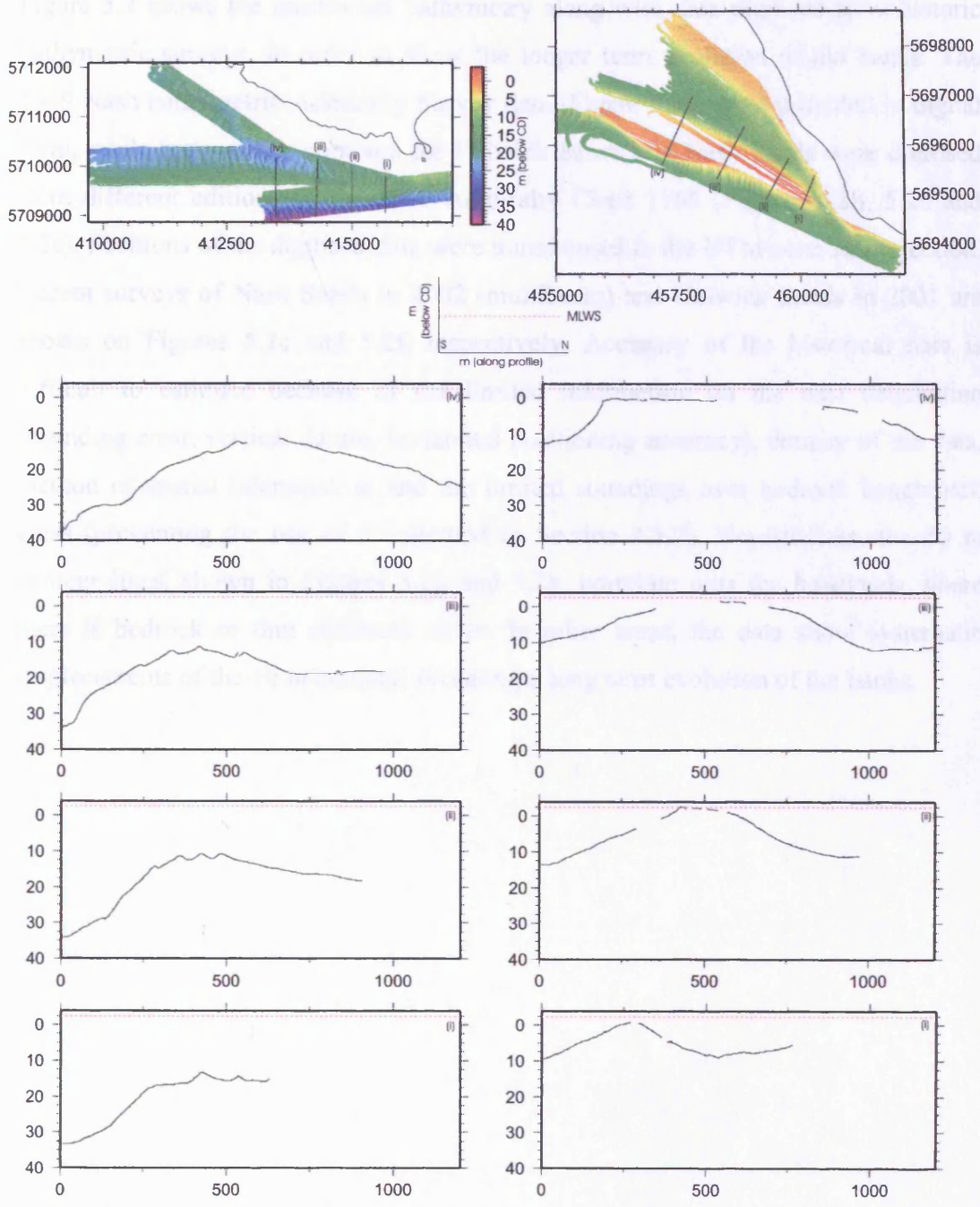

Figure 5.1 Comparison of the morphology of East Helwick (left) and East Nash (right) Sands. Cross-section profiles are plotted with the Mean Low Water Spring (MLWS) marked by dotted red lines. MLWS at Helwick was taken as equal to the Mumbles tide gauge station MLWS (i.e. 0.91m above Chart Datum). MLWS at Nash was taken as the average of Ilfracombe and Avonmouth tide gauge stations MLWS (i.e. 0.98 m above Chart Datum).

Figure 5.2 shows the multibeam bathymetry along with data digitised from historic bathymetric surveys, in order to show the longer term evolution of the banks. The 1949 Nash bathymetric Admiralty Survey data (Figure 5.2a) were provided in digital form, while bathymetric contours for Helwick Sands and Nash Sands were digitised from different editions of the 1949 Admiralty Chart 1165 (Figures 5.2b, 5.2d and 5.3e). Positions of the digitised data were transformed to the UTM zone 30 projection. Recent surveys of Nash Sands in 2002 (multibeam) and Helwick Sands in 2001 are shown on Figures 5.2c and 5.2f, respectively. Accuracy of the historical data is difficult to estimate because of the limited information on the data acquisition (sounding error, vertical datum, horizontal positioning accuracy), density of the data, method of spatial interpolation and the limited soundings over bedrock benchmark areas (preventing the use of the method in Section 2.3.2). Nevertheless, the 10 m contour lines, shown in Figures 5.2g and 5.2h, correlate near the headlands where there is bedrock or thin sediment cover. In other areas, the data show systematic displacements of the 10 m contour, revealing a long term evolution of the banks.

a

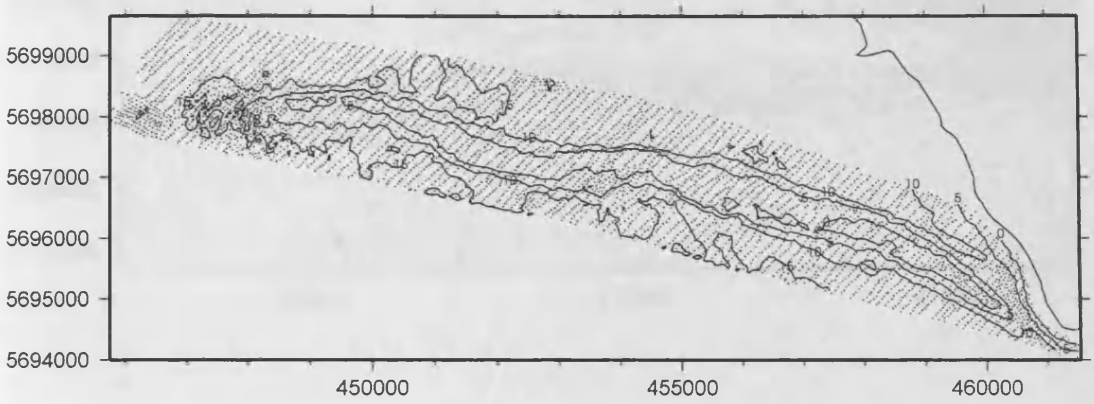
5699000
5698000
5697000
5696000
5695000
5694000
450000
455000
460000

b

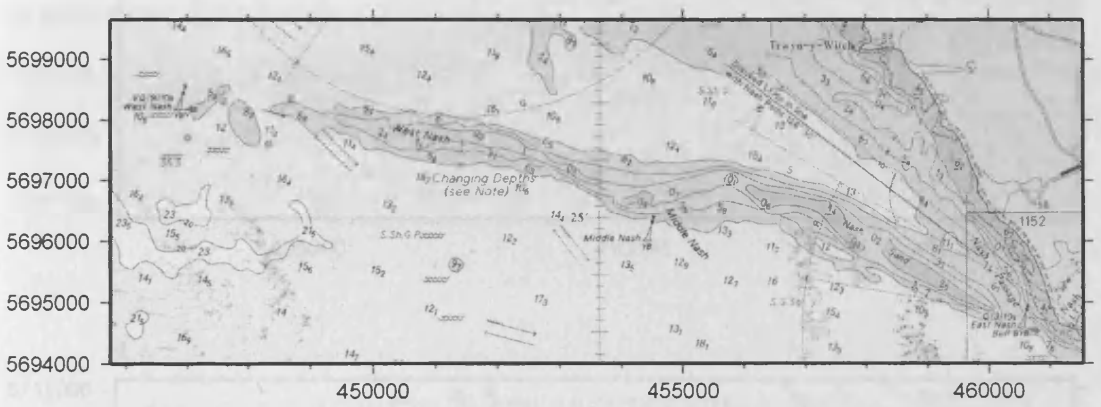
5699000
5698000
5697000
5696000
5695000
5694000
450000
455000
460000
Changing Depths
(see Note)
Middle Nash
1152

c

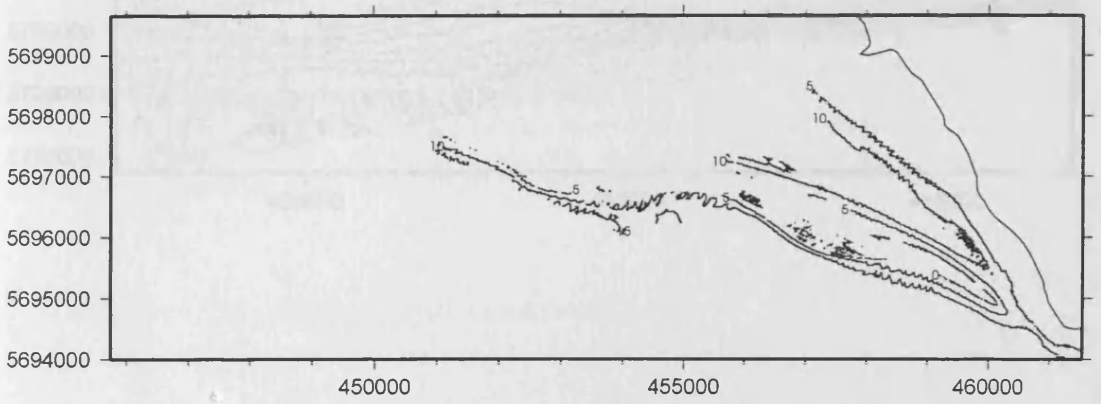
5699000
5698000
5697000
5696000
5695000
5694000
450000
455000
460000

d

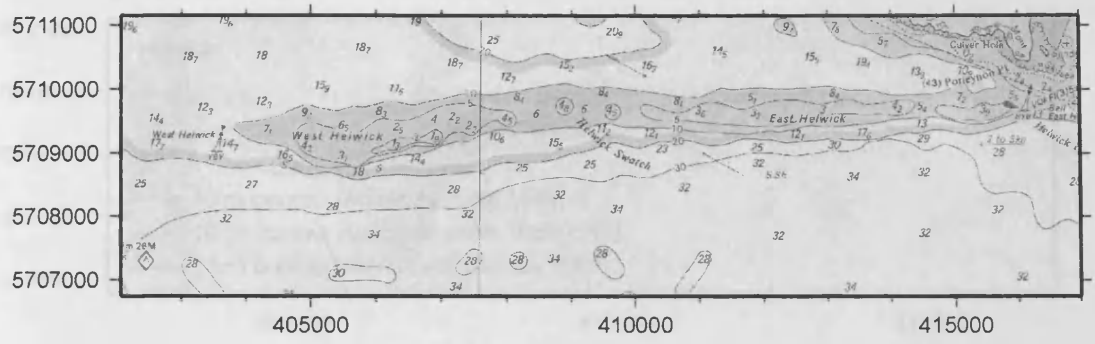
5711000
5710000
5709000
5708000
5707000
405000
410000
415000
West Helwick
East Helwick
Helwick Swatch
Port Eynon Point

e

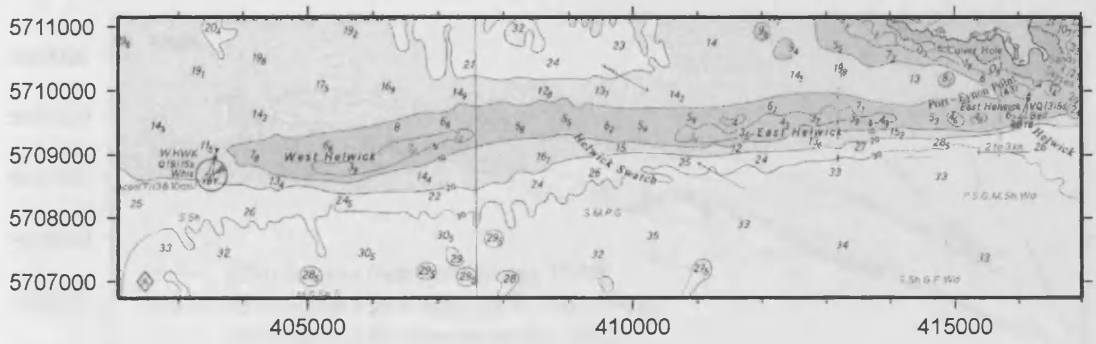
5711000
5710000
5709000
5708000
5707000
405000
410000
415000
West Helwick
East Helwick
Helwick Swatch
Port Eynon Point

f

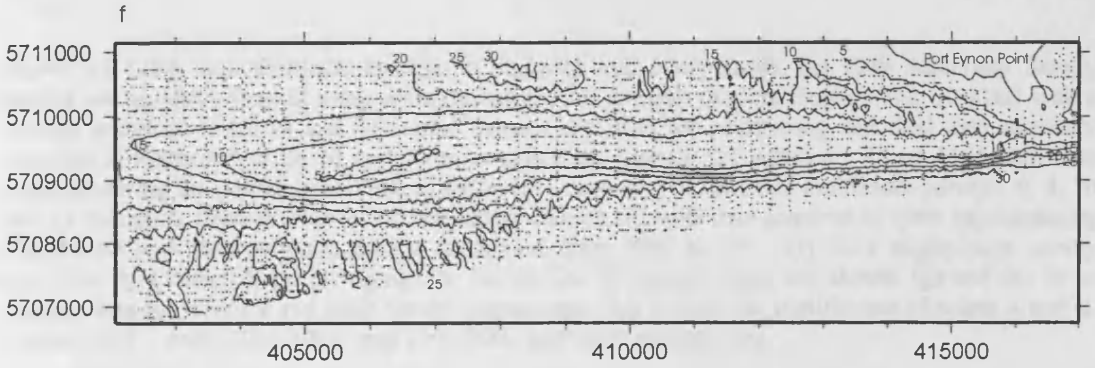
5711000
5710000
5709000
5708000
5707000
405000
410000
415000
Port Eynon Point

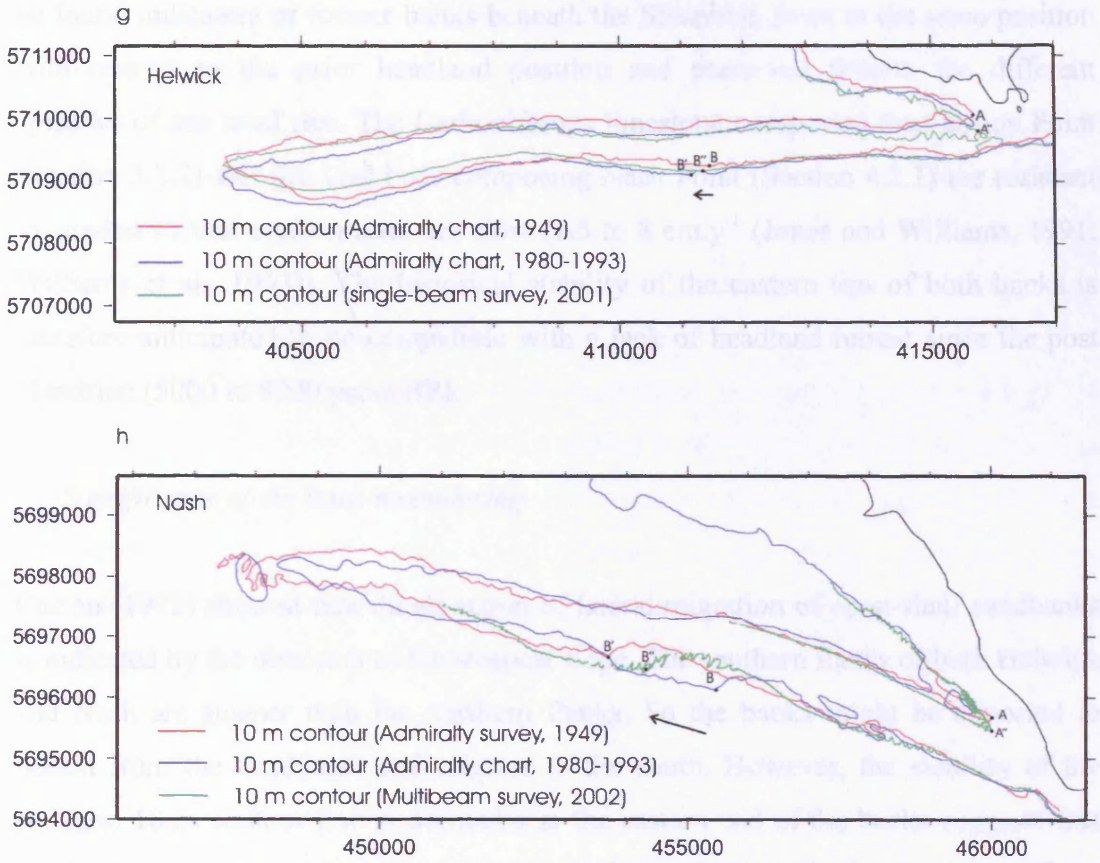

Figure 5.2 Long term planform changes of Helwick and Nash Sands. (a) 1949 Admiralty Survey carried out on HMS Seagull using a single-beam echo sounder (Kelvin Hughes 772, 30 kHz) with a vertical accuracy of 0.5 m and horizontal sextant resection for positioning and tidal data manually recorded at Porthcawl. 0, 5, 10 and 15 m contours are plotted. (b) Admiralty Chart 1165 with data acquired during the period from 1980 to 1993. (c) Composite of the 2002 multibeam surveys. 0, 5, 10 and 15 m contour lines are shown. (d) Admiralty Chart 1165 with data acquired in 1949. (e) Admiralty Chart 1165 with data acquired during the period from 1980 to 1993. (f) 2001 single-beam survey (provided by Llanneli Sand Dredging). 5, 10, 15, 20, 25 contour lines are shown. (g) and (h) 10 m contour lines for Helwick and Nash Sands, respectively. See text for the significance of points A and B. Primes ` and `` denote the 1980s' and 2001/2002 positions, respectively.

Evolution of the easterly termination of each bank.

Changes can be tracked from movement of the eastern ends of the 10 m contours marked A and A'' (Figures 5.2g and h). For Helwick Sands, A moved 58 m to the east to A'' (annual migration rate of 0.97 $m.y^{-1}$). For Nash Sands, A (Figure 5.2h) moved only 6 m to the east to A'' (annual migration rate of 0.11 $m.y^{-1}$). Despite the data uncertainties, these values suggest that the morphology of the easternmost end of each bank is relatively stable. Bastos et al. (2003a) suggested that the stability of banner banks is related to the stability of their associated headland. To support this assertion

he found indicators of former banks beneath the Shambles fixed in the same position with respect to the prior headland position and preserved despite the different episodes of sea level rise. The Carboniferous limestone composing Port Eynon Point (Section 3.2.2) and the Lias beds composing Nash Point (Section 4.2.1) are resistant to erosion so that erosion rates are slow (1.5 to 8 $cm.y^{-1}$ (Jones and Williams, 1991; Williams et al., 1993)). The historical stability of the eastern tips of both banks is therefore anticipated to be compatible with a lack of headland retreat since the post Flandrian (5000 to 8000 years BP).

Significance of the bank meandering.

Caston (1972) showed that the direction of lateral migration of open-shelf sandbanks is indicated by the direction of the steepest slope. The southern flanks of both Helwick and Nash are steeper than the northern flanks. So the banks might be expected to detach from the headlands and migrate to the south. However, the stability of the southern 10 m contour line in particular at the eastern end of the banks suggests that the bank asymmetry arises by other mechanisms. Any southerly migration of the banks caused by flood currents is counteracted by the direction of attack of the waves from the south-southwest and the corresponding cross-bank sand transport. Figure 5.2 reveals the displacement of the plan view sinuosity along the banks. Along the Helwick crest, this sinuosity is characterised by a ~4 km wavelength (2 inflexion points) and amplitude of 80 m. The Nash sinuosity has a wavelength of ~10 km (1 inflexion point) and amplitude of ~180 m. The temporal evolution of each bank is illustrated by movements of the points marked B, chosen where the 10 m southern flank contour line has maximum convexity to the north. The Nash point B migrated from UTM E453700 m, N5696670 m (1949), to UTM E455450 m, N5696125 m (1980's) and to UTM E454330 m, N5696410 m (2002). The Helwick, point B (chosen with the same geometrical criteria) is harder to locate as the morphological signature of the sinuosity is less well pronounced. Point B migrated from UTM E411430 m, N5709250 m (1949), to UTM E411130 m, N5709100 (1980's), to UTM E411330 m, E5709160 m (2001), which is much less than the Nash 'B' point. Aliasing (fast migration of the sinuosity compared to the long period between the different datasets) did not allow a determination of the period of migration of the sinuosity. However, the banks do not appear to break up as has been hypothesised by

Caston (1980) and proposed by Harris (1988a) for the neighbouring Scarweather Sands.

Although the sand flux records span only a short temporal interval, it is interesting to relate the transient patterns of sand deposition and erosion to the temporal oscillation of the banks. The mechanism behind the evolution is proposed as follows (Figure 5.3) for the southern flanks. (1) Sand accumulates in a local area near the headland along the southern flank as the response of the convergence of sand fluxes (Sections 3.5.5 and 4.5.4) (2) The bed shear stress increases because of a correlated increase of the flow velocity towards the top of the accumulation causing more sand to deposit on the lee side of this deposit. As the general sand transport pathway is oriented to the west along the southern flank (ebb-dominated), the sand deposit migrates westward. This phenomenon will cause the sinuosity of the bank to migrate to west.

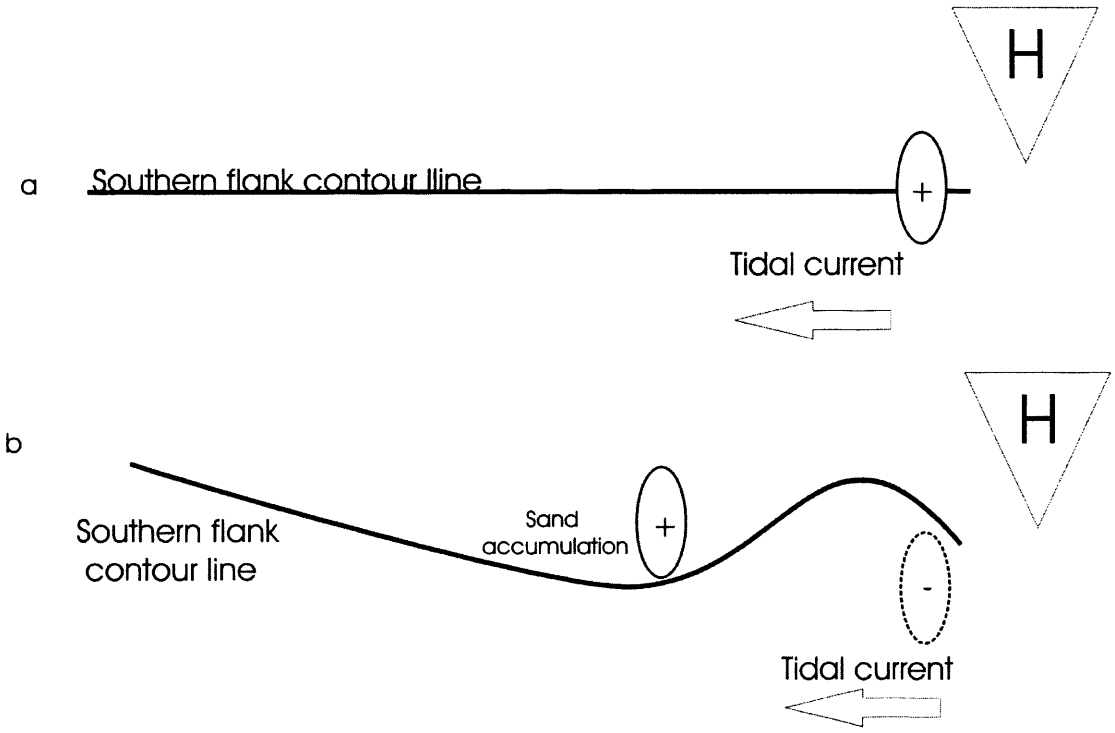

Figure 5.3 Conceptual model relating transient patterns of sand deposition/erosion near the headland (H) with the evolution of the bank sinuosity. The lines represent the mobility of a contour line along the southern flank. Thick arrows represent the direction of the dominant tidal current. (a) A Transient pattern of sand deposition first occur near the headland (marked "+") (b) This original pattern of sand deposition migrates westward while further sand is deposited on its lee side on its lee side, causing the sinuosity of the bank to develop and migrate in the same direction

5.3. How are the kinematics of the East Helwick and East Nash comparable?

All the specific fluxes computed from the migration rates and dune morphology of the sand dunes between the different bathymetric surveys (Sections 3.3.2.2 and 4.3.3) are contrasted in Figure 5.4. The data were grouped by morphological areas as defined in Sections 3.5.4 and 4.5.3: northern and southern flanks of each bank, passage and nearshore areas. The Helwick Passage was difficult to delimit morphologically. Its extent was defined by a rectangular area delimited by UTM 57109595 m on the north (northern limit of the bank as defined in Section 3.2.2), UTM 5709600 m on the south (crest of the Helwick as observed on Figure 3.4a), UTM 416000 m on the east (eastern limit of the flux sampling area along the northern flank) and UTM 417000 m on the west (1000 m from the border of the western border of the headland as shown on Figure 3.16 and discussed in Section 3.3.2.2.3). Spatially averaged values for each of the morphological areas are reported in Table 5.1 and histograms of all the data are displayed on Figure 5.5 (solid dot mark the mean average).

Area	Mean average sand flux magnitude ($kg.m^{-1}.s^{-1}$)	Sand flux magnitude standard deviation ($kg.m^{-1}.s^{-1}$)
Nash		
North flank	0.0262	0.0080
South flank	0.0514	0.0307
Passage	0.018	0.0219
Nearshore	0.0052	0.0037
Helwick		
North flank	0.023	0.0123
South flank	0.026	0.0186
Passage*	0.018	0.0125

Table 5. 1 Statistical characteristics of the population of sand transport fluxes in Figure 5.4. *The Helwick Passage was extracted from the north flank population (see text for details).

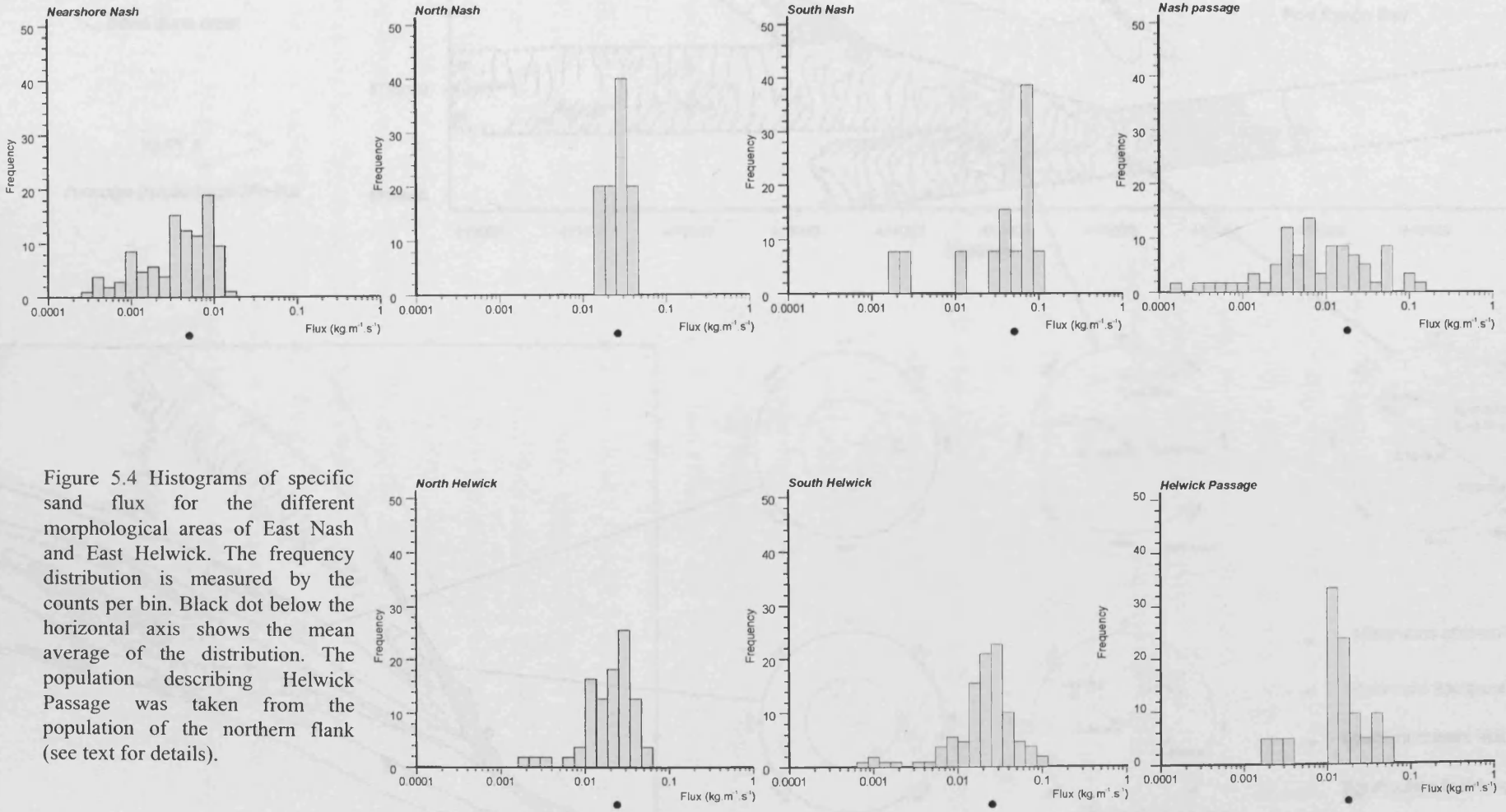

Figure 5.4 Histograms of specific sand flux for the different morphological areas of East Nash and East Helwick. The frequency distribution is measured by the counts per bin. Black dot below the horizontal axis shows the mean average of the distribution. The population describing Helwick Passage was taken from the population of the northern flank (see text for details).

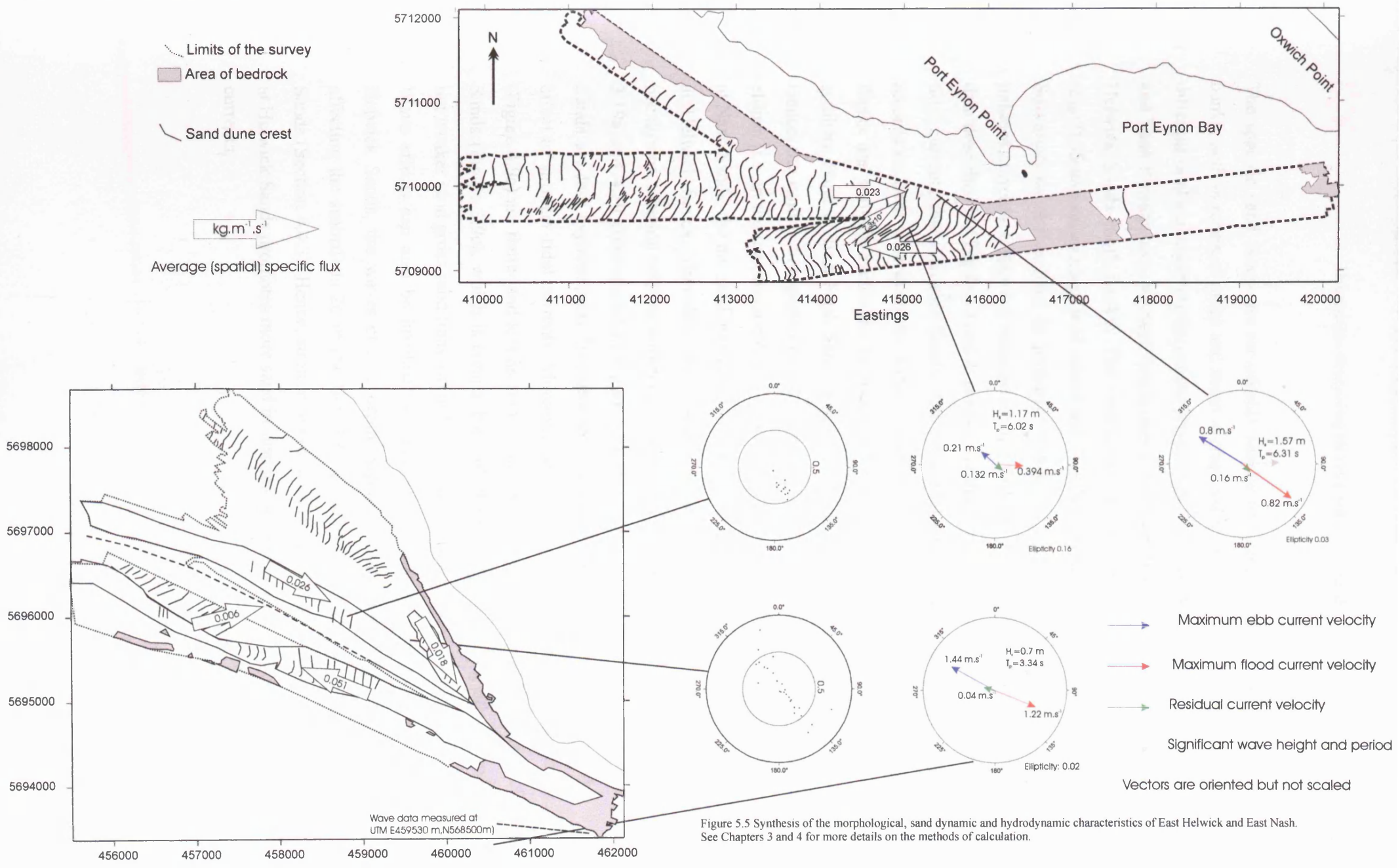

Figure 5.5 Synthesis of the morphological, sand dynamic and hydrodynamic characteristics of East Helwick and East Nash. See Chapters 3 and 4 for more details on the methods of calculation.

The specific sand fluxes are remarkably similar for corresponding areas of the two banks, both in terms of range and mean average value, which is surprising given their different tidal and wave environments (Figure 5.5). The East Nash Sands (both flanks and Nash Passage area) average flux is only 15% bigger than the average flux for East Helwick Sands (both flanks). The sand texture on both banks is relatively similar (d_{50}=0.35 mm on average, well sorted and slightly skewed, Sections 3.4.1 and 4.4.1). So variations in flux must be primarily related to variations in the tidal and wave-induced currents. Figure 5.5 summarises morphologic, sand fluxes and hydrodynamic data described in Chapters 3 and 4, confirming that Nash Sands is exposed to stronger tidal currents than Helwick Sands. The peak tidal current velocities for the longer records on both sites differ by 43% in magnitude. Moreover, tidal flows along the flanks are strongly rectilinear (ellipticity of 0.02 and 0.03, respectively along the southern flank of East Nash Sands and the northern flank of East Helwick Sands). Hence, the sand is transported primarily in the direction of the long axis of the tidal ellipse (i.e. in the maximum ebb and flood current directions). With stronger currents at Nash Sands, the net sand transport is larger during individual stages of the tide than at Helwick Sands. Therefore, the similarly specific sand fluxes presumably arise because of differing tidal asymmetry or wave influence. The tidal currents of Figures 3.19a and 4.19 (reproduced in Figure 5.5) show that the tidal currents near Nash Sands are less asymmetrical than near the Helwick Sands, hence counteracting the effect of stronger tidal currents. Moreover, sand dunes on the flanks of Nash Sands (Figure 4.9c) are flatter and less asymmetrical than those along the flanks of Helwick Sands (Figure 3.9c), which is compatible with the influence of strong tidal currents but weaker sand gross sand transport at Nash Sands, because of the reverse current.

Wave effects can also be invoked to explain the similar specific sand fluxes. At Helwick Sands, the waves closure depth (significant orbital motion of the waves affecting the seabed) is 26 m (Section 3.4.3), comparable with 9 m only for Nash Sands (Section 4.4.3). Hence, stronger wave-induced currents for a given water depth at Helwick Sands promotes more sand in suspension, which is then carried by the tidal currents.

5.4. Comparing dune morphology between the two banks

How dune morphology depends on the flow characteristics (water depth, velocity, directionality) has been shown (Allen, 1968; McCave, 1971; Yalin, 1977; Englund and Fredsoe, 1982; Dalrymple, 1984; Deigaard and Fredsoe, 1987; Flemming, 1988; Gabel, 1993; Kostaschuk and Villard, 1996; Flemming, 2000; Le Bot et al., 2000; Blondeaux, 2001; Hulscher and Van den Brink, 2001; Idier et al., 2002; Santoro et al., 2002; Best et al., 2003; Francken et al., 2004; Wienberg and Hebbeln, 2005 and in Section 1.4.2). Sections 3.3.3.1.2 and 4.3.2 have shown that some dependence exists between the geometry of the dunes and the associated water flow.

The morphology of dunes from the two banks is now compared using the method developed in Section 2.4.2 in order to describe their responses to the flow. Figure 5.6 shows the results of the autocorrelation and semi-variogram methods applied to dunes associated with both flanks and near the crest of each bank (Figure 5.3a). The method used to estimate the dune orientation, spacing, height and regularity parameter are as described in Section 2.4 and the results are given in Table 5.2

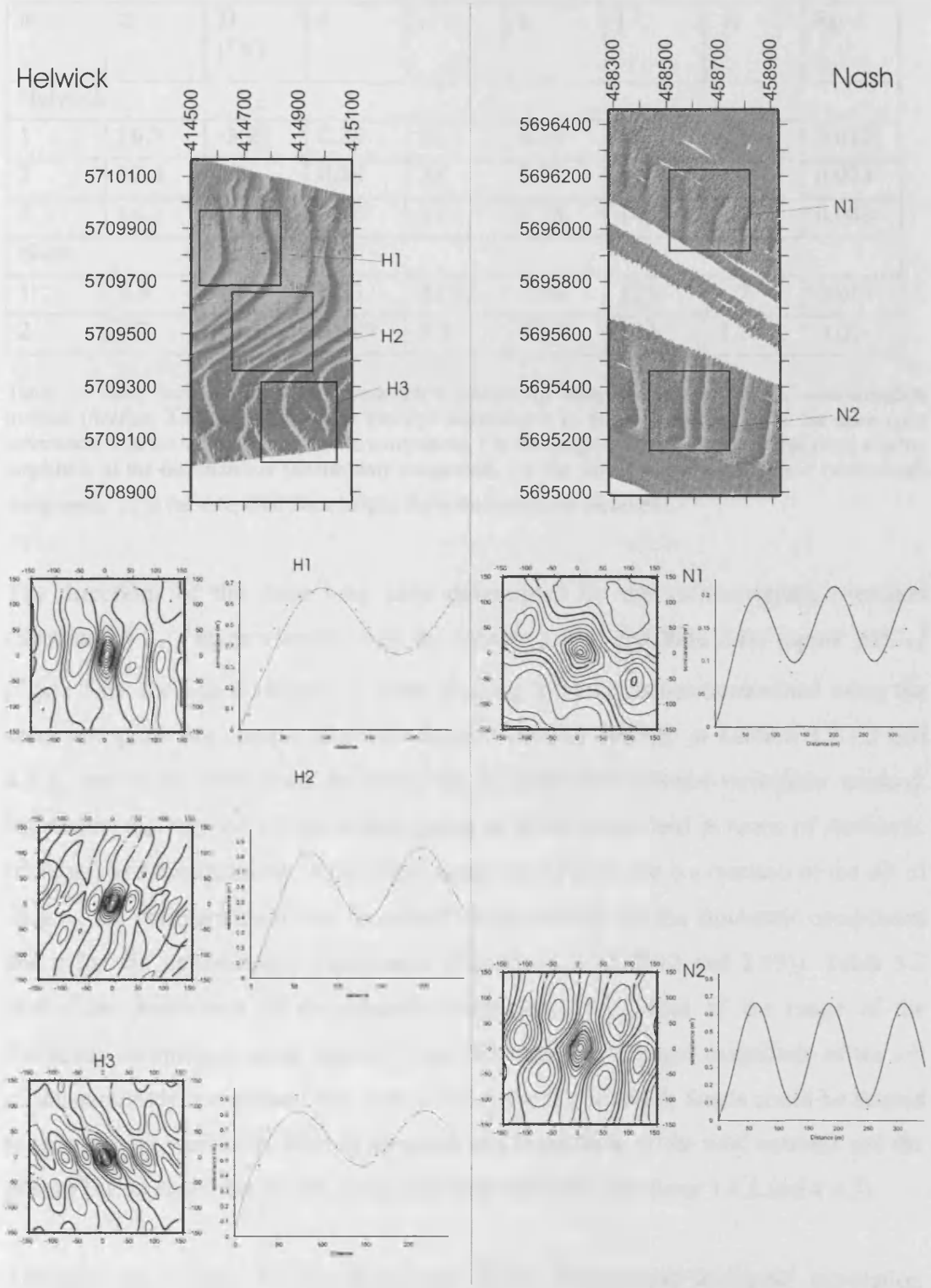

Figure 5.6 Comparison of sand dune morphology between Helwick Sands (left) and the Nash Sands (right) using the statistical method developed in Section 2.4. For each sandbank areas were chosen to represent the dune on the flanks and, for Helwick, the crest of the bank. For each area, the orientation of the axis of the dune was determined using the longer axis of the autocorrelation function (left in each column). Experimental (cross) and modelled (plain line) semi-variograms were computed perpendicular to the axis of the dune (right graph in each column). Results are reported in Table 5.2.

#	z	D (°N)	s	r	a	l	$\widetilde{H}$	Rp
Helwick								
1	16.3	-3.29	0.36	34	0.17	185	1.8	0.017
2	12.4	27	0.39	26	0.23	131	1.9	0.024
3	14.1	148.66	0.46	14	0.18	147	2	0.048
Nash								
1	3.3	7.92	0.23	31.22	0.24	125	1.7	0.017
2	6.7	13.3	0.099	9.8	0.128	123	1.13	0.03

Table 5.2 Sand dune morphological parameters interpreted using the autocorrelation/semivariogram method (Section 2.4.2) z refers to the average water-depth in the studied area. D is the dune crest orientation, s is the sill of the stochastic component, r is the range of the stochastic component, a is the amplitude of the deterministic (sinusoidal) component, l is the period of the deterministic (sinusoidal) component, $\widetilde{H}$ is the estimated dune height, Rp is the regularity parameter.

The directions of the dune long axes determined by the auto-correlation method (Section 2.4.2.1) agree visually with the orientation of the dune crest (upper part of Figure 5.6). Estimated Height ($\widetilde{H}$) and spacing (l) of the dunes determined using the semi-variogram are comparable with those measured directly in Section 3.3.1.2 and 4.3.2, providing confidence in using the auto-correlation/semi-variogram method. Moreover, this method allows a description of sand dunes field in terms of stochastic (random) and deterministic (sinusoidal) components from the comparison of the sill of each of the components of the modelled variograms (s for the stochastic component and a for the deterministic component (Equations 2.11, 2.12 and 2.13)). Table 5.2 shows the dominance of the periodic component, as values of the range of the stochastic component never exceed 40 m. Nonetheless, stronger magnitude of the sill of the stochastic component for Area 2 and 3 for the Helwick Sands could be related to the stronger variability both in direction and magnitude of the tidal currents and the greater influence of the waves, especially near the crest (Sections 3.4.3 and 4.4.3).

Although found only for uni-directional flows, Robert and Richards' correlation (Figure 2.25) suggests how the running tidal current may tend to affect the regularity of the dunes, with more regularity (large Rp) where the current is fast (large U) and/or shallow (small z). The regularity deduced from the data actually decreases going from deep areas to shallower, which is the opposite trend to that expected from Robert and Richards. Flow acceleration might be expected because of the tide being forced

through a narrow depth interval across the bank crest (Huthnance, 1982a,b), but this also suggests the opposite trend (increasing U and therefore increasing Rp) to that observed (decreasing Rp). Possible explanations could be that increasing relative influence of friction dominates here, slowing the current onto this part of the bank, or that other effects cause irregular dunes, such as stronger wave effects in shallow water.

5.5. Implications of the present work to the general understanding of banner sandbanks

The origin of banner sandbanks has been generally attributed to the presence of a near bed flow convergence within a large eddy in the tidal residual current, which is induced by the presence of the associated headland (Sections 1.2.1, 1.3.1.3 and Pingree, 1978; Pingree and Maddock, 1979). The sense of sand circulation as deduced from dune asymmetry and migration for both East Helwick Sands and East Nash Sands is away from the headland on the offshore flank and towards the headland in the nearshore flank. Hence, sand is transported around the banks in a similar pattern to Pingree's predicted near bed residual flow circulation. Although this model might explain the formation of a banner sand bank, the concept of an idealised eddy system in the residual current can not be used to explain the maintenance of banner sandbanks because Pingree did not take into account the influence of the bank after it has grown (Section 1.3.2.3 and Signell and Harris, 2000; Bastos et al., 2003b; Kenyon and Cooper, 2004).

The combination of multiple mechanisms in the maintenance of banner sandbanks must be invoked as suggested by Pattiarchi and Collins (1987). These mechanisms include the generation of transient eddies (Signell and Geyer, 1991 and Sections 1.2 and 1.3.2.3), bottom friction induced by the bank (Huthnance, 1982b; Huthnance, 1982a; Bastos 2003b; Bastos 2004 and Sections 1.2 and 1.3.2.2) and the presence of helicoidal (in the vertical plan) flows (Houbolt, 1968; Heathershaw, 1981 and Section 1.3.2.1). Despite the lack of extensive hydrodynamic field data measurements to test the existence of these mechanisms in the water flow circulation, morphological evidence for their presence can be found in the bathymetric data. Morphological

evidence of the effect of bottom friction induced by the sandbank is seen in the veering of dune crests towards the crest of the bank, most especially in the case of the Helwick (Section 3.3.1.2). Morphological evidence of helicoidal flows could be speculatively deduced from the asymmetric cross-section of the banks. From the short-term (over one spring tidal cycle) sand transport dynamic investigation over the Shambles banner sandbank, Bastos et al. (2004) argued that these different mechanisms may occur at different stages of the tidal cycle. In the case of the Shambles transient tidal eddies form on the lee side of the headland during the flood phase. During the ebb phase, sandbank-induced bottom-friction is the dominant process. As the flow geometry with respect to the headland is relatively similar, similar mechanisms may occur at the Helwick and at the Nash.

The geometry and magnitude of sand transport flux from dune-tracking (Figures 3.16 and 4.13) and the succession of deposition and erosion areas computed using the Continuity Equation (Sections 3.5.5 and 4.5.4) suggest that the pattern of sand erosion or deposition are transient. Such spatial variations of the sand transport flux have also been obserevd associated with the dispersive sand transport related to the presence of the transient eddies originating in the flow at the vicinity of an idealised Gaussian-shaped headland (Signell and Geyer, 1991; Signell and Harris, 2000).

This study has also demonstrated from morphological evidence and flux estimates that the dissipation of wave energy over the crest of Helwick and Nash (breaking waves) must be taken into account as a mechanism for transfer of sand across-bank. Wave-induced across-bank sand transfer has been mentioned (Bastos et al., 2003b) to enhance sediment transport in the case of banks near Portland Bill, which lie at about 25 m water-depth. For shallower water-depths such as those of Helwick Sands or Nash Sands, wave induced across-bank sand transport has a significant effect on the overall circulation of sand. It contributes to supplying sand to the north flank where it helps to replenish sand removed by strong tidal currents and thus helps to maintain the bank connected with the headland.

5.6. Limitations of the present work and recommendations for further investigations

In this project, observations of migrating sand dunes were used to derive sand transport fluxes around the tips of sandbanks. The method used to measure these fluxes is based on an assumption that the dunes maintain their shapes while migrating (Section 1.4.4). However, dunes in practice do change shape. Varied effects of the turbulent flow over them affect their morphology (Kostaschuk and Church, 1993; Bennett and Best, 1995; Kostaschuk and Villard, 1999; Best et al., 2004 and Section 5.4). Moreover, small dunes superimposed on the bigger ones do participate actively in the sand transport (Beck et al., 1991; Whitehouse et al., 2000). Those could not be tracked between the surveys because of the limitation of the resolution of the multibeam survey. The relatively good agreement between the areas of deposition/erosion derived from the divergence of the flux of sand transport and the simple differencing of consecutive surveys indicates that sand transport is essentially carried by the bigger dunes. Hydrodynamic (current and wave) data collected over a broader spatial extent and more continuously would benefit the understanding of the sedimentary mechanisms occurring at both the dune scale and at the bank scale. For example, Kostaschuk et al. (2005) presented the benefits of using Acoustic Doppler Current Profilers to measure the flow within the whole water column. ADCP measurements in the vicinity of Port Eynon Point and Nash Point would allow better constraining of Equation 1.25 (variation of the shape factor f), hence providing a better estimate of sand transport. They would also be valuable in in describing the short-term (over an individual tidal cycle) flow structure and confirm the presence of headland induced transient eddies, which have been observed previously (Bastos et al., 2004; Duffy et al., 2004). Using simultaneous ADCP measurements and multibeam data could potentially show the relation of transient sediment accumulation/erosion patterns (Section 4.5.4 for the Nash and more clearly in Section 3.5.5 for the Helwick) to changes in the flow structure. Moreover, Kostaschuk et al. (2005) also describe the potential of using ADCP to measure simultaneously the bedload flux from the difference of the velocity measured by the ADCP bottom tracking measurements and the boat DGPS, as well as the suspended load from the intensity of the acoustic return. Despite limitations due to the ADCP beam geometry and lack of calibration, the possibility of measuring the flow and sediment transport

characteristics simultaneously offers advantages over the use of conventional optical/acoustic flow/sediment load sensors This would particularly address the existence of a lag effect between the tidal current and the sediment transport (Stride, 1963). This effect consists of a lag effect in the direction of the sand transport with respect to the peak tidal flow direction. In the present work the migration of sand dunes was estimated to be in the same direction than the peak flow, which is often supposed.

Also, with the measurement periods used here (278 and 328 days for the Helwick; 19 days and 263 days for the Nash), it is questionable as to how representative such measurements are of the long term (decades or centuries) stability of the studied areas. Further high resolution bathymetric surveys would be highly beneficial in determining the relation between the long-term morphological changes of the sandbanks and the transient movements of the associated sand dunes. Hence, more frequent multibeam surveys (monthly on a long period of time, typically decades), complemented by concomitantly acquired ADCP data, are suggested to study further the maintenance of banner sandbanks and the kinematics of associated sand dunes. This method would provide the opportunity to investigate in more detail the effect of the flow structure on sand transport and hence on the morphology and kinematics of the bedforms (banks and dunes). In the case of the atypical sand dunes connected across the crest of Helwick Sands (Section 3.5.3), such a method would allow a more accurate quantification of the relative importance of wave- and current-driven transport mechanisms illustrated in Figure 3.23.

Dawson et al. (2004) documented evidence for an increase of North Atlantic storm frequency since circa AD 1400 and Figure 1.13 suggests that the Bristol Channel is prone to at least one strong storm (winds with a ground speed above 30 $m.s^{-1}$) per year. Erosion of the bank crests (by wave-currents) and increasing sand drift (from enhanced suspension) can be expected from increased storm frequency. Acquisition of "pre-storm" and "post-storm" bathymetric data could provide further insights on the morphological response of the banks. Houthuys et al. (1994) observed the lowering of the dunes over the crest of Middelkerke Bank and a broadening of the bank (deposition along the flanks) between two surveys undertaken before and after a storm (82 days apart). In that investigation, difficulties were encountered in unravelling morphological changes induced by the storm from those occurring during fair-

weather. This point also highlights the interesting question of the recovery time for banner banks to return to a state of dynamic equilibrium after a storm.

Finally, the question of the origin and development of both Nash and Helwick Sands remains still not fully answered and could involve a purely hydrodynamic hypothesis or a structural/topographical control. The hypothesis of a structural/topographical control could be tested by seismic surveys of both banks. However, poorly consolidated sand composing active sandbanks present a challenging environment in terms of penetration of the signal and resolution of internal stratigraphy. A seismic survey of the Helwick was undertaken by Britton (1978) but was unable to map unambiguously the underlying surface or delineate internal stratigraphic horizons. This was attributed to the limited penetration of the acoustic energy of the ORE pinger 1036 used for the survey (frequency of 3.5 kHz and power of the pulse of 500 Joules). Berné et al. (1994), Marsset et al. (1999), Reynaud et al., (1999b), Chaumillon et al. (2002) and Chaumillon et al. (2003) have more successfully delineated the internal structure of active open-shelf sandbanks (6 to 30 m water-depth) using Boomer/Sparker sources with high frequencies (1-10 kHz) and energy (700 Joules). Moreover, Reynaud et al. (1999b) have delineated the stratigraphic architecture of Kaiser Bank in the Celtic Sea with a Sparker coupled with a single channel streamer. They related the morphology of the different seismic units with the relative influence of the variation of sea-level, tidal and wave current intensity. From the data, they were able to show that the bank did not grow about a pre-existing topographic feature. These studies highlight the need for high quality seismic data, preferably coupled with coring, to resolve the origin of these features.

Chapter 6.

Principal conclusions

This thesis has presented the results of a study of sand dune dynamics and sedimentary processes at the connection of banner sandbanks (East Helwick and East Nash Sands) with their respective headlands, based on repeated high-resolution bathymetric surveys. These data, combined with sedimentary (grain size samples) and hydrodynamic (current and wave) data, prompted conclusions on the mechanisms of sand transport outlined in the following pages. First, advances in technique are outlined.

Sand transport mapping techniques

1. The first repeated multibeam swathe bathymetry surveys near headland-connected sandbanks have allowed an investigation of their complex morphology along with the morphology of the associated dunes.
2. A method for evaluating vertical bias and variability between repeated surveys directly from the data was developed. Such an error budget assessment provides the basis of any quantitative comparison of the bathymetric changes. This method relies on differencing patches of co-located survey data collected over a bedrock area used as a "benchmark". Progressive filtering of the data at different spatial length scales then shows different influences on the data.
3. Sand dune migration measured by tracking dunes coupled with their morphology was used to estimate specific flux of sand transport. The data computed herein provide specific sand transport flux vectors for both banks. Moreover, bathymetric changes computed from divergence of the specific fluxes using the Continuity Equation compared well with those measured independently from the difference of bathymetric surveys. Generally, differences in bathymetry derived by the two methods lie between -2 to 2 $mm.d^{-1}$ and provide confidence in the derivation of the specific fluxes from the dunes migration. However, uncertainties arise from the assumption that dunes migrate without changing their shape, and hence, the relative proportion of bed-load and suspended load could not be estimated.

Sand dune morphology and dynamics

4. Sand dune asymmetry and migration rates (ranging between 7 $m.y^{-1}$ and 715 $m.y^{-1}$) show a clockwise pattern of sand transport around these banner sandbanks. Net sand transport is oriented away from the headland along the offshore flank (ebb dominated) and towards the headland along the inshore flank (flood dominated).

5. Steep sand dunes are found along the flanks of the bank, while in places flatter sand dunes occur near the crest. This is interpreted as the result of stronger asymmetrical tidal current carrying sand predominantly as bedload, along the flanks and the combination of tidal currents (reaching the upper flow regime over the crest) with wave-induced currents at the crest, inducing stronger erosion and enhancing suspended sand transport.

6. Sand dunes laterally connect over the crest of Helwick Sands and have symmetrical profiles. The connection is curious as dunes on opposite flanks migrate in opposite directions. The elongation and connection of the sand dunes across the bank is primarily explained by the orientation of the average wave propagation which is almost exactly parallel with the dunes crest.

Hydrodynamic processes and sand dynamics

7. Sand transport fluxes derived by dune tracking along the flanks are comparable with those calculated from current meter data and using a well-established bedload formula. These results suggest that sand transport along the flanks is dominantly driven by tidal currents as bedload.

8. The average sand transport fluxes along both flanks of Nash Sands only exceeds the corresponding average flux for Helwick Sands by 15%, despite the stronger currents at Nash Sands. The smaller asymmetry of the tidal flow

at Nash Sands combined with a weaker wave regime induces a lower gross sand transport than might be expected from peak currents.

9. Net cross-bank sand transport is the result of the combined effect of the across-bank component of the tidal current and wave-driven currents. The average wave regime in the Bristol Channel transports sand in a north-easterly direction, from the southern flank to the northern flank. Shoaling and wave breaking occurs across the Nash crestal platform, limiting the vertical development of the bank and potentially inducing stronger across-bank sand transport there compared to the Helwick site.

10. Transient patterns of accretion/erosion have been revealed from the geometry of the dune tracking-derived sand flux vectors. These transient patterns could likely be related to the transient pattern of eddies in the flow also observed near other headland connected sandbanks.

Banner sandbanks maintenance with the shore

11. The idea that a residual tidal current eddy on the lee side of the headland maintains banner sandbanks appears to be too simplistic. Multiple mechanisms involving the generation of transient eddies system in the flow, bottom friction caused by the topography of the banks and across-bank wave-induced current must be considered. Morphological and sand dynamic evidence found in the data support the presence of these processes.

12. Over the period studied (2001-2003), East Nash and East Helwick Sands have been moderately stable features. The bank parallel components of the sand budget determined from dune tracking are roughly balanced and support the concept of dynamic equilibrium.

13. Based on long term (decadal) changes in the morphology of Helwick and Nash Sands, it has been shown that both banks have remained at stable distances from the coast. A plan view sinuosity of the banks was found to migrate. It is believed that bathymetric instabilities, originating as deposition/erosion

patterns near the headland, propagate along the transport path parallel to the bank.

References

A

Akal, T. and Hovem, J., 1978. Two dimensional space series analysis for sea-floor roughness. Marine Geotechnology, 3(2): 171-182.

Aliotta, S. and Perillo, G.M.E., 1987. A sand wave field in the entrance to Bahia Blanca Estuary, Argentina. Marine Geology, 76: 1-14.

Allen, J.R.L., 1968. Current ripples: their relation to patterns of water and sediment motion. North Holland Publishing Company, Amsterdam, 433 pp.

Allen, J.R.L., 1980a. Large transverse bedforms and the character of boundary-layers in shallow-water environments. Sedimentology, 27: 317-323.

Allen, J.R.L., 1980b. Sand Waves: A model of origin and internal structure. Sedimentary Geology, 26: 281-328.

Allen, J.R.L., 1982a. Sedimentary structures. Their character and physical basis. Developments in sedimentology, Volume I. Elsevier scientific publishing company, Amsterdam, 593 pp.

Allen, J.R.L., 1983. River bedforms: progress and problems. In: Modern and ancient fluvial systems, Collinson J.D. and Lewin J. (Editors). Special Publication of the International Association of Sedimentologists. Blackwell Scientific Publication, Oxford, pp. 19-33.

Allen, J.R.L., 2002. Interglacial high-tide coasts in the Bristol Channel and Severn Estuary, southwest Britain: a comparison for the Ipswichian and Holocence. Journal of Quaternary Science, 17(1): 69-76.

Allen, P.A., 1984. Evolution and Mechanics of a Miocene Tidal sandwave. Sedimentology, 31: 63-81.

Allen, P.A., 1997. Earth surface processes. Blackwell Science, Oxford, 404 pp.

Amos, C.L. and King, E.L., 1984. Bedforms of the Canadian eastern seaboard: a comparison with global occurrences. Marine Geology, 57: 167-208.

Anderson, R.S., 1990. Eolian ripples as examples of self-organization in geomorphological systems. Earth science Reviews, 29: 77-96.

Ashley, G.M., 1990. Classification of large-scale subaqueous bedforms: a new look at an old problem. Journal of Sedimentary Petrology, 60(1): 160-172.

Ashton, A., Murray, A.B. and Arnoult, O., 2001. Formation of coastline features by large-scale instabilities induced by high-angle waves. Nature, 414: 296-300.

B

Bagnold, R.A., 1963. Beach and near-shore processes. I: mechanics of marine sedimentation. In: The Sea, M.N. Hill (Editor). Interscience, New-York, pp. 507-549.

Bastos, A., Collins, M.B. and Kenyon, N.H., 2003a. Morphology and internal structure of sand shoals and sandbanks off the Dorset coast, English Channel. Sedimentology, 50(6): 1105-1122.

Bastos, A., Collins, M.B. and Kenyon, N.H., 2003b. Water and sediment movement around a coastal headland: Portland Bill, southern UK. Ocean Dynamics, 53(3): 309-321.

Bastos, A., Kenyon, N.H. and Collins, M.B., 2000. Symmetrical convergent bedload sand transport pattern associated with headlands: A preliminary indication from bedforms, sediment, distribution and bathymetry. In: Marine Sandwave Dynamics I, Trentesaux A., Garlan T. and Le Bot, S.(Editors), International Workshop, March 23-24 2000, University Lille 1, France, pp. 17-23

Bastos, A., Kenyon, N.H. and Collins, M.B., 2002. Sedimentary processes, bedforms and facies, associated with a coastal headland: Portland Bill, Southern UK. Marine Geology, 187(3-4): 235-258.

Bastos, A., Paphitis, D. and Collins, M.B., 2004. Short-term dynamics and maintenance processes of headland-associated sandbanks: Shambles Bank, English Channel, UK. Estuarine, Coastal and Shelf Science, 59(1): 33-47.

Beck, C. Clabaut P., Dewez, S., Vicaire, O., Chamley, H., Augris, C., Hoslin, R. and Caillot, A., 1991. Sand bodies and sand transport paths at the English Channel- North Sea border: morphology, hydrodynamics and radioactive tracing. Oceanologica Acta, 11, 111-121.

Belderson, R.H. and Stride, A.H., 1966. Tidal current fashioning of a basal bed. Marine Geology 4, 237-257.

Belderson R..H., 1986. Offshore tidal and non-tidal ridges and sheets: Differences in morphology and hydrodynamic setting. In: Knight, R.J., MacLean, J.R. (Eds.), Shelf Sands and Sandstones. Canadian Society of Petroleum Geologists, Calgary, pp. 293-301.

Belderson, R.H., Johnson, M.A. and Kenyon, N.H., 1982. Bedforms. In: Offshore tidal sands Processes and deposits, A.H. Stride (Editor). Chapman and Hall Ltd, Bristol, pp. 27-55.

Bennett, J.P. and Best, J.L., 1995. Mean flow and turbulence structure over fixed, two-dimensional dunes: implications for sediment transport and bedform stability. Sedimentology, 42: 491-513.

Berné, S., 1993. Morphology, internal structure and reversal of asymmetry of large subtidal dunes in the Gironde Estuary (France). Journal of Sedimentary Petrology, 63(5): 780-793.

Berné, S., Allen, G., Auffret, J.-P., Chamley, H., Durand, J. and Weber, O., 1989a. Essai de Synthese sur les dunes hydrauliques géantes tidales actuelles. Bulletin de la Société Géologique de France, 8(6): 1145-1160.

Berné, S., Bourillet, J.-F., Durand, J. and Lericolais, G., 1989b. Les dunes subtidales géantes de Surtainvilles. Centre de Recherches Exploration-Production Elf Aquitaine, 13(2): 398-415.

Berné, S., Lericolais, G., Marsset, T., Bourillet, J.-F. and De Batist, M., 1998. Erosional offshore sand ridges and lowstand shorefaces: Examples from tide and wave-dominated environments of France. Journal of Sedimentary Research, 68(4): 540-555.

Berné, S., Trentesaux, A., Stolk, A., Missiaen, T. and De Batist, M., 1994. Architecture and long term evolution of a tidal sandbank: The Middelkerke Bank. Marine Geology, 121(1-2): 57-72.

Best, J.L., Ashworth, P.J., Bristow, C.S. and Roden, J., 2003. Three-dimensional sedimentary architecture of a large, mid-channel sand braid bar, Jamuna River, Bangladesh. Journal of Sedimentary Research, 73: 516-530.

Best, J.L., Kostaschuk, R.A. and Hardy, R., 2004. The fluid dynamics of low-angle river dunes: results form integrated field monitoring, laboratory experimentation and numerical modeling. *In:* Marine Sandwave and river dune dynamics II, International workshop. Hulscher, S., Garlan, T., Idier, D., (editors) University of Twente, The Netherlands, pp. 17-23.

Blondeaux, P., 2001. Mechanics of Coastal forms. Annual Review of Fluid Mechanic, 33: 339-370.

Bourne, S.J. and Willemse, E.J.M., 2001. Elastic stress control on the pattern of tensile fracturing around a small fault network at Nash Point, UK. Journal of Structural Geology, 23(11): 1753-1770.

Brampton, A., 1999. Dredging on Nash Bank: Application for continued extraction - Coastal Impact Study. EX 4023, HR Wallingford.

Brampton, A., 2002. Extension of Dredging Licence, Helwick Bank. Coastal Impact Study Report. EX 4677, HR Wallingford.

Brampton, A., Ceri, J. and Selby, I., 2002. Gaining a resource, or losing a beach-marine aggregates and sandbank dredging (personal communication).

Britton, R., 1978. Structure of some marine sedimentary bodies and their dynamic environments. PhD Thesis, University of Wales, Swansea, 265 pp.

Brown, C.J., Hewer, A.J., Meadows, W.J., Limpenny, D.S., Cooper, K.M., Rees, H.L. and Vivian, C.M.G, 2001. Mapping of gravel biotopes and an examination of the factors controlling the distribution, type and diversity of their biological community. Sci. Ser. Tech. Rep. 114, CEFAS Lowestoft.

C

Cacchione, D.A., Drake, D.E., Ferreira, J.T. and Tate, G.B., 1994. Bottom stress estimates and sand transport on northern California inner continental shelf. Continental Shelf Research, 14(10-11): 1273-1289.

Cacchione, D.A., Grant, W.D., Drake, D.E. and Glenn, S.M., 1987. Storm dominated bottom boundary layer dynamics on the northern California continental shelf: Measurements and predictions. Journal of Geophysical research, 92(C2): 1817-1827.

Carbajal, N. and Montano, Y., 2001. Comparison between Predicted and Observed Physical Features of Sandbanks. Estuarine, Coastal and Shelf Science, 52(4): 435-443.

Carling, P.A., Gölz, E., Orr, H.G. and Radecki-Pawlik, A., 2000a. The morphodynamics of fluvial sand dunes in the River Rhine, near Mainz, Germany. I Sedimentology and morphology. Sedimentology, 47: 227-252.

Carling, P.A., Williams, J.J., Gölz, E. and Kelsey, A.D., 2000b. The morphodynamics of fluvial sand dunes in the River Rhine, near Mainz, Germany. II Hydrodynamics and sediment transport. Sedimentology, 47: 253-278.

Carmenen, B. and Larroudé, P., 2003. Comparison of sediment transport formulae for the coastal environment. Coastal Engineering, 48: 111-132.

Caston, V.N., 1970. Tidal sand movement between some linear sand banks in the North Sea off northeast Norfolk. Marine Geology, 9: 38-42.

Caston, V.N., 1972. Linear sand banks in the Southern North Sea. Sedimentology, 18: 63-78.

Cayocca, F. and Du Gardin, B., 2003. Assessing the impact of sand extraction on the shore stability: project for a methodological framework. In: Marine Sand and Gravel: shaping the future (conference), European Marine Sand and Gravel Group (Editor), Delft University, The Netherlands.

Chaumillon, E., Gillet, H., Weber, N. and Tesson, M., 2002. Evolution temporelle et architecture interne d'un banc sableux estuarien: la Longe de Boyard (littoral atlantique, France). Compte Rendu de l'Academie des Sciences - Géosciences, 334: 119-126.

Chaumillon, E., Weber, N., Tesson, M. and Tessier, B., 2003. Preservation of Sandbanks within Present-Day Estuaries (Atlantic Coast of France) revealed by Very High Resolution Seismic Surveys, *In:* AAPG Annual Convention, Salt Lake City, Utah.

Collins, M.B., 1987. Sediment transport in the Bristol Channel: a review. Proceedings of the Geologists' Association, 98: 367-383.

Collins, M.B. and Ferentinos, G., 1984. Residual circulation in the Bristol Channel as suggested by Woodhead sea-bed drifter recovery patterns. Oceanologica acta, 7: 33-42.

Collins, M.B., Ferentinos, G. and Banner, F.T., 1979. The hydrodynamics and sedimentology of a high (tidal and wave) energy embayment (Swansea Bay, Northern Bristol Channel). Estuarine and Coastal Marine Science, 8: 49-74.

Collins, M.B., Shimwell, S. J., Gao, S., Powell, H., Hewitson, C. and Taylor, J.A., 1995. Water and sediment movement in the vicinity of linear sandbanks: the Norfolk Banks, southern North Sea. Marine Geology, 123 (3-4): 125-142.

Costello, W.R. and Southard, J.B., 1981. Flume experiments on lower-flow-regime bed forms in coarse sand. Journal of Sedimentary Petrology, 51(3): 849-864.

Crickmore, 1967. Measurement of sand transport in rivers with special reference to tracer method. Sedimentology, 8: 175-228.

Cuadrado, D.G. and Perillo, G.M.E., 1997. Migration of intertidal sandbanks, Bahía Blanca Estuary, Argentina. Journal of Coastal Research, 13(1): 155-163.

Culver, S.J., 1976. A study of the post-glacial foraminifera of Swansea Bay, South Wales. Unpublished Ph. D. Thesis, University of Wales.

D

Dalrymple, R.W., 1984. Morphology and internal structure of sandwaves in the Bay of Fundy. Sedimentology, 31: 365-382.

Dalrymple, R.W. and Rhodes, R.N., 1995. Estuarine dunes and bars. In: Geomorphology and sedimentology of estuaries, Perillo G.M.E. (Editor). Elsevier Science, pp. 359-422.

Damgaard, J.S. and Chesher, T., 1997. Morphodynamic simulation of Helwick Bank. TR31, HR Wallingford.

Davies, P.A., Dakin, J.M. and Falconer, R.A., 1995. Eddy formation behind a coastal headland. Journal of Coastal Research, 11(1): 154-167.

Davis, J.C., 2002. Statistics and data analysis in geology. Wiley, New York, 638 pp.

Dawson, A., Elliot, L., Noone, S., Hickey, K., Holt, T., Wadhams, P. and Foster, I., 2004. Historical storminess and climate 'sea-saws' in the North Atlantic region. Marine Geology 210(1-4): 247-259.

De Moustier, C., 1998. State of the Art in Swath Bathymetry Survey Systems. International Hydrographic Review, 65(2): 25-64.

Deigaard, R. and Fredsoe, J., 1987. Offshore sandwaves. In: International Conference on Coastal Engeeniring. ASCE (editor), Taipei, Taiwan, pp. 1047-1061.

Deleu, S., Van Lancker, V., Van den Eynde, D. and Moerkerke, G., 2004. Morphodynamic evolution of the kink of an offshore tidal sandbank: the Westhinder Bank (Southern North Sea). Continental Shelf Research, 24(15): 1587-1610.

Dewicke, A., Cattrijsse, A., Mees, J. and Vincx, M., 2003. Spatial patterns of the hyberbenthos of subtidal sandbanks in the southern North Sea. Journal of Sea Research, 49: 27-45.

Dinehart, 2002. Bedform movement recorded by sequential single-beam surveys in tidal rivers. Journal of Hydrology, 258: 25-39.

Driver, J.S., 1980. A guide to sea wave recording. Report number 103, Institue of Oceanographic Sciences, 93pp.

Duffy, G.P., Hughes Clarke, J.E. and Parrot, R., 2004. Application of current measurement and time lapsed bathymetric multibeam surveying to the investigation of Banner Bank, Mispec Bay, New Brunswick, Canada. In: Marine sandwave and river dune dynamics II, Hulscher S., Garlan, T., Idier, D. (Editors), University of Twente, The Netherlands, pp. 72-79.

Dunn, R.A., Scheirer, D.S. and Forsyth, D.W., 2001. A detailed comparison of repeated bathymetric surveys along 300-km-long section of the southern East Pacific Rise. Journal of Geophysical research, 106(B1): 463-471.

Dyer, K.R., 1986. Coastal and Estuarine Sediment Dynamics. Wiley Interscience, Chippenham, 342 pp.

Dyer, K.R. and Huntley, D.A., 1999. The origin,classification and modelling of sand banks and ridges. Continental Shelf Research, 19: 1285-1330.

E

EMU plc, 1999. Bank environmental assessment for aggregate extraction from Nash Bank, Bristol Channel, 12 pp.

Engel, P. and Lau, Y.L., 1980. Computation of bedload using bathymetric data. Journal of the Hydraulics division, American Society of Civil Engineers, 106: 369-380.

Engelund, F. and Fredsoe, J., 1982. Sediment ripples and dunes. Annual Review of Fluid Mechanics, 14: 13-37.

Evans, D.J., 1973. The stratigraphy of the Central Part of the Bristol Channel, Unpublished PhD thesis, University of Wales, Swansea.

F

Farr, H.K., 1990. Multi-beam Bathymetric Sonar: SeaBEAM and HYDROCHART. Marine Geodesy, 2(4): 7-10.

Farrow, G.E., Allen, N.H. and Akpan, E.B., 1984. Bioclastic carbonate sedimentation on a high-latituded, tide-dominated shelf: northeast Orkney Islands, Scotland. Journal of Sedimentary Petrology, 54(2): 373-393.

Fenster, M.S., Fitzgerald, D.M., Bojlen, D.M., Lewis, R.S. and Baldwin, C.T., 1990. Stability of giant sand waves in eastern Long Island Sound, USA. Marine Geology, 91(3): 207-225.

Ferentinos, G., 1978. Hydrodynamic and sedimentation processes in Swansea Bay and along the central Northern Bristol Channel coastline. Unpublished PhD thesis, University of Wales, Swansea.

Ferentinos, G. and Collins, M.B., 1980. Effects of shoreline irregularities on a rectilinear tidal current and their significance in sedimentation. Journal of Sedimentary Petrology, 50(4): 1081-1094.

Finkelstein, K., 1982. Morphological variations and sediment transport in crenulate bay beaches, Kodiak Island, Alaska. Marine Geology, 47 (3-4): 261-281.

Flemming, B.W., 1988. Zur Klassification subaquatischer, strömungstransversaler Transportkörper. Bochumer geologische und geotechnische Arbeiten, 29: 44-47.

Flemming, B.W., 2000. The role of grain size, water depth and flow velocity as scaling factors controlling the size of subaqueous dunes. In: Marine Sandwave Dynamics I, Trentesaux A., Garlan T. and Le Bot, S.(Editors), International Workshop, March 23-24 2000, University Lille 1, France, pp. 55-60.

Fox, C.G., Chadwick, W.W. and Embley, R.W., 1997. Detection of changes in ridge-crest morphology using repeated multibeam sonar surveys. Journal of Geophysical research, 97(B7): 11149-11162.

Francken, F., Wartel, S., Parker, R. and Taverniers, E., 2004. Factors influencing subaqueous dunes in the Scheldt Estuary. Geo-Marine Letters, 24: 14-21.

G

Gabel, S.L., 1993. Geometry and kinematics of dunes during steady and unsteady flows in the Calamus River, Nebraska. Sedimentology 40: 237-269.

Gadd, P.E., Lavelle, J.W. and Swift, D.J., 1978. Estimate of sand transport on the New York shelf using near-bottom current meter observations. Journal of Sedimentary Petrology, 48: 239-252.

Gilboy, T.P., Dickey, T.D., Sigurdson, D.E., Yu, X. and Manov, D., 2000. An intercomparison of current measurements using a vector measuring current meter, an acoustic Doppler current profiler and recently developed acoustic current meter. Journal of Atmospheric and Oceanic Technology, 17: 561-574.

Goff, J.A. and Jordan, T.H., 1988. Stochastic modeling of seafloor morphology: Inversion of SEABEAM data for second order statistic. Journal of Geophysical Research, 93(B11): 13589-13608.

Goff, J.A., Jordan, T.H., Edwards, M.H. and Fornari, D.J., 1991. Comparison of a stochastic seafloor model with Seamarc II bathymetry and Sea Beam near the East Pacific Rise. Journal of Geophysical Research, 96(B3): 3867-3885.

Goff, J.A. and Kleinrock, M.C., 1991. Quantitative comparison of Bathyemetric survey systems. Geophysical Research Letters, 18(7): 1253-1256.

Gonzalez, R.C. and Woods, R.E., 1992. Digital image processing. Addison-Wesley Publishing Company, New York, 716 pp.

Grant, J.A. and Schreiber, R., 1990. Modern swathe sounding and sub-bottom profiling technology for research applications: The Atlas Hydrosweep and Parasound systems. Marine Geophysical Research, 12(1-2): 9-19.

Grant, W.D. and Madsen, O.S., 1986. The continental-shelf bottom boundary layer. Annual Review of Fluid Mechanic, 18: 265-305.

Gringarten, E. and Deutsch, C.V., 2001. Teacher's aide Variogram Interpretation and modeling. Mathematical Geology, 33(4): 507-534.

H

Haas, K. and Hanes, D.M., 2003. Processed based modelling of total longshore sediment transport. Journal of Coastal Research, 20(3): 853-861.

Haine, C., 2000. Bristol Channel marine aggregates: Resources and constraints research project, Postford Duvivier and ABP MER.

Hallet, B., 1990. Spatial self-organization in geomorphology: from periodic bedforms and pattern ground to scale-invariant topography. Earth Science Reviews, 29: 57-75.

Hamilton, E., Watson, P.J., Cleary, J.J. and Clifton, R.J., 1979. The geochemistry of recent sediment in the Bristol Channel - Severn Estuary System. Marine Geology, 31(1-2): 139-182.

Harbor, 1998. Dynamics of bedforms in the lower Mississippi River. Journal of Sedimentary Research, 68(5): 750-762.

Hare, R., Godin, A. and Mayer, L.A., 1995. Depth and position error budgets for multibeam echosounding. International Hydrographic Review, 72(1): 37-69.

Harms, J.C., 1969. Hydraulic significance of some sand ripples. Bulletin of the Geological Society of America, 80: 363-396.

Harris, P.T., 1982. The distribution and dynamics of sedimentary bedforms in the central and inner Bristol Channel. M.Sc. Thesis, University College Swansea, Swansea.

Harris, P.T., 1988a. Large-scale bedforms as indicator of mutually evasive sand transport and sequential infilling of wide-mouthed estuaries. Sedimentary Geology, 57: 273-298.

Harris, P.T., 1988b. Sediments, bedforms and bedload transport pathways on the continental shelf adjacent to Torres Strait, Australia-Papua New Guinea. Continental Shelf Research, 8(8): 979-1003.

Harris, P.T. and Collins, M.B., 1984. Side-Scan sonar investigation into temporal variation in sand wave morphology: Helwick Sands, Bristol Channel. Geo-Marine Letters, 4: 91-97.

Harris, P.T. and Collins, M.B., 1988. Estimation of annual bedload flux in macrotidal estuary: Bristol Channel, UK. Marine Geology, 83(1-4): 237-252.

Harris, P.T. and Collins, M.B., 1991. Sand transport in the Bristol Channel: Bedload parting zone or mutualy evasive transport pathways? Marine Geology, 101(1-4): 209-216.

Harris, P.T., Pattiaratchi, C.B., Collins, M.B. and Dalrymple, R.W., 1995. What is bedload parting? Special Publication international Association of Sedimentologists, 24: 3-18.

Harrisson, S.E., Locker, S.D., Hine, A.C., Edwards, J.H., Naar, D.F, Twichell, D. C. and Mallinson, D.J., 2003. Sediment-starved sand ridges on a mixed carbonate/siliclastic inner shelf off west-central Florida, 200(1-4): 171-194.

Haslett, S.K. Davies, P., Curr, R.H.F., Kennington, K., King, C.P. and A.J., Margetts, 1998. Evaluating late-Holocene relative sea-level change in the Somerset Levels, southwest Britain. The Holocene, 8(2): 197-207.

Hasselmann, K., Barnett, T.P., Bouws, E., Carlson, H., Cartwright, D. E., Enke, K., Ewing, J.A., Gienapp, H., Hasselmann, D.E., Kruseman, P., Meerburg, A., Muller, P., Olbers, D.J., Richter, K, Sell, W. and Walden, H., 1973. Measurements of wind-wave growth and swell decay during the Joint North Sea Wave Project (JONSWAP). Deutsche Hydrographische Zeitung, 12(A8): 95.

Heath, R.A., 1981. Resonant Period and Q of the Celtic Sea and Bristol Channel. Estuarine, Coastal and Shelf Science, 12: 291-301.

Heathershaw, A.D., 1981. Comparison of measured and predicted sediment transport rates in tidal currents. Marine Geology, 42(1-4): 75-104.

Herzfeld, U.C., 1993. A method for seafloor classification using directional variograms, demonstrated for data from the western flank of the Mid-Atlantic ridge. Mathematical Geology, 25(7): 901-924.

Hoekstra, P., Bell, P., Van Santen, P., Roode, N., Levoy, F. and Whitehouse, R.J.S., 2004. Bedform migration and bedload transport on an intertidal shoal. Continental Shelf Research(24): 1249-1269.

Holman, R., 1999. Pattern formation in the nearshore. In: River, coastal and estuarine morphodynamics, Seminara G. and Blondeaux P. (Editors). Springer, Berlin, pp. 141-161.

Houbolt, J.J.H.C., 1968. Recent Sediments in the Southern Bight of the North Sea. Geologie en Mijnbouw, 47: 245-273.

Houthuys, R., Trentesaux, A. and De Wolf, P., 1994. Storm influences on a tidal sandbank's surface (Middelkerke Bank, southern North Sea). Marine Geology, 121(1-2): 23-41.

Hulscher, S.J.M.H., 1996. Tidal-induced large-scale regular bed from patterns in a three-dimensional shallow water model. Journal of Geophysical research, 101(C9): 20727-20744.

Hulscher, S.J.M.H. and Van den Brink, M.G., 2001. Comparison between predicted and observed sand waves and sand banks in the North Sea. Journal of Geophysical Research, 106(C5): 9327-9338.

Huthnance, J.M., 1982a. On one mechanism forming linear sand banks. Estuarine, Coastal and Shelf Science, 14: 74-99.

Huthnance, J.M., 1982b. On the formation of Sand Banks of finite extent. Estuarine, Coastal and Shelf Science, 15: 277-299.

I

Idier, D., Ehrold, A. and Garlan, T., 2002. Morphodynamique d'une dune sous-marine du détroit du Pas-de-Calais. Compte rendu Académie des Sciences, Géosciences, 334: 1079-1085.

Isaaks, E.H. and Srivastava, R.M., 1990. Applied geostatistics. Oxford University Press, New York, 580 pp.

J

Jennings, S.C., Orford, J.D., Canti, M., Devoy, R.J.N. and Straker, V., 1998. The role of relative sea-level rise and changing sediment supply on Holocene gravel barrier development: the example of Porlock, Somerset, UK. The Holocene, 8(2): 165-181.

Jones, C., 2003. Wales' best beaches are vanishing, The Western Mail, Cardiff.

Jones, D.G. and Williams, A.T., 1991. Statistical analysis of factors influencing cliff erosion along a section of the west Wales coast, UK. Earth Surface Processes and Landforms, 16(2): 95-111.

Johnson, M.A., Kenyon, N., Belderson, R.H. and Stride, A.H., 1982. Sand transport. In: Offshore tidal sands, Processes and deposits, Stride A.H. (Editor). Chapman and Hall Ltd., Bristol: 58-94.

Journel, A.G. and Huijbregts, C.J., 1978. Mining geostatistics. Academic Press, London, 600 pp.

K

Kalnay, E., Kanamitsu, M., Kistler, R., Collins, W., Deaven, D., Gandin, L., Iredell, M., Saha, S., White, G., Woollen, J., Zhu, Y., Chelliah, M., Ebisuzaki, W., Higgins, W., Janowiak, J., Mo, K. C., Ropelewski, C., Wang, J., Leetmaa, A., Reynolds, R., Jenne, R. and Dennis, J., 1996. The NCEP/NCAR reanalysis 40-year project. Bulletin of the American Meteorological Society, 77: 437-471.

Kammerer, E., 2000. New method for the removal of refraction artifacts in multibeam echosounder systems. Unpublished PhD Thesis, University of New Brunswick, Canada.

Kenyon, N.H., Belderson, R.H. and Stride, A.H., 1981. Offshore tidal sand banks as indicators of net sand transport and as potential deposits. In: Holocene marine sedimentation in the North Sea basin , Nio, S.D., Schuttenhelm R.T.E. and Van Weering, T.C.E. (Editors). Blackwell Scientific, Oxford.

Kenyon, N.H., 1970. Sand ribbons of European tidal seas. Marine Geology, 9(1):25-39

Kenyon, N.H. and Cooper, W., 2004. Sand banks, sand transport and offshore wind farms. Report commissioned by the DTI in view of the second phase of the Strategic Environmental Assessment for Offshore Wind. Draft report

Kenyon, P.M. and Turcotte, D.L., 1985. Morphology of a delta prograding by bulk sediment transport. Geological Society of America Bulletin, 96: 1457-1465.

Kerleguer, L., 1992. Evaluation et procédures d'exploitation du sondeur multifaisceaux Lennemor. Report Number 001/92, Service Hydrographique et Océanographique de la Marine.

Knaapen, M.A.F., Hulscher, S.J.M.H. and De Vriend, H., 2001. A new type of sea-bed waves. Geophysical Research Letters, 28(7): 1323-1326.

Komar, P.D., 1983. CRC Handbook of coastal processes and erosion. CRC Press, Boca Raton, 305 pp.

Komar, P.D., 1998. Beach processes and sedimentation. Prentice Hall, 544 pp.

Kostaschuk, R.A., 2000. A field study of turbulence and sediment dynamics over subaqueous dunes with flow separation. Sedimentology, 47: 519-531.

Kostaschuk, R.A., Best, J.L., Villard, P., Peakall, J. and Franklin, M., 2005. Measuring flow velocity and sediment transport with acoustic Doppler current profiler. Geomorphology, 68(1-2): 25-37.

Kostaschuk, R.A. and Church, M.A., 1993. Macroturbulence generated by dunes: Fraser River, Canada. Sedimentary Geology, 85: 25-37.

Kostaschuk, R.A. and Villard, P., 1996. Flow and sediment transport over large subaqueous dunes: Fraser River, Canada. Sedimentology 43: 849-863.

Kostaschuk, R.A. and Villard, P., 1999. Turbulent sand suspension over dunes. In: Fluvial Sedimentology, Smith, D.B. and Rogers, J., (Editors). International Association of Sedimentologists, pp. 3-13.

L

Lanckneus, J. and De Moor, G., 1991. Present-day evolution of sand waves on a sandy shelf bank. Oceanologica acta, Special issue 11: 123-127.

Lanckneus, J. and De Moor, G., 1995. Bedforms on the Middelkerke Bank, southern North Sea. In: Tidal Signatures in Modern and Ancient Sediments, Flemming, B.W. and Bartolomä, A. (Editors). International Association of Sedimentologists Special Publication, pp. 33-51.

Langhorne, D.N., 1973. A sandwave field in the Outer Thames Estuary. Marine Geology, 14(2): 129-143.

Langhorne, D.N., 1982. A study of the dynamics of a marine sandwave. Sedimentology, 29: 571-594.

Le Bot, S., Idier, D., Garlan, T., Trentesaux, A. and Astruc, D., 2000. Dune dynamics: from field measurements to numerical modelling. Aplication to bathymetric survey frequency in the Calais-Dover Strait. In: Marine Sandwave Dynamics I, Trentesaux A., Garlan T. and Le Bot, S. (Editors), International Workshop, March 23-24 2000, University Lille 1, France, pp. 101-108.

Le Bot, S. and Trentesaux, A., 2004. Types of internal structure and external morphology of submarine dunes under the influence of tide- and wind-driven

processes (Dover Strait, northern France). Marine Geology, 211(1-2): 143-168.

Lees, B.J., 1983. The relationship of sediment transport rates and paths to sandbanks in a tidally dominated area off the coast of East Anglia, UK. Sedimentology, 30: 461-483.

Li, M.Z. and Amos, C.L., 2001. SEDTRANS96: the upgraded and better calibrated sediment-transport model for continental shelves. Computer and Geosciences(27): 619-645.

Lin, B. and Falconer, R.A., 2001. Numerical modeling of 3-D tidal currents and water quality indicators in the Bristol Channel. Proceedings of the Institution of Civil Engineering, 148(3): 155-166.

Lobo, F.J., Hernandez-Molina, F.J., Somoza, L., Rodero, J., Maldonado, A. and Barnolas, A., 2000. Patterns of bottom current flow deduced from dune asymmetries over the Gulf of Cadiz shelf (southwet Spain). Marine Geology, 164: 91-117.

Lyne, V.D., Butman, B. and Grant, W.D., 1990a. Sediment movement along the US east coast continental shelf – I. Estimates of bottom stress using the Grant-Madsen model and near-bottom wave and current measurements. Continental Shelf Research, 10(5): 397-428.

Lyne, V.D., Butman, B. and Grant, W.D., 1990b. Sediment movement along the US east coast continental shelf – II. Modeling suspended sediment concentration and transport rate during storms. Continental Shelf Research, 10(5): 429-460.

M

Maddux, T.B., Nelson, J.M. and McLean, S.R., 2003. Turbulent flow over three dimensional dunes: 1. Free surface and flow response. Journal of Geophysical Research, 108(F1): 10-1 - 10-20.

Mallet, C., Howa, H.L., Garlan, T., Sottolichio, A. and Le Hir, P., 2000. Residual transport model in correlation with sedimentary dynamics over an elongate tidal sandbar in the Gironde estuary (Southern France). Journal of Sedimentary Research, 70(5): 1005-1016.

Marsset, T., Tessier, B., Reynaud, J.-Y., De Batist, M. and Plagnol, C., 1999. The Celtic Sea banks: an example of sand body analysis from very high-resolution seismic data. Marine Geology 158(1-4): 89-109.

McCave, I.N., 1971. Sand waves in the North Sea off the coast of Holland. Marine Geology, 10(3): 199-225.

McCave, I.N., 1979. Tidal currents at the North Hinder lightship, Southern North Sea: flow directions and turbulence in relation to maintenance of sand banks. Marine Geology, 31(1-2): 101-114.

McCave, I.N. and Langhorne, D.N., 1982. Sand waves and sediment transport around the end of a tidal sand bank. Sedimentology, 29: 95-110.

McComb, P., Gorman, R., Black, K. and Kun, A.L., 2001. Measuring directional wave spectra using the 3D-ACM WAVE on a fixed and taut wire moorings. IEEE Journal of Oceanic Engineering, 26(2): 171-182.

McLaren, P., Collins, M.B., Gao, S. and Powys, R.I.L., 1993. Sediment dynamics of the Severn Estuary and inner Bristol Channel. Journal of the Geological Society, London, 150: 589-603.

McLean, S.R., 1989. The stability of ripples and dunes. Earth science Reviews, 29: 131-144.

Mei, C.C. and Liu, P.L.F., 1993. Surface waves and coastal dynamics. Annual Review of Fluid Mechanics, 25, 215-240

Miller, M.C., McCave, I.N. and Komar, P.D., 1977. Threshold of sediment motion under unidirectional currents. Sedimentology, 24:507-525.

Mohrig, D. and Smith, J.D., 1996. Predicting the migration rates of subaqueous dunes. Water Resources Research, 32(10): 3207-3217.

Molgat, M. and Arnott, R.W.C., 2001. Combined tide and wave influence on sedimentation patterns in the Upper Jurassic Swift Formation, south-eastern Alberta. Sedimentology, 48(6): 1353-1369.

Mosher, D.C. and Thomson, R.E., 2002. The foreslope hills: large-scale, fine grained sediment waves in the Strait of Geogia, British Columbia. Marine Geology 192 (1-3): 275-295.

N

Neville, G., 1970. British regional geology. South Wales. Her Majesty's Stationery Office, London, 152pp.

Nittrouer, C.A. and Wright, L.D., 1994. Transport of particles across continental shelves. Reviews of Geophysics, 32(1): 85-113.

Nordin, C.F. and Algert, J.H., 1966. Spectral analysis of sand waves. Journal of the Hydraulics division, American Society of Civil Engineers, 92: 95-114.

North, F.J., 1964. The evolution of the Bristol Channel with special reference to the coast of South Wales. National Museum of Wales, Cardiff, 110 pp.

O

Off, T., 1963. Rythmic linear sand bodies caused by tidal currents. Bulletin of the American Association of Petroleum Geologists, 47: 324-341.

Oliver, M.A. and Webster, R., 1986. Semi-variogram for modelling the spatial pattern of landform and soil properties. Earth surface processes and landforms, 11: 491-504.

P

Pantin, H.M., 1991. The sea-bed sediments around the United Kingdom. Their bathymetric and physical environment, grain size, mineral composition and associated bedforms. Report number SB/90/1, British Geological Survey.

Park, M.J. and Wang, D.P., 2000. Tidal vorticity around a coastal promontory. Journal of Oceanography, 56: 261-273.

Pattiaratchi, C.B. and Collins, M.B., 1984. Sediment transport under waves and tidal currents: a case study from the northern Bristol Channel, U. K. Marine Geology, 56(1-4): 27-40.

Pattiaratchi, C.B. and Collins, M.B., 1985. Sand transport under the combined influence of waves and tidal currents: an assessment of available formulae. Marine Geology, 67(1-2): 83-100.

Pattiarchi, C.B. and Collins, M.B., 1987. Mechanisms for linear sandbank formation and maintenance in relation to dynamical oceanographic observations. Progress in Oceanography, 19: 117-176.

Perillo, G.M.E. and Ludwick, J.C., 1984. Geomorphology of a sand wave in Lower Chesapeake Bay, Virginia, USA. Geo-Marine Letters, 4: 105-112.

Pethick, J. and Thompson, A., 2002. Some aspects of the Geomorphology and Sedimentology of the coast of South East Wales. (Unpublished)

Pingree, R.D., 1978. The formation of the shambles and other banks by tidal stirring of the seas. Journal of the Marine Biological Association of U.K., 58: 211-226.

Pingree, R.D. and Maddock, L., 1979. The tidal physics of headland flows and offshore tidal bank formation. Marine Geology, 32(1-4): 269-289.

Pirmez, C., Pratson, L.F. and Steckler, M.S., 1998. Clinoform development by advection-diffusion of suspended sediment: Modeling and comparison to natural systems. Journal of Geophysical Research, 103(B10): 24141-24157.

R

RESON, 2001. 6042 Version 7 Quickstart Handbook.

Reynaud, J.-Y., Tessier, B., Auffret, J.-P., Berné, S., De Batist, M., Marsett, T. and Walker, P., 2003. The offshore Quaternary sediment bodies of the English Channel and its Western Approaches. Journal of Quaternary Science, 18(3-4): 361-371.

Reynaud, J.-Y., Tessier, B., Berné, S., Chamley, H. and De Batist, M., 1999a. Tide and wave dynamics on a sand bank from the deep shelf of the Western Channel approaches. Marine Geology, 161(2-4): 351-359.

Reynaud, J.-Y., Tessier, B., Proust, J.-N., Dalrymple, R. W., Marsett, T., De Batist, M., Bourillet, J.-F. And Lericolais, G., 1999b. Eustatic and hydrodynamic controls on the architecture of a deep shelf sand bank (Celtic Sea). Sedimentology, 46(4): 703-721.

Robert, A. and Richards, K.R., 1988. On the modeling of sand bedforms using semi-variogram. Earth Surface Processes and Landforms, 13: 459-473.

Robinson, I.S., 1983. Tidally induced residual flows. In: Physical oceanography of coastal and shelf seas, Johns B. (Editor). Elsevier, New-York, pp. 321-356.

Roos, P.C. and Hulscher, S., 2003. Large-scale seabed dynamics in offshore morphology: modeling human intervention. Reviews of Geophysics, 41: 5-1-5-19.

Rubin, A.M., 2000. Time-lapse movies of migrating bedforms. In: Marine Sandwave Dynamics I, Trentesaux A., Garlan T. and Le Bot, S.(Editors), International Workshop, March 23-24 2000, University Lille 1, France, pp. 177

Rubin, D.M. and Hunter, R.E., 1982. Bedform climbing in theory and nature. Sedimentology, 29: 121-138.

Rubin, D.M. and Hunter, R.E., 1987. Bedform alignment in directionally varying flows. Science, 237: 276-278.

Rubin, D.M. and Ikeda, H., 1990. Flume experiments on the alignment of transverse, oblique and longitudinal dunes in directionally varying flows. Sedimentology, 37: 673-684.

Rubin, D.M. and McCulloch, D.S., 1980. Single and superimposed bedforms: a synthesis of San Francisco bay and flume observations. Sedimentary Geology, 26: 207-231.

S

Santoro, V.C., Amore, E., Cavallaro, L., Cozzo, G. and Foti, E., 2002. Sand waves in the Messina Strait, Italy. Journal of Coastal Research, Special issue 36: 640-653.

Seminara, G., 1998. Stability and morphodynamics. Meccanica, 33(1): 59-99.

Seymour, R.J., 1977. Estimating wave generation on restricted fetches. Journal of Waterway, Port and Ocean Division, Proceeding of the American Society of Civil Engineering(103): 251-264.

Shaw, P.R. and Smith, D.K., 1990. Robust description of statistically heterogeneous seafloor topography through its slope distribution. Journal of Geophysical research, 95(B6): 8705-8722.

Signell, R.P. and Harris, C.K., 2000. Modeling sand bank formation around tidal headlands. In: Estuarine and Coastal modeling, 6th International Conference, Spaulding, M.L. and Blumberg, A.F. (Editors), New Orleans.

Signell, R.P. and Geyer, W.R., 1991. Transient eddy formation around headlands. Journal of Geophysical research, 96(C2): 2561-2575.

Smith, J.D., 1969. Geomorphology of sand ridge. Journal of Geology, 77: 39-55.

Smith, W.H.F. and Wessel, P., 1990. Gridding with continuous curvature splines in tension. Geophysics, 55: 293-305.

Soulsby, R., 1997. Dynamics of marine sands. A manual for practical applications. Thomas Telford Publication, Bath, 249 pp.

Squibb, S., 2004. Survey under extreme conditions or just another day in the office. Hydro International, 8(4): 24-25.

Stride, 1963. Current-swept sea floor near the southern half of Great-Britain. Quarterly Journal of the Geological Society of London, 119:175-199.

Stride, A.H. and Belderson, R.H., 1990. A reassessment of sand transport paths in the Bristol Channel and their regional significance. Marine Geology, 92(3-4): 227-236.

Stride, A.H. and Belderson, R.H., 1991. Sand transport in the Bristol Channel east of the Bull Point and Worms Head: A bed-load partiting model with some indications of mutually evasive sand transport paths. Marine Geology, 101(1-4): 203-207.

Stride, A.H., Belderson, R.H., Kenyon, N. and Johnson, M.A., 1982. Offshore tidal deposits : sand sheet and sand bank facies. In: Offshore tidal sands. Processes and deposits, Stride A.H. (Editor), Chapman and Hall, pp. 95-125.

Swift, D.J., 1975. Tidal sand ridges and shoal-retreat massifs. Marine Geology, 18(3): 105-134.

Swift, D.J. and Field, M.E., 1981. Evolution of a classic sand ridge field: Maryland sector, North American Inner shelf. Sedimentology, 28: 461-482.

T

Tappin, D.R., Chadwick, R.A., Jackson, A.A., Wingfield, R.T.R. and Smith, N.J.P., 1994. The geology of the Cardigan Bay and the Bristol Channel. United Kingdom offshore regional report. British Geological Survey. Her Majesty's Stationery Office, London.

Ten Brinke, W.B.M., Wilbers, A.W.E. and Wesseling, C., 1999. Dune growth, decay and migration rates during a large-magnitude flood at a sand and mixed sand-gravel bed in the Dutch Rhine river system. In: Fluvial sedimentology VI, Special Publication Number 28 of the International Association of Sedimentologists, Smith, N.D. and Rogers, J. (Editors). Blackwell Science, Northampton, pp. 15-32.

Terwindt, J.H.J., 1971. Sand waves in the southern bight of the North Sea. Marine Geology, 10(1): 51-67.

Terwindt, J.H.J. and Brouwer, M.J.N., 1986. The behaviour of intertidal sandwaves during neap-spring tide cycles and the relevance for paleoflow reconstruction. Sedimentology, 33: 1-31.

Thorne, P.D. and Hanes, D.M., 2002. A review of accoustic measurement of small-scale sediment processes. Continental Shelf Research 22: 603-632.

Thornton, E. and Guza, R., 1982. Energy saturation and phase speeds measured on a natural beach. Journal of Geophysical research, 87(C12): 9499-9508.

TSS, 1999. POS/MV model 320 Position and orientation system for marine vessels. Training notes

Turner, S.R., 1976. Some aspects of sedimentary bodies in parts of the Bristol Channel, Unpublished PhD thesis, University College Swansea, Swansea, 232 pp.

Twichell, D.C., 1983. Bedform distribution and inferred sand transport on Georges Bank, United States, Atlantic Continental Shelf. Sedimentology, 30: 695-710.

U

Uncles, R.J., 1983. Modeling tidal stress, circulation and mixing in the Bristol Channel as a prerequisite for ecosystem studies. Canadian Journal of Fisheries and Aquatic Sciences, 40: 8-19.

Urgeles, R., Locat, J., Schmitt, T. and Hughes Clarke, J.E., 2002. The July 1996 flood deposit in the Saguenay Fjord, Quebec, Canada: implications for sources of spatial and temporal backscatter variations. Marine Geology, 184(1-2): 41-60.

V

Van den Berg, J.H., 1987. Bedform migration and bedload transport in some rivers and tidal environments. Sedimentology, 34: 681-698.

Van der Wal, D. and Pye, K., 2003. The use of historical bathymetric charts in a GIS to assess morphological change in estuaries. The Geographical Journal, 169(1): 21-31.

Van Lancker, V.R.M. and Jacobs, P., 2000. The dynamical behaviour of shallow-marine dunes, In: Marine Sandwave Dynamics I, Trentesaux A., Garlan T. and Le Bot, S.(Editors), International Workshop, March 23-24 2000, University Lille 1, France, pp. 213-220.

Vanoni, V.A., 1974. Factors determing bedforms of alluvial streams. Journal of the Hydraulics division, American Society of Civil Engineers, 100(3): 363-377.

Villard, P. and Church, M.A., 2002. Dunes and associated sand transport in a tidally influenced sand-bed channel: Fraser River, British Columbia. Canadian Journal of Earth Sciences, 40: 115-130.

Vincent, C.E., Stolk, A. and Porter, C.F.C., 1998. Sand suspension and transport on the Middelkerke Bank (southern Nor Sea) by storms and tidal current. Marine Geology, 150(1-4):113-129.

Voulgaris, G. and Collins, M.B., 1991. Linear features on side-scan sonar images: An algorithm for the correction of angular distortion. Marine Geology, 96(1-2): 187-190.

W

Wienberg, C. and Hebbeln, D., 2005. Impact of dumped sediments on subaqueous dunes, outer Weser Estuary, German Bight, southeastern North Sea. Geo-Marine Letters, 25(1): 43-53.

Werner, B.T. and Kocurek, G., 1997. Bed-form dynamics: does the tail wag the dog? Geology, 25(9): 771-774.

Wessel, P. and Smith, W.H.F., 1998. New, improved version of Generic Mapping Tools released. EOS, Transaction, American Geophysical Union, 79(47): 579.

Wever, T.F., 2003. Speed of migrating bedforms on the seafloor - a review. FWG-Report 50, Forschungsanstalt der Bundeswehr für Wasserschall und Geophysik.

Whitehouse, R.J.S., Damgaard, J.S. and Langhorne, D.N., 2000. Sandwaves and seabed engineering ; the application to submarine cables. In: Marine Sandwave Dynamics I, Trentesaux A., Garlan T. and Le Bot, S.(Editors), International Workshop, March 23-24 2000, University Lille 1, France, pp. 227-234

Wilbers, A.W.E. and Ten Brinke, W.B.M., 2003. The response of subaqueous dunes to floods in sand and gravel bed reaches of the Dutch Rhine. Sedimentology, 50(6): 1013-1034.

Williams, A.T., Davies, P. and Bomboe, P., 1993. Geometrical simulation studies of coastal cliff failures in Liassic strata, South Wales, UK. Earth Surface Processes and Landforms, 18(8): 703-720.

Williams, T. and Kelley, C., 1998. Gnuplot an interactive plotting program. www. ucc.ie/gnuplot/gnuplot.html

Wolanski, E., Imberger, J. and Heron, M., 1984. Island wakes in shallow coastal waters. Journal of Geophysical Research, 89(C14): 10553-10569.

Woolf, D.K., Cotton, P.D. and Challenor, P.G., 2003. Measurements of the offshore wave climate around the British Isles by satellite altimeter. Philosophical Transaction of the Royal Society of London, 361: 27-31.

Y

Yalin, M.S., 1977. Mechanics of sediment transport, 2nd edition. Pergamon Press, Oxford., 298pp.

Yalin, M.S., 1992. River Mechanics. Pergamon Press, Oxford, 219 pp.

Yu, Y., Sternberg, R.W. and Beach, R.A., 1993. Kinematics of breaking waves and associated suspended sediment in the nearshore zone. Continental Shelf Research, 13(11): 1219-1242.

Z

Zeiler, M., Schulz-Ohlberg, J. and Figge, K., 2000. Mobile sand deposits and shoreface sediment dynamics in the inner German Bight (North Sea). Marine Geology, 170(3-4): 363-380.

Zimmerman, J.T.F., 1981. Dynamics, diffusion and geomorphological significance of tidal residual eddies. Nature, 290: 549-555.

Annexes

A.1. Auto-correlation source code

```
/*************************************************************************
                acf.c  -  Autocorrelation function in 2 dimension
                  ------------------
   begin          : Wed May 21 15:25:16 BST 2003
   copyright        : (C) 2003 by Thierry Schmitt
   email          : schmittt@cf.ac.uk
*************************************************************************/


#include <stdio.h>

#define EXIT_USAGE 10
#define EXIT_FILE 11
#define EXIT_MEMORY 12

                        /*****************************
                        Functions used to compute the ACF
                        *****************************/


float** fmatrix_allocate_2d(int vsize,int hsize)

/*************************************************************************
aim: allocate memory for a 2d regular grid with known dimension
method: allocate a vsize pointers matrix on a 2d matrix imptr, init
*************************************************************************/
{
 int i;
 float** matrix;
 float *imptr;
 matrix=(float**)malloc(sizeof(float*)*vsize);
 if (matrix==NULL)
        {
        printf("Exiting – memory problem\n");
        exit(12) ;
        }
 imptr=(float*)malloc(sizeof(float)*hsize*vsize);
 if (imptr==NULL)
        {
        printf("Exiting – memory problem\n ");
        exit(12) ;
        }
 for(i=0;i<vsize;i++,imptr+=hsize)
        matrix[i]=imptr;
free(imptr) ;
return matrix;
}
```

```
void free_2d_matrix(float **mat)

/*************************************************************************
aim: free memory of a 2d grid
*************************************************************************/
{
free(mat[0]);
free(mat);
}

void load_matrix(FILE *file,float **tab,int row,int col)

/*************************************************************************
aim: load a file and put it into an array
method: read each value and put it in the array, starting in the top left of the grid ie
use grd2xyz -ZTL method row by row
*************************************************************************/
{
float z;
int i_col=0,i_row=0;

while (fscanf(file,"%f",&z)!=EOF)
        {
                if (i_col<col)
                {
                        tab[i_row][i_col]=z;
                        i_col++;
                }
                else
                {
    i_col=0;
                        i_row++;
                        tab[i_row][i_col]=z;
                        i_col++;
                }
        }
}
```

```
float mean(float **ttab, int sizex,int sizey)

/*********************************************************************
aim: compute the mean of the data within a square window ttab
*********************************************************************/
{
float M=0;
int i,j;
for (i=0;i<sizex;i++)
        {
        for (j=0;j<sizey;j++)
                {
                M=M+ttab[i][j];
                }
        }
return M/(sizex*sizey);
}

float std_dev(float **raw_tab, int window_size_x, int window_size_y)

/*********************************************************************
aim: compute the standard deviation of the data within a square window raw_tab
*********************************************************************/
{
 float moy,variance=0;
 int i,j;
 moy=mean(raw_tab,window_size_x,window_size_y);
 for (i=0;i<window_size_x;i++)
        {
         for (j=0;j<window_size_y;j++)
        {
        variance=variance+(raw_tab[i][j]-moy)*(raw_tab[i][j]-moy);
        }
return variance/(window_size_x*window_size_y);
}
```

```
                    /*******************************
                    Autocorrelation function in 2 dimension
                    *******************************/

float **ACF2D(float **raster,int nrows, int ncols)

/*************************************************************************
aim: Calculate spatial autocorrelation for any lag in a window raster with the
topographic information (height)
method: For a specified lag we first need to calculate mean within the common area
of the raster window with its lagged copy we can then calculate the variance and
covariance within this same area

*************************************************************************/
{
float zibar,zjbar,covar,vari,varj,var,zi,zj;
int row,col, xoffset,yoffset,n;
float **result;

result=fmatrix_allocate_2d(nrows+1,ncols+1);

        /*For any lag defined by xoffset and yoffset*/

for (yoffset=-1*(nrows/2);yoffset<=(nrows/2);yoffset++)
        {
        for (xoffset=-1*(ncols/2);xoffset<=(ncols/2);xoffset++)
                {
                zibar= 0.0;
                zjbar= 0.0;
                n= 0;
                covar= 0.0;
                vari = 0.0;
                varj = 0.0;

                /* First pass - find number of samples and calculate the mean */

                for (row=0;row<nrows;row++)
                        if ((row+yoffset<nrows) && (row+yoffset>=0))
                                for (col=0;col<ncols;col++)
                                        if ((col+xoffset<ncols) && (col+xoffset>=0))
                                                {
                                                zi = raster[row][col];
                                                zj = raster[row+yoffset][col+xoffset];
                                                zibar += zi;
                                                zjbar += zj;
                                                n++;
                                                }
                zibar /= n;
                zjbar /= n;
```

```
                /* Second pass - find variance and co-variance  */

                for (row=0;row<nrows;row++)
                        if ((row+yoffset<nrows) && (row+yoffset>=0))
                                for (col=0;col<ncols;col++)
                                        if ((col+xoffset<ncols) && (col+xoffset>=0))
                                                {
                                                zi = raster[row][col];
                                                zj = raster[row+yoffset][col+xoffset];
                                                covar += (zi - zibar) * (zj - zjbar);
                                                vari  += (zi - zibar) * (zi - zibar);
                                                if ((row + yoffset*2 >=nrows) || (row +
                                                yoffset*2 < 0) || (col + xoffset*2 >=
                                                ncols) || (col + xoffset*2 < 0))
                                                        varj  += (zj - zjbar) * (zj - zjbar);
                                                }
                var = (vari + varj);

                if (var != 0.0)
                        result[yoffset+nrows/2][xoffset+ncols/2] = *covar/var;
                        else
                        result[yoffset+nrows/2][xoffset+ncols/2] = 1;

                } /*end of xoffset lag*/
        }/*end of yoffset lag*/
 return result;
} /*end of acf2d function*/


                                /***********
                                Main Function
                                ***********/


int main (int argc, char *argv[])
{
FILE *zfile;
int nrow, ncol,i,j;
float **array;
float **array_acf;

if (argc !=4)
        {
        printf("usage: acf file nrow ncol\n");
        exit(EXIT_USAGE);
        }
else
        zfile=fopen(argv[1],"r");

if (zfile==NULL)
```

```
        {
        printf("error opening %s --------abort\n",argv[1]);
        exit(EXIT_FILE);
        }
nrow=atoi(argv[2]);
ncol=atoi(argv[3]);

/* Arrays creation*/
array=fmatrix_allocate_2d(nrow,ncol);
array_acf=fmatrix_allocate_2d(nrow,ncol);
load_matrix(zfile,array,nrow,ncol);

/*Computation of ACF*/
array_acf=ACF2D(array,nrow,ncol);
/*Outputting to standard output*/
for (j=0;j<nrow;j++)
        {
        for (i=0;i<ncol;i++)
                printf("%f\n",array_acf[j][i]);
        }
/*Freeing memory space*/
free_2d_matrix(array_acf);
free_2d_matrix(array);
}
```

A.2. Sand dune migration and associated specific sand flux for the Helwick

UTM Easting (m)	UTM Northing (m)	Dune Migration ($m.y^{-1}$)	Specific Flux ($kg.m^{-1}.s^{-1}$)
Singlebeam vs. multibeam surveys			
414059.3	5709224	27.38486	0.01702
414176.3	5709230	58.19268	0.03159
414287.9	5709241	47.92341	0.021595
414412.1	5709255	51.34638	0.019855
416319.5	5709443	0.001095	6.56E-07
415240	5709502	51.72671	0.018399
415372.3	5709505	54.76971	0.024297
415511	5709513	60.85499	0.030688
415607.8	5709525	30.4275	0.009218
415733	5709525	24.34222	0.011627
415846.7	5709526	3.04264	0.001753
413058.1	5709634	85.57754	0.032907
413188.5	5709631	106.1161	0.038878
413326.8	5709633	89.00051	0.032021
413493.7	5709631	85.57754	0.030225
413618.7	5709635	102.6931	0.034557
413855.9	5709632	82.15457	0.024652
413965.4	5709640	95.84681	0.032683
414098.6	5709639	78.73123	0.029095
414213.1	5709640	44.50044	0.012832
414348.7	5709643	61.61565	0.023068
414520.8	5709644	58.19268	0.025785
414729.4	5709643	71.88529	0.033255
415203.8	5709644	6.846196	0.0042828
415339.3	5709656	47.92341	0.019986
415438.6	5709648	41.0771	0.013468
415542.9	5709652	51.34638	0.014397
415636.5	5709665	34.23116	0.012606
415811.2	5709661	6.846305	0.002776
415876.5	5709661	20.53855	0.003054
415949.6	5709659	6.846305	0.001901
414127.4	5709732	69.98328	0.033495
414266.5	5709722	63.898	0.023374
414403.2	5709717	79.11156	0.034326
414577.1	5709712	82.15457	0.041158
414780.9	5709725	69.98328	0.033705
415170.2	5709734	79.11156	0.041443
415346.5	5709733	54.76971	0.021715
415441.4	5709733	42.59842	0.016382
415555.2	5709729	57.81235	0.013165
415659.4	5709731	48.68407	0.018409
415840.6	5709730	24.34222	0.011027
415166	5710096	13.44332	0.007058
413254.9	5710086	20.16479	0.011172
413416.4	5710080	23.52571	0.008805
413492.6	5710071	36.96866	0.017678
413602.2	5710059	33.60811	0.021917

413872.7	5710041	53.77253	0.02956
414019.7	5710015	40.32958	0.023947
415163.3	5709930	53.77253	0.013479
413083.8	5709964	26.88627	0.00885
413222.1	5709952	29.87379	0.014262
413328.7	5709942	47.79785	0.020646
413456.1	5709939	47.79785	0.022314
413846.9	5709922	47.79785	0.030055
413993.5	5709914	83.64632	0.059695
414390	5709893	59.74758	0.0229
414610.7	5709884	65.72227	0.044997
414769.4	5709879	65.72227	0.033061
414937.7	5709867	83.64632	0.031083
415142.8	5709864	56.76006	0.016139
415236	5709856	56.76006	0.012572
415419.5	5709844	71.69695	0.049456
415519.8	5709841	47.79785	0.013367

2001 and 2002 multibeam survey comparison

413309.6	5708908	27.42172	0.016466
413377.1	5708916	22.85156	0.029299
413475.4	5708928	36.56242	0.018533
413537	5708935	34.27715	0.03719
413614.4	5708944	31.99225	0.013952
413672	5708951	31.99225	0.027848
413732.6	5708958	36.56242	0.021372
413814.1	5708968	27.42172	0.019443
413893.5	5708977	38.84768	0.022721
413954.1	5708985	31.99225	0.029313
414041.5	5708995	31.99225	0.03193
414139.8	5709007	36.56242	0.029909
414219.2	5709016	43.41785	0.027331
414259	5709021	41.13258	0.009944
414324.5	5709028	38.84768	0.023727
414399	5709037	36.56242	0.038153
414504.3	5709050	47.98801	0.057716
414618.5	5709063	29.70699	0.051213
414765.4	5709080	57.12871	0.048048
414867.7	5709092	59.41397	0.084016
415005.8	5709109	63.98414	0.093729
415567.9	5709175	70.83957	0.108445
415668.2	5709187	75.4101	0.046772
415743.6	5709196	84.55043	0.070435
413301.6	5708958	27.42172	0.010661
413375.1	5708966	29.70699	0.03464
413505.2	5708982	18.28139	0.021304
413648.2	5708998	31.99225	0.024626
413772.3	5709013	20.56629	0.017625
413871.7	5709025	29.70699	0.016012
413928.3	5709032	27.42172	0.020752
414019.6	5709042	29.70699	0.028775
414371.2	5709084	36.56242	0.030423
414456.6	5709094	34.27715	0.024804
414802.2	5709135	20.56629	0.010117
414961.1	5709154	63.98414	0.063144

415528.1	5709220	77.695	0.079897
413345.3	5709013	9.140695	0.009728
413483.4	5709029	11.4256	0.012171
413624.4	5709046	36.56242	0.016338
413748.5	5709060	34.27715	0.031031
413997.8	5709090	31.99225	0.020664
414329.5	5709129	25.13682	0.013781
414434.7	5709141	25.13682	0.018095
414560.9	5709156	68.55467	0.060256
414666.1	5709169	66.2694	0.043982
413424.8	5709122	18.97197	0.012108
413853.8	5709173	59.28695	0.026359
413948.1	5709184	66.40153	0.031203
414038.5	5709195	56.91555	0.009511
414136.8	5709206	47.42956	0.025206
414269.9	5709222	54.54414	0.034628
414379.1	5709235	56.91555	0.031812
414514.2	5709251	71.14471	0.030213
414637.3	5709265	66.40153	0.038312
416159.8	5709445	23.71478	0.006012
416293.8	5709461	42.68675	0.021594
413730.6	5709208	66.40153	0.040101
413834.9	5709220	61.65872	0.040356
414022.6	5709243	85.3735	0.030964
414124.9	5709255	59.28695	0.038899
414260	5709271	64.03013	0.037029
415066.4	5709366	52.17274	0.022341
415218.3	5709384	16.60057	0.007207
415726.8	5709444	42.68675	0.013696
415942.3	5709469	18.97197	0.009063
416032.6	5709480	47.42956	0.027754
416201.5	5709500	47.42956	0.026844
414116	5709304	66.40153	0.033135
414256	5709320	73.51611	0.027884
414358.3	5709332	61.65872	0.021885
415146.8	5709425	4.74281	0.001456
415345.4	5709449	35.57217	0.015832
415553	5709473	14.2288	0.00383
415659.2	5709486	59.28695	0.035181
415791.3	5709502	47.42956	0.020936
415951.2	5709520	18.97197	0.007254
416213.4	5709551	30.82936	0.018214
413800.2	5709316	52.17274	0.025606
413923.3	5709331	64.03013	0.026702
414034.5	5709344	75.88752	0.025635
414250	5709370	49.80133	0.019751
414367.2	5709383	40.31535	0.015211
414666.1	5709419	49.80133	0.018495
415389.1	5709504	14.2288	0.006103
415522.2	5709520	2.371405	0.000969
415826.1	5709556	59.28695	0.029013
415951.2	5709570	28.45796	0.014248
413587.6	5709341	73.51611	0.015766
413677	5709352	42.68675	0.01477
413825	5709369	61.65872	0.024106
413921.3	5709381	26.08619	0.009891

414048.4	5709396	42.68675	0.015547
414654.2	5709467	83.0021	0.021705
414986.9	5709507	61.65872	0.019173
415127.9	5709523	59.28695	0.021128
415281.9	5709541	2.371405	0.000806
415425.9	5709558	14.2288	0.004651
415538.1	5709572	2.371405	0.000882
415851.9	5709609	80.63033	0.030152
415967.1	5709622	37.94394	0.014747

A.3. Sand dune migration and associated specific sand flux for East Nash

UTM Easting (m)	UTM Northing (m)	Dune Migration ($m.y^{-1}$)	Specific Flux ($kg.m^{-1}.s^{-1}$)
	19 days comparison		
459008.4	5695123	83.6	0.042624
458915.9	5695147	3.8	0.001948
458802.5	5695184	128.8	0.071927
458683.2	5695235	67.0	0.032816
458591.3	5695279	23.0	0.012606
458446.5	5695343	117.4	0.078396
458289.6	5695413	5.4	0.002845
458197.9	5695451	194.8	0.040308
460023.2	5695193	147.0	0.016862
459959.1	5695262	35.3	0.003225
459873.4	5695327	217.0	0.04227
459814.3	5695366	117.3	0.0166
459741.2	5695426	233.0	0.02934
459672	5695502	423.5	0.047169
459725	5695563	137.7	0.013166
459765.1	5695513	172.9	0.021554
459831	5695428	134.7	0.019502
459892.5	5695352	144.3	0.026808
459960	5695286	231.4	0.051772
460037.5	5695215	46.1	0.011075
460114	5695136	27.5	0.008113
459714.7	5695674	94.4	0.015983
459746.1	5695642	4.0	0.000349
459788.1	5695585	84.4	0.013921
459835.8	5695525	1.2	0.000271
459872.9	5695474	5.6	0.000677
459905.6	5695435	41.5	0.003972
459939.1	5695396	36.6	0.006404
459988.4	5695333	207.2	0.054462
460044.7	5695257	171.2	0.026658
460114.7	5695163	715.5	0.150622
460184.6	5695083	608.7	0.109094
460264.2	5694992	697.9	0.097135
460125.5	5695233	22.1	0.009599
460062.3	5695325	205.4	0.054598
459907.1	5695527	45.8	0.018715
459854.9	5695599	15.2	0.006224
459803.4	5695663	31.7	0.012224
459777.3	5695696	32.6	0.003524
459755.2	5695732	26.1	0.004886
459729.1	5695771	19.9	0.004421
459709.1	5695794	44.1	0.004126
459692.1	5695813	79.5	0.003471
459673.1	5695839	36.4	0.006288
459647.2	5695879	79.9	0.005774
459596.3	5695954	10.6	0.000583
459561.3	5695990	139.1	0.013428

460103.5	5695347	221.4	0.051472
460030.1	5695445	52.6	0.016183
459957	5695556	13.8	0.003422
459916.3	5695608	16.5	0.003115
459902.1	5695625	11.0	0.000892
459825.2	5695726	28.0	0.002026
459807.5	5695752	51.9	0.005447
459785.1	5695784	7.7	0.00219
459761.1	5695815	52.3	0.007336
459734.9	5695845	15.4	0.003033
459703	5695882	121.9	0.020106
459680.8	5695906	55.1	0.004841
459658.9	5695931	9.4	0.001482
459779.1	5695882	49.6	0.002378
459789.1	5695861	27.3	0.002461
459805.5	5695833	58.7	0.011708
459820.4	5695813	9.8	0.001513
459842.6	5695782	27.3	0.006659
459860.2	5695757	66.0	0.007057
459994	5695542	1.9	0.000176

263 days comparison

458450.9	5695342	144.1	0.09496
458290.2	5695413	147.3	0.076082
458455.8	5695418	173.6	0.077897
458693.3	5695351	217.2	0.083461
458443.5	5695469	134.8	0.05267
460648.1	5694656	7.7	0.002041
460610.5	5694727	2.5	0.000554
458973.6	5696639	28.2	0.008764
458919.1	5696677	36.7	0.008325
458871.1	5696711	31.6	0.008158
458823.6	5696741	25.8	0.006602
458707.9	5696818	6.5	0.001821
458620.1	5696890	2.5	0.000983
458552.5	5696950	5.2	0.002052
458516.2	5696986	9.0	0.001553
458470.6	5697028	7.8	0.001972
458413.9	5697076	8.9	0.00381
458352.1	5697129	3.2	0.001128
458287.4	5697184	5.2	0.001027
458221.9	5697240	9.8	0.003117
458153.4	5697293	5.2	0.000953
457868.3	5697574	19.2	0.003531
457920.9	5697530	18.0	0.003962
457987.2	5697473	14.1	0.003015
458074.2	5697398	12.7	0.003529
458144.9	5697337	18.0	0.005098
458177.3	5697312	10.9	0.002035
458227.3	5697271	5.6	0.001752
458302.6	5697212	7.7	0.001003
458359.5	5697166	3.2	0.000759
458419.6	5697114	10.2	0.003433
458481.4	5697064	8.4	0.001679
458555.9	5697001	2.5	0.001336

458635.5	5696932	5.0	0.001232
458720.1	5696865	7.1	0.003522
458788.2	5696813	16.9	0.006002
458848	5696768	21.9	0.008965
458896.1	5696728	25.8	0.008128
458944.1	5696690	27.0	0.008858
458992.5	5696648	27.0	0.010995
459045.8	5696597	32.2	0.008834
459091	5696556	30.2	0.006005
459141.7	5696515	39.3	0.006795
459189.2	5696473	26.5	0.003932
459278.7	5696489	4.0	0.001107
459192.8	5696567	0.9	0.000346
459152.2	5696599	7.5	0.001162
459071	5696670	26.8	0.006853
459013.2	5696718	28.4	0.012759
458961.1	5696760	27.2	0.009355
458884.2	5696816	22.2	0.009186
458832.6	5696858	27.8	0.011568
458746.6	5696934	15.1	0.008894
458366.2	5697244	9.5	0.003197
458296.4	5697301	15.2	0.003696
458228.8	5697354	23.3	0.004701
457999.3	5697541	14.2	0.004306
457938.6	5697599	18.5	0.004372
458018.7	5697602	33.6	0.009564
458075.8	5697553	28.3	0.004904
458133.3	5697506	27.0	0.006694
458212.4	5697451	19.3	0.004859
458298.6	5697385	29.5	0.005253
458590.5	5697142	29.0	0.011709
458636.8	5697100	26.1	0.009272
458682.5	5697059	21.5	0.00338
458749.9	5697004	23.9	0.013102
458809.8	5696956	23.8	0.010008
458853.3	5696917	14.8	0.003439
458928.8	5696858	15.7	0.010534
459013.3	5696792	10.7	0.002445
459060.7	5696756	13.0	0.005605
459095.4	5696727	12.9	0.002748
459142.4	5696684	1.8	0.000715
459191.2	5696640	3.9	0.000468
459219.8	5696617	19.3	0.006567
459267.9	5696581	14.3	0.003863
459344.2	5696519	47.1	0.017292
459439.5	5696448	4.5	0.000596
459466.5	5696424	8.0	0.000846
459347.6	5696605	32.9	0.008456
459237.1	5696696	8.7	0.004217
459141.9	5696778	2.5	0.001358
459077.7	5696835	13.5	0.004358
459021.9	5696879	1.0	0.000355
458973.2	5696916	0.6	0.000262
458869.4	5696991	5.7	0.002447
458789.4	5697060	16.4	0.008759
458702.8	5697134	24.7	0.009762

458645	5697185	32.9	0.007004
458590.2	5697236	32.3	0.00946
458523.8	5697296	25.2	0.007365
458438	5697364	26.8	0.013082
458362.6	5697422	26.3	0.00793
458264.9	5697495	31.3	0.011411
458170.5	5697575	36.5	0.011498
458213.3	5697605	35.3	0.007276
458319.4	5697518	27.2	0.007523
458399.6	5697453	21.1	0.005549
458480.7	5697387	31.5	0.009089
458559.3	5697321	25.7	0.00475
458618.4	5697273	13.3	0.004449
458674.4	5697220	23.1	0.004917
458740.9	5697161	16.4	0.005303
458824	5697088	6.1	0.002365
458919.4	5697013	1.4	0.000383
459014.9	5696939	5.1	0.001467
459082.7	5696889	3.5	0.001085
459150.2	5696834	1.4	0.000343
459206.9	5696785	5.6	0.000958
459283	5696720	31.0	0.003042
459337.4	5696673	28.5	0.003873
459410.2	5696609	51.6	0.006275
458675.8	5697281	78.4	8.56E-05
457555.2	5696612	163.5	0.037843
457614.8	5696573	189.4	0.021708
457679.1	5696528	168.6	0.029303
457793.9	5696457	107.8	0.02797
457966.3	5696351	54.0	0.013957